AD-E300 375

(12) LEVEL II

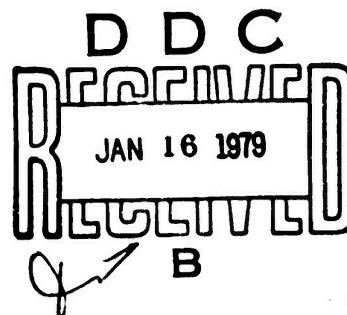ADA063393

DNA 4620T

STRESS PROGRAM

PROCEEDINGS OF THE STRESS DATA REVIEW MEETING,
29-30 NOVEMBER 1977

Compiled by: D. R. McDaniel

SRI INTERNATIONAL
333 Ravenswood Avenue
Menlo Park, California 94025

DDC FILE COPY

DDC
RECEIVED
JAN 16 1979
B

June 1978

Topical Report

APPROVED FOR PUBLIC RELEASE;
DISTRIBUTION UNLIMITED

Prepared for: Director

DEFENSE NUCLEAR AGENCY
Washington, D.C. 20305

Copy No. 6

REPORT DOCUMENTATION PAGE	READ INSTRUCTIONS BEFORE COMPLETING FORM

1. REPORT NUMBER DNA 4620T	2. GOVT ACCESSION NO. DNA, SBIE 4620T AD-E300 375	3. RECIPIENT'S CATALOG NUMBER

4. TITLE (and Subtitle) PROCEEDINGS OF THE STRESS DATA REVIEW MEETING, 29-30 November 1977	5. TYPE OF REPORT & PERIOD COVERED Topical Report, 29-30 November 1977
	6. PERFORMING ORG. REPORT NUMBER SRI Project 4960

7. AUTHOR(s) Compiled by D. R. McDaniel	8. CONTRACT OR GRANT NUMBER(s) Contract DNA001-76-C-0223

9. PERFORMING ORGANIZATION NAME AND ADDRESS SRI International 333 Ravenswood Avenue Menlo Park, CA 94025	10. PROGRAM ELEMENT, PROJECT, TASK AREA & WORK UNIT NUMBERS NWET 62710H, I25AAXHX X63531

11. CONTROLLING OFFICE NAME AND ADDRESS Director Defense Nuclear Agency Washington, D.C. 20305	12. REPORT DATE June 1978
	13. NUMBER OF PAGES 372

14. MONITORING AGENCY NAME & ADDRESS(if different from Controlling Office)	15. SECURITY CLASS (of this report) UNCLASSIFIED
	15a. DECLASSIFICATION/DOWNGRADING SCHEDULE

16. DISTRIBUTION STATEMENT (of this Report)

Approved for public release; distribution unlimited.

355 p

17. DISTRIBUTION STATEMENT (of the abstract entered in Block 20, if different from Report)

I25AAXH   X635

18. SUPPLEMENTARY NOTES

19. KEY WORDS (Continue on reverse side if necessary and identify by block number)

Barium releases	Plasma physics
Upper atmospheric physics	Striations
Propagation	Nuclear effects
Satellite communications	

20. ABSTRACT (Continue on reverse side if necessary and identify by block number)

A STRESS (Satellite Transmission Effects Simulations) data review meeting was held at Headquarters DNA on 29-30 November 1977. These proceedings contain the reports of the various STRESS experimenters and program participants as presented at the meeting. STRESS was a communications experiment conducted at Eglin AFB during February and March 1977. The purpose of the experiment was to evaluate satellite communication

(continued)

DD ,FORM 1473   EDITION OF 1 NOV 65 IS OBSOLETE
1 JAN 73

links under artificially produced conditions that simulated many
aspects of a post-nuclear-burst environment. This environment was
produced by the use of barium plasma clouds in the lower F-region
of the ionosphere.

CONTENTS

INTRODUCTION

General

The STRESS (Satellite TRansmission Effects SimulationS) experiment took place at Eglin AFB, Florida during the period 29 November 1976 to 15 March 1977. The principal purpose of the experiment was to evaluate satellite communication links under conditions that simulate many aspects of a post-nuclear-burst environment. This environment was produced by use of ionospheric barium releases at an altitude of 185 km. An airborne receiving station was positioned so that it was occulted by the barium cloud while receiving UHF signals from a synchronous communication satellite.

A data review meeting on the results of STRESS was held at Headquarters, DNA, on 29-30 November. While some of the experimenters had not yet completed their analysis in detail, it was felt that enough of the results were in to provide a significant impact on future test planning. The presentation of each experimenter at the meeting is presented in these proceedings.

Objectives

The detailed objectives of the STRESS experiment were as follows:

(1) Demonstrate a capability to predict, from communication theory and striated-plasma propagation theory, both the UHF communication-channel characteristics of a striated plasma cloud and the performance of a communication system operating through such a cloud.

(2) Obtain data on the dissipation of striated plasma structure in the ionosphere by optical and UHF probe signal measurements.

(3) Measure the performance of the LES-8/9 Forward-to-Force Element and Report-Back communication links operating through the fading environment created by the barium plasma cloud, and assess the implications for operation in a HANE environment.

3

Test Concept

The STRESS experiment consisted to two phases: Pre-STRESS, occurring in November-December 1976, and STRESS itself, occurring in February-March 1977.

Pre-STRESS consisted of a single 48-kg barium event, launched on 1 December 1976. The purposes of this event were to (1) ascertain that the aircraft positioning system worked as planned, (2) determine whether any biases existed between the cloud positions as determined by radar and TV tracking instrumentation, (3) check ion cloud phenomenology, such as motion and striation formation, and (4) make preliminary satellite-transmission measurements. Test elements of Pre-STRESS were as follows:

- 48-kg barium release
- FPS-85 radar system
- TV tracking system
- AFAL aircraft No. 662
- Ground optics
- Range support systems.

STRESS consisted of five 48-kg barium releases, launched during the period 22 February to 14 March 1977. Only one event was scheduled on any given day. Event times varied from the time at 3° solar depression angle (evening twilight) for the first release to up to 78 minutes earlier for the fifth release. Time-phasing of the releases in this manner allowed observation of late-time striations--phenomenology that had not heretofore been observed. During each of these releases, the AFAL aircraft was directed so that it made multiple passes through the ion cloud shadow, recording signals from the satellite as it did so. Concurrently with the satellite measurements, auxiliary ground instrumentation gathered data on the evolution of the barium plasma structure to assist in the interpretation of the UHF propagation effects observed and to further current knowledge in

4

striation decay phenomenology. In addition, rocket-borne probes were fired through the ionized cloud to make in-situ measurements of electron density. Test elements of STRESS were as follows:

- Five 48-kg barium releases
- Six rocket-borne, electron-density probes
- FPS-85 radar system
- TV tracking system
- AFAL aircraft No. 662
- Ground optics
- Fabry-Perot optical interferometer
- Ionosonde
- Range support systems.

In addition to the above-listed test elements, Los Alamos Scientific Laboratory participated in STRESS in investigating the very-late-time spatial decay of plasma striations. They provided an array of intensified optical instruments, collocated at Tyndall AFB with the TV tracker, ground optics, and FP interferometer.

Test Organization

The STRESS satellite measurements were planned and carried out by ESL, Inc. The STRESS field operations necessary to accomplish the satellite measurements were planned and carried out by SRI International. The program participants and their areas of responsibility were as follows:

- SRI-Test planning and direction, and operation of TV tracking system, FPS-85 radar, and ionosonde
- ESL--Satellite measurements
- TIC--Ground photography
- SDC--Rocket operations
- USU--Probe payloads
- Thiokol--Barium payloads
- LMSC--Optical interferometer

- AFAL--Aircraft support and satellite measurements
- ESD--Satellite support
- RDA--Probe rocket coordination.

Figure 1 depicts the test organiza ion.

Summary of STRESS Events

The STRESS event summary is shown in Table 1, and c map showing the location of the releases and supporting instrumentation is depicted in Figure 2.

Table 1

SUMMARY OF STRESS EVENTS

Event	Date	Time Before Solar Depression Angle (min) = 6°	No. of Probes
ANNE	1 Dec 1976	0	0
BETTY	26 Feb 1977	13	0
CAROLYN	2 Mar 1977	15	0
DIANNE	7 Mar 1977	11	2
ESTHER	13 Mar 1977	75	2
FERN	14 Mar 1977	91	2
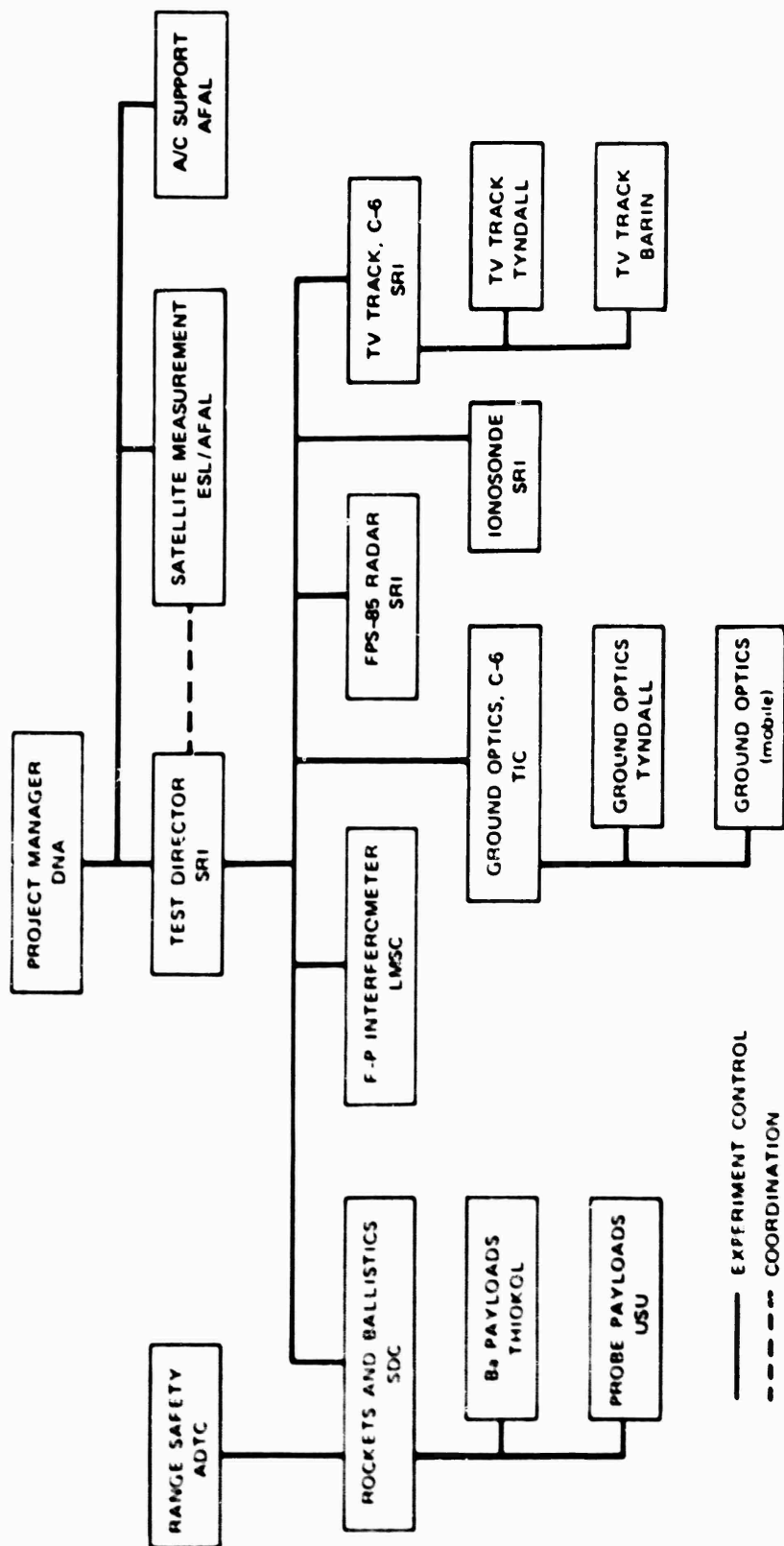
FIGURE 1 STRESS TEST OPERATIONS ORGANIZATION

7

FIGURE 2   RELEASE AND INSTRUMENTATION LOCATIONS

HIGH-RESOLUTION GROUND OPTICS MEASUREMENTS

W. P. Boquist

Technology International Corporation
Bedford, Massachusetts

9

HIGH-RESOLUTION GROUND OPTICS MEASUREMENTS

W. P. Boquist

Technology International Corporation
Bedford, Massachusetts

I INTRODUCTION

The participation of Technology International Corporation in DNA Project STRESS was for the purpose of providing general optical coverage of the barium release phenomenology during the time period a given cloud would be visible from the ground. Such coverage included:

(1) A photographic history of the morphological development of the neutral and ion coulds and evolving structure.

(2) Radiometric measurements of the ion cloud radiance and minimum column density.

(3) Two-station triangulation measurements of the obserable cloud motion(s).

(4) High-resolution coverage of plasma striations and spatial frequency.

The end requirement of this data acquisition was to aid in the interpretation and correlation of data obtained by other DNA experimenters in the areas of radar track and satellite transmission experiments. In addition, of course, an inherent result of the optical coverage is the general augmentation of the barium release phenomenological data base, particularly for the condition of early (pre-sunset) releases.

Table 1 summarizes the release parameters for the PRE-STRESS (one event) and STRESS (five events) experiments. All events involved a 48-kg payload of barium reactant mixture and were programmed for a nominal 185-km release altitude. The time of release with respect to a nominal solar zenith angle (namely, 96°) was varied from zero up to 90 minutes

Table 1

PROJECT STRESS OPERATIONAL PARAMETERS

EVENT	DATE	YIELD	HOB	RELEASE ANGLES	REMARKS
ANNE	1 DEC 1976	48KG	181±.5KM	96°	LES 9
BETTY	26 FEB 1977	48KG	(179)	96°-13 MIN	LES 9
CAROLYN	2 MAR 1977	48KG	(191)	96°-15 MIN	LES 9
DIANNE	7 MAR 1977	48KG	(185.5)	96°-11 MIN	LES 9
ESTHER	13 MAR 1977	48KG	(189)	96°-75 MIN	LES 8
FERN	14 MAR 1977	48KG	(186)	96°-90 MIN	LES 8

( ) INDICATES UNTRIANGULATED DETERMINATION

12

before release, as shown in Table 1. Thus, the last two events were actually released before sunset, as will be seen in more detail later. Optical observations of barium clouds at these altitudes are linked in a practical sense to solar angles of between about 96° and about 102°, regardless of the release times.

The satellite(s) used in conjunction with the STRESS transmission experiments were the Lincoln Laboratory LES-8 and LES-9 semi-synchronous satellites. LES-9 (to the east) was used on Events ANNE, BETTY, CAROLYN, and DIANNE. LES-8 (to the west) was used on Events ESTHER and FERN. A total of six ion-cloud sounding rockets were fired from the Eglin launch complex against the last three events.

Figure 1 is a map of the Eglin Gulf Test Range area showing the locations of the sub-release point of each event and the realtive locations of the ground optics sites. Eglin C-6 and Tyndall 9702 sites were for primary data acquisition. A mobile site was operated at different positions between the Eglin and Tyndall vicinities, as dictated by predictions for each event. A fourth site was operated by SRI for TIC at Barin Field, Alabama, and an AFAL crew member on board A/C 662 operated a fifth camera station for supplementary data.

Table 2 presents the actual release time for each of the STRESS events together with the relative release angle and local sunset time. Figure 2 plots, as a function of local time, the extent of optical coverage, the relative sunset time, and the times of rocket penetration in the ion cloud. The circles indicate the release time of a given experiment. When the release point was observed, the circle is shown as a solid. In the case of Event BETTY, natural clouds obscured the burst point, whereas for Events ESTHER and FERN the ambient (pre-sunset) sky background negated recording the release expansion.

II PHOTOGRAPHIC DATA

This section contains a selected sampling of the extensive photographic coverage obtained by TIC of the six barium release experiments in Project STRESS. For each event a photograph of the matured ion cloud
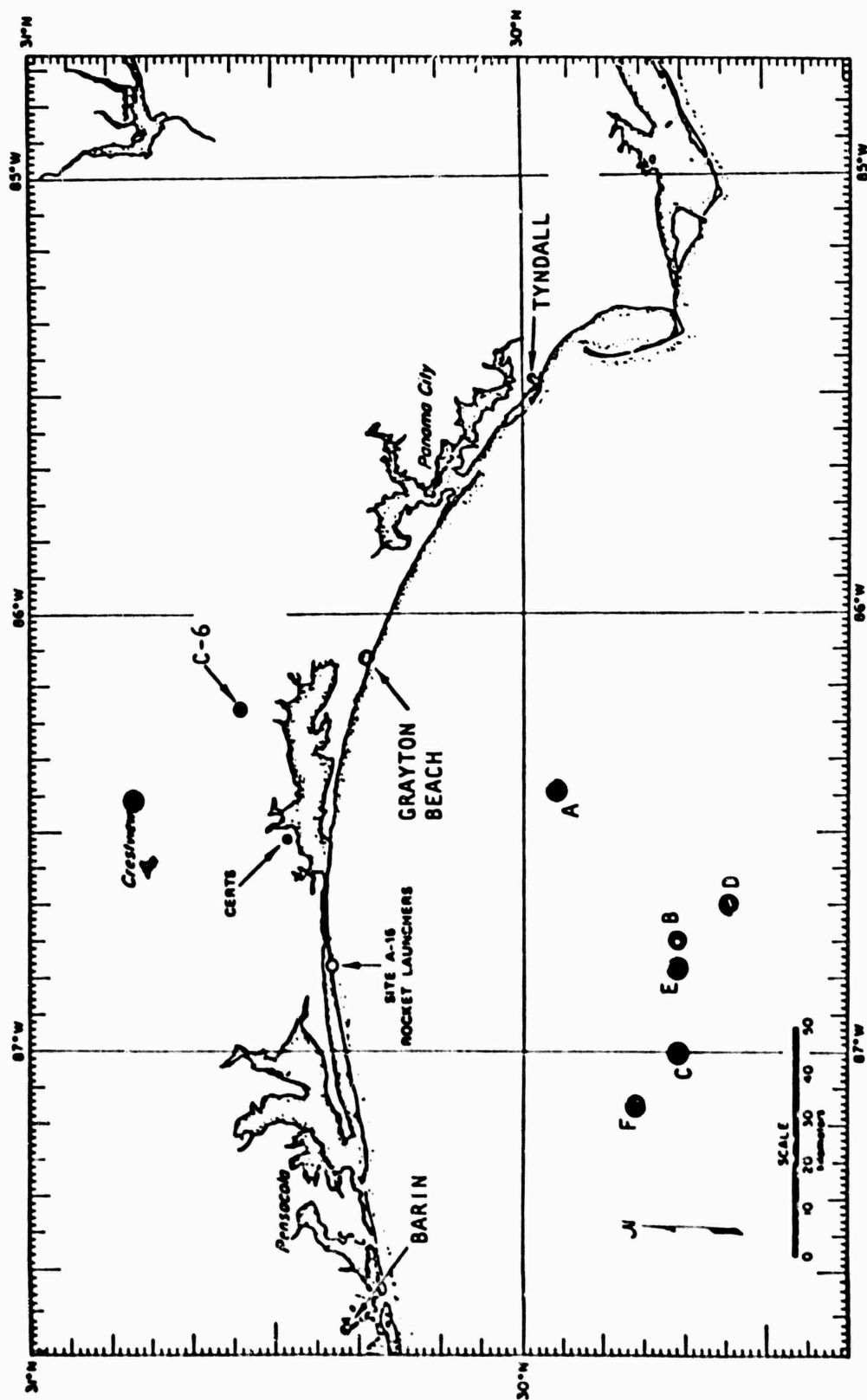
13

FIGURE 1   PROJECT STRESS SUB-RELEASE POINTS

14

Table 2

PROJECT STRESS RELEASE TIMES

EVENT	DATE	RELEASE TIME	RELEASE ANGLE	TIME OF 96°	SUNSET
	(LOCAL/GMT)	(LOCAL/GMT)	(SOLAR ZENITH)	(LOCAL/GMT)	(LOCAL)
ANNE	1 DEC 1976	5 11 43 PM (23 11 43)	96°	5 12 PM (23 12)	4 45 PM
BETTY	26 FEB 1977	5 52 29 PM (23 52 29)	96° - 13 MIN (93°)	6 06 PM (00 06)	5 39 PM
CAROLYN	2 MAR 1977	5 54 10 PM (23 54 10)	96° - 15 MIN (93°)	6 09 PM (00 09)	5 42 PM
DIANNE	7 MAR 1977 (8 MAR 1977)	6 01 10 PM (00 01 10)	96° - 11 MIN (93 1/2°)	6 12 PM (00 12)	5 45 PM
ESTHER	13 MAR 1977	5 01 08 PM (23 01 08)	96° - 75 MIN (79°)	6 16 PM (00 16)	5 ( ) PM
FERN	14 MAR 1977	4 46 09 PM (22 46 09)	96° - 90 MIN (76°)	6 16 PM (00 16)	5 49 PM

LOCAL TIME = GMT - 6 HOURS
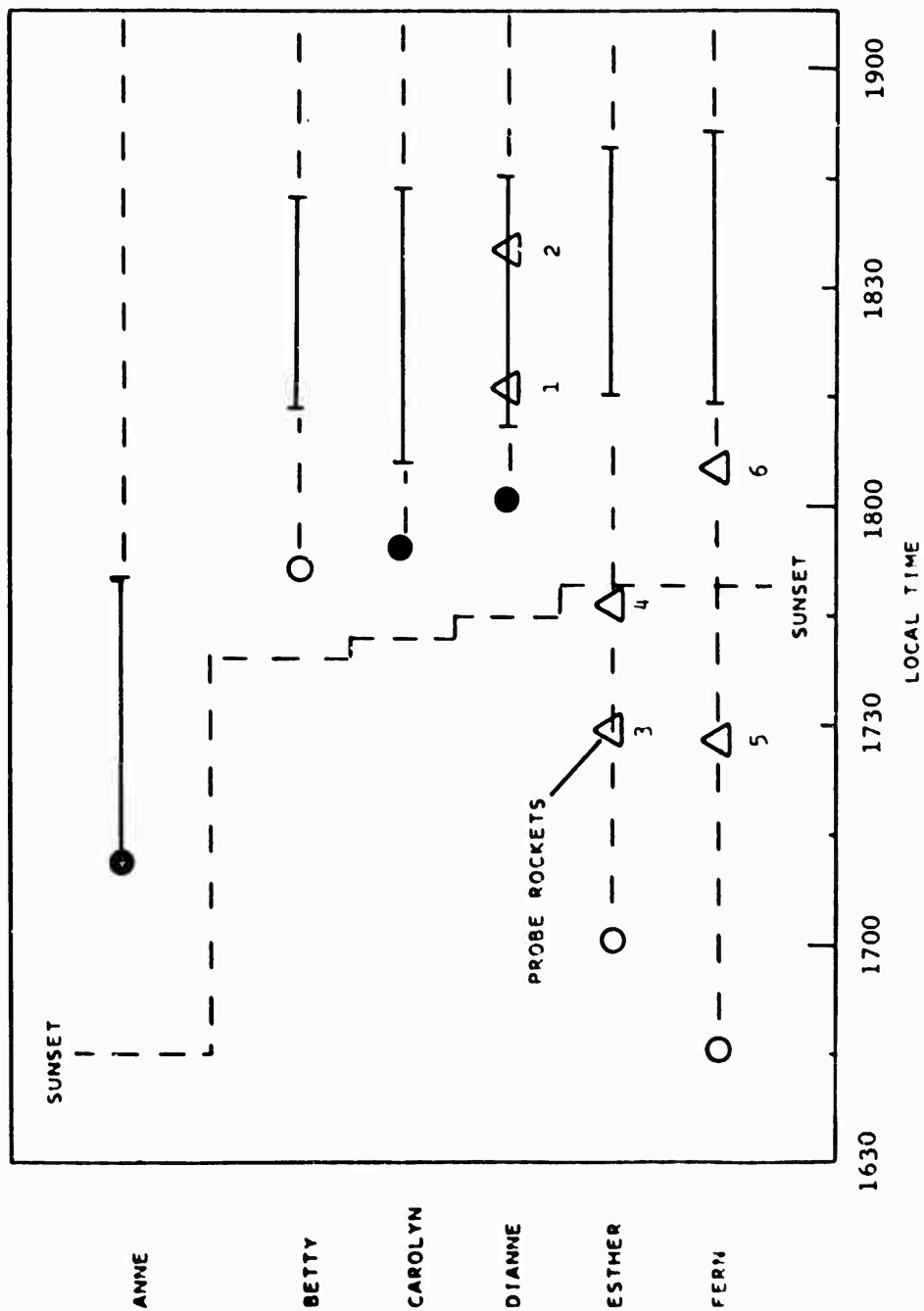
SOLAR RATE = APPROX. 4.4 MIN/DEGREE

15

FIGURE 2 PROJECT STRESS OPTICAL DATA COVERAGE

16

as seen from both the Tyndall 9702 and the Eglin C-6 ground optics sites is presented in a side-by-side comparison.

Figure 3 shows both the neutral and the ion cloud at R + 21 and R + 26 min for PRE-STRESS Event ANNE, from the Tyndall and C-6 site, respectively. In the Tyndall photograph the slope of the field-aligned (and straited) ion cloud from upper left to upper right corresponds to higher (southern) and lower (northern) altitudes along the field lines. In the C-6 photograph, however, because of the critical perspective with respect to the field lines, upper left is the lower (northern) end of the ion cloud striations, while lower right is the upper (southern, converging) end of the striations.

In Figure 4 the ion cloud of Project STRESS Event BETTY is shown at R + 30 and R + 33 min as seen from the Tyndall and C-6 site, respectively. (Note that the Tyndall photograph is of significantly greater magnefication than the C-6 photograph in this one instance, since it was taken from a large-format triangulation camera record because of moon flare in other Tyndall records.) In each instance, the left portion of the photographic image represents the lower, northerly end of the ion cloud. Some residual neutral cloud is still visible in the C-6 photograph.

Figure 5 shows the comparative views of Event CAROLYN at R + 36 and R + 40 min. In both the Tyndall and C-6 photographs, the left-most end of the striations is down and to the north. No neutral cloud is evident in these photographs. At later times, the Tyndall site was able to view the ion cloud essentially up the field lines passing through the striated cloud for a short period just before the sun set on the cloud.

The complementary perspectives of Event DIANNE from Tyndall and C-6 are shown in the Figure 6 ion cloud photographs at R + 34 and R + 35 min. This event was somewhat unique relative to the two previous events released at about the same solar depression angle, in that the cloud exhibited both significant east-west longitudinal distortion and detailed striated structure in its midsection at later times. This latter observation is more clearly evidenced in Figure 24 (see Section V of this paper), taken from a C-6 high-resolution photographic record.

17
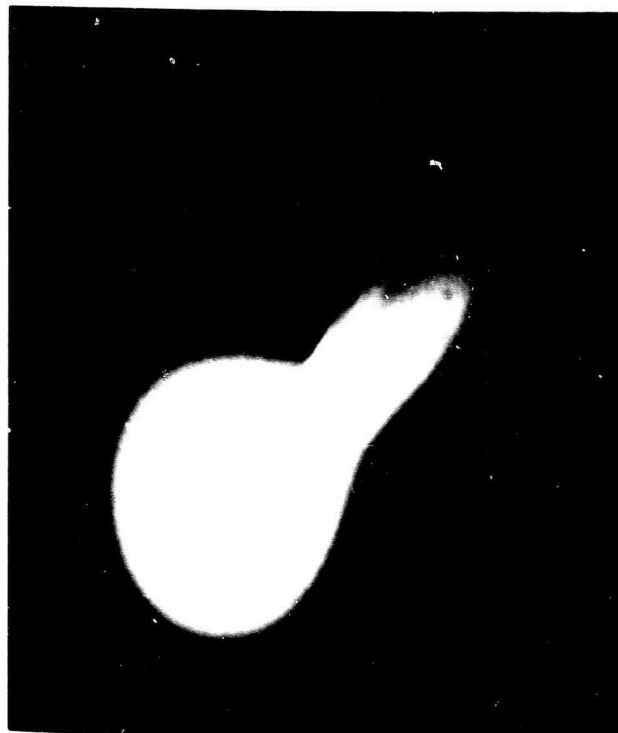
(a) R + 21 min, TYNDALL SITE

(b) R + 26 min, C-6 SITE

FIGURE 3   PROJECT PRE-STRESS, EVENT ANNE, RELEASE TIME 0511:43 LT

18

(a) R + 30 min, TYNDALL SITE

(b) R + 33 min, C-6 SITE

FIGURE 4   PROJECT STRESS, EVENT BETTY, RELEASE TIME 0552:29 LT

(a) R + 35 min, TYNDALL SITE

(b) R + 40 min, C-6 SITE

FIGURE 5   PROJECT STRESS, EVENT CAROLYN, RELEASE TIME 0554:10 LT

(a) R + 34 min, TYNDALL SITE

(b) R + 35 min, C-6 SITE

FIGURE 6   PROJECT STRESS, EVENT DIANNE, RELEASE TIME 0601:10 LT

Figure 7 shows the relative shapes of the Event ESTHER ion cloud at R + 1 hr 38 min as seen from the Tyndall and C-6 triangulation sites. Because of the nearly up-the-field-line prespective of the Tyndall site the striation images from this site show remarkable definition and identity. Event ESTHER was the first of two events released significantly before (approximately one hour) sunset to ascertain the late-time striation formation and longevity characteristics.

The late-time ion cloud of Event FERN is shown in Figure 8 at R + 1 hr 45 min, and R + 1 hr 54 min from Tyndall and C-6 sites, respectively. The FERN ion cloud moved very slowly. From C-6 the cloud appeared very diffuse with undefined structure. From Tyndall, however, portions of the cloud located close to an up-the-field-line perspective were much more definite. An example of this is the fine structure near the bottom-left region of the ion image.

III   RADIOMETRIC MEASUREMENTS

In order to provide for a limited optical determination of peak ion column density and reactant-ion yield of the STRESS barium releases, a calibrated filter camera system was operated on each of the events from the C-6 site area. The filter camera was fitted with a 4934-$\mathring{A}$ (50-$\mathring{A}$ passband) filter and had an effective field of view of approximately 20'.

The ion line at 4934 $\mathring{A}$ is one of the five ion emmissions that account for the majority of Ba II energy. A multi-slit spectrograph operated as part of the ground optics at Tyndall 9702 site provided data on the relative strengths of these lines. Figure 9 shows a representative sample of a transmission profile of one ion cloud spectrograph, showing the relative strength of 4934 $\mathring{A}$. (Note that 6497 $\mathring{A}$ is artificially weak because of the sensitivity fall-off of the particular film used in this instrument.)

For each event analyzed, approximately six data frames were chosen for reduction. A two-dimensional densitometric profile (contour) is made of each image, using a sensitometric calibration scale which, at this stage, can be either absolute or relative. From the isodensity trace

(a) R + 1 hr 36-1/2 min, TYNDALL SITE

(b) R + 1 hr 38 min, C-S SITE

FIGURE 7 PROJECT STRESS, EVENT ESTHER, RELEASE TIME 0501:08 LT

23

(a) R + 1 hr 45 min, TYNDALL SITE

(b) R + 1 hr 54 min, C-6 SITE

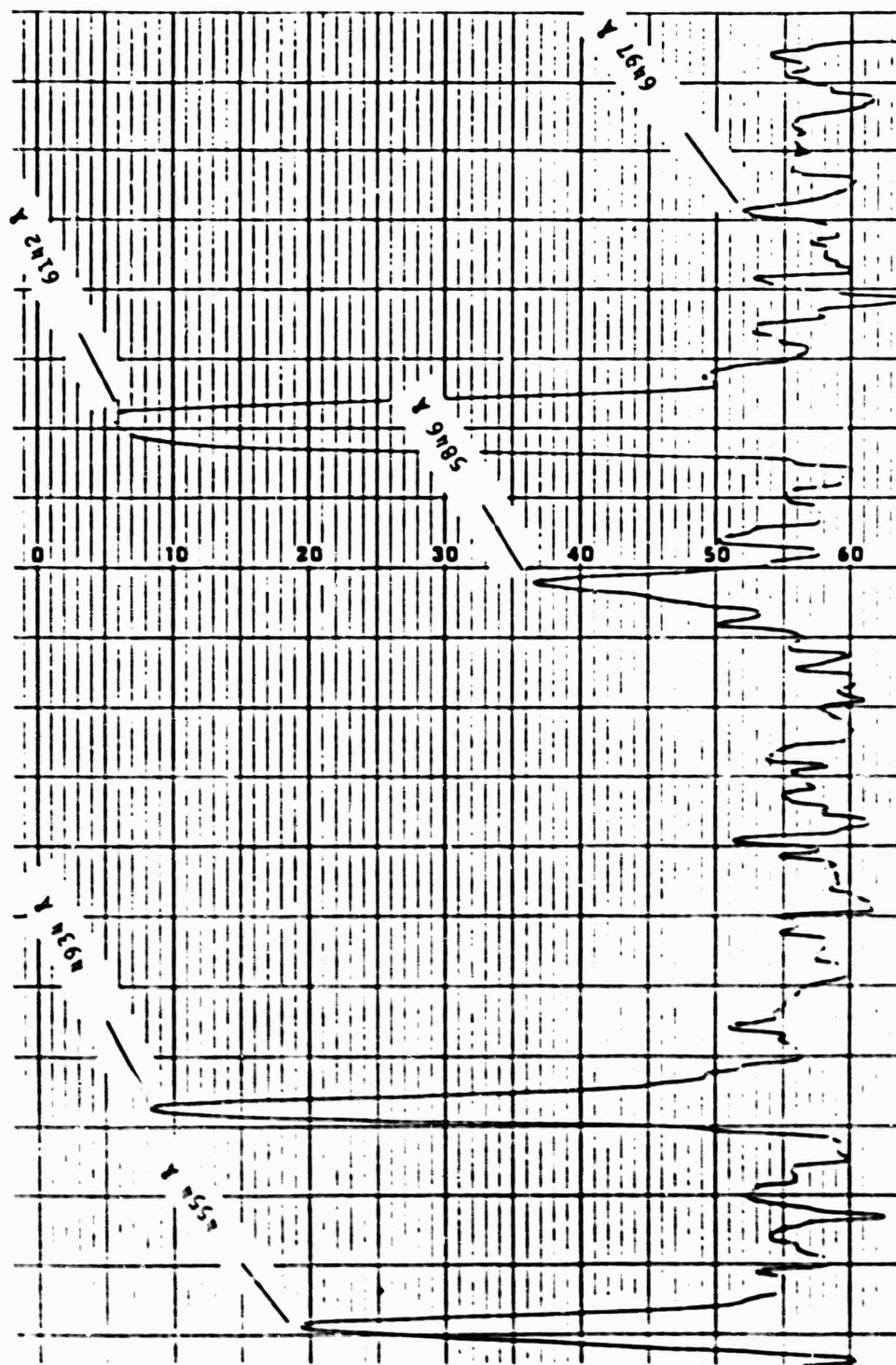FIGURE 8   PROJECT STRESS, EVENT FERN, RELEASE TIME 0446:09 LT

FIGURE 9 ION CLOUD SPECTRA SAMPLE

contours (IDTs) the peak density can be determined, and from these data, together with the system parameters and estimated value of atmospheric transmission, the source peak apparent radiance can be determined.

Figure 10 shows the measured peak radiance of four STRESS events as a function of time after release. The integrated radiance (over cloud profile area) or optical power is shown in Figure 11 for the same times. The radiated power will of course begin to fall as the sun sets at the cloud altitude, and this is evidenced in data covering the time of sunset.

The peak and integrated radiance data were subsequently converted to peak column density (ions/cm^2) and ion yield (%). The conversion of peak radiance to maximum column density was performed using the optically thick model of B. Kivel. A mean of the two Kivel solar radiation source models was used for this analysis, based on past experience and observations. The integrated radiance was converted to integrated ion yield, treating the clouds as if they were optically thin. The resulting yields represent minimum values, therefore. The calculated values of peak ion column density and yield are presented in Tables 3, 4, 5, and 6 for Events CAROLYN, DIANNE, ESTHER, and FERN.

IV TRIANGULATION RESULTS

Two 5-inch-format triangulation cameras were operated at each primary optics site, Tyndall 9702 area, and Eglin C-6 area. The cameras were fitted with EK Aero Ektar lenses with a focal length of 152.7 mm and a focal ratio of 2.5. These lenses have a maximum displacement distortion of 0.3 mm and cover a 41°-by-41° field of view in the triangulation cameras. Whenever possible a color negative record was used for measurement of features of the ion cloud or the neutral cloud center.

The triangulation calculation routine developed by TIC determines-- for a common feature definable in the photographic image from each triangulation site-- the geodetic position in latitude, longitude, and
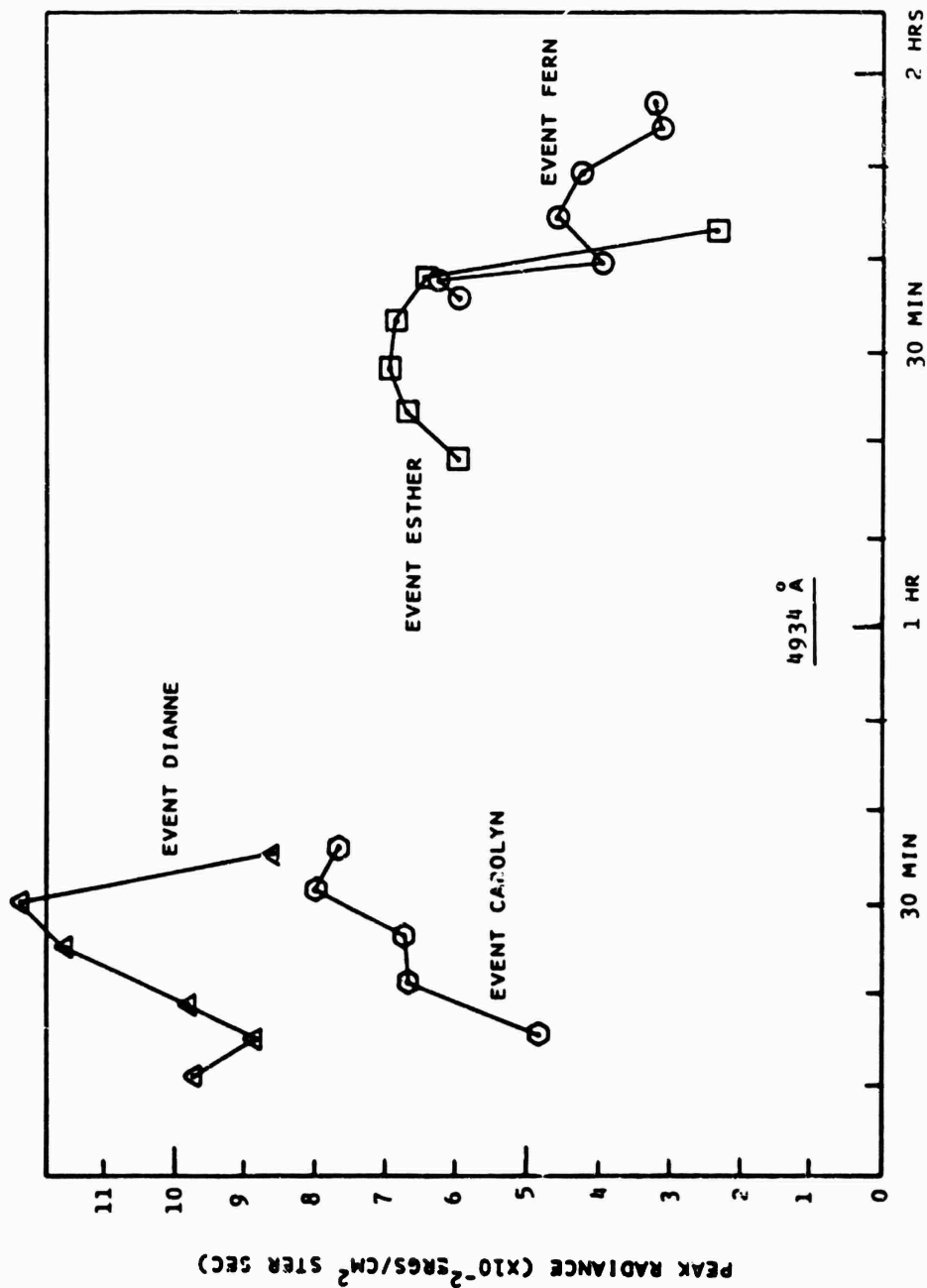
FIGURE 10   STRESS PEAK RADIANCE
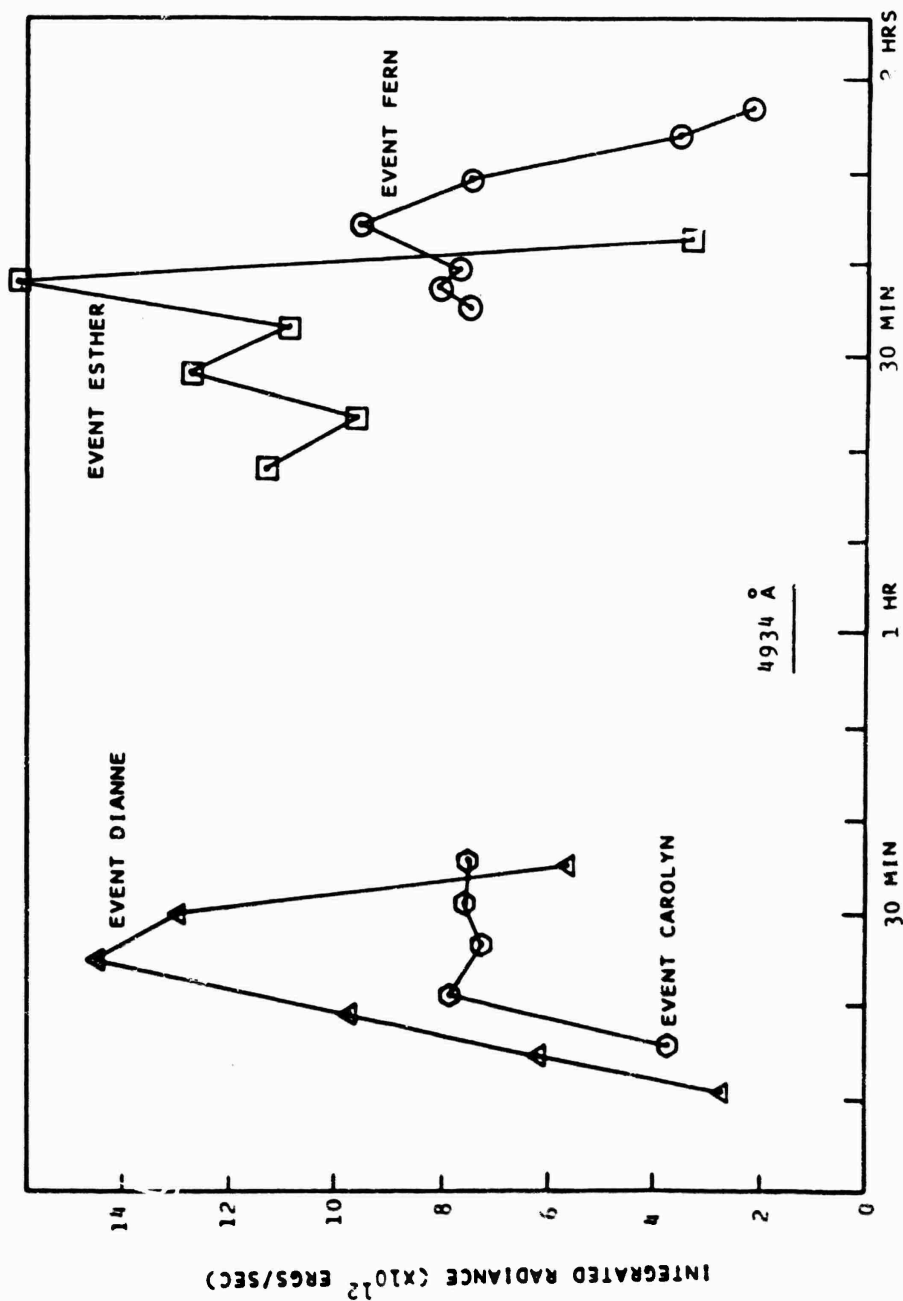
FIGURE 11 STRESS INTEGRATED RADIANCE

28

Table 3

EVENT CAROLYN -- ION COLUMN DENSITY AND YIELD

| TIME | | PEAK COLUMN DENSITY | MINIMUM YIELD |
(LOCAL)	(RELEASE)	(IONS/CM^2)	(%)
18:10:04	00:15:54	8.5×10^{11}	8.4
18:15:37	00:21:27	1.65×10^{12}	17.5
18:20:30	00:26:20	1.7×10^{12}	16.1
18:25:16	00:31:06	2.3×10^{12}	16.7
18:29:58	00:35:48	2.1×10^{12}	16.4

29

Table 4

EVENT DIANNE -- ION COLUMN DENSITY AND YIELD

TIME		PEAK COLUMN DENSITY	MINIMUM YIELD
(LOCAL)	(RELEASE)	(IONS/CM^2)	(%)
18:12:20	00:11:10	3.0×10^{12}	7.07
18:16:08	00:14:58	2.7×10^{12}	15.8
18:20:03	00:18:53	3.2×10^{12}	24.9
18:25:52	00:24:42	4.1×10^{12}	37.0
18:31:01	00:29:51	4.3×10^{12}	33.3
18:36:00	00:34:50	2.55×10^{12}	14.4

30

Table 5

EVENT ESTHER -- ION COLUMN DENSITY AND YIELD

TIME		PEAK COLUMN DENSITY $(IONS/CM^2)$	MINIMUM YIELD $(\%)$
(LOCAL)	(RELEASE)		
18:19:20	1:18:12	1.3×10^{12}	26.3
18:24:12	1:23:04	1.65×10^{12}	22.6
18:29:13	1:28:05	1.7×10^{12}	29.5
18:34:18	1:33:10	1.7×10^{12}	25.4
18:39:01	1:37:53	1.5×10^{12}	21.7
18.44:14	1:43:06	1.9×10^{11}	7.72

Table 6

EVENT FERN -- ION COLUMN DENSITY AND YIELD

TIME (LOCAL)	(RELEASE)	PEAK COLUMN DENSITY $(IONS/CM^2)$	MINIMUM YIELD (%)
18:21:42	1:35:33	1.3×10^{12}	19.1
28:23:46	1:37:37	6.0×10^{11}	20.5
18:25:51	1:39:42	4.8×10^{11}	19.5
18:30:31	1:44:22	7.0×10^{11}	24.4
18:35:16	1:49:07	6.0×10^{11}	18.9
18:40:21	1:54:12	3.0×10^{11}	9.3
18:42:50	1:56:41	3.2×10^{11}	5.6

32

altitude above sea level in kilometers.[*] A calculated miss-distance of
the triangulation vectors is also obtained. If this value is greater than
1 to 1-1/2 km, the triangulation is repeated.

In general, the triangulation records are first timed to ±1 s; the
camera pointing attitude is then determined using images of identified
celestial bodies. The selected feature position is measured with respect
to the optical axis and plotted as a function of time for each triangula-
tion site record. At this point the plot is smoothed, if required, and
image feature positions are determined for selected common times. A
target vector is then developed mathematically (in geocentric coordinates)
for each site/feature at a common time and the two vectors are triangu-
lated to obtain the feature position, which is tranformed into geodetic
coordinates.

The results of the STRESS triangulation measurements are varied in
that some events presented distinct features that could be easily identi-
fied from each site and readily triangulated, whereas some events presented
very diffuse indistinctive images for which only approximate edges could
be identified. Whenever possible, an attempt was made to triangulate the
following features:

- The center of the neutral cloud.
- The sharp (trailing) edge of the ion cloud, or end-most
  striation.
- The diffuse-end (leading) edge of the ion cloud.

On the accompanying plots of barium cloud motion the nominal sub-
release point is drawn as a solid circle, with the release time in hours
and minutes. The symbols for cloud feature position as a function of
time symbols for cloud feature position as a function of time are shown
as minutes after the (same) hour (not release-plus times), except for
ESTHER and FERN, which are shown as minutes after the following hour.

---

[*] Based upon the Clarke spheroid model of 1866.

Figure 12 shows the neutral and ion cloud tracks of Event ANNE from
release to R + 24 min (neutral) and R + 30 min (trailing striation). At
R + 30 min (2342), the striation was measured to extend from 150 km at
the northern lower end to an altitude of 205 km at the southern upper
end, as shown.

Figure 13 shows the cloud tracks of the Event BETTY neutral cloud
to R + 32 min and the lower end of a striation, identified as "A", to
R + 38 min. Also shown is the last measurable position of the leading
edge at R + 41 min. Both the center of the neutral cloud and the trail-
ing edge of the ion cloud moved very nearly due east during this event.

Figure 14 plots the motion of the Event CAROLYN neutral cloud center,
the western (leading) edge of the ion cloud, and the upper end (only) of
the foremost eastern (trailing) striation (U). The neutral cloud was
measured out to R + 33 min, and the ion cloud to R + 39 min. In this
instance the overall cloud motion was east-southeast.

The triangulated cloud tracks of Event DIANNE are shown in Figure 15.
The neutral center is plotted to R + 20 min. The foremost trailing-edge
striation is plotted out to R + 32 min. The lower (northern) and upper
(southern) edges of the edge-most striation are shown for 15, 21, and 27
minutes after the hour. A dashed line connects the lower end of the
striation with the corresponding position symbol for the leading edge at
a given time. At 33 min an ensemble of three striations is shown--also
connected to the corresponding leading-edge position by dashed lines.
At this latter time, the lower end of the edge striation was triangulated
to a height of 160 km and the upper end to a height of 210 km altitude.

Figure 16 shows the results of triangulation measurements on the
late-time Event ESTHER ion cloud. No neutral cloud was apparent. The
motion of a group of five striations (later four) from R + 1 hr 29 min
(0030) to R + 1 hr 41 min (0042) at 150 km altitude is plotted. The
position of the striation group at a given time is shown connected with
dashed lines. The extent of the cloud at R + 1 hr 23 min (0024) is
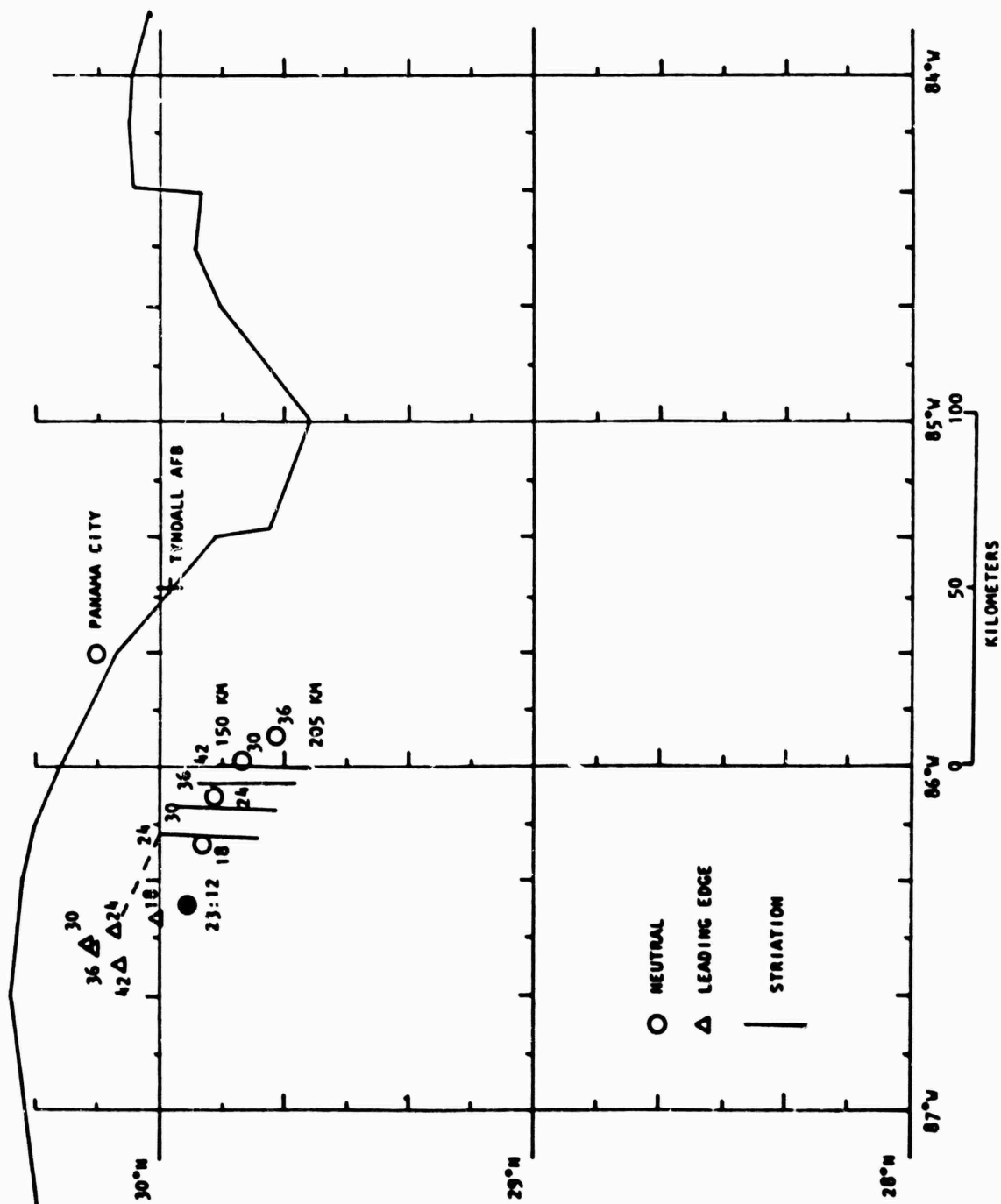also shown as a dashed line connecting the leading edge and a single
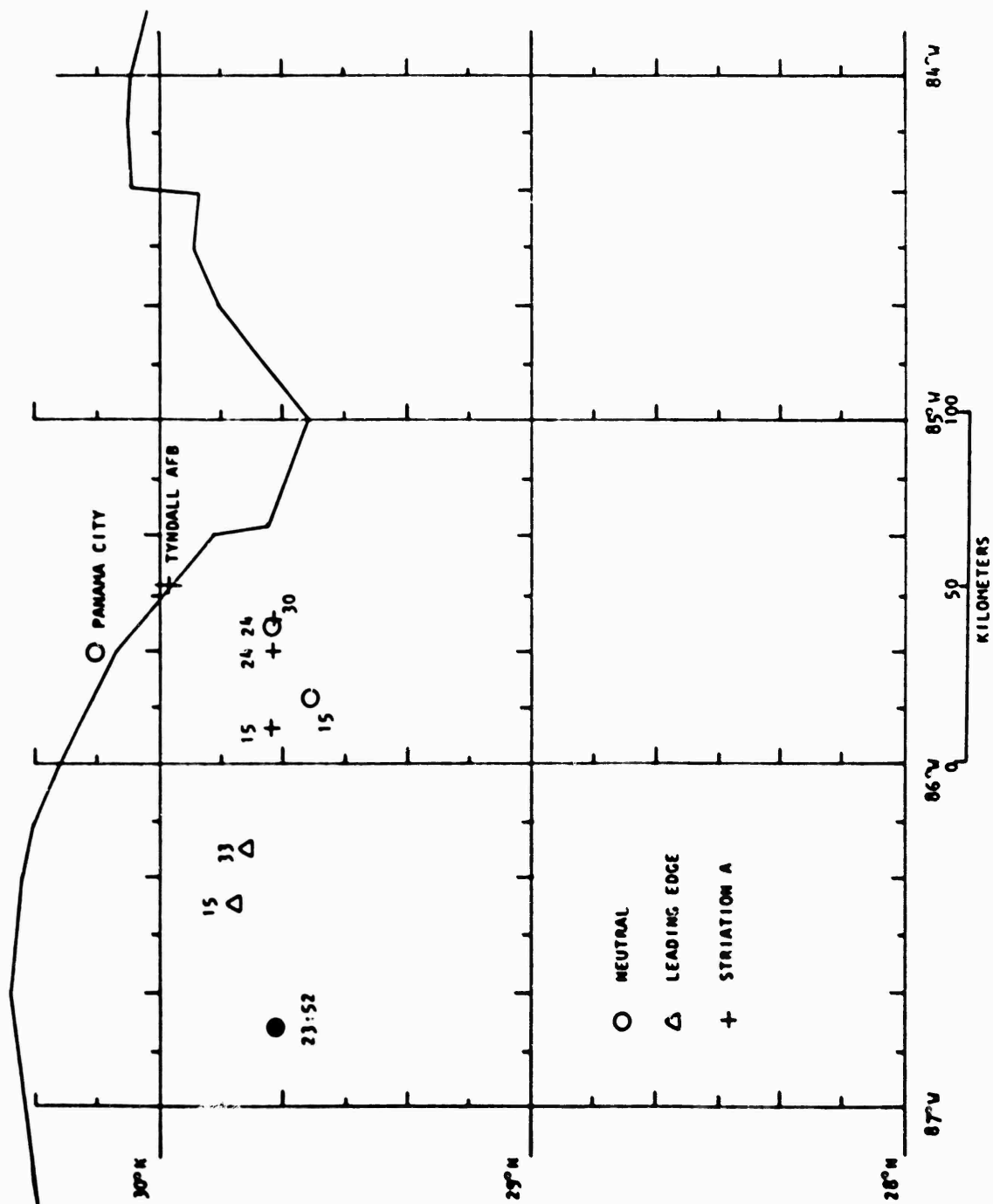striation.

34

FIGURE 12   CLOUD TRACKS — EVENT ANNE

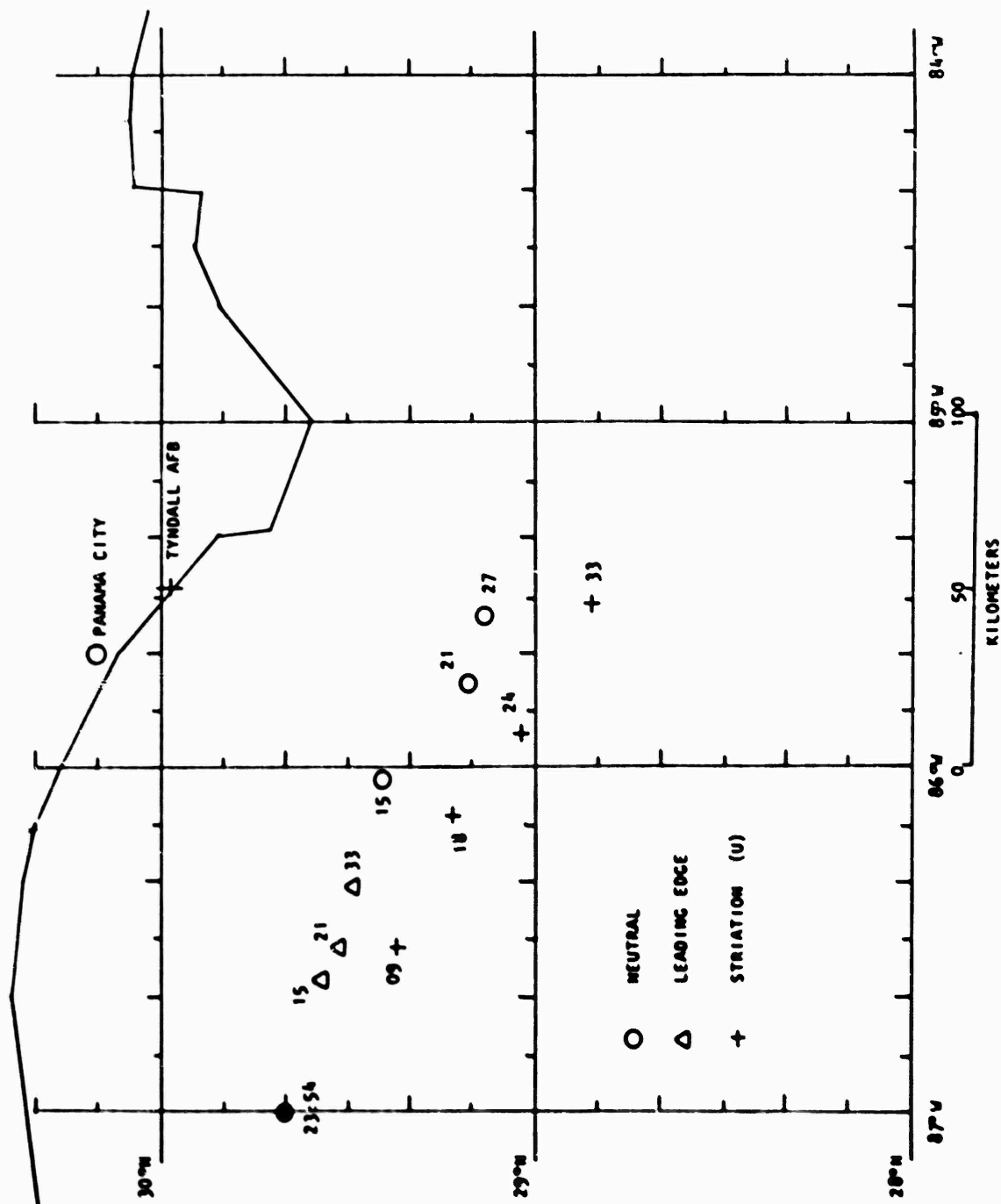FIGURE 13   CLOUD TRACKS — EVENT BETTY

36

FIGURE 14 CLOUD TRACKS — EVENT CAROLYN

37

FIGURE 15   CLOUD TRACKS — EVENT DIANNE

O PANAMA CITY

TYNDALL AFB

23:01 ●

● RELEASE
△ LEADING EDGE
· STRIATION

00:24
△

00:30
00:36
00:42

150 KM

84°W   85°W   86°W   87°W

30°N   29°N   28°N

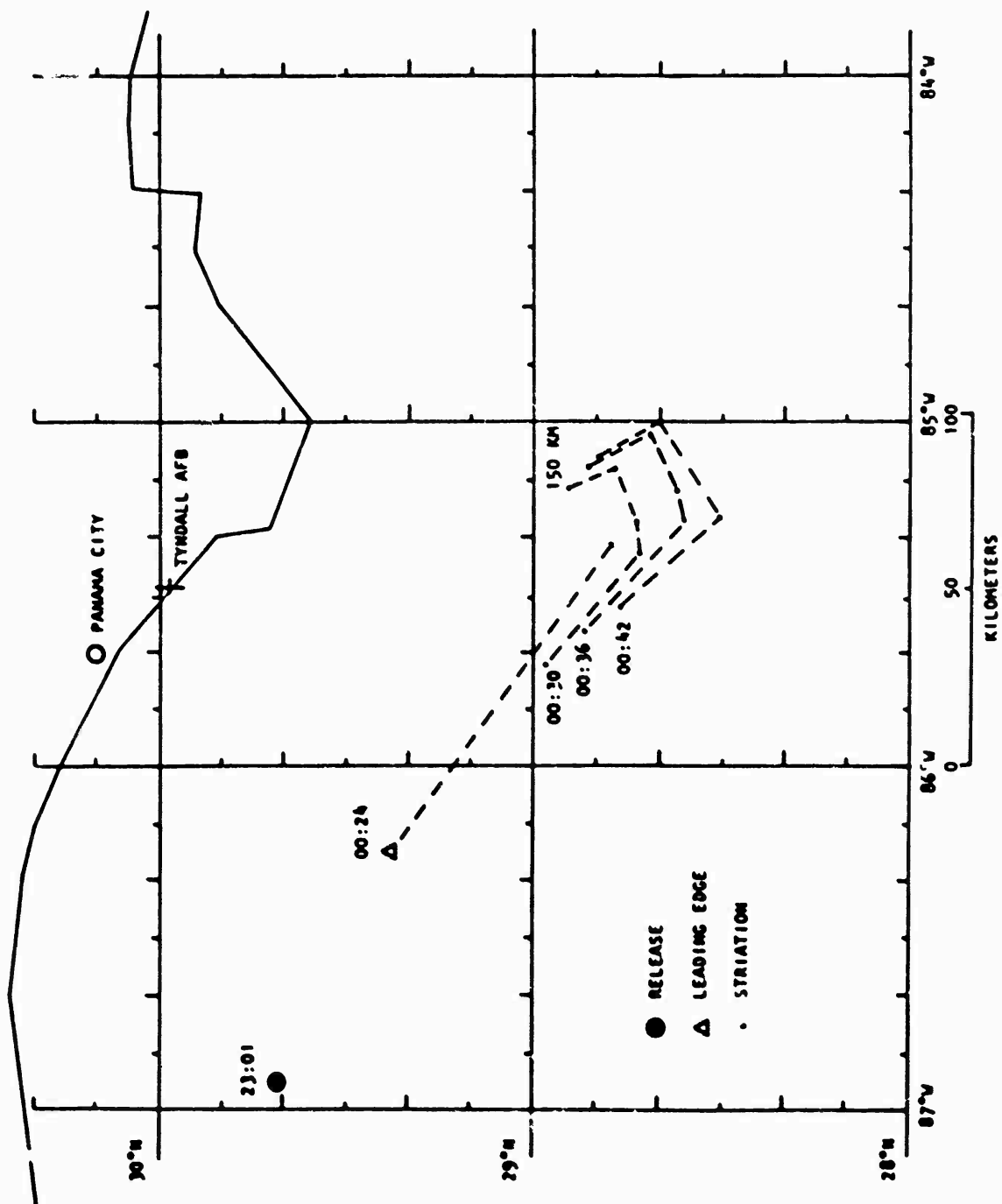0   50   100

KILOMETERS

FIGURE 16   CLOUD TRACKS — EVENT ESTHER

Event FERN, as in the case of ESTHER, did not exhibit a neutral cloud at the late times for which photographic coverage was obtained. Moreover, little structure was readily identifiable from two triangulation sites. Two significant striations were triangulated as best possible and are plotted in Figure 17, over a period of R + 1 hr 35 min to R + 1 hr 56 min. In general the ion cloud moved with a relatively slow velocity and was not as distinctive in structure as the prior events.

V STRIATION SPATIAL-FREQUENCY ANALYSIS

High-resolution black and white film records were made from the Eglin C-6 site for each of the STRESS barium ion clouds. Of these five events, four exhibited significant striations and suitable perspectives for analysis. These were Events BETTY, CAROLYN, DIANNE, and ESTHER.

Data frames were selected from each of these events (two from CAROLYN and one from each of the other three) as being most appropriate technically (and suitably representative of the event) for spatial frequency analysis. All data discussed here were obtained from the 300 mm Position 34 camera located at the Eglin C-6 site. The film used in this camera was Tri-X Pan and was developed to a D log E slope greater than unity.

The data frames were scanned on a transmission microphotometer with an effective scanning aperture of 50 μm by 0.5 mm. The long axis of the slit was scanned perpendicular to the direction of motion. The values of transmission versus image position were digitized, with approximately 2000 data points being obtained over a typical dimension of 20 mm. The sensitometric processing curve was scanned next, and a density-versus-log-exposure curve computed. With the aid of this curve the transmission profile of the image was then converted to relative radiance.

The relative radiance is next Fourier transformed with a large computer utilizing a Cooley-Tukey algorithm fast Fourier transform. The resulting data are plotted as power (amplitude squared) versus log spatial frequency in lines/mm.
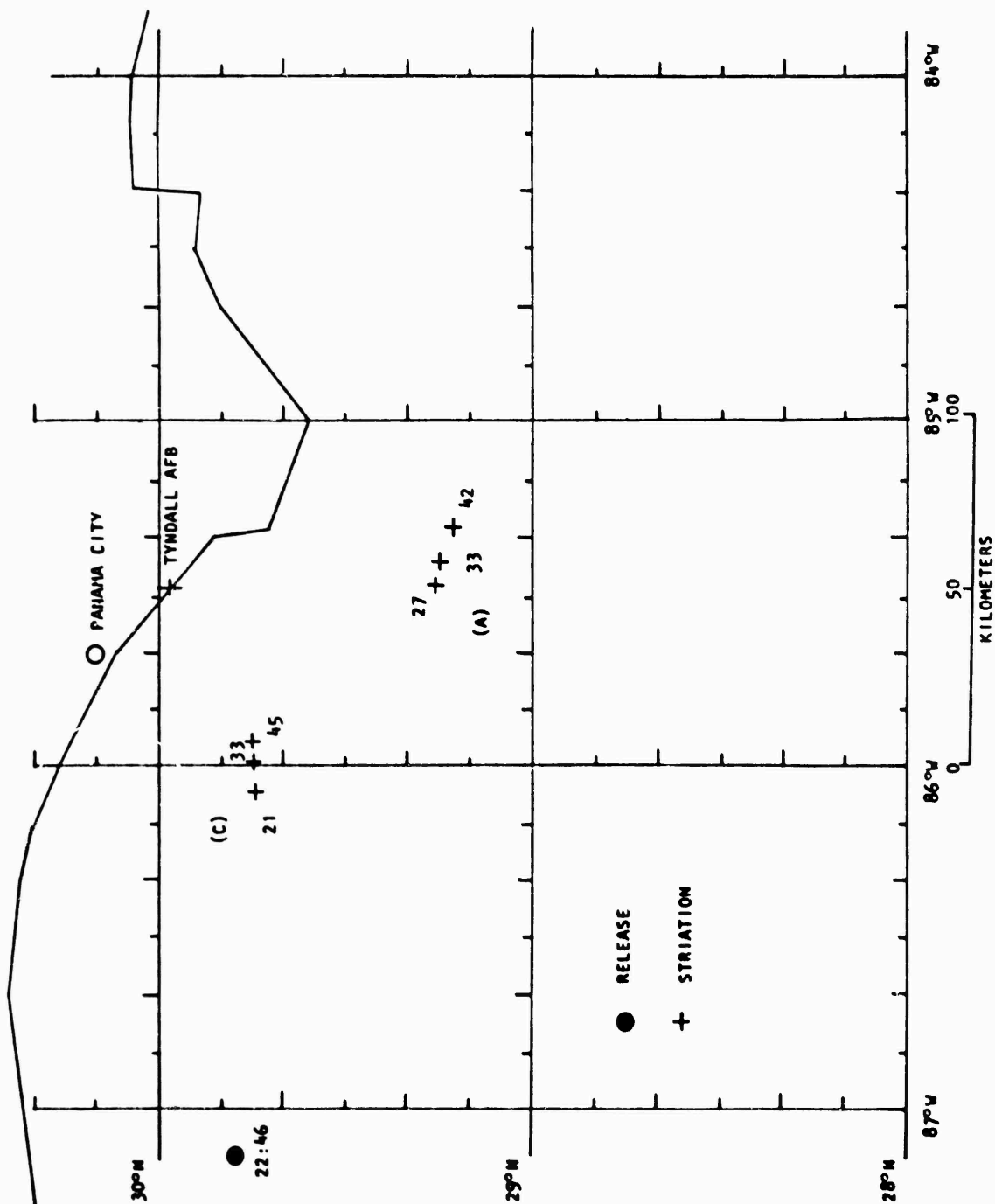
FIGURE 17   CLOUD TRACKS — EVENT FERN

41

Figure 18 shows the data frame selected from Event BETTY at R + 39 min
47 s. In this as well as subsequent photographic figures the inked line
shows the image profile scan direction. Figure 19 shows the resulting
plot of power versus spatial frequency for this event. Beyond about log
1.0 (10 lines/mm) the grain noise of the film begins to limit the useful-
ness of any higher-frequency data.

Figures 20, 22, 24, and 26 show the striations scanned for Events
CAROLYN, DIANNE, and ESTHER at the times indicated on the figures. The
corresponding spatial frequency transforms are presented in Figures 21,
23, 25, and 27 respectively. It should be pointed out that no artificial
filtering was introduced into this analysis, as is sometimes done.

The data given above in lines/mm can be converted to object dimen-
sions if the focal length of the lens and range to the object are known.
Assuming a nominal range of 200 km and using a focal length of 300 mm,
a spatial frequency of one, for example, would correspond to an object
dimension of about 660 m.

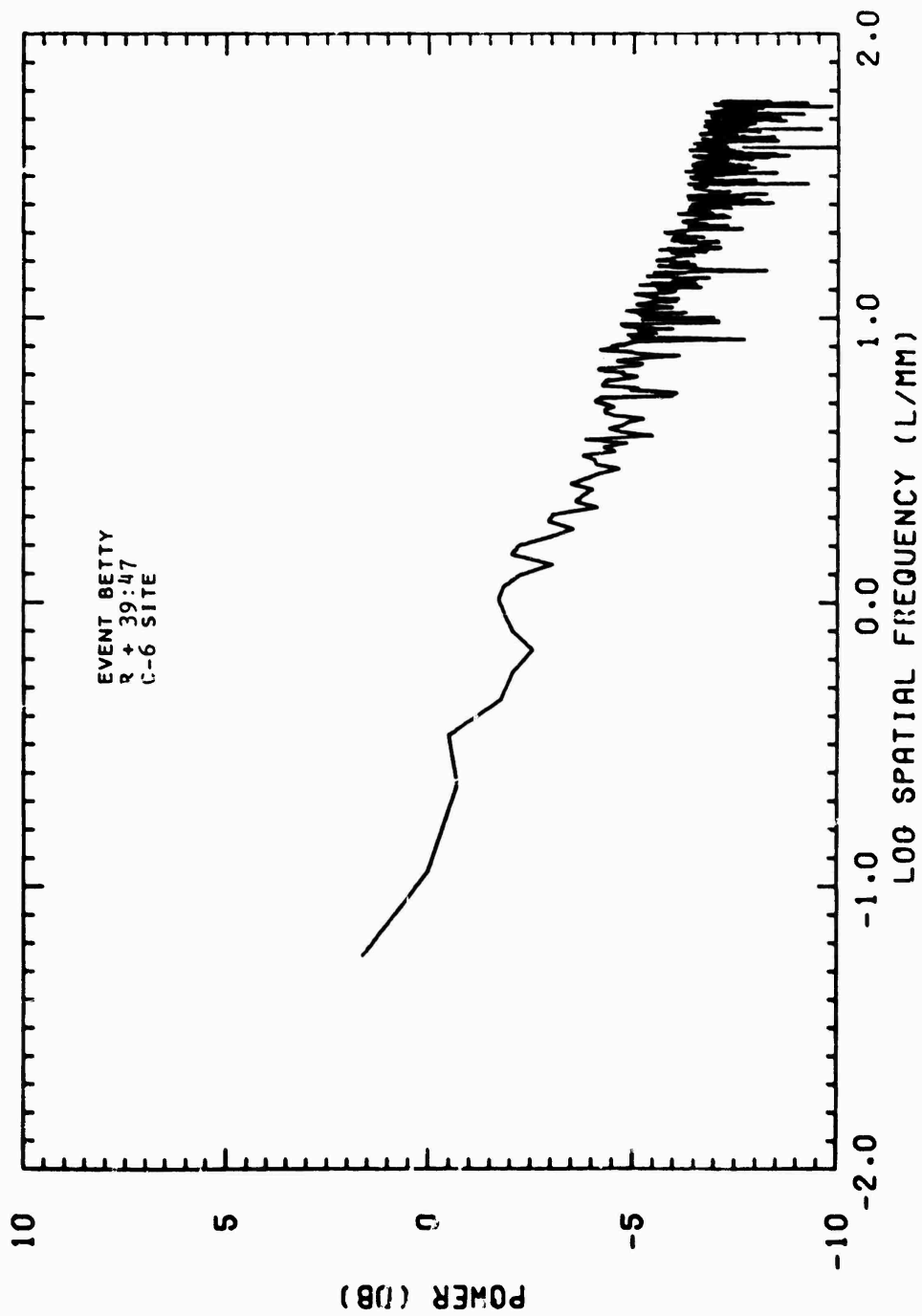FIGURE 18   EVENT BETTY, C-6 SITE, R + 39 min 47 s

FIGURE 19   EVENT BETTY — POWER vs SPATIAL FREQUENCY

44

FIGURE 20   EVENT CAROLYN, C-6 SITE, R + 28 min 04 s
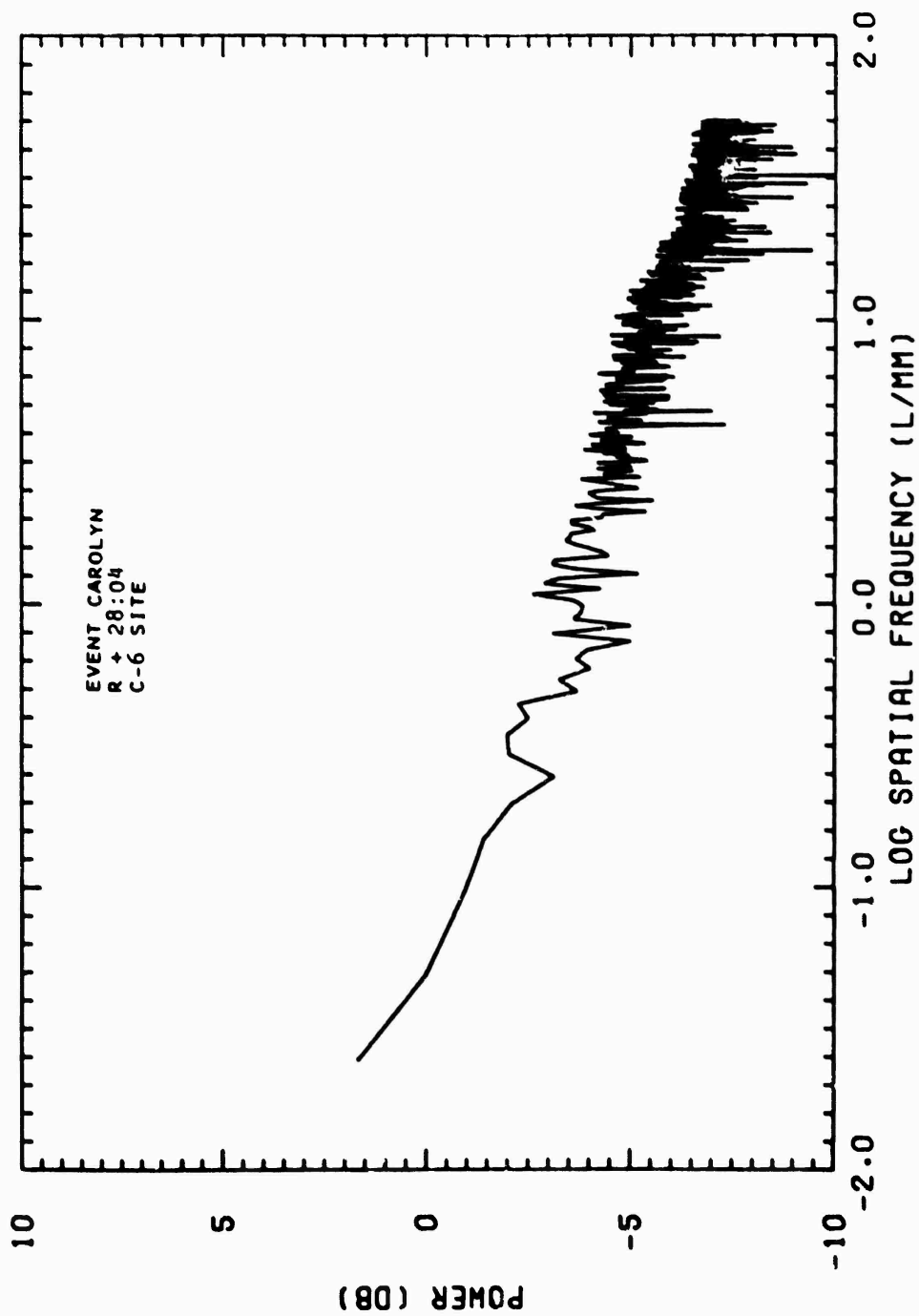
FIGURE 21   EVENT CAROLYN — POWER vs SPATIAL FREQUENCY

EVENT CAROLYN
R + 28:04
C-6 SITE

LOG SPATIAL FREQUENCY (L/MM)

POWER (DB)

46

FIGURE 22   EVENT CAROLYN, C-6 SITE, R + 37 min 08 s
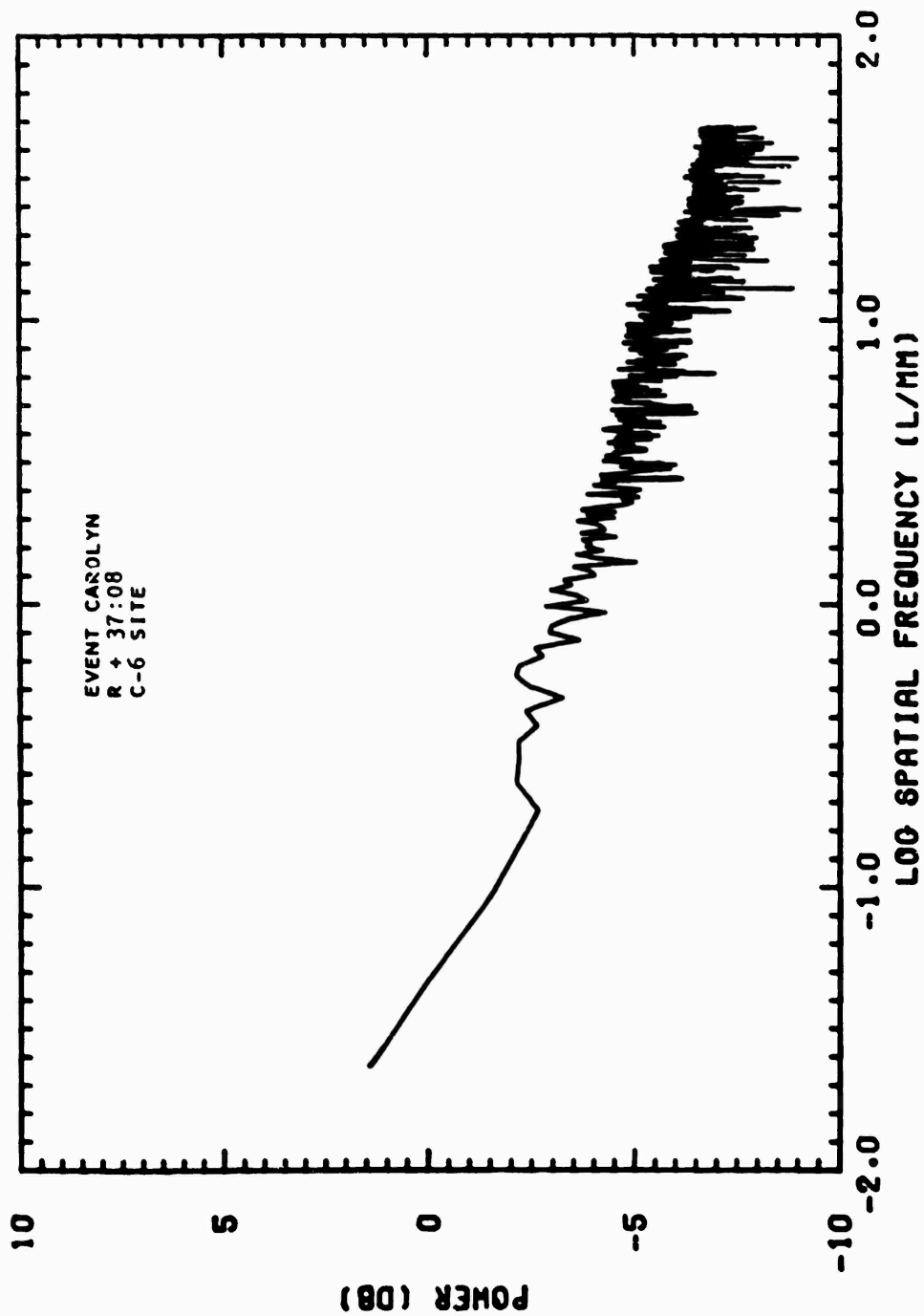
FIGURE 23   EVENT CAROLYN — POWER vs SPATIAL FREQUENCY

EVENT CAROLYN
R + 37:08
C-6 SITE

LOG SPATIAL FREQUENCY (L/MM)

POWER (DB)

48
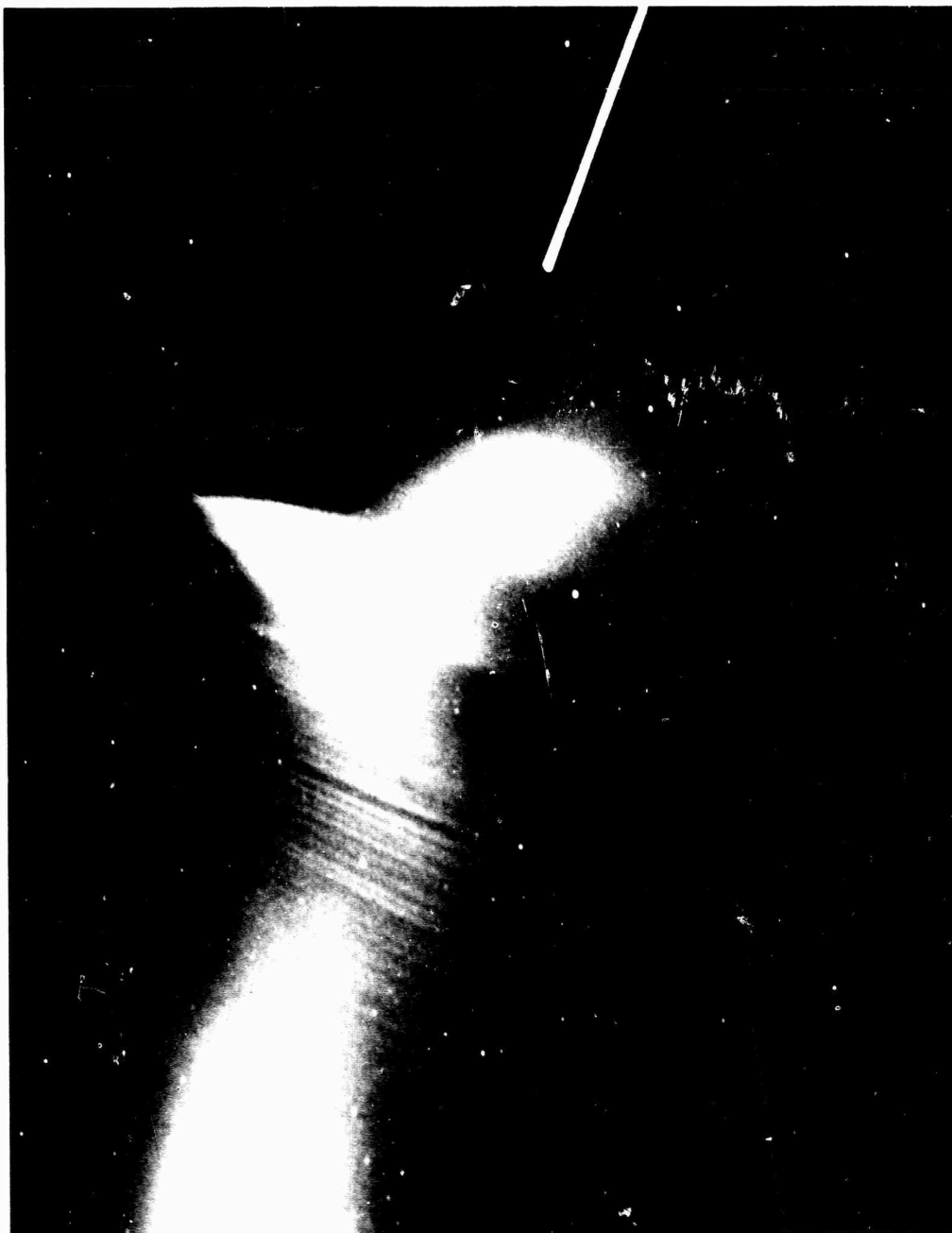
FIGURE 24   EVENT DIANNE, C-6 SITE, R + 37 min 26 s
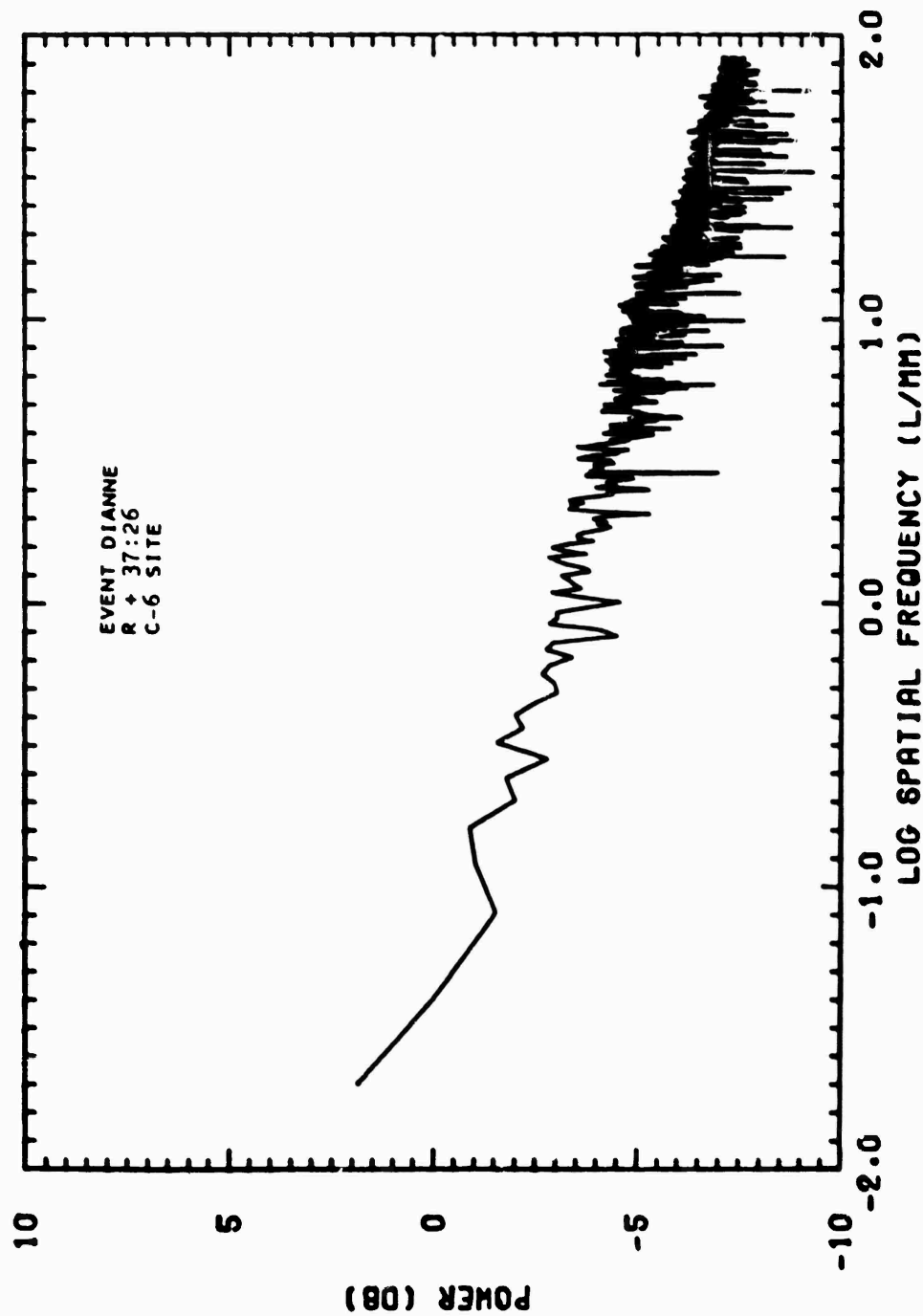
FIGURE 25   EVENT DIANNE — POWER vs SPATIAL FREQUENCY

EVENT DIANNE
R + 37:26
C-6 SITE

FIGURE 26   EVENT ESTHER, C-6 SITE, R + 1 hr 31 min 16 s
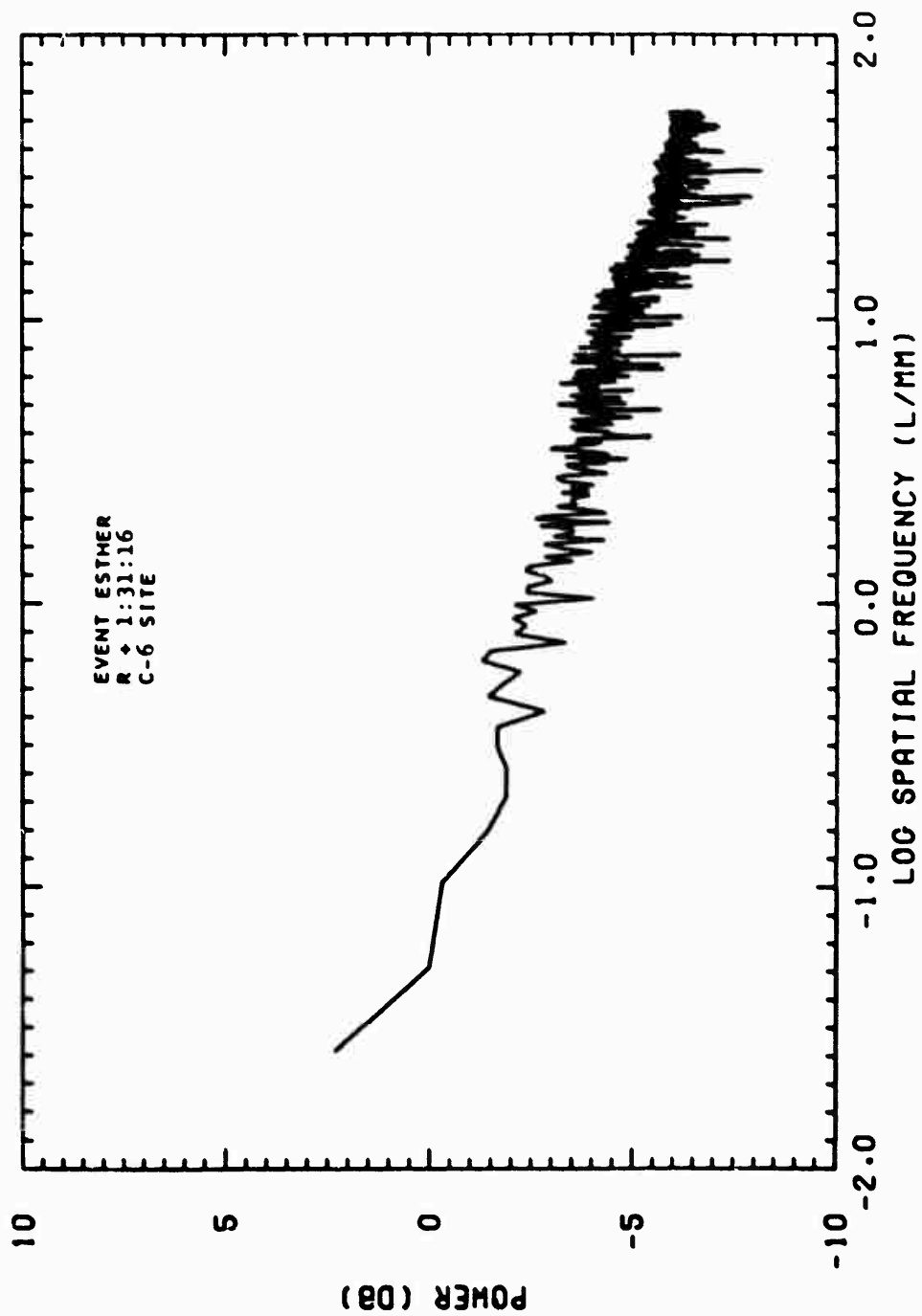
FIGURE 27   EVENT ESTHER — POWER vs SPATIAL FREQUENCY

EVENT ESTHER
R + 1:31:16
C-6 SITE

LOG SPATIAL FREQUENCY (L/MM)

POWER (DB)

52

INTENSIFIED OPTICS MEASUREMENTS

J. H. Wolcott

Los Alamos Scientific Laboratory
Los Alamos, New Mexico

INTENSIFIED OPTICS MEASUREMENTS

J. W. Wolcott

Los Alamos Scientific Laboratory
Los Alamos, New Mexico

I INTRODUCTION

The Los Alamos Scientific Laboratory (LASL) participated in project STRESS, a series of rocket-borne, barium thermite release experiments sponsored by the Defense Nuclear Agency (DNA). For DNA, the principal objective of STRESS (Satellite Transmission Effects Simulation) was the study of actual satellite communication links through structured barium plasma clouds known to simulate many aspects of the highly disturbed, post-nuclear-explosion upper atmosphere. For LASL, the principal objective was the investigation of the very-late-time spatial decay of plasma striations, or filaments, embedded within the barium ion cloud. Most operational aspects of this experimental project were well suited to address both principal objectives.

The release or injection, of barium has now become a standard technique for simulation of the highly structured plasmas that follow a high-altitude nuclear detonation. Complex computer models that predict nuclear weapons effects are validated by application to such simulation events. From a scientific viewpoint, barium experiments aid greatly in the understanding of the dynamics of plasma processes that ultimately affect a number of planned or operational systems. The performance of systems that depend on electromagnetic propagation can be severely degraded when a transit through highly disturbed environments is necessary.

Numerous observations of the behavior of ionized barium clouds and jets have resulted in a relatively thorough understanding of the plasma

processes leading to the formation and growth of striations within a
plasma cloud. Little experimentation to date has been directed to the
processes that result in striation decay.

Project STRESS, conducted at Eglin AFB, Florida, actually included
two phases, with all experiments involving a 48-kg barium thermite release
at 185 km altitude. The first phase, Pre-STRESS, was completed on 1
December 1976 when a single release occurred at 2312 UT and ~29° 55'N,
86°30'W; background and signal level data were obtained by LASL during
Pre-STRESS. The second and more extensive phase occurred between 26
February and 14 March 1977, when five releases were conducted at widely
varying local times.

II   PRE-STRESS RESULTS

As mentioned above, the single event of Pre-STRESS occurred at
2312 UT (1712 CST), 1 December 1976 with release of barium vapor from a
rocket launched at Eglin AFB, Florida. The experiment was conducted in
order to exercise the operational interfaces that would be involved later
during STRESS, but it also provided LASL with the opportunity to perform
optical measurements during a local time period and lunar phase similar
to those to be encountered during the STRESS operation.

Sky background measurements obtained on the evenings of 30 November
and 1 December 1976 are presented in Figure 1. Comparable data obtained
on 6 June 1976 are also included. Look angles were those to a nominal
STRESS event location, and a 3/4 moon was above the horizon. These data
were sufficient for design of the STRESS instrument plan and an operational
program for temporal adjustments of instrument sensitivities.

Averaged over a 2°-diameter field of view (FOV), the radiance of the
fully solar-illuminated Pre-STRESS release was ~2.5 $\times$ 10^{-9} W cm^{-2} sr^{-1} at
455.4 nm. Assuming optically thin radiators, this radiance corresponds
to a barium ion column density of ~5 $\times$ 10^{10} cm^{-2}. Based on these results
and a minimum signal-to-background ratio of 0.5 with 1-nm-wide spectral
filtering, photographic recording of the release appeared feasible at
solar depression angles of ~6° and greater. Signal-to-background ratios
would improve with time until the cloud was no longer illuminated by the
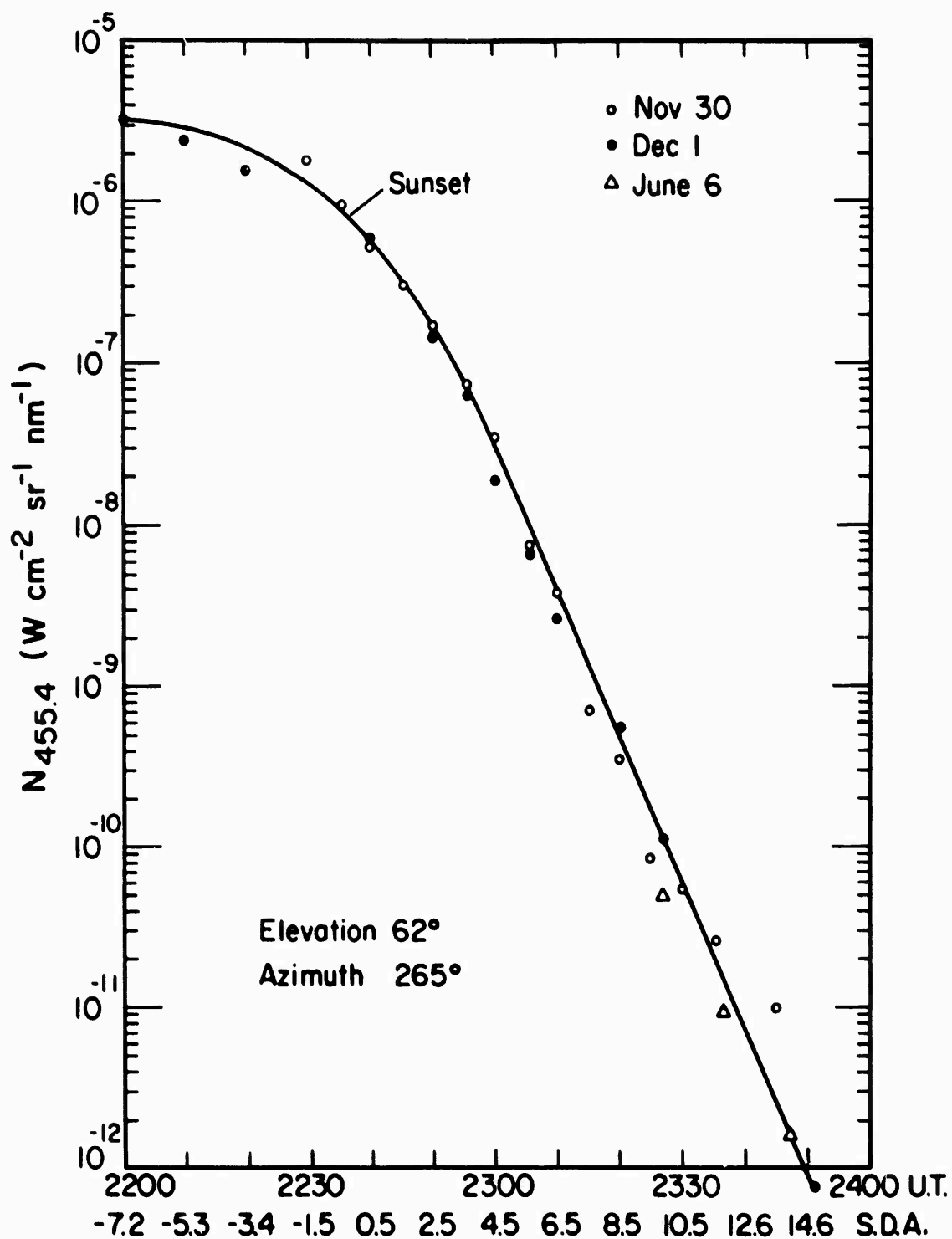sun at a depression angle of ~13°.

FIGURE 1   SKY BACKGROUND MEASUREMENTS OBTAINED ON 30 NOVEMBER AND
1 DECEMBER 1976 AND 6 JUNE 1976

57

III   STRESS OPERATIONS

Realization of the LASL objectives for STRESS depended on the ability to identify and observe optically thin regions of the structured barium ion cloud. Comparisons with current models for decay of striated plasmas require observation of the spatial inhomogeneities within the total ion cloud with no obscuration by intervening optically thick regions.

One approach--observation of a barium-ion spectral-line shape--was utilized by Lockheed, a DNA contractor. Here, an imaging Fabry-Perot interferometer was spectrally scanned across the line profile at 455.4 nm. The LASL approach involved a search for optically thin regions of the cloud by real-time TV observations. A series of filtered (455.4 nm) cameras with high time and space resolution were then pointed toward those volumes. Since Lockheed selected the Tyndall AFB location early in the STRESS planning, and direct comparison of the two optical techniques was highly desirable, the LASL optical site was also located at Tyndall (29°58'N, 85°28'W), east of Panama City.

The tracking TV was an ISIT, a single-stage intensified, and cooled, SIT TV camera. Two of the camera systems employed three-stage electrostatically focused intensifiers, while the third contained a three-stage, magnetically focused tube. Focal lengths used were 50 mm, 400 mm, and 1250 mm, and the 1250-mm lens was used with the magnetic intensifier. With this selection of optics and cameras, FOVs ranged from about 1° to 30°, and spatial resolution at the barium cloud location ranged from about 20 to 250 m. To achieve these spatial resolutions, in view of the fact that cloud motion is expected to be of the order of 20 m s^{-1}, fraction-of-a-second exposures possible only with intensified systems are required. Exposures as short as 0.1 s were used. Kodak 2484 film was used, and it was force-processed to an ASA of ~2000. All camera systems were radiometrically calibrated and the film processing was controlled so that absolute cloud radiance could be obtained.

Table 1 gives a summary of the five STRESS events. Event ESTHER provided the best data, and analysis has been concentrated on this event. The cloud was highly striated when it was first observed. It had drifted

Table 1

SUMMARY OF STRESS EVENTS

	Event BETTY 26 Feb 77 LT	Event CAROLYN 2 Mar 77 LT	Event DIANNE 7 Mar 77 LT	Event ESTHER 13 Mar 77 LT	Event FERN 14 Mar 77 LT
Release Time (Z)	2352	2354	0001	2301	2246
Altitude of release (km)	179	191	186	189	186
ΔT^* (min)	14	15	11	75	90

*ΔT is defined as the difference between release time and the time when the sun reaches a 6° depression angle at the nominal sub-event point.

southeast and passed south of the local magnetic zenith. Figure 2 shows the ion cloud at 0035 UT as viewed by the intensified camera systems.

400mm CAMERA ⎯⎯ 500 m
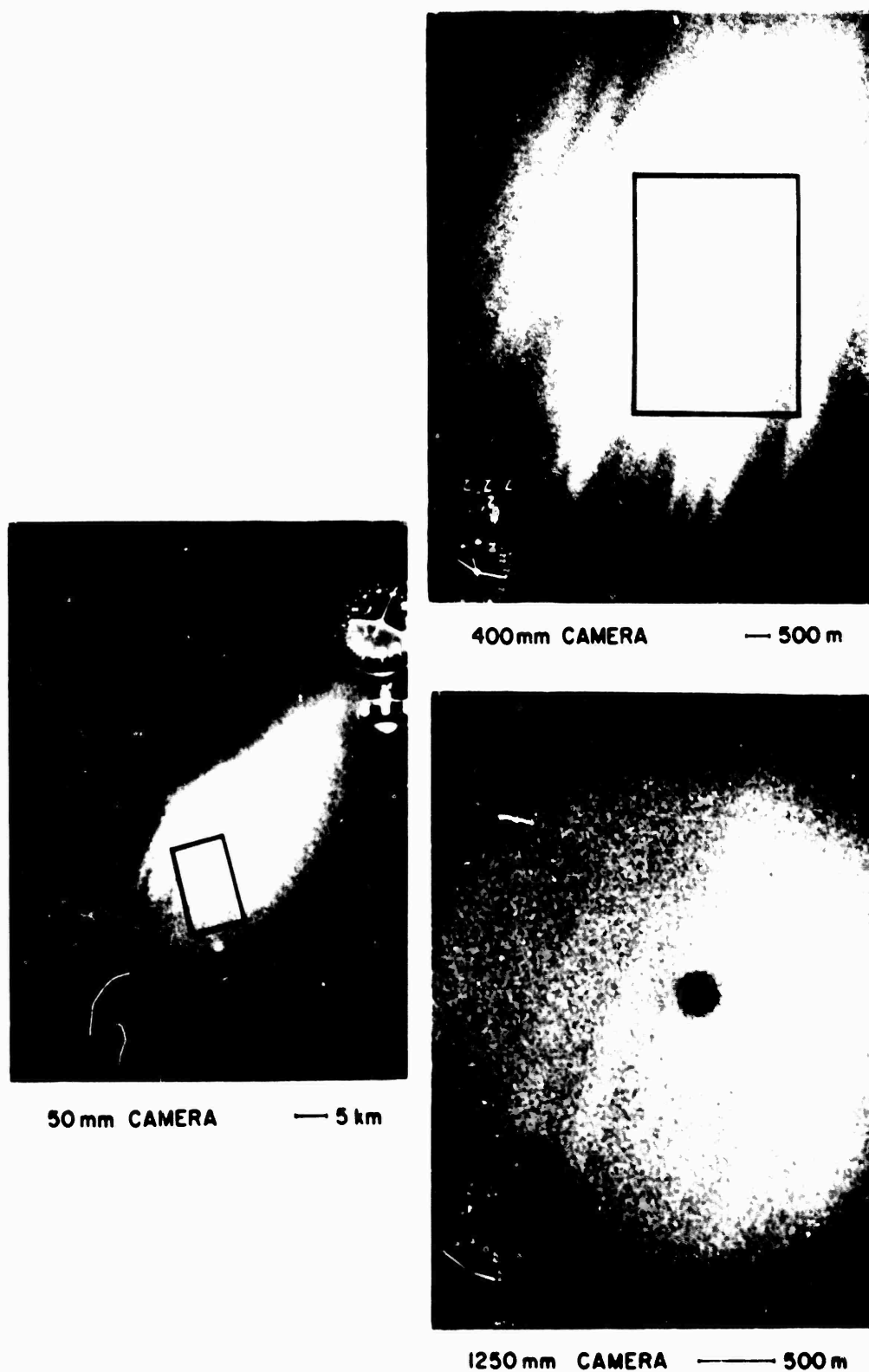
50 mm CAMERA ⎯⎯ 5 km

1250 mm CAMERA ⎯⎯⎯ 500 m

FIGURE 2   DATA FRAMES FROM STRESS/ESTHER AT 0035 UT SHOWING THE 400-mm
AND 1250-mm CAMERA FIELDS OF VIEW ON THE 50-mm AND 400-mm
FRAMES, RESPECTIVELY

ROCKET OPERATIONS

E. F. Allen

Space Data Corporation
Tempe, Arizona

ROCKET OPERATIONS

E. F. Allen

Space Data Corporation
Tempe, Arizona

I INTRODUCTION

Twelve two-stage sounding rockets were successfully launched from
Site A-15A, Eglin Air Force Base, Florida. Six Honest John-Hydac vehicles
carried barium payloads, and six Nike-Hydac vehicles carried probe pay-
loads with electron density experiments and VHF transmission experiments.
The objectives were to deploy the barium payloads at nominally 185 km
altitude and then launch the probe experiments through the striated por-
tion of the barium ion cloud. This report gives a rocket flight summary
and describes the rocket vehicle systems. Also, it lists related Space
Data Corporation (SDC) documents that further describe rocket operations
and give detailed flight results.

SDC provided rocket vehicles, C-band beacon modules on the barium
vehicles, VHF experiment modules, and VHF receiving stations;[1] assisted
ASL with launcher installations and vehicle rocket buildup and prelaunch
check; provided wind weighting ballistics inputs to ADTC;[3-5] provided
rocket vehicle coordination;[6-9] assisted RDA with probe vehicle aiming;[10]
assisted with probe and VHF experiment data reduction;[1,11,12] and as-
sisted with the field data reduction of probe data.[1]

Rocket trajectory data used in this report were obtained from ADTC,
Eglin.

II ROCKET VEHICLE SYSTEM DESCRIPTION

Figure 1 is the Honest John-Hydac vehicle with the barium payload (Vehicles ST610.31-1 and ST710.31-2 through ST710.31-6). Figure 2 is the Nike-Hydac rocket with the probe and VHF experiment payload (Vehicles ST707.51-1 through ST707.51-6).

Additional vehicle system description is given in Refs. 2, 3, 6, 8, 9, and 10.

III ROCKET FLIGHT RESULTS

Table 1 is the STRESS rocket flight results summary, giving barium cloud release and probe intercept time and position.

Additional rocket vehicle trajectory information is given in Ref. 14.

REFERENCES

1. "VHF Experiment Plan," SDC TM-1308A, Space Data Corporation, Tempe, Arizona (February 1977).

2. "Honest John-Hydac Ballistics Inputs for STRESS," SDC TM-1266C, Space Data Corporation, Tempe, Arizona (February 1977).

3. "Nike-Hydac Ballistic Inputs for STRESS," SDC TM-1267E, Space Data Dorporation, Tempe, Arizona (February 1977).

4. "Honest John-Hydac Performance Estimates for STRESS," SDC TM-1107B, Space Data Corporation, Tempe, Arizona (February 1977).

5. "Nike-Hydac Performance Estimates for STRESS," SDC TM-1265A, Space Data Corporation, Tempe, Arizona (February 1977).

6. "STRESS Rocket Flight Plan," SDC TM-1220-1, Space Data Corporation, Tempe, Arizona (February 1977).

7. "Rocket Work Request--STRESS," SDC TM-1104D, Space Data Corporation, Tempe, Arizona (June 1976).

8. "Honest John-Hydac Ground Safety," SDC TM-1251A, Space Data Corporation, Tempe, Arizona (August 1976).

9. "Ground Safety Data (Nike-Hydac)," SDC TM-629C, Space Data Corporation, Tempe, Arizona (April 1975).

10. "STRESS Probe Rocket Plan," SDC TM-1292D, Space Data Corporation, Tempe, Arizona (February 1977).

11. "Data Reduction Planning Information," SDC TM-1217H, Space Data Corporation, Tempe, Arizona (February 1977).

12. "STRESS VHF Experiment Data Reduction," SDC TM-1326, Space Data Corporation, Tempe, Arizona (March 1977).

13. "Field Data Reduction, STRESS, Vehicles ST705.51-1 Through -6," SDC TM-1321, Space Data Corporation, Tempe, Arizona (March 1977).
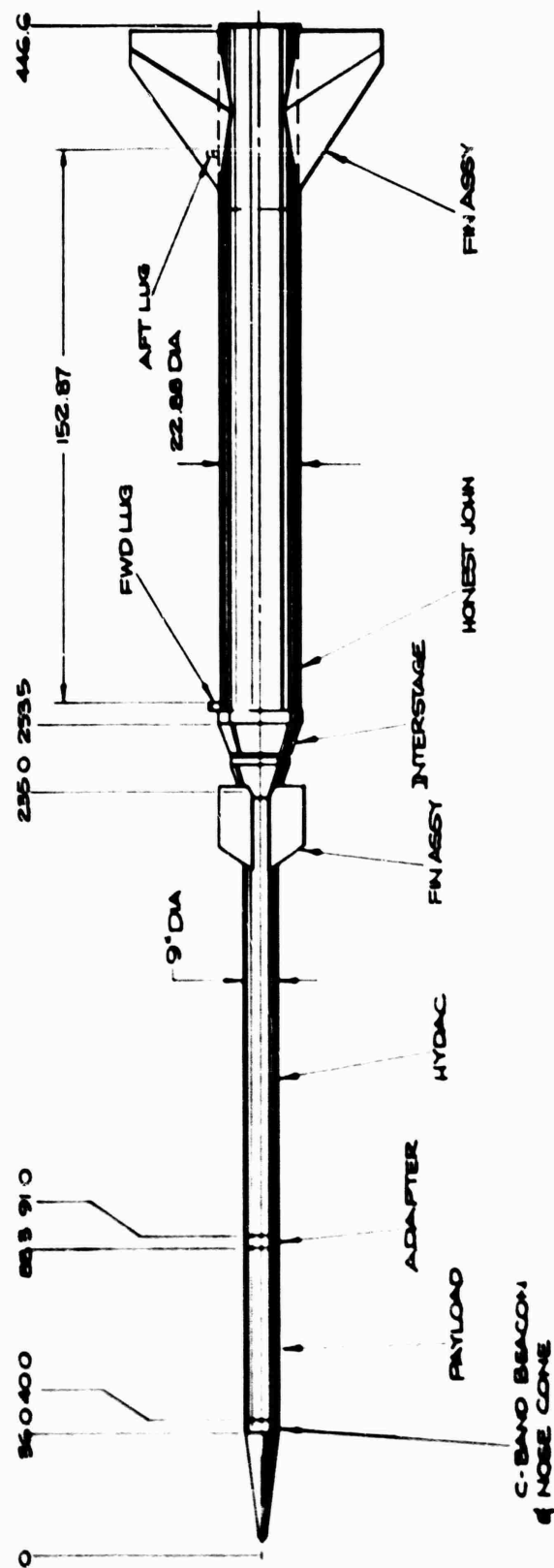
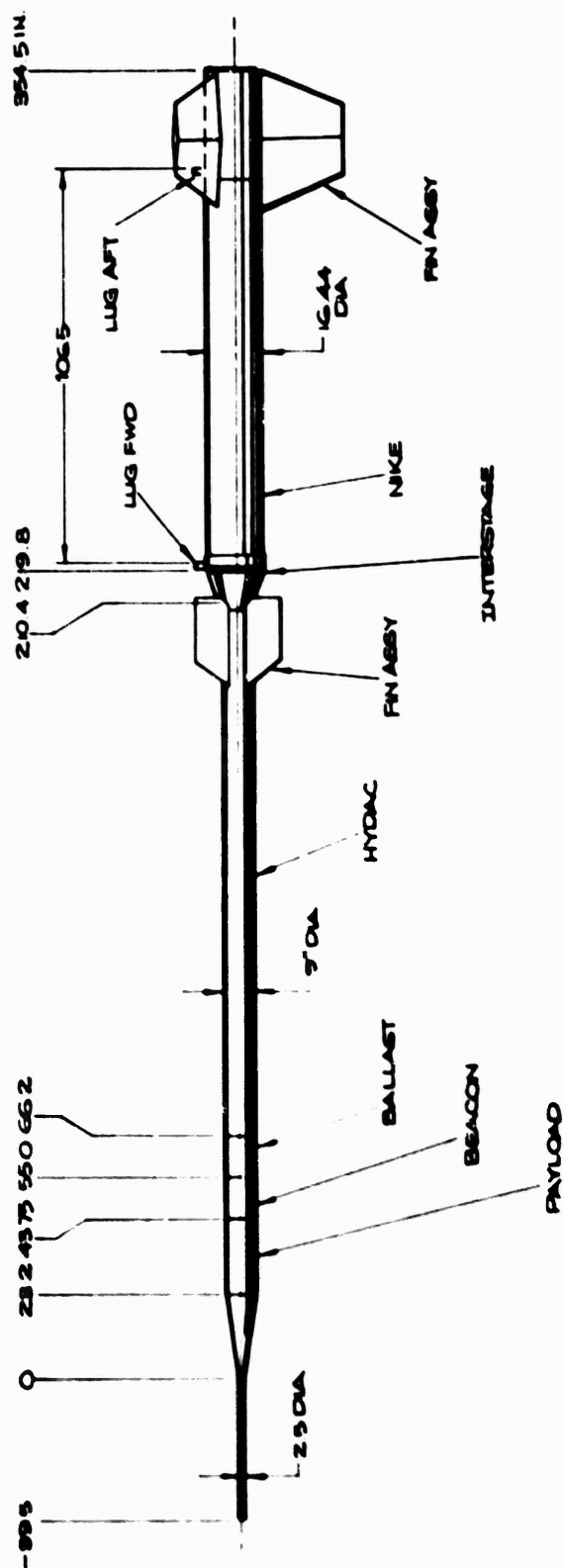FIGURE 1   HONEST JOHN-HYDAC VEHICLE ST610.31-1 AND ST710.31-2 THROUGH -6

66

FIGURE 2   NIKE-HYDAC ST707.51-1 THROUGH -6

67

Table 1

STRESS ROCKET FLIGHT SUMMARY

Vehicle	Experiment	Pad	Launch Date, GMT	Launch Time, GMT	Release or Intercept[5]			
					Time[4]	Altitude (km)[6]	North Latitude	West Longitude
S1210.21-2	Barium[1] KITTY	3[2]	26 Feb 77	2349:33	T + 174.2 s	2352:27.2	178.8 ± 0.2[7]	29° 42.1 ± 0.5'[7]	86° 45.1'
S1210.21-3	Barium CAROLYN	3	2 Mar 77	2351:00	T + 190.5 s	2354:10.5	191.1 ± 0.2	29° 41.3 ± 0.5'	87° 0.5'
S1210.21-4	Barium DIANNE	3	7 Mar 77	2358:00	T + 188.0 s	0001:38.0	185.5 ± 0.2	29° 37.4 ± 0.5'	86° 39.7'
S1707.51-1	Probe	2[3]	8 Mar 77	0014:05	T + 130 s	0016:15	162.2	29° 28.4 ± 0.5'	86° 18.3'
S1707.51-2	Probe	2	8 Mar 77	0032:04	T + 162 s	0034:46	181.9	29° 13.6 ± 0.5'	85° 52.2'
S1210.21-5	Barium ESTHER	3	13 Mar 77	2258:00	T + 188.8 s	2301:08.8	189.2 ± 0.2	29° 41.9 ± 0.5'	86° 48.4'
S1707.51-3	Probe	2	13 Mar 77	2327:00	T + 140 s	2329:20.0	176.3	29° 30.4 ± 0.5'	86° 18.7'
S1707.51-4	Probe	3	13 Mar 77	2344:50	T + 150 s	2347:20	171.2	29° 17.5 ± 0.5'	85° 56.0'
S1210.21-6	Barium FERN	3	14 Mar 77	2243:00	T + 188.8 s	2246:08.8	185.7 ± 0.2	29° 47.4 ± 0.5'	87° 06.9'
S1707.51-5	Probe	2	14 Mar 77	2325:20	T + 145.0 s	2327:45	196.1	29° 38.2 ± 0.5'	86° 29.8'
S1707.21-6	Probe	2	15 Mar 77	0003:10	T + 170 s	0006:00	200.4	29° 04.2 ± 0.5'	85° 52.2

[1] 48 kg Net chemical.
[2] Pad 3 coord. 86° 48' 12.236" W; 30° 23' 15.016" N.
[3] Pad 2 coord. 86° 48' 13.286" W; 30° 23' 14.544" N.
[4] Stop watch. Site A-15A.
[5] Enter region of highest electron density (from probe TM data).
[6] Altitude is above earth.
[7] Tolerance due to timing and tracking uncertainty.

ELECTRON DENSITY STRUCTURE IN BARIUM CLOUDS--
MEASUREMENTS AND INTERPRETATION

K. D. Baker,   J. C. Ulwick,   M. C. Kelley,
L. C. Howlett,   G. D. Allred,   D. Delorey,
N. Grossbard

Utah State University
Logan, Utah

ELECTRON DENSITY STRUCTURE IN BARIUM CLOUDS--
MEASUREMENTS AND INTERPRETATION

K. D. Baker   J. C. Ulwick   M. C. Kelley
L. C. Howlett   G. D. Allred   D. Delorey
N. Grossbard

Utah State University
Logan, Utah

I   INTRODUCTION

A program of measurements to investigate radio-wave propagation
through ionospheric regions perturbed by the presence of ionized,
barium-vapor clouds, was undertaken during the period extending from
December 1976 through mid-March 1977. These investigations have been
termed the STRESS (Satellite Transmission Effects Simulations) Program.
The primary objective of the program was to define the effects, on
radio-wave propagation, of the ionized barium regions through which
the radio waves were propagated, and to correlate these effects with
observed characteristics. Fundamental to these studies were high-
spatial-resolution measurements of ionospheric electron density structure
within the ionized barium regions and particularly within the striated
portions of the clouds. These investigations were the objective of the
rocket probe measurements program reported herein.

The desired measurements were achieved by releasing barium vapor
from rockets upon attaining altitudes of approximately 185 km. The
timing of the releases was such that the region was sunlit. Subse-
quently, as the barium vapor was ionized and developed striations,
additional rocket-borne payloads, equipped with instrumentation to make
fine-scale measurements of electron density, were launched in an effort
to penetrate the striated portion of the ionized clouds. These probes

71

provided profiles of electron density and fine-scale structure (~1 m) internal to the clouds as the payloads traversed these regions, and external to the clouds throughout the remainder of the flights.

The investigations were conducted from Eglin Air Force Base, Florida. Twelve rockets were used in the program. Six of these were two-stage, Honest John-Hydac vehicles equipped for 48-kg chemical (barium) releases at predetermined altitudes. Six additional vehicles, two-stage Nike-Hydacs, were instrumented with electron density probes and VHF transmitters. Ground-based and aircraft-borne instrumentation provided coverage related to vehicle and cloud tracking and radio-wave propagation effects.

The initial barium release (ANNE) was accomplished in December 1976 as a certification round for program readiness and was not probed for electron density measurements or propagation effects. Subsequent flights were conducted during late February and early March 1977, with electron density probes accomplished for the last three barium releases. After each barium release, radar and optical tracking (where possible) of the resulting cloud provided inputs for computer prediction of probe launch azimuth and elevation for a given launc'· time. These coordinates were planned to permit the probes to intercept and penetrate the ionized portion of the barium cloud. Figure 1 is a scenario of STRESS launches for a typical barium event. Table 1 is a summary of launches accomplished during the STRESS program.

II PAYLOADS--CONFIGURATION AND INSTRUMENTATION

A.   General

All of the six payloads for probing the barium ion clouds were identical, and all were propelled by two-stage Nike-Hydac motors. The main payload, illustrated in Figure 2, contained two electron density measuring instruments, a plasma frequency probe, and a dc probe. Each of these probes utilized a portion of the 1-m-long, 6.35-cm-diameter nose spike as their sensing element in contact with the ionospheric
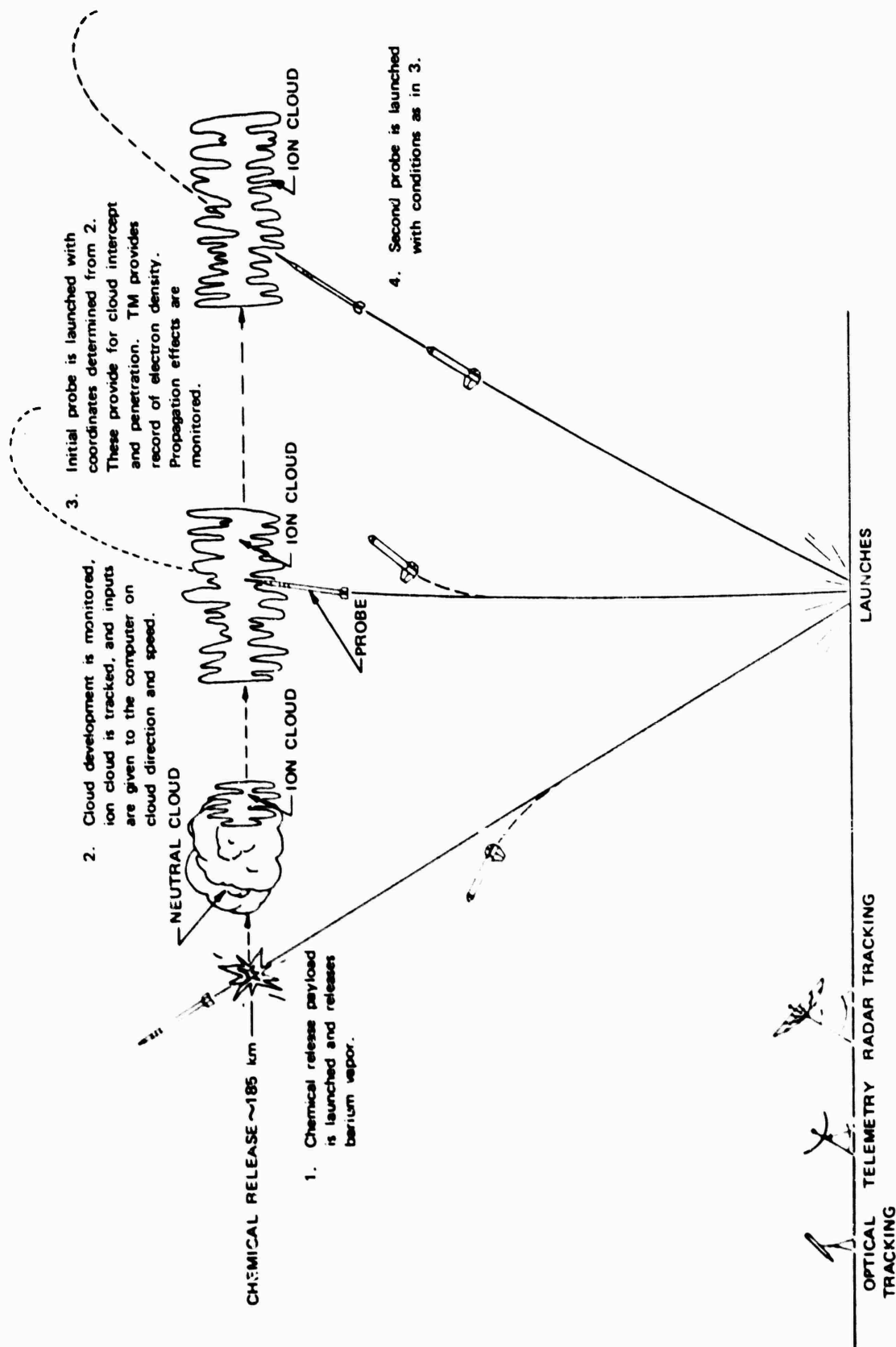
CHEMICAL RELEASE ~185 km

NEUTRAL CLOUD

ION CLOUD

ION CLOUD

ION CLOUD

ION CLOUD

PROBE

LAUNCHES

OPTICAL   TELEMETRY   RADAR TRACKING
TRACKING

1. Chemical release payload is launched and releases barium vapor.

2. Cloud development is monitored. ion cloud is tracked, and inputs are given to the computer on cloud direction and speed.

3. Initial probe is launched with coordinates determined from 2. These provide for cloud intercept and penetration. TM provides record of electron density. Propagation effects are monitored.

4. Second probe is launched with conditions as in 3.

FIGURE 1   SCENARIO OF ROCKET LAUNCHES FOR A TYPICAL BARIUM EVENT DURING PROJECT STRESS

73

Table 1

VEHICLE LAUNCH SUMMARY--PROJECT STRESS

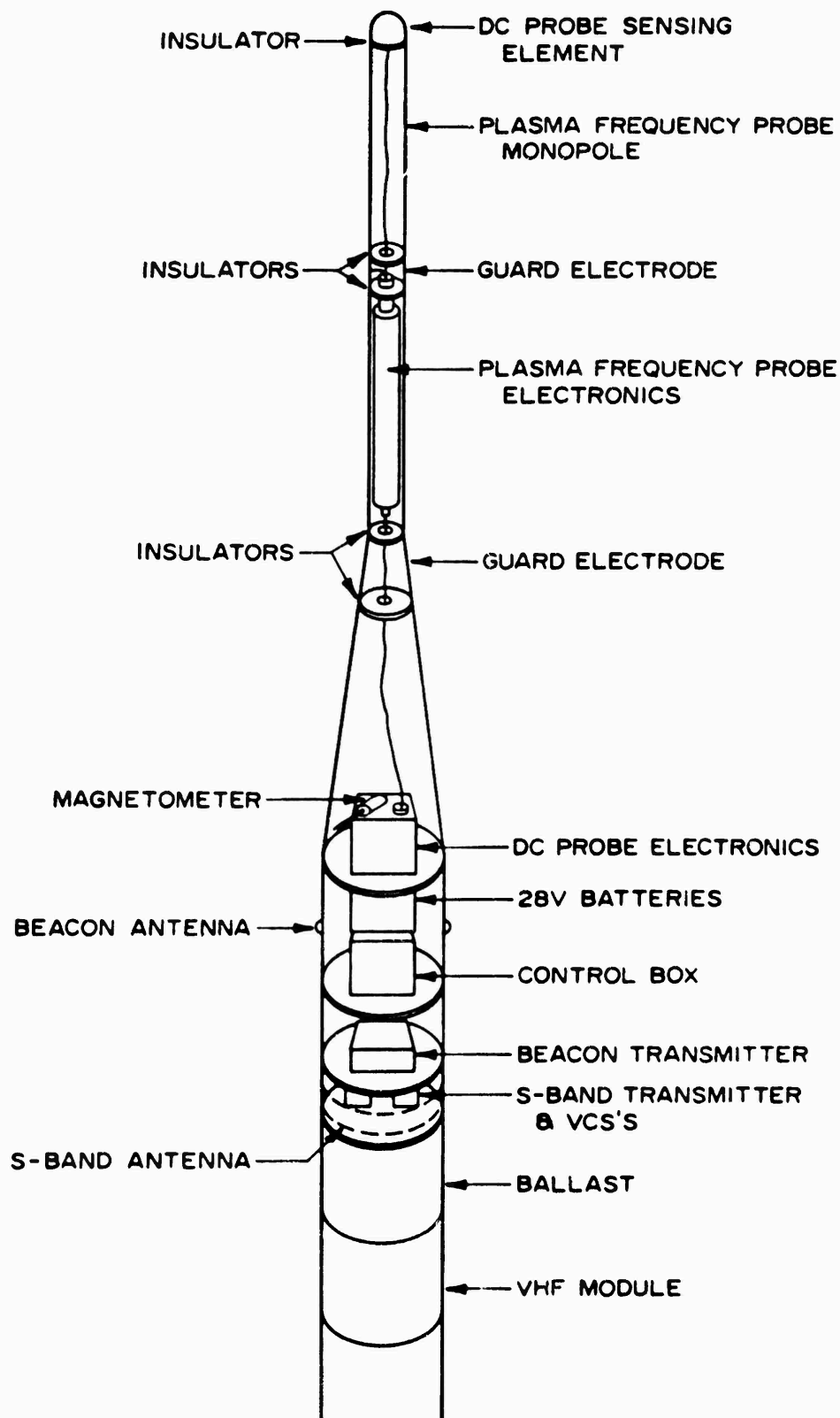| Vehicle	Event Name	Experiment	Launch Date and Time (GMT)	Remarks
ST610.31-1	ANNE	Barium release	1 Dec 76 2308:37	Certification
S7710.31-2	BETTY	Barium release	26 Feb 77 2349:33	Not probed
ST710.31-3	CAROLYN	Barium release	2 Mar 77 2351:00	Not probed
ST710.31-4	DIANNE	Barium release	7 Mar 77 2358:00	Probed at R + 15 min by ST707.51-1 Probed at R + 33 min by ST707.51-2
ST707.51-1	DIANNE	Probe	8 Mar 77 0014:05	DIANNE early probe R + 15 min
ST707.51-2	DIANNE	Probe	8 Mar 77 0032:04	DIANNE late probe R + 33 min
ST710.31-5	ESTHER	Barium release	13 Mar 77 2258:00	Probed at R + 28 min by ST707.51-3 Probed at R + 46 min by ST707.51-4
ST707.51-3	ESTHER	Probe	13 Mar 77 2327:00	ESTHER early probe R + 28 min
ST707.51-4	ESTHER	Probe	13 Mar 77 2344:50	ESTHER late probe R + 46 min
ST710.31-6	FERN	Barium release	14 Mar 77 2243:00	Probed at R + 41 min by ST707.51-5 Probed at R + 80 min by ST707.51-6
ST707.51-5	FERN	Probe	14 Mar 77 2325:20	FERN early probe R + 41 min
ST707.51-6	FERN	Probe	15 Mar 77 0003:10	FERN late probe R + 80 min

INSULATOR → **DC PROBE SENSING ELEMENT**

PLASMA FREQUENCY PROBE MONOPOLE

INSULATORS → **GUARD ELECTRODE**

PLASMA FREQUENCY PROBE ELECTRONICS

INSULATORS → **GUARD ELECTRODE**

MAGNETOMETER

DC PROBE ELECTRONICS

28V BATTERIES

BEACON ANTENNA → **CONTROL BOX**

BEACON TRANSMITTER

S-BAND TRANSMITTER & VCS'S

S-BAND ANTENNA → **BALLAST**

VHF MODULE

FIGURE 2   STRESS PAYLOAD CONFIGURATION

plasma. The payload spin axis symmetry and freedom from payload doors and mechanisms produced a flight unit that was simple, rugged, and caused minimal effects from wakes or spin modulation in the obtained data.

In addition to the instrumentation for measurement of ionospheric electron density, each payload included a Heliflux RAM 5C mangetic-aspect sensor mounted across the rocket's major axis to provide a measure of rocket spin and to give some indication of vehicle attitude and stability. A C-band radar transponder was included to provide a signal for solid radar tracking, and an S-band telemetry system, operating at a link frequency of 2251.5 MHz, provided for data transmission to the ground station. Total payload weight for the probes was 130 lb, with the main payload weighing 70 lb.

B. DC Probe

The dc probe operates on the principle that the electron flow to a small, positively charged electrode immersed in the ionospheric plasma is directly related to the electron density of the plasma. Figure 3 is a conceptual block diagram of the dc probes used in the STRESS program. As its sensing electrode in contact with the ionospheric plasma, the dc probe uses the foremost segment of the payload nose spike (see Figure 2) with dimensions as noted in Figure 3.

The operation of the dc probe is exceptionally simple and is illustrated in Figure 3. The current collected by the 63-cm^2 probe electrode (the forward 4.76 cm of the payload nose spike), which is biased at +3 V with respect to the rest of the payload, is fed to the electronics system preamplifier at B. With a finite sensing electrode current caused by electron flow from the plasma to the electrode, the voltages at C and D are not equal, and the differential stage amplifies the difference, giving an output that is proportional to the sensing-electrode current flow. The output from the differential amplifier is fed to four amplifiers having gains of x1, x10, x100, and x1000 with the four outputs going to the payload telemetry section.
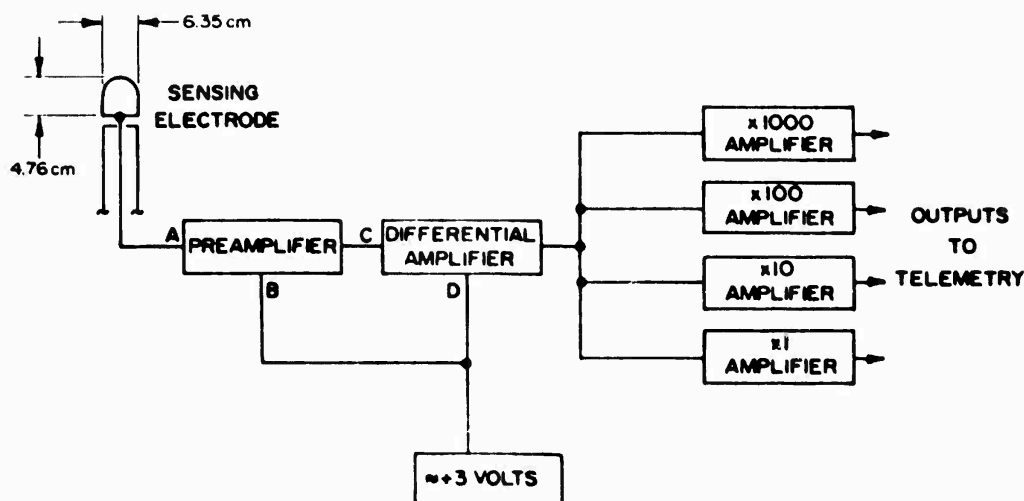
76

FIGURE 3   BLOCK DIAGRAM OF DC PROBE

C.   Plasma-Frequency Probe

The plasma-frequency probe (PFP) utilizes the well established relationships between plasma frequency, electron density, and the reactance of a probe immersed in the plasma to provide a measurement of electron density.[*]   In the version of the PFP flown in the STRESS program, a phase-locked loop is used to track the frequency that produces zero phase angle between RF current and voltage being fed to the sensing antenna.   This frequency of resonance is closely related to the electron plasma frequency, in Hz:

$$f_N^2 = \frac{e^2 N_e}{4\pi^2 m_e} = 80.6 \times 10^6 N_e \qquad . \tag{1}$$

In the absence of a magnetic field the resonance occurs at this electron plasma frequency.   The effect of the magnetic field is to

---

[*] K. D. Baker, E. F. Pound, and J. C. Ulwick, "Digital Plasma Frequency Probe for Fine Scale Ionospheric Measurements," Small Rock Instrumentation Techniques, K.-I. Maeda, ed., p. 49 (North-Holland Publishing Co., Amsterdam, 1969).

77

shift the resonance slightly higher in frequency to the upper hybrid frequency:

$$f_H = \sqrt{f_N^2 + f_B^2} \quad , \quad \text{where } f_B = \frac{eB}{2\pi m_e} \quad . \tag{2}$$

The phased-locked version of the PFP, which is shown in the block diagram in Figure 4, utilizes the forward half of the 1-m-long nose as its antenna. The system is designed to sense the zero phase condition of the antenna impedance at the hybrid resonant frequency and to cause a phase-locked loop to force the RF oscillator to track the frequency producing the zero-phase-angle condition. The frequency of the oscillator is digitally counted for 1 ms and forms the data for a digital plasma frequency readout. Additionally, the voltage controlling the loop oscillator is monitored to provide an analog measurement of plasma frequency and loop operation. The digital output provides excellent accuracy in the measurement of electron density at samples with about a meter spatial dimension separated in space by the distance the payload travels in a 16-ms sample period (~25 m). In order to provide higher-spatial-resolution measurements, a continuous analog channel and accoupled ×10 amplified channel (ΔPFP) were provided that responded down to fluctuations of about 1 meter scale size. The range of electron densities covered by the plasma frequency probe is from about 10^5 to 7×10^6 el/cm^3.

III   STRESS PROBE FIRING SUMMARY AND GEOMETRY

The electron density probe rockets were flown in pairs into the last three barium clouds as briefly summarized earlier in Table 1 and elaborated on in Table 2, which includes a listing of parameters relevant to the description of each flight.

Probe encounters with the barium clouds are described in Table 3, where entries under "Probe Residence in Ba Cloud" were determined from significant electron density enhancements over background as determined
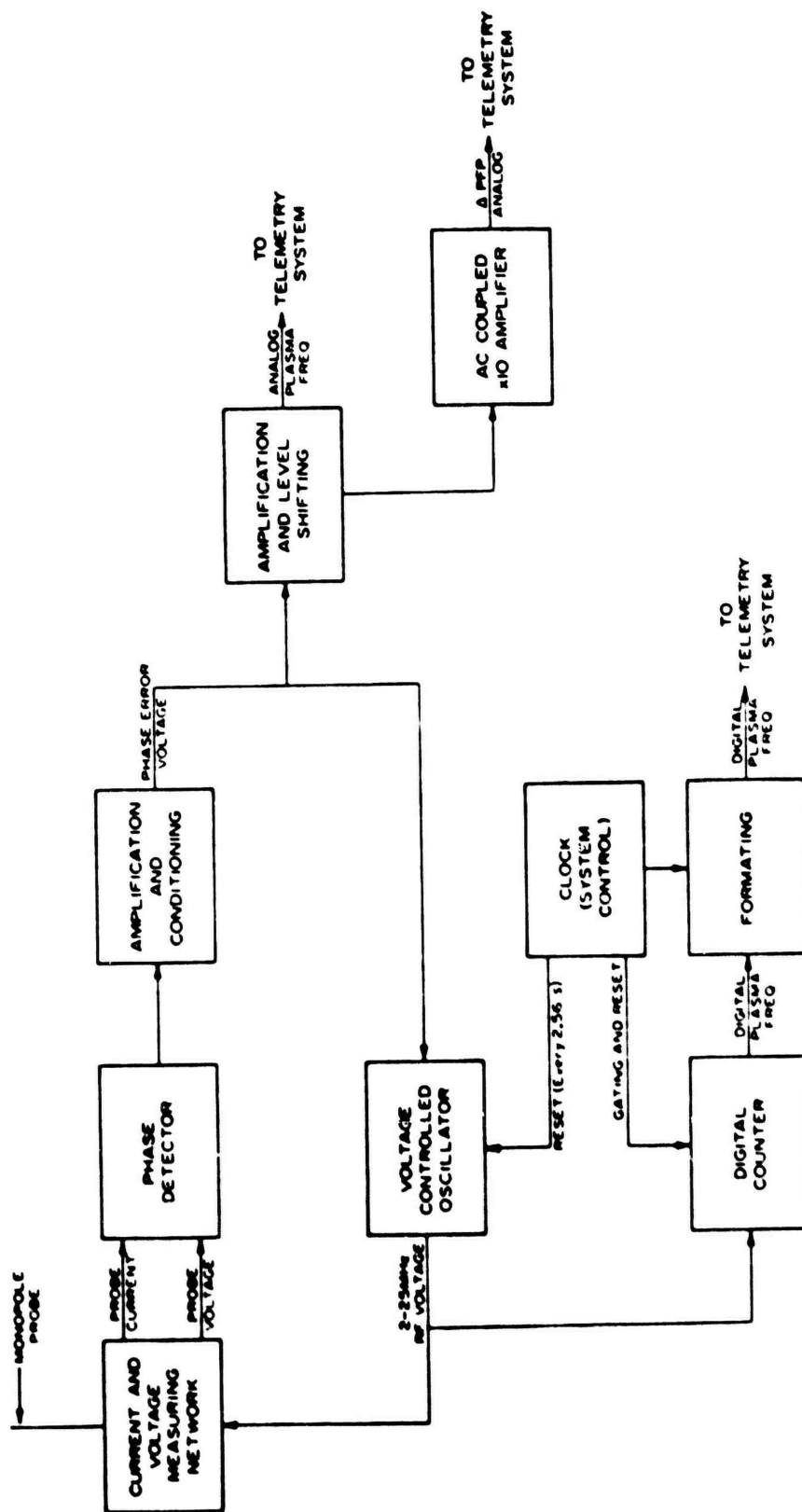
78

FIGURE 4   BLOCK DIAGRAM OF PLASMA-FREQUENCY PROBE

79

Table 2

SUMMARY OF PROBE ROCKET FLIGHT CHARACTERISTICS

Event	Rocket No.	Launch Time (UT)	Apogee (km)	Range (km)	Flight Azimuth (deg)	Roll Rate (rps)	Precession Period (s)	Approximate Precession Half-Angle (deg)
DIANNE	ST707.51-1	0014:05	213	221	156	7	34	8
DIANNE	ST707.51-2	0032:04	203	231	146	7	36	7
ESTHER	ST707.51-3	2327:00	220	191	156	7	37	5
ESTHER	ST707.51-4	2344:50	199	238	146	6.4		0
FERN	ST707.51-5	2325:20	249	164	162	7	32	3
FERN	ST707.51-6	0003:10	222	204	149	7	36	5

80

Table 3

SUMMARY OF STRESS PROBE FLIGHTS

Event	Probe Vehicle No.	Probe Launch Time, UT	Probe Residence in Barium Cloud		Age of Cloud (min)	Cloud Features
			Altitude (km)	Time After Launch (s)		
DIANNE	ST707.51-1	0014:05	151-175	120-145	15	Cloud developed a kink
DIANNE	ST707.51-2	0032:04	178-183	156-164	34	Two striated portions of cloud
ESTHER	ST707.51-3	2327:00	160-192	123-160	28	Striations not yet developed
ESTHER	ST707.51-4	2344:00	155-181	130-165	46	Well-developed striations
FERN	ST707.51-5	2325:20	131-203	92-152	42	Cloud dropped rapidly (no optical coverage)
FERN	ST707.51-6	0003:10	112-206	83-180	80	Beginning of optical coverage

81

from the in-situ probe results. The age of the cloud is given in minutes after release for the maximum observed electron density on each probe flight.

To assist in visualizing the probe/cloud encounter and penetration, Figures 5 through 9 are conceptual drawings that include the geographic coordinates of the launches, the vehicle ground track and trajectory, coordinates of the barium release, and subsequent development of the barium cloud. Probe entry point into the cloud, point of maximum electron density, and exit point (all from electron density results) are marked by dots along the rocket trajectory. Rocket apogee is noted in each figure, as is the track of the barium cloud versus time.

The flight of rocket ST707.51-6 is omitted from these conceptual drawings because the cloud track on this probe was doubtful, and the electron density measurements were of limited usefulness, as noted later in this report (Section IV).

In viewing the electron density results presented in Section IV of this report, it is important to consider the velocity of each probe as it moves through the ion-cloud region. Since the ion-cloud structure will be aligned along magnetic field lines, perhaps the most important velocity will be that normal to the magnetic field. To aid in viewing the data, the pertinent rocket velocities for each probe flight are summarized in Table 4 for the region of the maximum measured electron density in each case.

IV ELECTRON DENSITY RESULTS

Electron density measurements were attained on all six flights. The plasma-frequency probe indicated proper lock onto the plasma resonance frequency during all regions of interest, with data being available on both the straight analog channel and the ΔPFP channel. The digital counter, however, failed at liftoff on all but rocket ST707.51-5. The failure did not negate the probe measurements but did make absolute electron density values more difficult to ascertain. The repeating difficulty was attributed to failure of an integrated circuit comparator
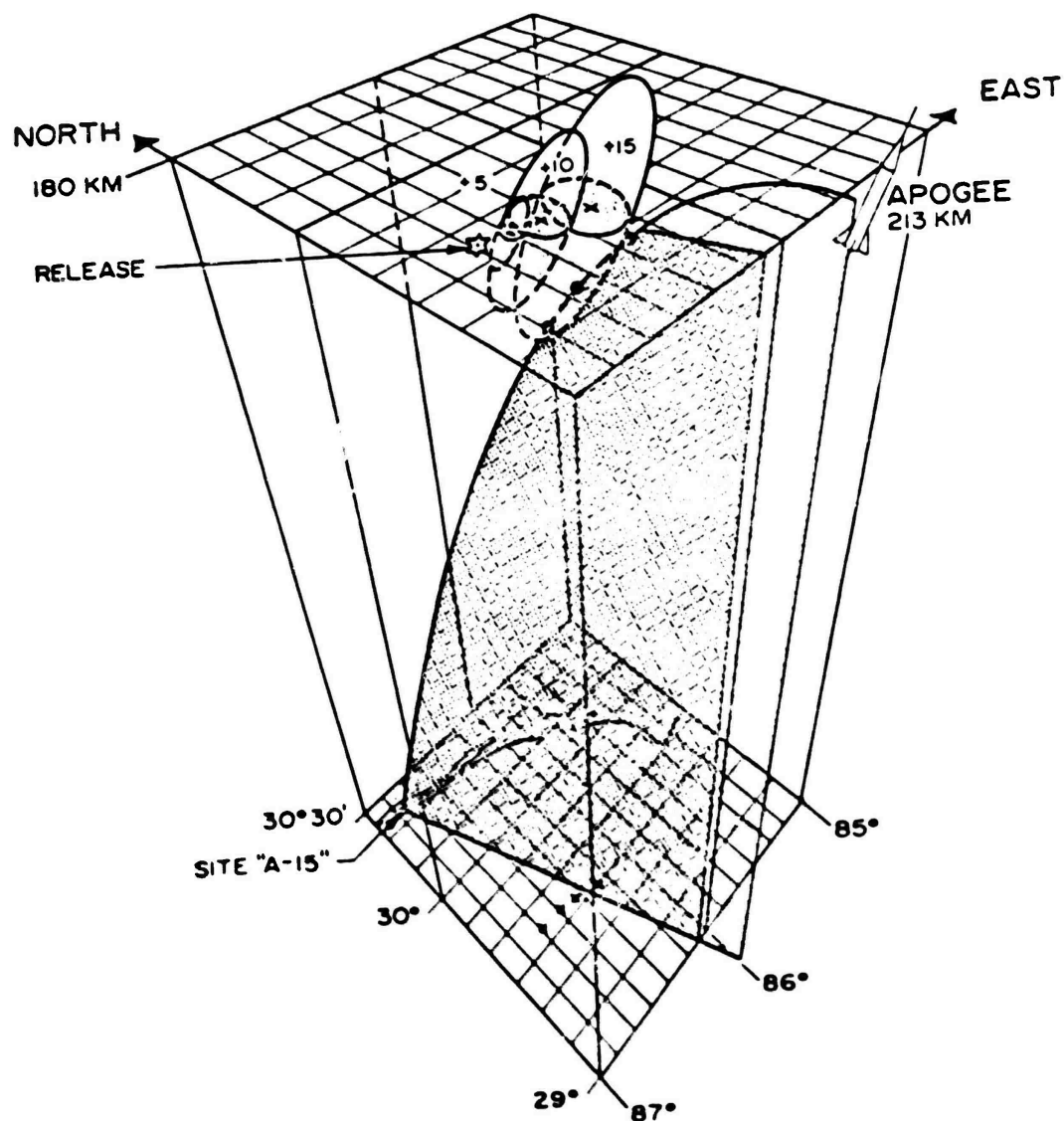
82

FIGURE 5 TRAJECTORY OF ROCKET PROBE ST707.51-1 Release point of Event DIANNE is shown along with the visible ionized cloud track points at R + 5, 10, and 15 min. Rocket entry point into the cloud, maximum point, and exit point (from electron density results) are indicated by the three dots along the trajectory.
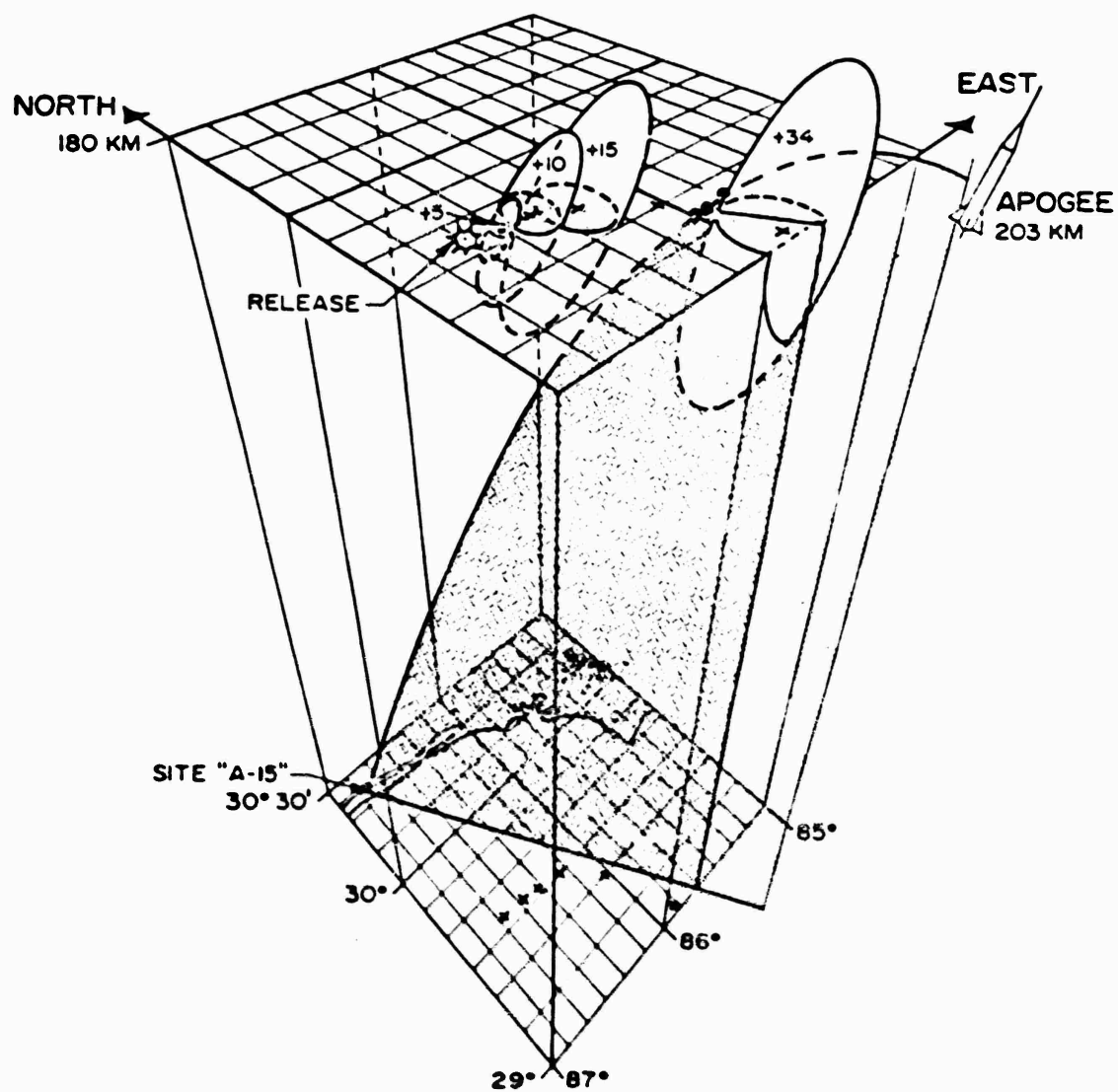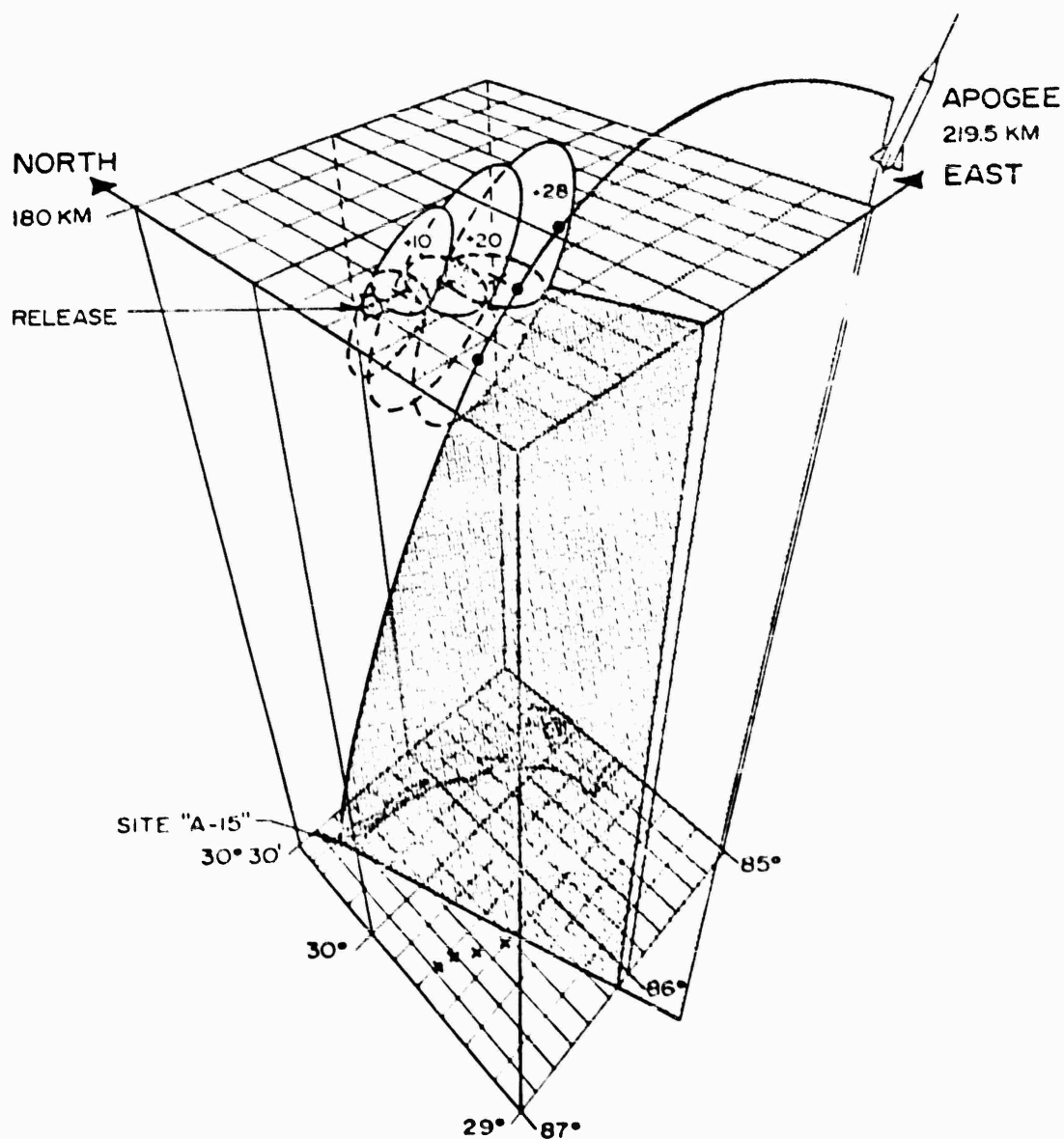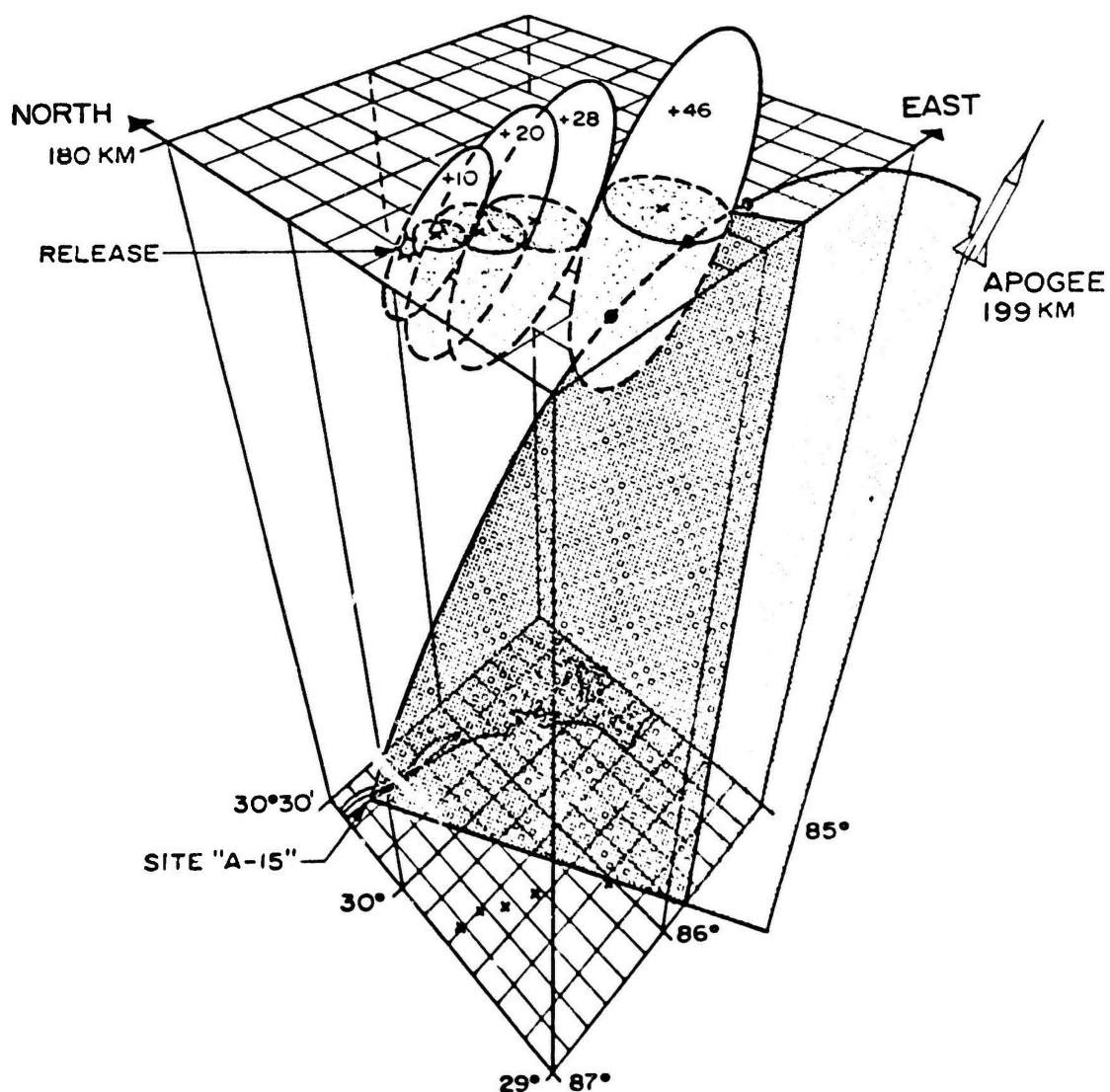
FIGURE 6   TRAJECTORY OF ROCKET PROBE ST707.51-2   Release point of Event DIANNE is shown along with the visible ionized cloud track points at R + 5, 10, 15, and 34 min.   Rocket entry point into the cloud, maximum point, and exit point (from electron density results) are indicated by the three dots along the trajectory.
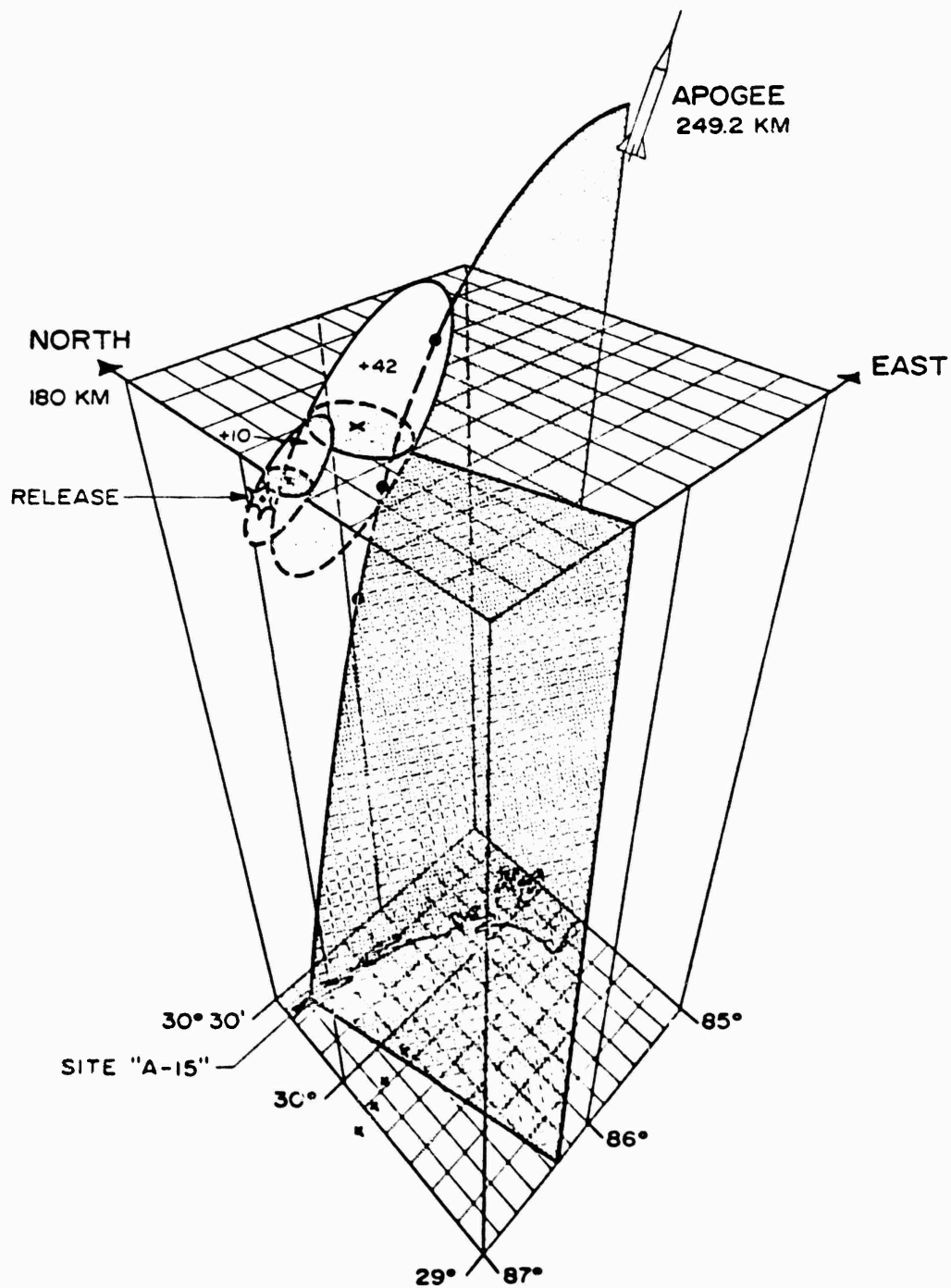
FIGURE 7   TRAJECTORY OF ROCKET PROBE ST707.51-3   Release point of Event ESTHER is shown along with the visible ionized cloud track points at R + 10, 20, and 28 min.   Rocket entry point into the cloud, maximum point, and exit point (from electron density results) are indicated by the three dots along the trajectory.

FIGURE 8   TRAJECTORY OF ROCKET PROBE ST707.51-4   Release point of Event ESTHER is shown along with the visible ionized cloud track points at R + 10, 20, 28, and 46 min.   Rocket entry point into the cloud, maximum point, and exit point (from electron density results) are indicated by the three dots along the trajectory.

86

FIGURE 9   TRAJECTORY OF ROCKET PROBE ST707.51-5   Release point of Event FERN is shown along with the visible ionized cloud track points at R + 10 and 42 min. Rocket entry point into the cloud, maximum point, and exit point (from electron density results) are indicated by the three dots along the trajectory.

Table 4

SUMMARY OF ROCKET PROBE VELOCITIES

Rocket No.	Altitude of Maximum N_e (km)	V_t (km/s)	V_v (km/s)	V_h (km/s)	$V_\parallel$ (km/s)	$V_\perp$ (km/s)
ST707.51-1	162	1.41	0.98	1.01	-1.29	0.58
ST707.51-2	182	1.25	0.62	1.09	-0.95	0.81
ST707.51-3	177	1.25	0.89	0.88	-1.15	0.50
ST707.51-4	173	1.31	0.71	1.10	-1.04	0.80
ST707.51-5	171	1.37	1.19	0.68	-1.34	0.26
ST707.51-6	160	1.41	1.06	0.93	-1.29	0.56

used to interface the RF oscillator to the digital frequency counter. In the field, attempts to determine the exact cause of the failure and to alleviate the problem were not successful, with the possible exception of probe ST707.51-5, which did give complete results on the digital channel as well as the analog channel. The cause of the integrated-circuit failures is still not understood past the fact that it appears that a high-voltage transient is somehow generated in conjunction with the rocket ignition that is coupled back through the antenna to the comparator and wipes it out.

The dc probe provided consistently good results on all but the last flight (ST707.51-6). Some difficulty was encountered with the high humidity at the launch site, producing leakage currents, but these did not impair the measurements in the region of the barium cloud except on rocket ST707.51-6, which did not yield any meaningful data. Data were obtained on the analog PFP channel but are of limited accuracy.

The electron density profiles are presented below for each rocket flight.

88

A.   Rocket ST707.51-1 (Event DIANNE, R + 15 min)

The electron density profile measured on Rocket ST707.51-1 flown at
R + 15 min for Event DIANNE is shown in Figure 10. Also shown for
comparison is the approximate electron density profile of the undisturbed
ionosphere (dashed line) as determined by probe measurements on rocket
descent. A check was also made by comparing the F-region density with
the ground based ionosonde value. It is obvious that the rocket probe
traversed the region of enhanced electron density associated with the
barium ion cloud over the altitude range from about 150 to 180 km. The
peak electron density of the barium cloud layer of 1.4×10^6 el/cm^3
found at 162 km is about a factor of 100 larger than the electron density
at that altitude in the undisturbed ionosphere. The layer is relatively
smooth and devoid of large-scale structure that would be expected if
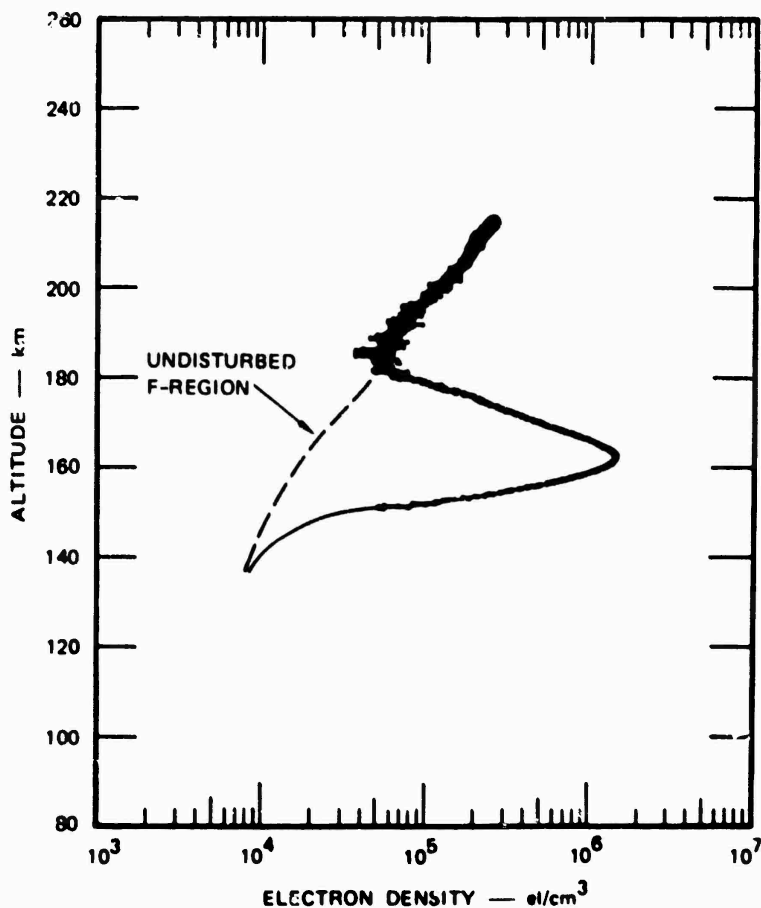
FIGURE 10   ELECTRON DENSITY PROFILE, PROBE ST707.51-1,
EVENT DIANNE (R + 15 min)

89

cloud striations had been penetrated. The layer has a width at half amplitude of 10 km in vertical extent, which would correspond to a movement of the rocket probe of 6 km across the terrestrial magnetic field.

B. Rocket ST707.51-2 (Event DIANNE, R + 34 min)

Rocket probe ST707.51-2 was flown in Event DIANNE about 19 minutes after ST707.51-1 and just penetrated the edge of the ion cloud, as can be seen in the profile presented in Figure 11. The peak density found was the same as that found by the earlier probe (1.4×10^6 el/cm^3), but the penetration was at the higher altitude of 182 km. The sharp feature at 182 km has an electron density about two orders of magnitude over the ambient density and is imbedded in a broader region of enhanced
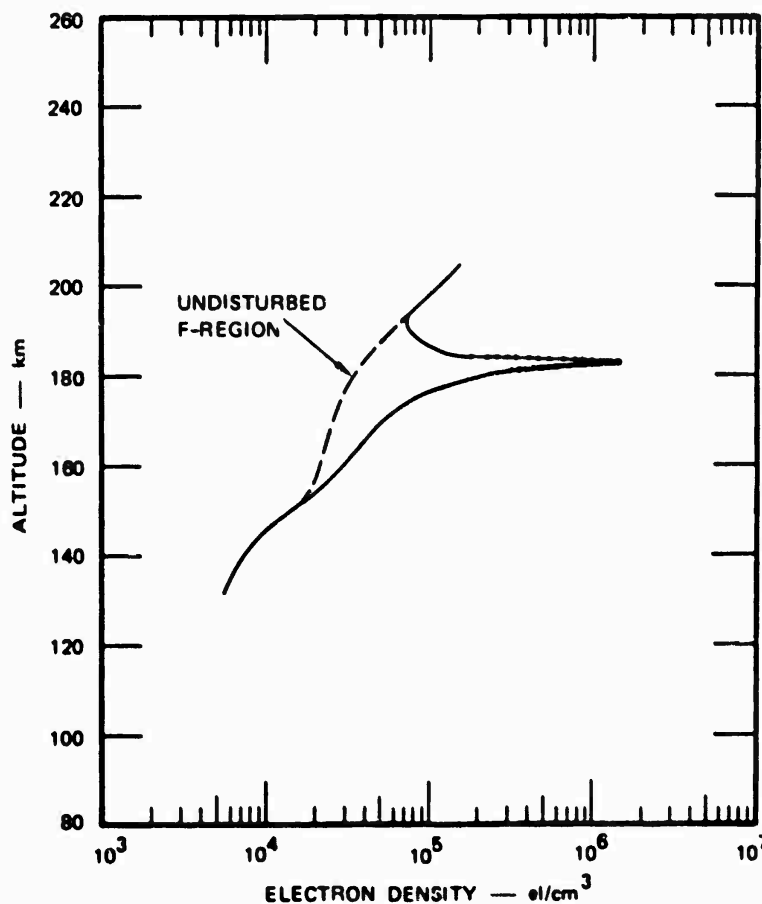
FIGURE 11   ELECTRON DENSITY PROFILE, PROBE ST707.51-2,
EVENT DIANNE (R + 34 min)

density more of the shape of the profile found on ST707.51-1, but with less density and at a higher altitude. The apparent higher altitude of the layer is due to the late penetration of the cloud since the rocket flew to the north of the cloud (see Figure 6). The sharp finger rises above the broader region by about an order of magnitude. The finger has a width (half amplitude) of about 1.5 to 2 km in extent either vertically or normal to B.

C. Rocket ST707.51-3 (Event ESTHER R + 28 min)

The electron density profile measured on probe rocket ST707.51-3, which penetrated the barium cloud ESTHER at about R + 28 min is shown in Figure 12. The profile is smooth, showing no large-scale structures or
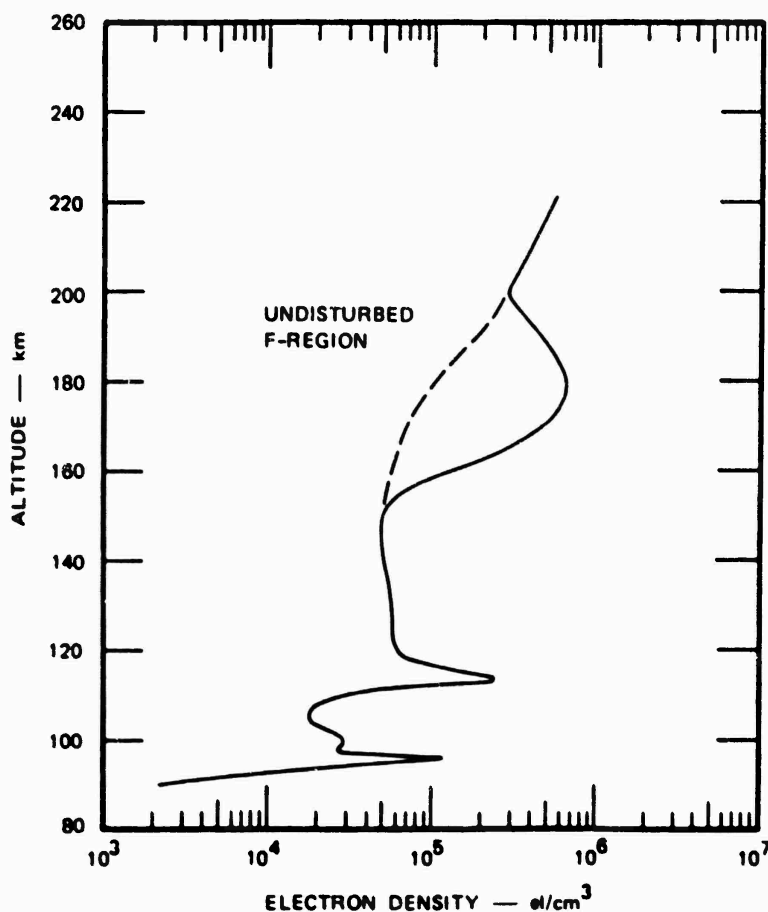
FIGURE 12 ELECTRON DENSITY PROFILE, PROBE ST707.51-3, EVENT ESTHER (R + 28 min)

91

evidence of cloud striations. The sharp peaks in the B region are sporadic E layers not associated with the barium release. The layer has a peak electron density of 7×10^5 el/cm^3 at 177 km with a width (half amplitude) of 24 km. At the peak of the layer the density is enhanced over the ambient (determined by rocket descent) by nearly an order of magnitude.

D.   Rocket ST707.51-4 (Event ESTHER R + 46 min)

The second probe rocket (ST707.51-4) flown into barium cloud ESTHER at R + 46 min penetrated the ion cloud and produced an electron density profile (Figure 13) that showed large-scale structures in the 165-to-175-km region embedded in a general layer similar to the layer probed by rocket ST707.51-3. The observed layer was moved down from the
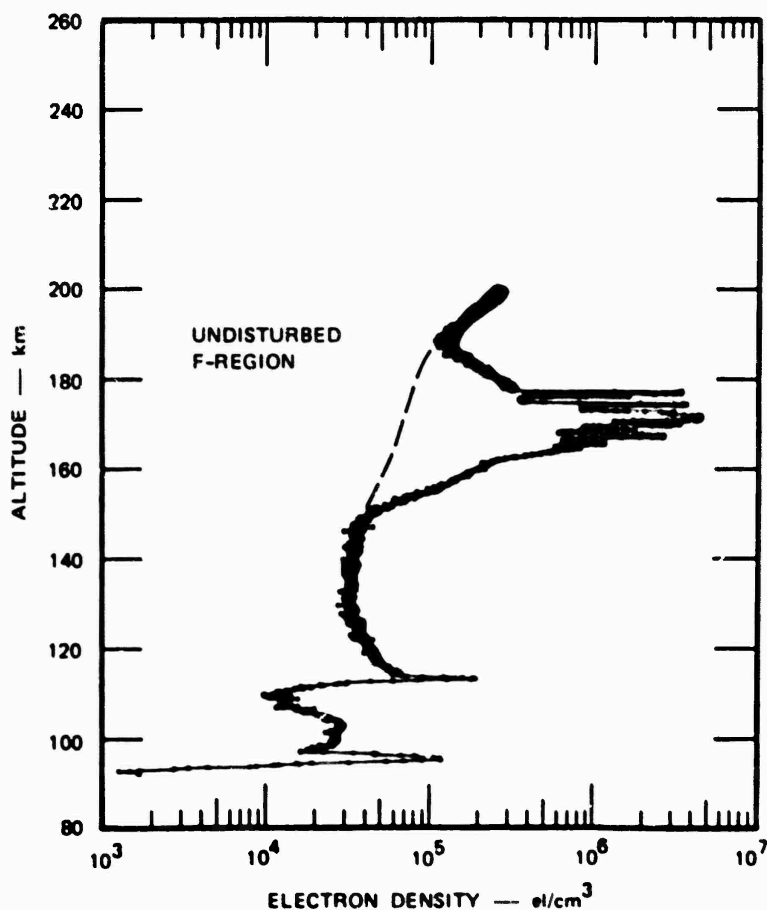
FIGURE 13   ELECTRON DENSITY PROFILE, PROBE ST707.51-4, EVENT ESTHER (R + 46)

92

earlier 177 km height to being centered at about 170 km. The peak electron density of 5×10^6 el/cm^3 at 173 km shows an enhancement of about two orders of magnitude over the normal ionosphere.

The entry of the rocket probe into the striated cloud region is consistent with the cloud geometry as determined from electron density contours furnished by SRI from the ground-based radar returns (courtesy of Victor Gonzales) (due to the ambient light level, no optical images of cloud and striations were possible). An expanded version of the electron density structure as theprobe penetrated the striated region is shown in the time plot of Figure 14. This plot shows the electron density from T + 140 to T + 160 s of probe rocket flight time. This includes all of the striations penetrated by the probe in the altitude region between 163 and 178 km. For discussion, the striation fingers
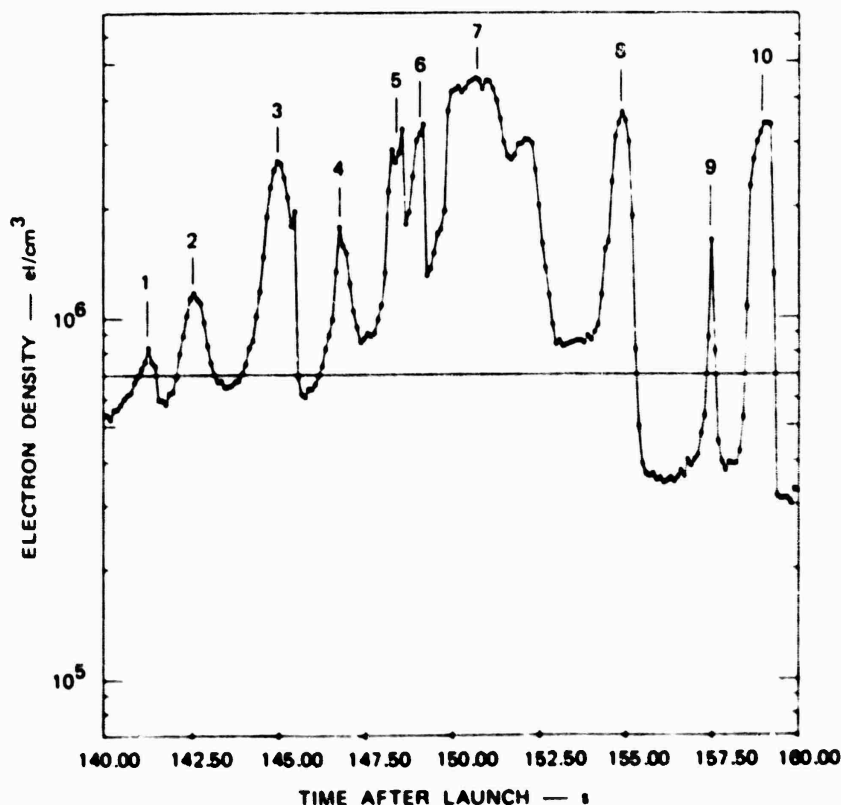

FIGURE 14   REGION OF ELECTRON DENSITY STRIATIONS MEASURED
FROM T + 140 TO 160 s (163 TO 178 km) BY PROBE
ST707.51-4 (ESTHER R + 46 min). The density striations
are numbered to aid discussion.

93

have been numbered. The features have varying widths (half amplitude)
from 0.17 s (feature 9) to 2.45 s on feature 7. Note how some of the
fingers--notably 3 and 6--have very fast fall times (about 20 ms).
Figures 15 and 16 show a further magnification of portions of the
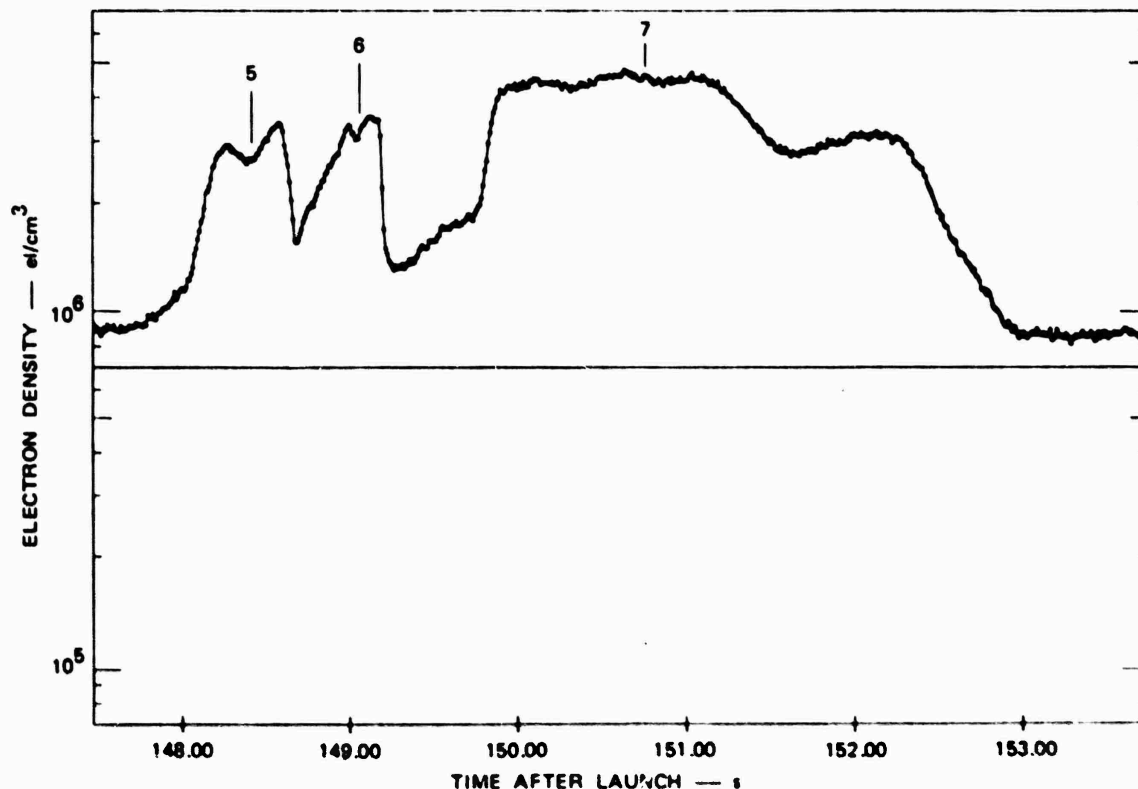striated region to facilitate a better visualization of the structure
shapes.

FIGURE 15   MAGNIFICATION OF ELECTRON DENSITY STRIATIONS MEASURED BY
             PROBE ST707.51-4 SHOWING FEATURES 5, 6, AND 7

Relating the observed variations to spatial-feature geometry is
not simple, since the observations represent a single path cut through
the spatial structure. The observations of the striation features
(fingers) are summarized in Table 5. As a first attempt to relate the
observations to spatial structure, the dimensions of the features across
magnetic field lines are given by utilizing the component of the rocket
velocity perpendicular to the terrestrial magnetic field (260 m/s). The

94

Table 5

SUMMARY OF STRIATION FEATURES
(ST707.51-4)

| Feature	Peak Time (s)	N_e ($\times 10^6$ el/cm^3)		Width $\perp\vec{B}$		1/e rise $\perp\vec{B}$		1/e fall $\perp\vec{B}$	
		Peak	Valley Following	Seconds	Meters	Seconds	Meters	Seconds	Meters
1	141.3	0.82	0.56	0.63	504	1.27	1016	0.42	336
2	142.6	1.2	0.65	0.65	520	0.84	672	0.62	496
3	145.0	2.7	0.61	0.96	588	0.37	296	0.02	16
4	146.8	1.9	0.88	0.40	320	0.12	96	0.11	88
5	148.6	3.4	1.6	0.48	384	0.18	144	0.10	80
6	149.1	3.5	1.3	0.34	272	0.38	304	0.02	24
7	150.6	4.7	0.84	2.45	1960	0.13	104	0.35	280
8	154.9	3.7	0.37	0.62	496	0.39	312	0.12	96
9	157.5	1.7	0.38	0.17	136	0.11	88	0.07	56
10	159.1	3.5	0.33	0.73	584	0.08	64	0.02	16
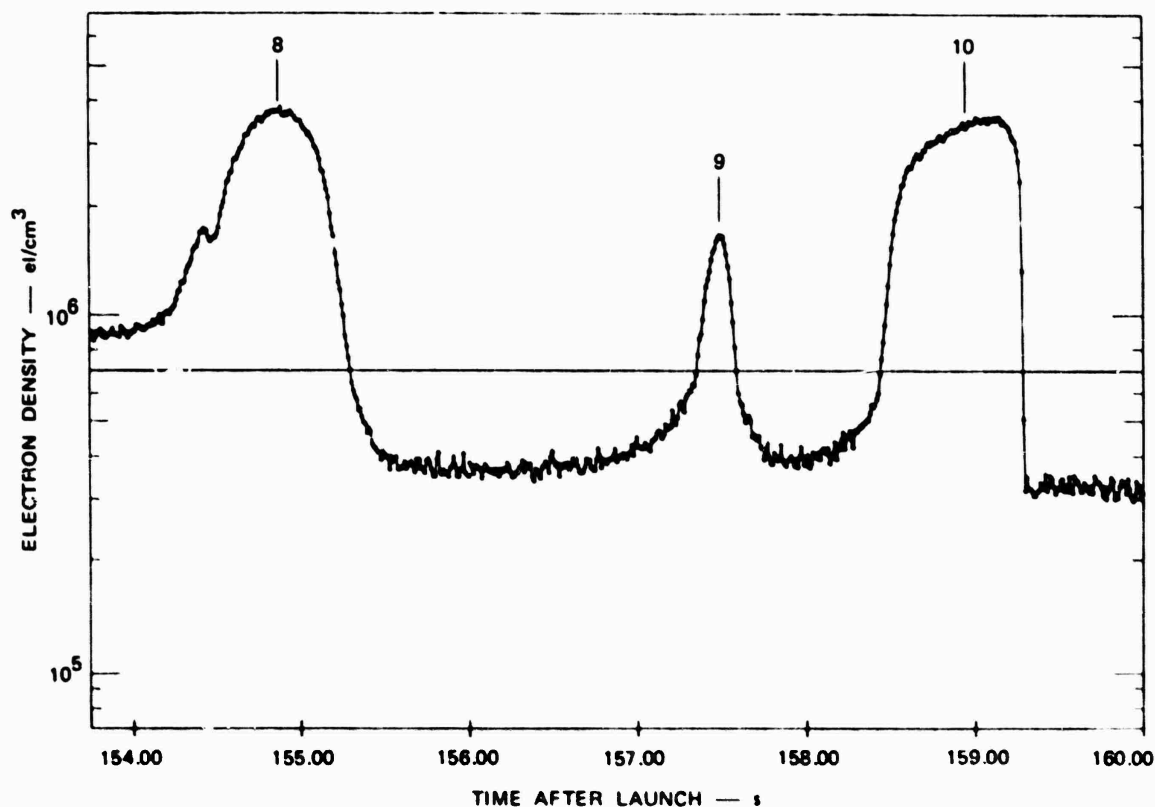
FIGURE 16   MAGNIFICATION OF ELECTRON DENSITY STRIATIONS MEASURED BY
PROBE ST707.51-4 SHOWING FEATURES 8, 9, AND 10

total rocket velocity at this time is about 1370 m/s, so all dimensions
would be increased by about a factor of 5, as measured by the actual
rocket probe cut through the structures along the flight path. If the
velocity normal to the $\vec{V}_n - \vec{E} \times \vec{B}/B^2$ direction (345 m/s) were used, the
features would be 30% larger than given in Table 5. The peak density
(feature 7) of 4.7×10^6 el/cm^3 is a factor of 6 larger than the valley
following it. After the last structure (feature 10) the density falls
from a value of 3.5×10^6 el/cm^3 over an order of magnitude in about
10 m travel normal to $\vec{B}$.

E.   Rocket ST707.51-5 (Event FERN, R + 42 min)

Probe ST707.51-5 penetrated barium cloud FERN at R + 42 min, giving
the electron density profile of Figure 17. The probe entered the
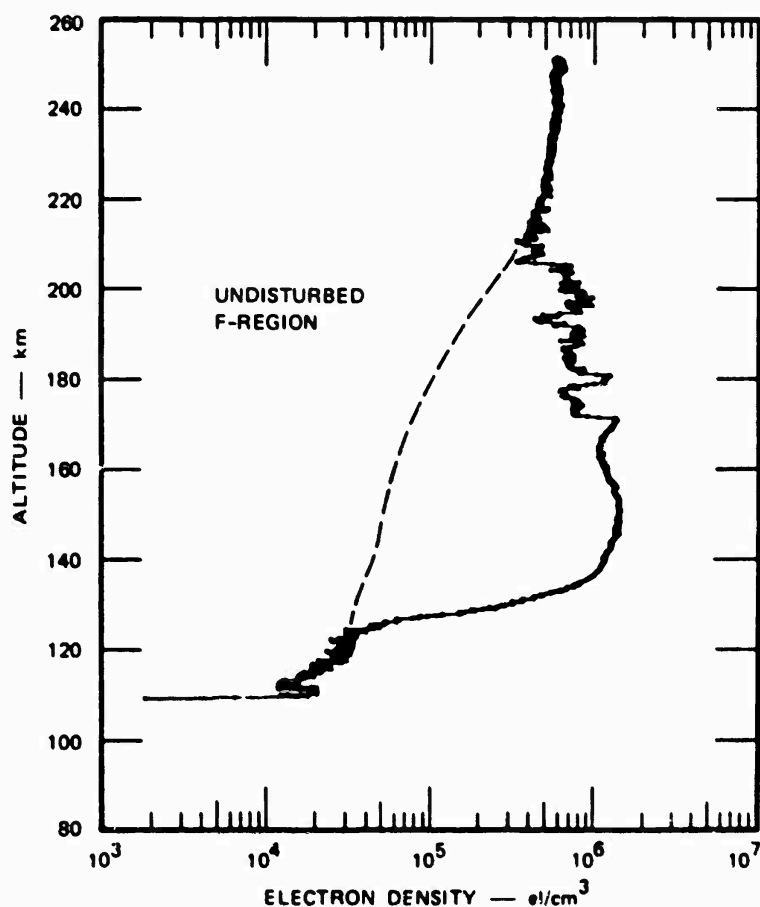
96

FIGURE 17   ELECTRON DENSITY PROFILE, PROBE ST707.51-5,
EVENT FERN (R + 42 min)

enhanced region due to the cloud at 130 km, indicating that the effects of the cloud extended well down into the E region. The enhanced region extended on the high side to over 200 km. The main electron density layer showed a broad peak of 13×10^5 el/cm^3 at about 150 km, and showed a relatively smooth profile up to about 170 km when structures appeared giving evidence of passing through a striated region of the cloud. This region of striations persists until the electron density appears to return to the normal F-region values at about 210 km. The region of striations is shown in the time plot of Figure 18 to allow a better visualization of the structure of the striations.
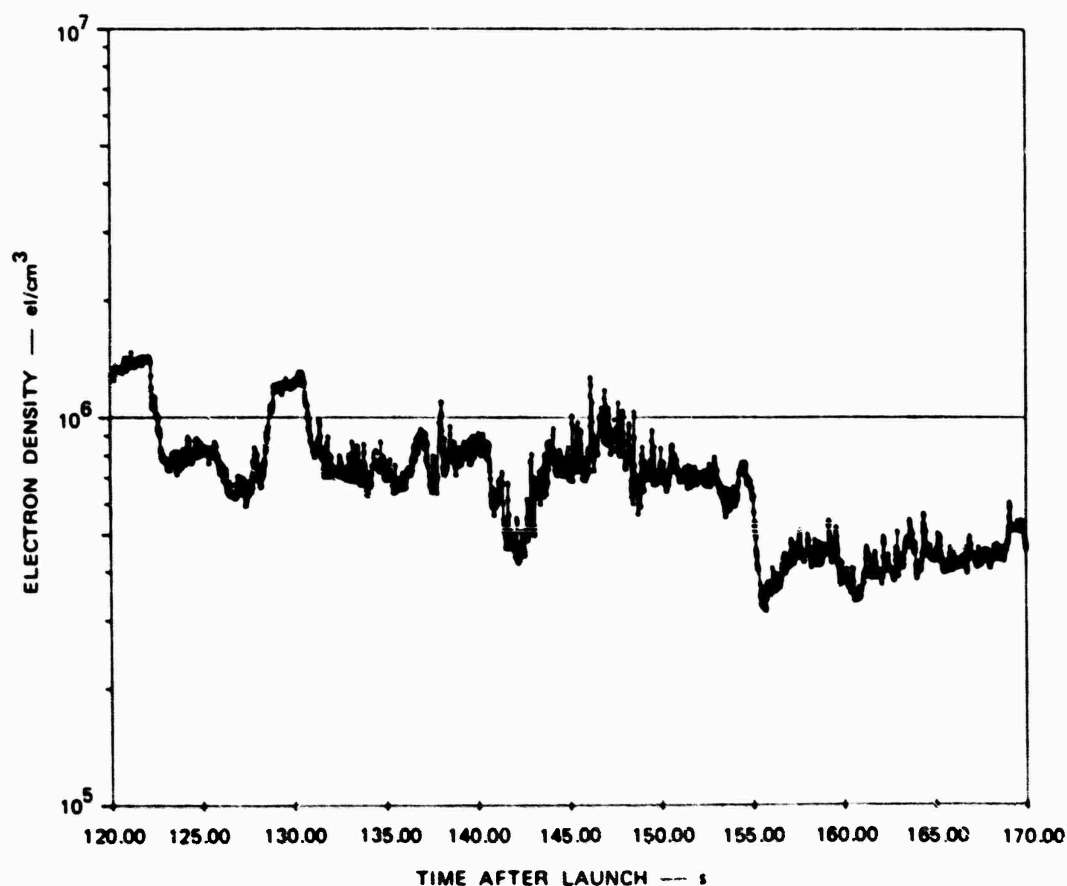
FIGURE 18   REGION OF ELECTRON DENSITY STRIATIONS MEASURED BETWEEN 170 AND
210 km BY PROBE ST707.51-5 (FERN, R + 42 min)

F.   Rocket ST707.51-6 (Event FERN R + 80 min)

No profiles are presented for probe ST707.51-6, since the electron density measurements were of limited usefulness. The enhanced region of electron density associated with the ion cloud was observed and extended over a large altitude range from about 112 to over 200 km.

Table 6 is a summary of the STRESS probe results.

V   SPECTRAL ANALYSIS OF THE ELECTRON DENSITY VARIATIONS

A.   General

This section concerns the examination and comparison of the spectral analysis of the variations of the electron density results that were

Table 6

SUMMARY OF STRESS PROBE RESULTS

Event (Time from Release)	Probe Rocket No.	Description of Probe Traversal Region	$N_{e_{max}}$ ($\times 10^6$ el/cm^3)	Altitude (km)	Time After Launch (s)
DIANNE (R + 15 min)	51-1	Smooth layer (~10 km)	1.4	162	130
DIANNE (R + 34 min)	51-2	One sharp finger (~1.5 km) imbedded in layer	1.4	182	162
ESTHER (R + 28 min)	51-3	Smooth layer (~24 km)	0.7	177	141
ESTHER (R + 46 min)	51-4	Ten striation fingers imbedded in layer	5	173	153
FERN (R + 42 min)	51-5	Enhanced region over large altitude range (130-200 km) striations from 170 to 210 km	1.3	171	122
FERN (R + 80 min)	51-6	Slight enhanced region over large altitude range (112-209 km)			

99

presented as height profiles in the previous section. These data
are presented in two subsections, dealing with short-wavelength charac-
teristics (less than 50 m) and long-wavelength characteristics (greater
than 50 m). Only the long-wavelength results will be presented here.
The dc probe results from xl gain range (IRIG channel 20) were utilized.

With respect to the long-wavelength characteristics, preliminary
calculations have shown that only the rockets that penetrated the
striated barium regions exhibit spectral distributions that increase in
amplitude at these wavelengths (and only in the striated regions). For
rocket ST707.51-4 (ESTHER), the striated region is from 140 to 160 s
rocket flight time, corresponding to rocket altitude from 165 to 178 km.
For rocket ST707.51-5 (FERN), the striated region is from 120 to 160 s
rocket flight time, corresponding to rocket altitude 169 to 210 km.

B. Long-Wavelength Characteristics

The power spectrum shown in Figure 19 was obtained over the time
interval from 140 to 153 s of rocket ST707.51-4 (ESTHER) utilizing the
dc probe xl data. These data were decimated by averaging together 16
points and detrended by fitting to a polynomial of degree 3. Note the
uniform slope between 0.2 and 50 Hz. Figure 20 shows the power spectrum
for rocket ST707.51-5 (FERN) in the striated region. The data were
decimated by averaging together 80 points and detrended by fitting to a
polynomial of degree 3. These results are very similar to Figure 19,
with the slope not quite as steep, however.

VI SUMMARY AND FUTURE EXPERIMENTAL DIRECTIONS

A. Summary

We have measured late-time striations in barium clouds and found
their development to be in excellent agreement with the computer codes
developed by the group at NRL. For example, they predicted the wave-
number power-law index to be in the range -2 to -3, which compares
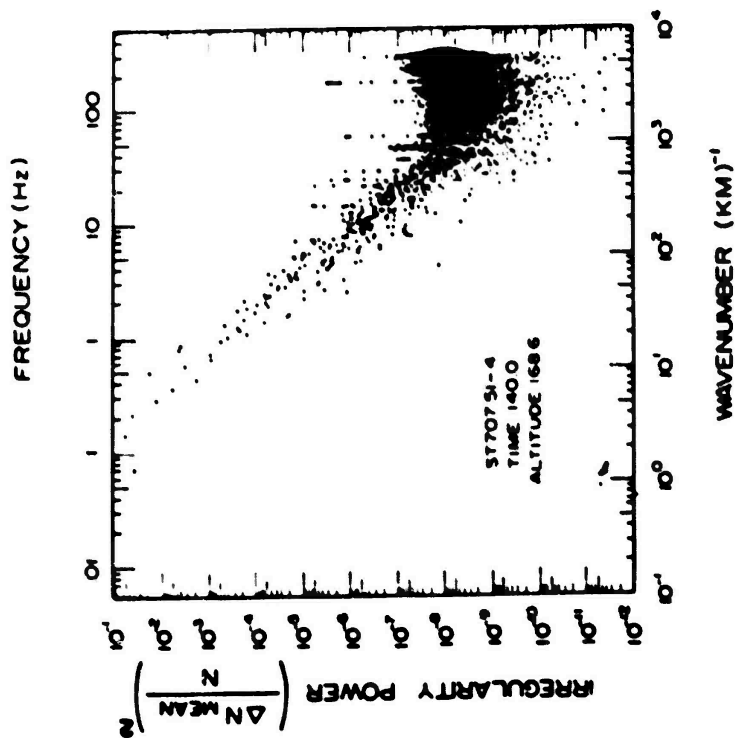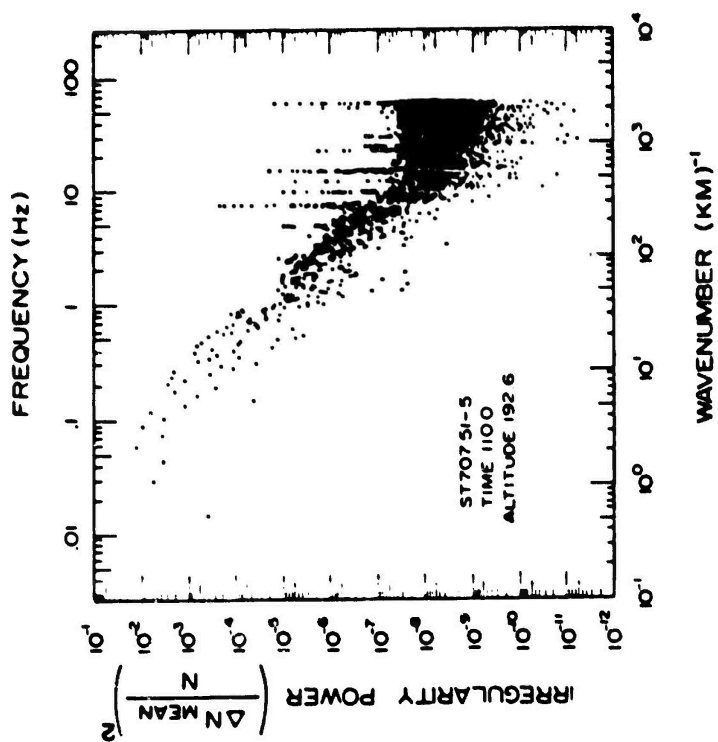favorably to the observed index of -2.16.

100

FIGURE 20   POWER SPECTRAL DENSITY OF ELECTRON
DENSITY IRREGULARITIES (LONG-WAVE
ANALYSIS) FOR ROCKET PROBE ST707.51-5
(FERN) IN THE REGION OF STRIATIONS.
The upper scale was obtained by multiplying
the wavenumber (lower scale) by the 180-m/s
rocket velocity component in the direction of
unstable wave vectors (see section VII) divided
by 2π.

FIGURE 19   POWER SPECTRAL DENSITY OF ELECTRON
DENSITY IRREGULARITIES (LONG-WAVE
ANALYSIS) FOR ROCKET PROBE ST707.51-4
(ESTHER) IN THE REGION OF STRIATIONS.
The upper scale was obtained by multiplying
the wavenumber (lower scale) by the 345-m/s
rocket velocity component in the direction of
unstable wave vectors (see Section VII) divided
by 2π.

A phase analysis of the data indicates that modeling the structures with an anisotropic power law, as typically done in existing scintillation calculations, may not properly take into account the physical structure of the irregularities. The power law results from nonlinear steepening of the large-scale structures and not from plasma turbulence.

The results are remarkably similar to the bottomside instability in naturally occurring equatorial spread-F. This implies that the nonlinear development of the two phenomena is identical. We also suggest that the $\vec{E} \times \vec{B}$ instability at times is more important than collisional Rayleigh-Taylor processes in bottomside equatorial spread-F.

A bandlimited short-wavelength instability operates in the portion of the cloud undisturbed by the striation process. No viable theory has been identified for this process. Depending on the direction of the wave vectors, such irregularities may have strong effects on VHF and UHF radars propagating through such a medium.

B.   Future Experimental Directions

It can safely be said that the major process affecting large-plasma-cloud development in the midlatitude ionosphere is well understood theoretically and that the theories have been checked in detail by experiment. Development of such a cloud at high latitudes may be significantly modified, however.

The major difference of importance is the large ambient electric field at high latitudes. The linear growth rate will, of course, be higher by a factor of ten (for $E = 50$ mV/m, which is not atypical). This may just decrease the time for full nonlinear development. It seems likely, though, that modest amplitude structures will peel off the edges of the backside and flow in the $\vec{E} \times \vec{B}$ direction. Since this ambient flow is east-west, this will lead to an elongated curtain of irregularities stretching across the sky upstream from the cloud.

Other processes at high latitudes may affect the cloud development. Velocity shear instabilities may play a role, as may feedback from

102

enhanced cold plasma density onto particle precipitation on the same field lines, and the existance of ambient irregularities.

As in the midlatitude STRESS experiment, a detailed controlled experiment at high latitudes may yield important insights into the processes that create the irregularities in the natural disturbed F-region at high latitude.

SATELLITE LINK MEASUREMENTS

C. W. Prettie
J. M. Marshall

ESL Incorporated
Sunnyvale, California

SATELLITE LINK MEASUREMENTS

C. W. Prettie
J. M. Marshall

ESL Incorporated
Sunnyvale, California

I INTRODUCTION

This paper is a summary of various topics of interest in the ongoing satellite link data-reduction effort. Other satellite link data-reduction information has been published earlier,[*] and results of further data reduction will appear in future reports.

The following sections discuss the topics of systems effects data, downlink hop frequency-selective measurements, pancaking of scintillation effects, a back-propagation example, and ESTHER back-propagation results. This section closes with some summarizing observations.

Efforts to date have been primarily devoted to processing and reducing the available data. The link measurements utilized advanced channel probing techniques--e.g., the uplink tone measurement of amplitude and phase through the hard-limited 1-bit sampling report-back channels, and the time-varying channel transfer function measurement using the downlink-hopped forward message. Since the data from this experiment are the first of their kind, considerable learning experience of how best to process it has been acquired. Future

---

[*] C. W. Prettie, et al. "Project STRESS Satellite Communications Tests Results," Report No. AFAL-TR-77-158, Air Force Avionics Laboratory (July 1977).

efforts will be directed toward assessing these data and their implications for satellite communications.

The preliminary results of the communications tests uphold system effects predictions. The performance of the coded/interleaved LES-8/9 forward link was mostly as expected, showing a 6-dB loss at the 50% average error rate. It was noted that improvements could be made of the synchronization scheme utilized by the modems to give it a better capability for performing through nuclear fading environments.

Theoretical results of software simulation of the sea multipath spatial-diversity concept have been obtained. These results indicate that potentially 5 dB of the 6-dB fading performance loss can be recovered through the use of a diversity combiner and a bottom blade antenna (Figure 1).

The propagation results uphold numerical angular-spectrum techniques. These techniques were used in the back-propagation processing of amplitude and phase data, and the behavior of scintillation index was as expected. Some selective features have also been observed in the channel transfer function. While these features do not indicate a strong decorrelation in the passes reduced to date, they do indicate some decorrelation. The passes parallel to the field lines indicate that it is difficult to obtain fades below 75 dB lasting for durations as long as the 4.4-s message lengths.

The fading results indicate that barium structure persists for hours. Apparently, effects are predominantly diminished by a lessening of the integrated content through the effects-producing regions. The back-propagation processing indicates that the frozen-in approximation is applicable to the barium structure, as expected. Phase power spectra indicate structure; phase power spectra have 30-to-50-dB/decade slopes. Early implications are that these slopes are insensitive to the age of the cloud.

II SYSTEMS EFFECTS RESULTS

Message throughput rates for FERN and DIANNE have been calculated. The values have been carefully lined up with fading intervals and
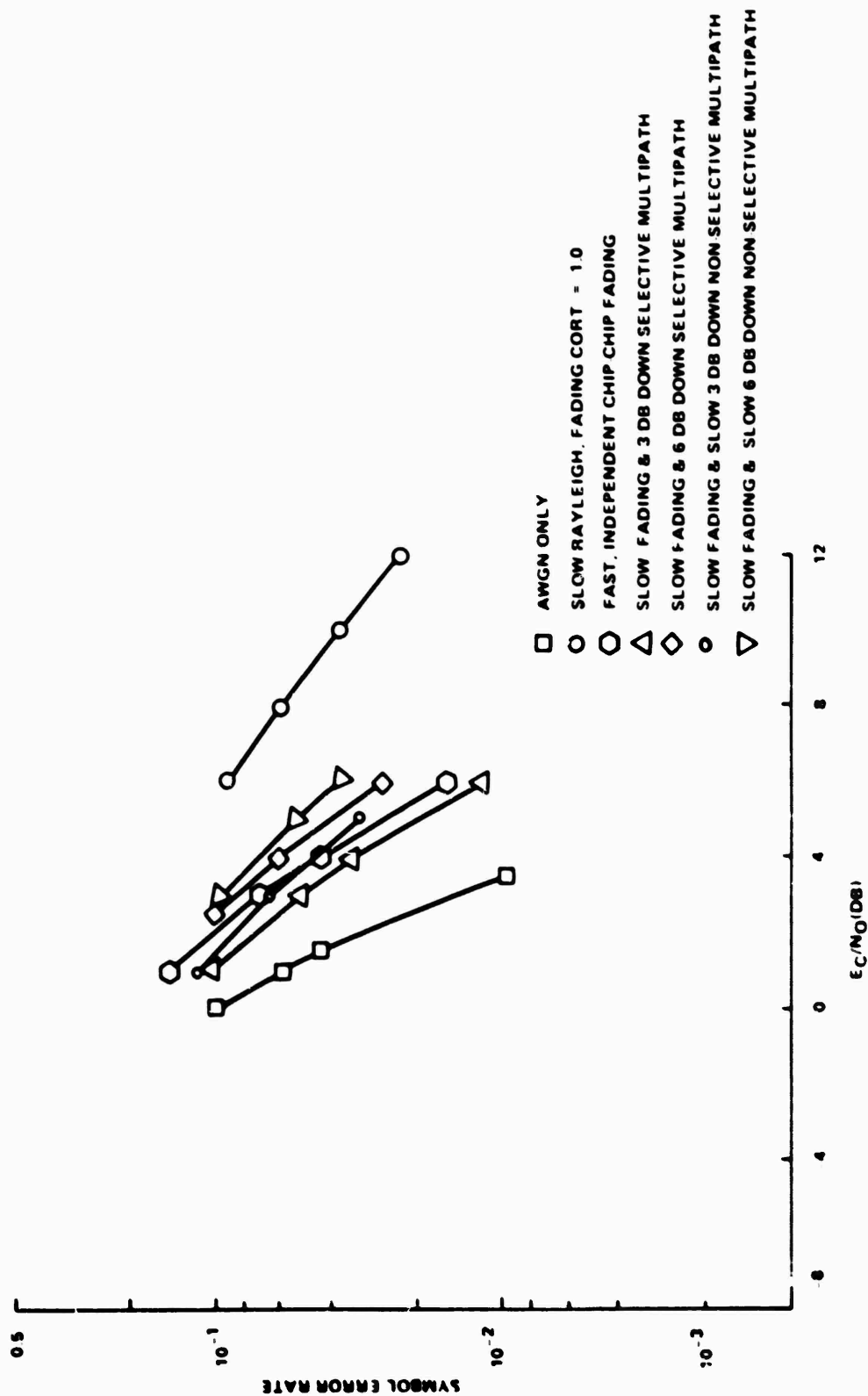
FIGURE 1   RESULTS OF SOFTWARE SIMULATION OF THE (STRESS-Inspired) SEA MULTIPATH SPATIAL-DIVERSITY CONCEPT. The 3-dB-down selective multipath fading case could be potentially realized in Rayleigh fading by use of diversity combined bottomside and topside airborne antennas.

adjusted allowing for antenna gair. differences from pass to pass.
Results for Rayleigh-like fading passes during FERN and DIANNE have
been plotted on the previously obtained Rayleigh throughput performance
for ESTHER, with good agreement. A loss of about 6 dB at the 50% message
error rate is indicated. While the gross behavior of the data is as
expected, minor discrepancies have occurred at the higher and lower
throughput rates that require further assessment.

Also analyzed have been the channel quality indices. These numbers
are related to the number of errors in each message. A good handle
on the detailed form of the relationship between channel quality and
symbol errors has been obtained; however, the data have not been assessed
to date. These data will give information on the error rate into the de-
coder and on the code efficiency.

III FREQUENCY SELECTIVE FADING

Our investigation of the frequency-selective properties of fading
through the barium cloud have just begun. To date only one fading pass,
Pass 8 at R + 50 min for Event DIANNE has been examined. The fading on
this pass was quite intense, as shown in Figure 2. Figures 2 and 3
were constructed from the downlink hopping signal. The hopping band
was divided into eight frequency bins of which the sixth bin from the
low end of the band was plotted. A comparison of Bin 6 with Bin 7,
each of which spans approximately 500 kHz, shows a surprising degree of
difference between the two bins during deep fade intervals. Figure 3
shows the fading observed in hopping Bin 7, which can be compared with
Figure 2. Note, for instance, the difference in fading around 21, 25,
and 27 s.

A movie was made of the received hopping signal amplitude versus
frequency for two deep fades, each lasting approximately 1 s. While
the data are noisy and need to be further processed, they do show cer-
tain trends. Figure 4 and 5 show the most radical selective fading
during the first interval. These plots consist of eight frequency hops,
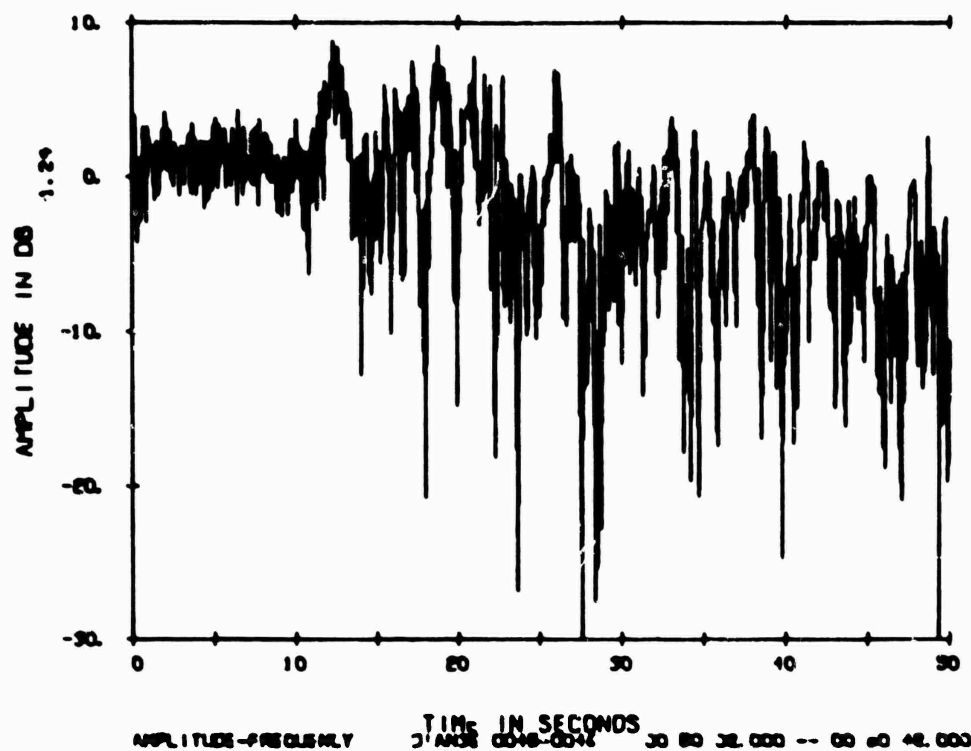each hop of 5 ms duration; thus, the eight points shown span 40 ms it.

FIGURE 2   FREQUENCY-SELECTIVE FADING DURING DIANNE, FREQUENCY BIN 6 OF 8
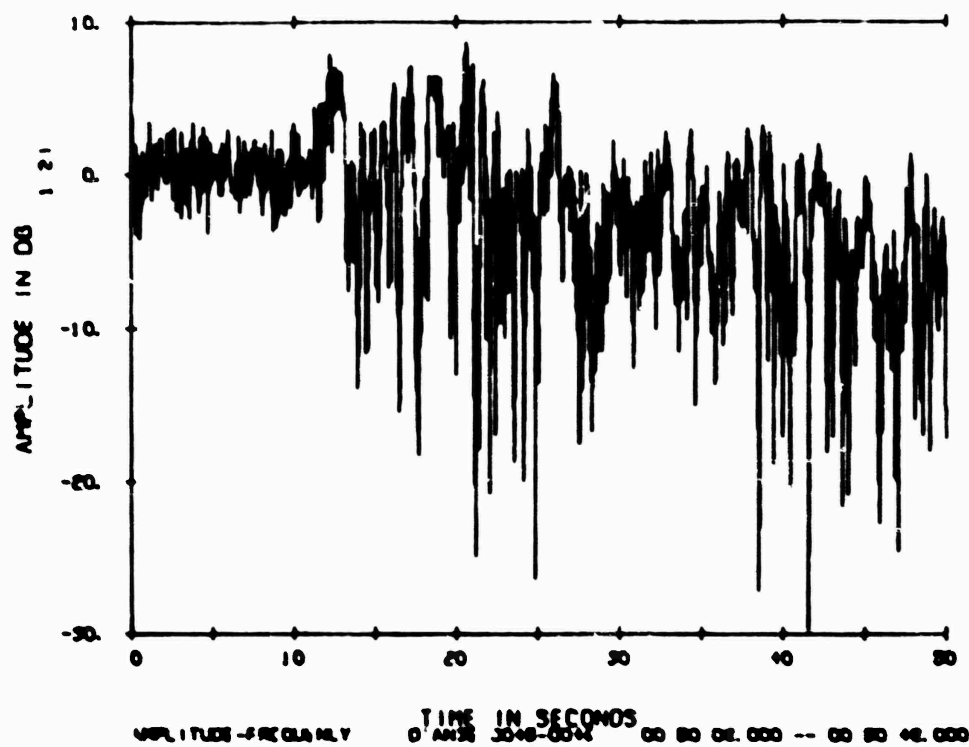

FIGURE 3   FREQUENCY-SELECTIVE FADING DURING DIANNE, FREQUENCY BIN 7 OF 8
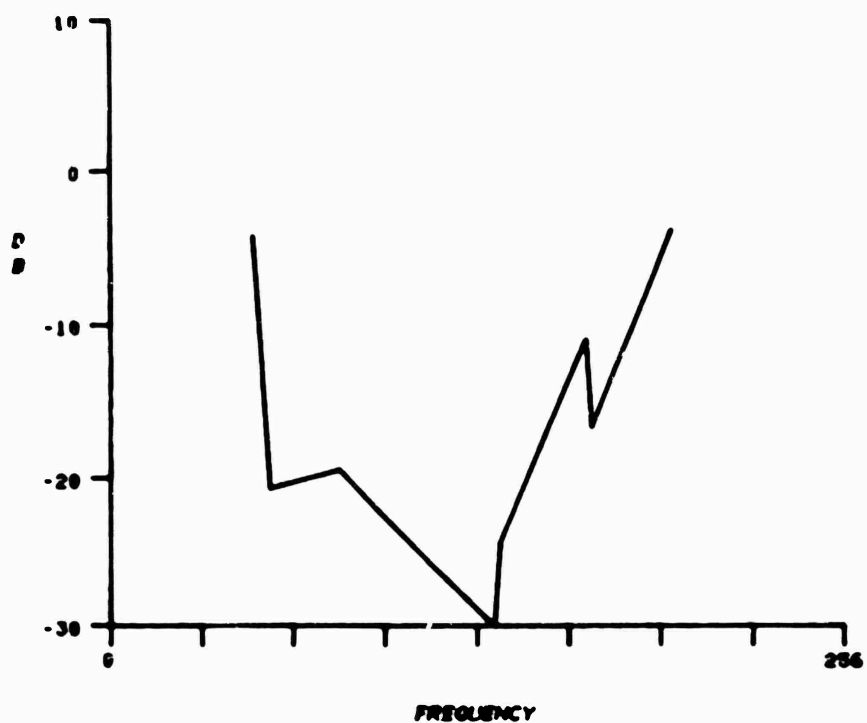
111

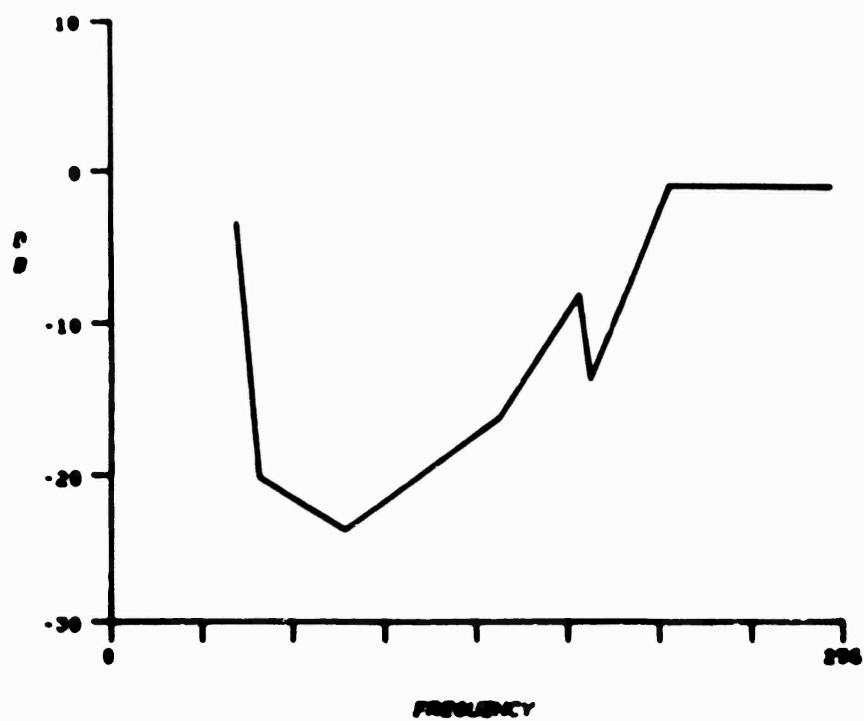FIGURE 4   DIANNE CHANNEL AMPLITUDE TRANSFER FUNCTION AT 0050:31.680Z

FIGURE 5   DIANNE CHANNEL AMPLITUDE TRANSFER FUNCTION AT 0050:31.720Z

time. The hopping bandwidth was divided into 256 intervals to make these plots; the eight larger divisions shown are approximately 500 kHz in width. Figure 5 shows the next 40-ms interval of time for the fade interval shown in Figure 4, and illustrates the degree of correlation in the measured channel transfer function. Figures 6 and 7 show the most radical selective fading during the second fade interval. Each figure consists of a different 40-ms set of eight frequency-hop data points.

Considerably more work needs to be done before drawing any major conclusions from these data. Again, this frequency selectivity is observed only during the deep fades. The implication is that the 4-chip frequency-hopped error-correction code used on the LES-8 and -9 could be made more effective by increasing the code word length and by widening the hopping pattern. However, these features of code design that maximize gain during selective fading must be traded off against the desire to minimize acquisition time and code complexity.

IV LATE-TIME PANCAKING OF SCINTILLATION EFFECTS

The projection of ionized barium cloud from the direction of LES-9 or LES-8 satellites onto the ground presented a rather large target through which the aircraft was to be flown. Based on calculations performed by Dr. Ralph Kilb of MRC following the ANNE release, indications were that by an hour and a half after release an ionization density of approximately 10^6 el/cm^3 would exist from ~135 to ~190 km in altitude along a field line. Rocket probe data taken during FERN bears out Kilb's calculations at least qualitatively; however, scintillation-effects data exhibit, the some degree, a stronger altitude dependence. Prior propagation calculations show that scintillation effects for a nominal barium cloud with a peak striation density of 10^6 el/cm^3 at the 250-MHz downlink frequency would approach Rayleigh amplitude statistics. Thus, the a priori expectation was that strong scintillation effects would be obtained over at least 55-km extent along the field-line projection. The flight plan called for flying transverse to this
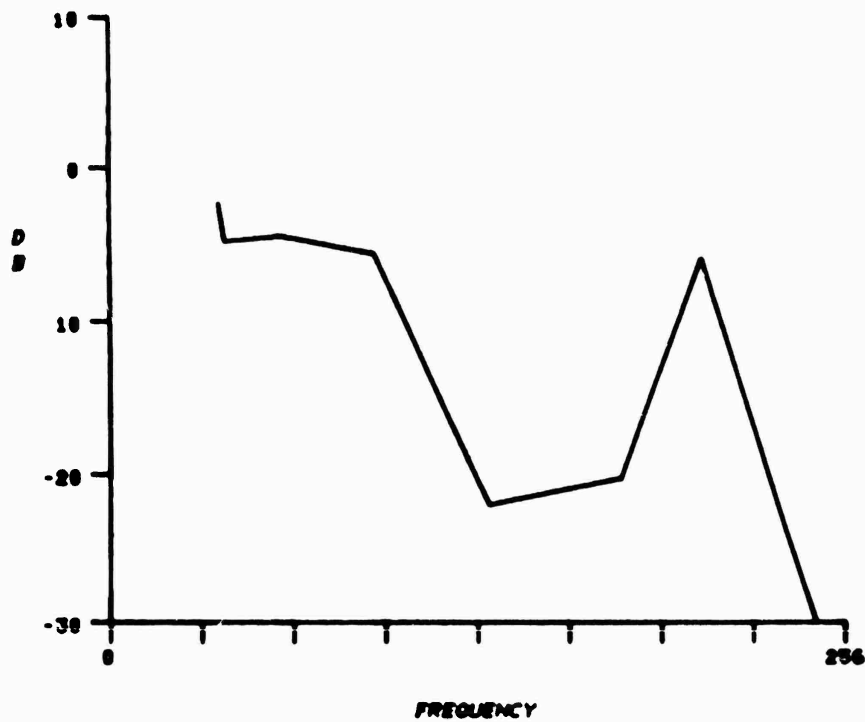
113

FIGURE 6   DIANNE CHANNEL AMPLITUDE TRANSFER FUNCTION AT 0050:35.480Z
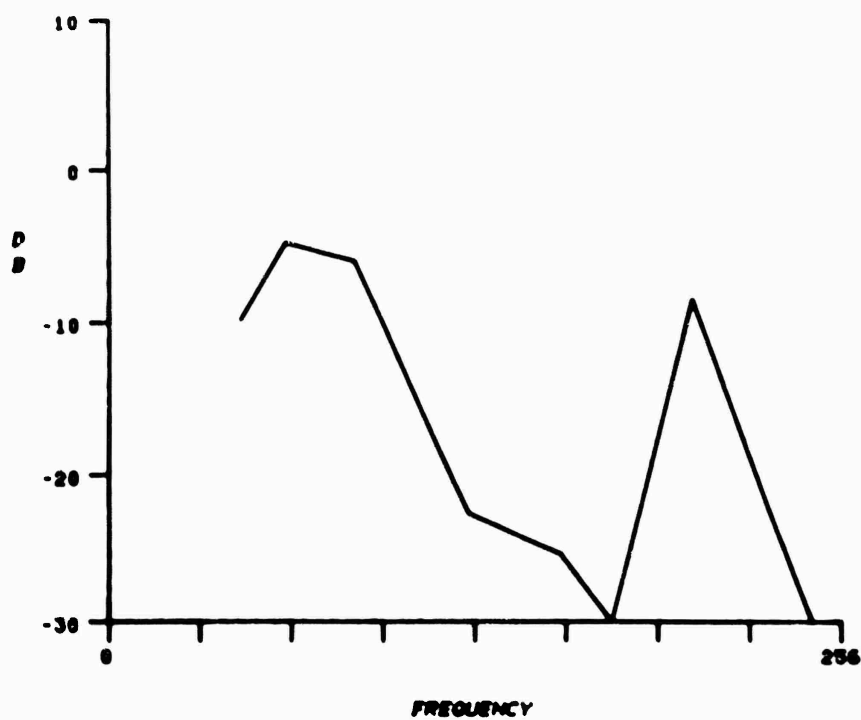

FIGURE 7   DIANNE CHANNEL AMPLITUDE TRANSFER FUNCTION AT 0050:35.520Z

field-line projection and occasionally a flight route down the field lines to look at the slow variation in the diffraction pattern along the field lines.

It was noted throughout these tests that at late times (~1.5 hours) it was difficult to fly the aircraft on a route that would produce strong fading on the received signal. The total altitude extent along a projected field line over which strong fading was observed was 15 to 25 km, not the 55 km expected. The optically visible structure extended more than 60 km during the visible windows throughout these tests. An unanswered question at this time is, why were scintillation effects noted only over such a small altitude extent?

Figure 8 is a plot of the aircraft ground track during Event BETTY from 0106Z to 0148Z, approximately R + 1.5 hr. Also shown on the ground track is a description of the fading intensity observed. Shown for a relative size comparison is the shadow that the ANNE barium ion cloud would have made for the LES-9 satellite geometry during Event BETTY. It was noted that for the third pass shown during the period from 0118Z to 0120Z there was reasonably well developed deep fading, but on the prior two passes no significant fading was observed. These fading patterns show a consistent pattern when corrected for the cloud drift velocity obtained from the FPS-85 radar track, as shown in Figure 9. The projection of the field line from LES-9 is shown. The small circle is at the indicated track altitude, which was relatively constant during these passes; the ground projection point followed a smooth path, indicating that the radar track point had not changed its relative position within the cloud. The fading pattern shows that only a few dB of fading was observed on the pass of the aircraft through the 164-km altitude on the field line through the cloud-track point determined by the radar. However it is possible to see that the aircraft had flown through the ion cloud shadow. The transmission frequency was ~340 MHz. The fading record is shown in Figure 10. The pass of the aircraft through the 171-km altitude on the radar track field line produced only a few 10-dB fades, as shown in Figure 11. The pass through 174-km altitude (Figure 12) shows a few more deep fades to 15 to 20 dB depth. The pass through 178 km

115

R = 2362:28Z
PASSES 14, 15, 16, 17, 18, 19, 20

A VIOLENT FADING
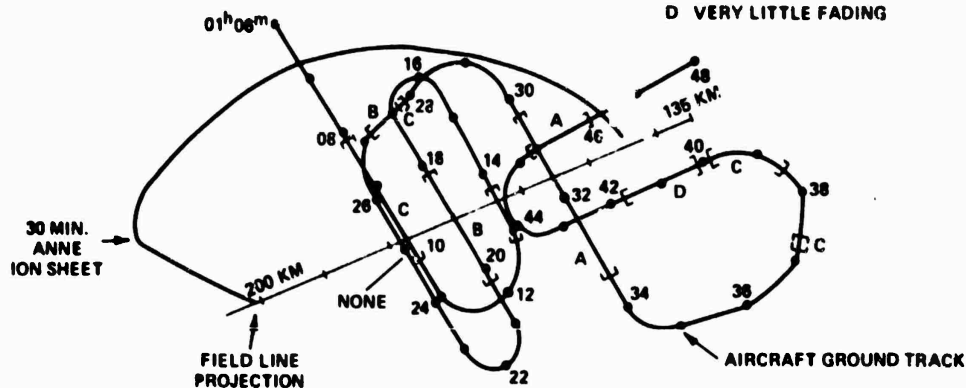
B STRONG FADING

C SOME FADING

D VERY LITTLE FADING

FIGURE 8   BETTY AIRCRAFT GROUND TRACK, 0106Z TO 0148Z (R + 1 hr 30 min)

R = 2362:28Z
PASSES 14, 15, 16, 17, 18
TRACK ALTITUDE - 175 KM ± 2 KM

A VIOLENT FADING

B STRONG FADING

C SOME FADING
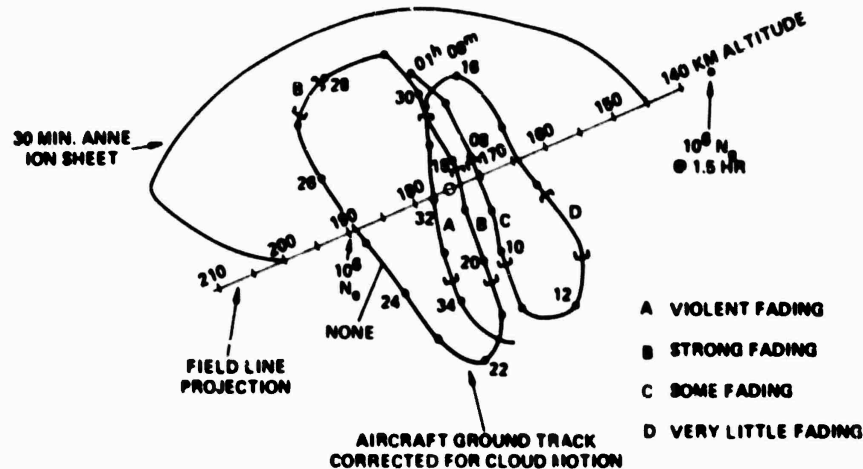
D VERY LITTLE FADING

FIGURE 9   BETTY ADJUSTED AIRCRAFT GROUND TRACK, 0106Z TO 0148Z (approximately R + 1 hr 30 min)
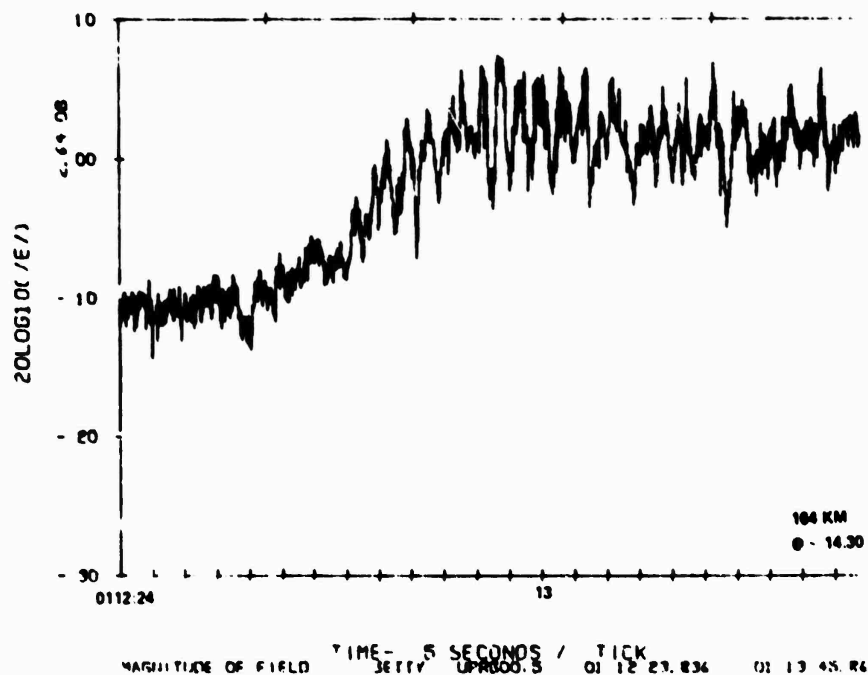
116

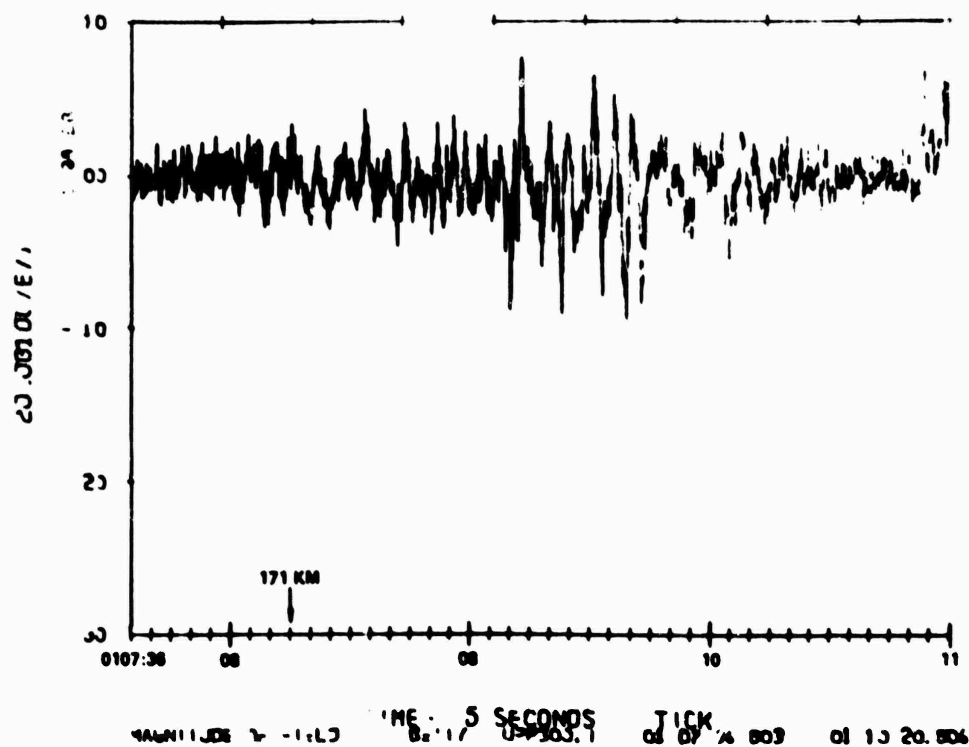FIGURE 10   BETTY PASS 15 THROUGH 164 km ALTITUDE

FIGURE 11   BETTY PASS 14 THROUGH 171 km ALTITUDE

117

altitude shows a well developed Rayleigh fading pattern (Figure 13),
while the pass through 189 km altitude (Figure 14) shows no fading,
although there is a 1- or 2-dB fluctuation in the signal that was
commonly noted when the aircraft was flying through the ion cloud
shadow. The corresponding phase records all show four or five 2π radian
phase accumulation as the aircraft passed through the shadow. However,
these phase records need to be processed further to quantify the actual
phase patterns and total amount of phase change for each pass. The
total phase change is not necessarily available from these records;
it appears that the time interval processed and shown here did not in
all passes span the entire pass through the cloud shadow. It is planned
to completely process this data in the near future.

Figure 15 shows the next consecutive two passes, which were
essentially parallel to the field-line projection. Because it is
difficult to fly down a deep fade, it is difficult to determine much
about the altitude dependence of the fading from such a pass. Nonethe-
less, the pattern obtained appears consistent with the motion of a
restricted altitude dependence for the fading. The intense fading in
the upper left corner apparently well back in the ion cloud is consis-
tent with the patch noted in Figure 9. Again the apparent extent along
the field line is ~15 km. It should be noted, however, there is some
room for error here. Around 0134Z the radar track appears to wander
back into the ion cloud, as evidenced by the northward motion of the
ground projection point; also the altitude of track changed. The
adjusted ground track was obtained by using the average velocity and
direction from the preceding 20-minute track interval, which was
approximately 50 m/s in a southeasterly direction.

During Event ANNE there was an indication of late-time effects
pancaking to a limited altitude region, but the limited data made it
difficult to draw conclusions. Nonetheless, this question was raised
during the Pre-STRESS data review meeting. The two passes, one at
0036Z, and the other connecting with it but down the field lines start-
ing about 0042Z, provide the best indication as shown in Figure 16. The
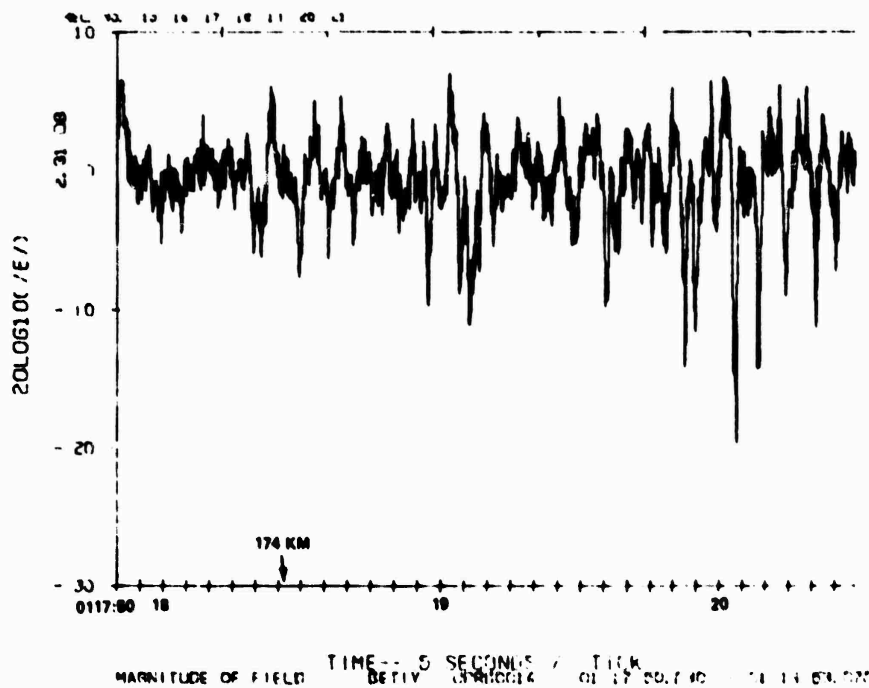strong fading effects apparently span approximately 25 km at about R +

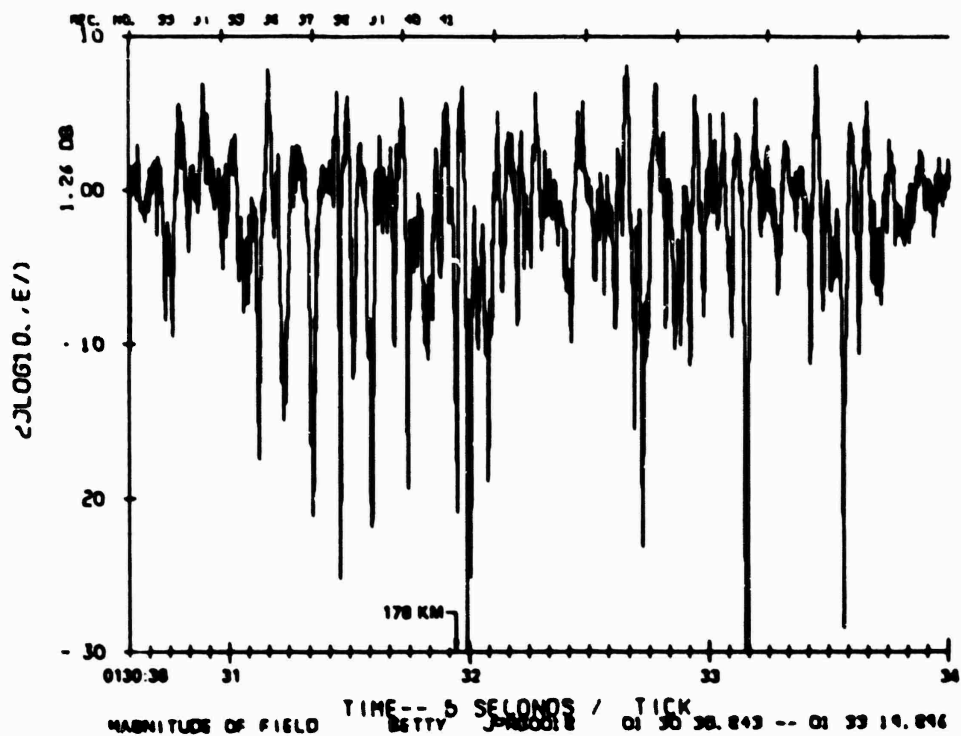FIGURE 12   BETTY PASS 16 THROUGH 174 km ALTITUDE

FIGURE 13   BETTY PASS 18 THROUGH 178 km ALTITUDE

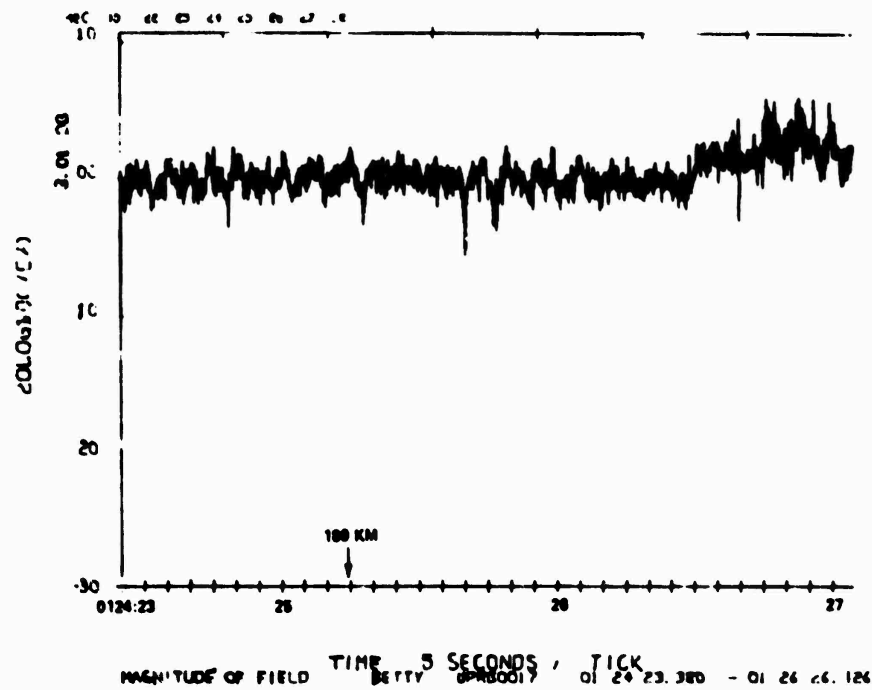119

FIGURE 14   BETTY PASS 17 THROUGH 189 km ALTITUDE

A   VIOLENT FADING
B   STRONG FADING
C   SOME FADING
D   VERY LITTLE FADING

PASSES 19, 20
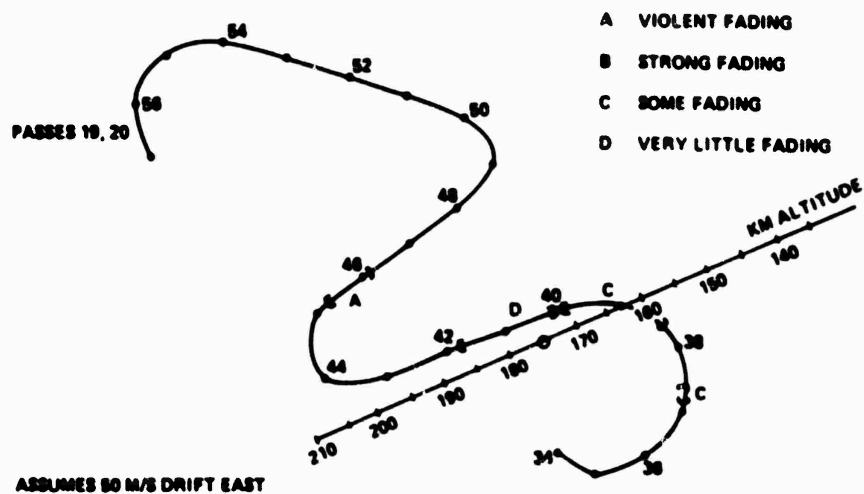
ASSUMES 50 M/S DRIFT EAST

FIGURE 15   BETTY ADJUSTED AIRCRAFT GROUND TRACK, 0134Z TO 0157Z

90 min. Still later, if we can trust these data in spite of the cloud tracking difficulties, the effects appear to span 10 to 15 km in altitude.

CAROLYN shows similar results at about R + 1 hr 20 min (Figure 17). Here the effects of strong fading are clearly confined to a 10-to-15-km altitude range.

A discussion of the late-time pancaking of effects during Event DIANNE is deferred until Section V, below, which discusses the reasons for the premature loss of scintillation effects. The data show that significant fading at late times spans at least 15 km and not more than 25 km in altitude. Figure 18 shows the fading at early times from the first development of the striations during DIANNE. The first two passes clearly show strong fading over approximately 10-s intervals as the structure develops. These two passes span 20 km in altitude; thus, the extent of effects clearly exceeds this at early times. Subsequent passes continue to encounter strong fading and indicate how easy it was to obtain strong fading at early times.

Event ESTHER has not yet been examined for the pancaking effect. It appeared to be easier to obtain strong fading during ESTHER. The ESTHER data will be examined to see if this event was different in any way. It is possible that the radar was tracking more consistently and the aircraft positioning was better than during the other events, or that the magnetic aspect angle of the propagation paths made the results insensitive to altitude effects.

Figure 19 shows the adjusted aircraft ground track during the opitcal tracking interval of FERN from 0007Z to 0046Z. This interval is around R + 90 min. The extent of strong fading along the field lines appears to extend over 35 to 40 km in altitude, based on the longitudinal pass data, but this does not appear to be supported by the transverse pass data, which show less than 30 km extent. Again, it is difficult to draw conclusions from the longitudinal passes.

Around 0046Z the optics track ceased and the aircraft was sent to determine what, if anything, the radar was tracking (Figure 20). The
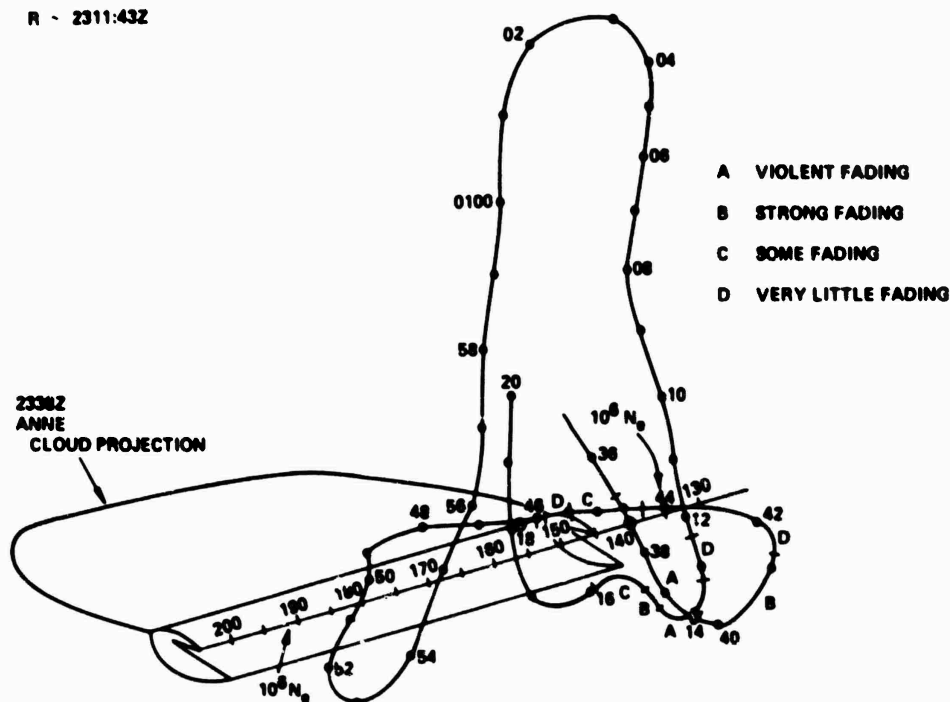
121

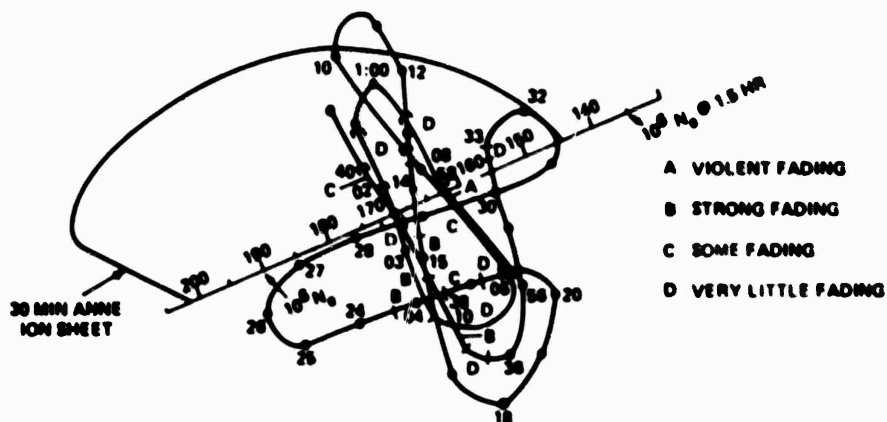FIGURE 16   ANNE ADJUSTED AIRCRAFT GROUND TRACK, 0035Z TO 0120Z (approximately R + 1 hr 45 min)

FIGURE 17   CAROLYN ADJUSTED AIRCRAFT GROUND TRACK, 0056Z TO 0141Z (approximately R + 1 hr 20 min)

122

20 KM DROP
IN TRACK ALTITUDE

A VIOLENT FADING
B STRONG FADING
C SOME FADING
D VERY LITTLE
FADING

30 MIN
ANNE
ION SHEET

@ 1.5 HR

FPS-85 TRACK PT.
SLIDING BACK INTO ION CLOUD
CLOUD APPEARS TO STOP MOVING
0100—0110

FIGURE 18   DIANNE ADJUSTED AIRCRAFT GROUND TRACK AT EARLY TIMES,
0009Z TO 0037Z (approximately R + 20 min)

R = 2246:20Z

OPTICAL
TRACK

A VIOLENT FADING

B STRONG FADING

C SOME FADING

D VERY LITTLE FADING

FIGURE 19   FERN ADJUSTED AIRCRAFT GROUND TRACK DURING OPTICS CLOUD
TRACK, 0007Z TO 0046Z (approximately R + 1 hr 45 min)

123

flight route took the plane essentially on a line down the field lines connecting the optics and radar track points. The projecting of the 145-km altitude contour of the ion cloud as seen by the radar is shown for comparison. Along this flight route a well developed 10 dB fade lasting 30 s was encountered. The strong fading would cover approximately 40 km in altitude. The diffraction pattern observed was similar to that noted during the early development of barium cloud. That is, the onset of effects was very abrupt, as was the cessation of effects. Because of the short fading interval and a limitation on the flight time of the air- craft, the test was terminated around ∼ 0110Z. Despite the optical pictures of the cloud, which show it covering a vast region of the sky, only a small portion appeared to be structured with sufficient intensity to produce fad- ing at 340 MHz.

The data presented here leave many questions. It would be good to further process the data discussed to obtain more quantitive results on this pancaking effect. It would be good to resolve any unforeseen physi- cal processes involved and, likewise, it is important to understand this problem should a similar experiment ever be attempted.

V PREMATURE LOSS OF FADING EFFECTS

Throughout these tests the radar tracked the region with the highest apparent average electron density. The center of this region was projected down to the aircraft altitude along a line from the LES-9 to LES-8 satel- lite. At late times it was clear from the observed fading that this region was northwest of the most intense structure. In fact, it is believed that for ANNE, BETTY, CAROLYN, DIANNE and to a lesser extent FERN the loss of scintillation effects at late times was a result of the radar track point moving back into the relatively lightly structured (or unstructured) ion cloud. That is, the apparent loss of fading was not due to the disappear- ance of the structure.

Figure 21, showing the fading during DIANNE, is a particularly good example. Around 0100Z the radar track was indicating that the cloud had nearly stopped moving. This was preceded by a 20-km drop in the cloud track altitude around 0040Z. When the fading pattern is plotted
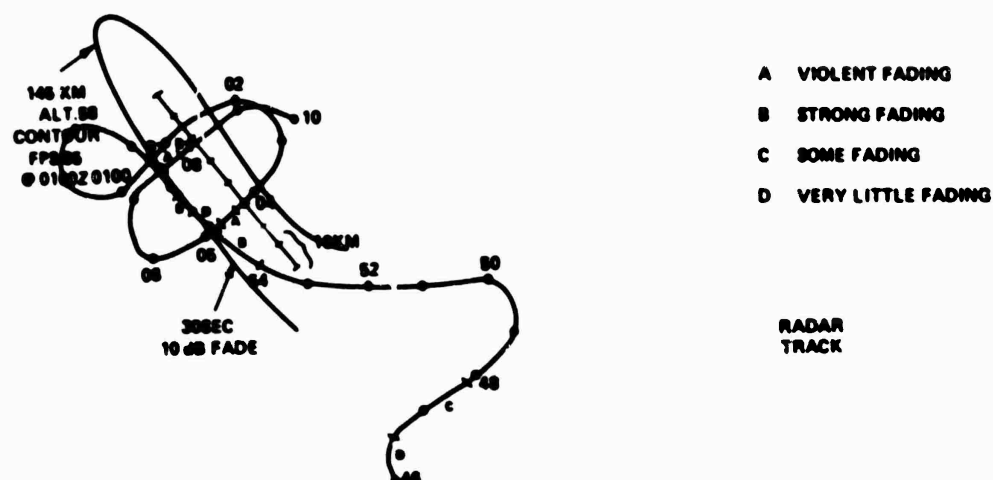
124

FIGURE 20   FERN ADJUSTED AIRCRAFT GROUND TRACK DURING RADAR CLOUD
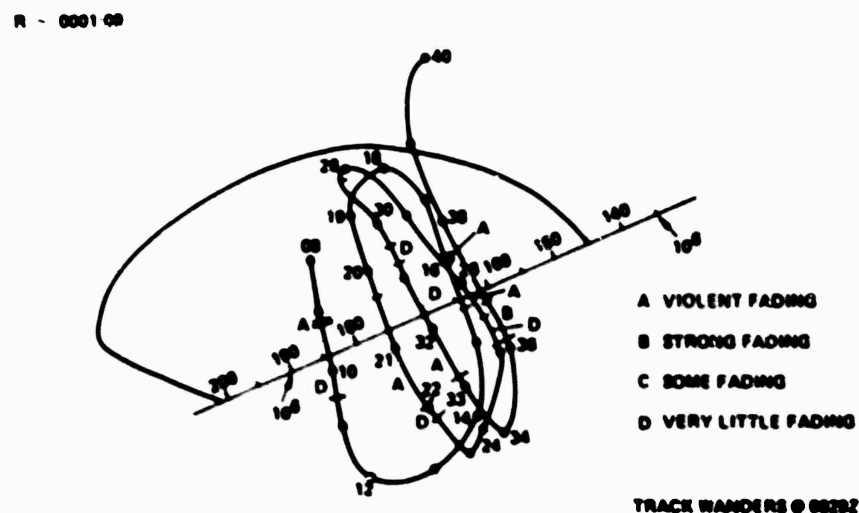TRACK, 0046Z TO 0110Z (approximately R + 2 hr 15 min)

FIGURE 21   DIANN ADJUSTED AIRCRAFT GROUND TRACK, 0042Z TO 0117Z
(approx mately R + 1 hr)

125

relative to the radar track point, the pattern shown in Figure 21 results. Note that first (~0050Z) intense fading is encountered followed by strong but less intense fading on the next pass (0054Z). This pattern is repeated on the next two passes (~0100Z to 0109Z and 0109Z to 0114Z). However, these passes were moving to the southeast of the radar track point. The following pass was back through the radar track point and produced no significant fading; that was the last fading observed during Event DIANNE. The combination of a restricted altitude zone through which fading effects occur and the migration of the radar track point back into the ion cloud away from this structure resulted in the apparent loss of fading effects at R + 1 hr 15 min.

If such a test were ever to be repeated, it would be better to determine from the radar during a stable track period the average drift velocity and direction, and from the aircraft when strong fading is observed; then the region of strong scintillation effects should be tracked by updating the position of the strongest fading throughout the lifetime of the experiment and assigning the velocity vector to this position.

While more passes at differing altitude crossings are needed, these DIANNE data also indicate that the significant fading spans at least 14 km and not more than 25 km in altitude.

VI BACK-PROPAGATION EXAMPLE

This section discusses back-propagation of uplink tone data from ESTHER Pass 11. Two important points are noted:

(1) The phase at the ground is not proportional to the integrated content of the cloud; diffraction effects alter its form somewhat.

(2) The power spectrum of the phase at the ground has a shallower slope than the power spectrum of the phase at the cloud (integrated electron content).

Figure 22 shows the behavior of the scintillation index of the field obtained during ESTHER pass 11 as the field is back-propagated. Note

the minimum near 150 km. This distance represents the distance to the center of the barium cloud propagation disturbance when the proper aircraft cross-striation velocity is entered. A 200-m/s velocity has, in fact, been entered for utility--a number somewhat lower than the actual value. Adjustment of the S_4 minimum distance obtained with the 200-m/s velocity, in order to achieve a physically significant number, is possible by modifying the 150-km number by the square of the ratio of the exact velocity to the assumed velocity.

Figures 23 through 28 show the field amplitude at the ground and at propagation distances of 100, 140, 150, 160 and 200 km, respectively. The S_4 of Figure 22 was measured over the second and third records of the four records denoted by the upper abscissa. The 100-km case is close to the distance where the S_4 exceeded unity (attaining a value of 1.2). Note the strong focusse obtained in this region, as would be expected from this S_4 behavior. The 150-km case is not devoid of amplitude fluctuations. In addition to the fluctuations present because of noise, some diffractive fading remains. The fading may be due to the effects of the cloud thickness along the propagation path. This length tended to be large (15 km or more) during ESTHER and FERN.

Figures 29 through 34 show the phases associated with the amplitudes in Figures 23 through 28. Note that as the back-propagation distance increases, the phase becomes narrower in extent and smoother until the scintillation minimum is reached. Note also that the phases at 140, 150, and 160 km are very similar, indicated that the measurement of the integrated content fluctuation is insensitive to the exact back-propagation distance.

Figures 35 through 40 show the power spectra associated with these phases. Note that the spectrum measurement has a noise floor of -26 dB and a processing filter cutoff at 10 Hz. The spectra are obtained by power averaging the four linearly detrended records, divided according to the upper abscissa on the phase plots. For presentation purposes, the power-spectra abscissa is divided into 60 bins of equal length. If more than two points fall into a bin they are power-averaged and connected with the next bin by a straight line. If two or fewer points fall

127
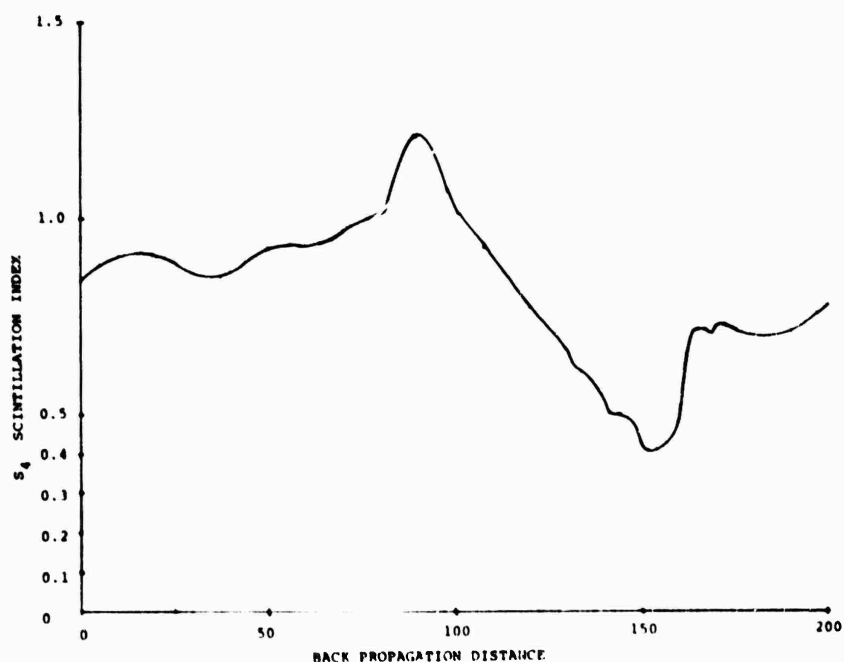
FIGURE 22   SCINTILLATION INDEX, S_4, vs BACK-PROPAGATION DISTANCE FOR ESTHER
PASS 11 UPLINK DATA
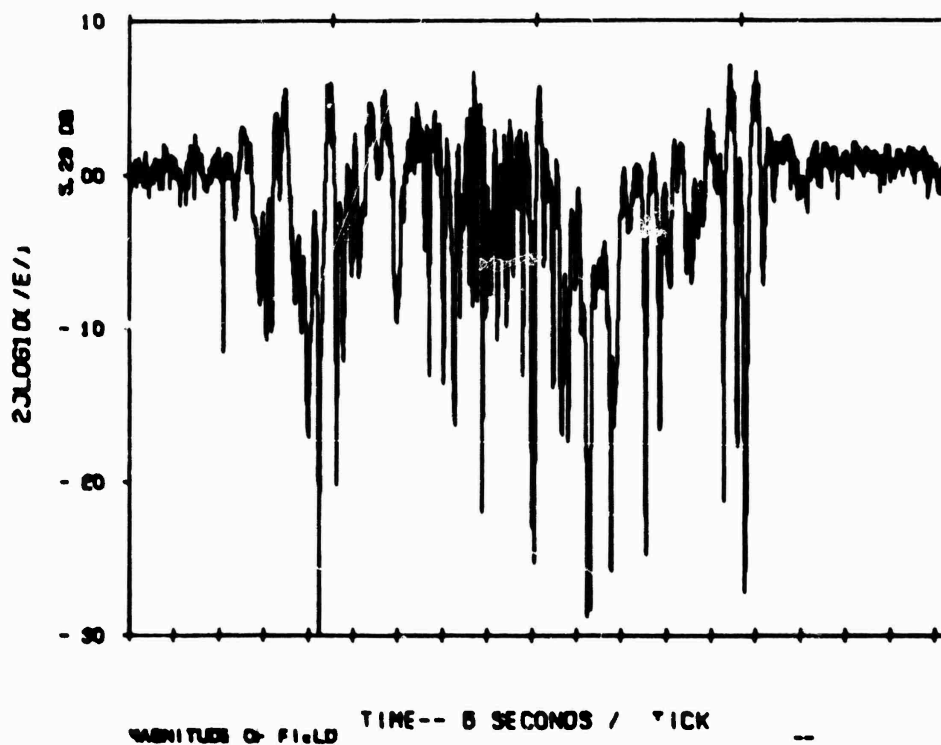
FIGURE 23   RELATIVE FIELD AMPLITUDE MEASURED AT THE GROUND IN ESTHER
PASS 11 WITH UPLINK PROBE

FIGURE 24   AMPLITUDE OF THE FIELD BACK-PROPAGATED 100 km OBTAINED FROM
ESTHER PASS 11 UPLINK PROBE
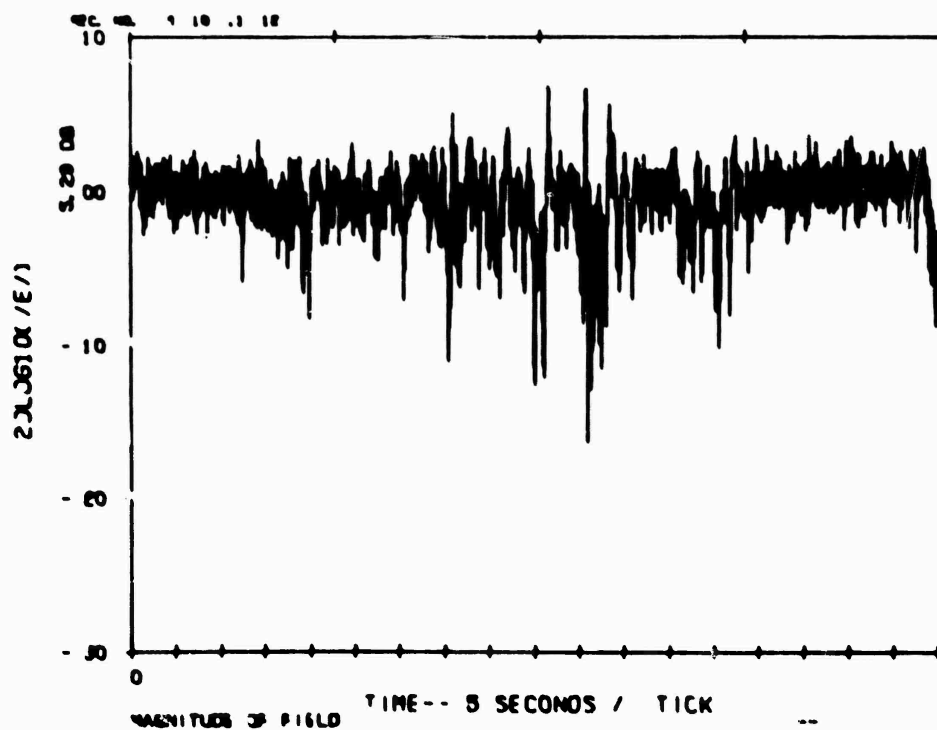
FIGURE 25   AMPLITUDE OF THE FIELD BACK-PROPAGATED 140 km OBTAINED FROM
ESTHER PASS 11 UPLINK PROBE

129
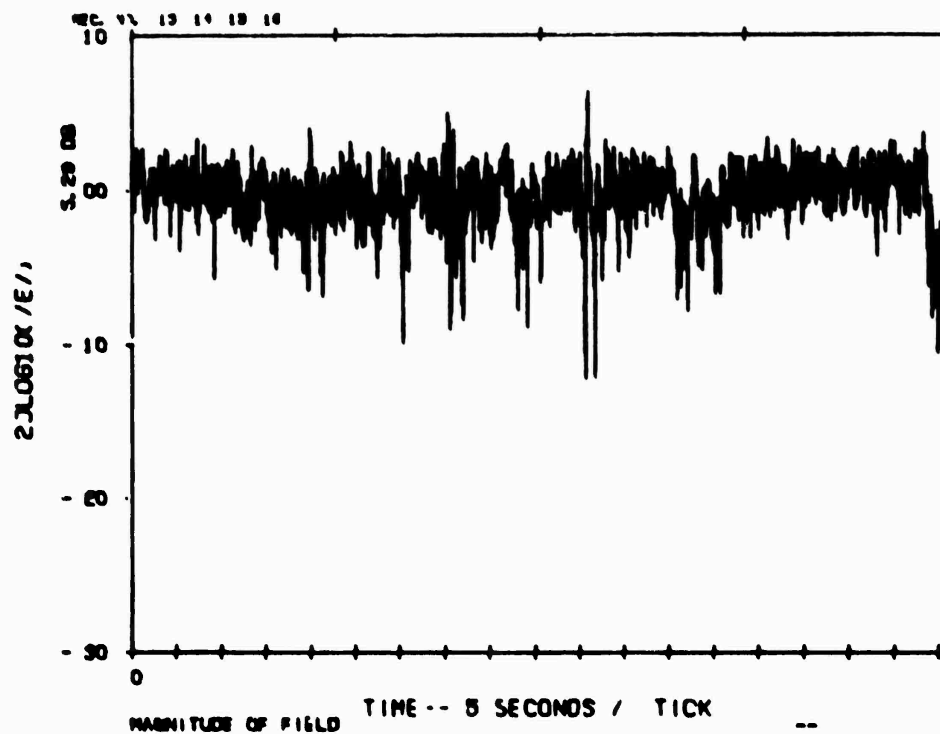
FIGURE 26   AMPLITUDE OF THE FIELD BACK-PROPAGATED 150 km OBTAINED FROM
ESTHER PASS 11 UPLINK PROBE
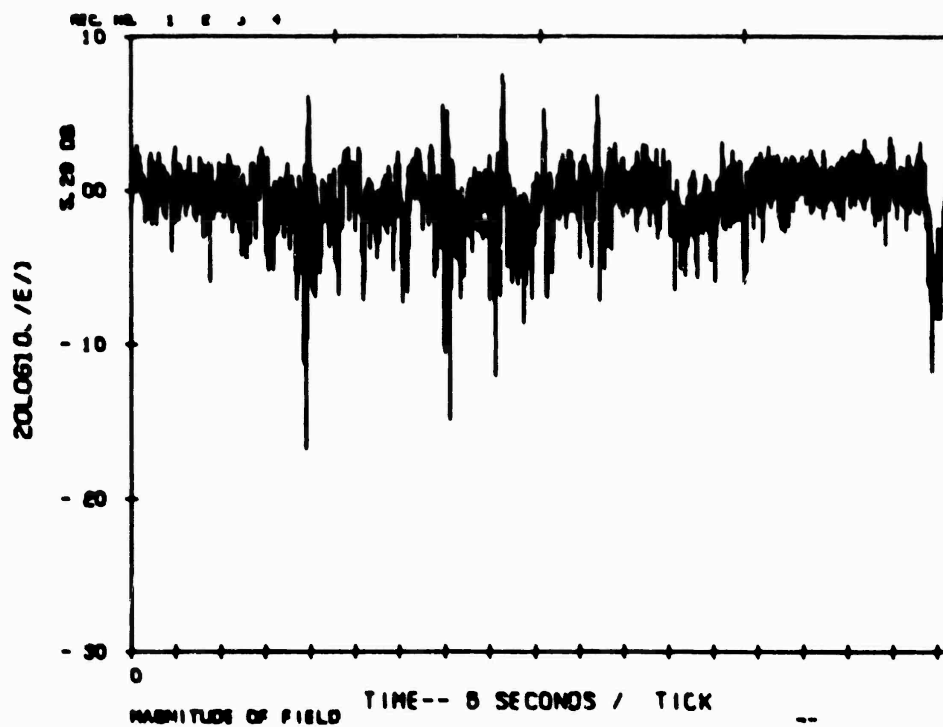
FIGURE 27   AMPLITUDE OF THE FIELD BACK-PROPAGATED 160 km OBTAINED FROM
ESTHER PASS 11 UPLINK PROBE

130
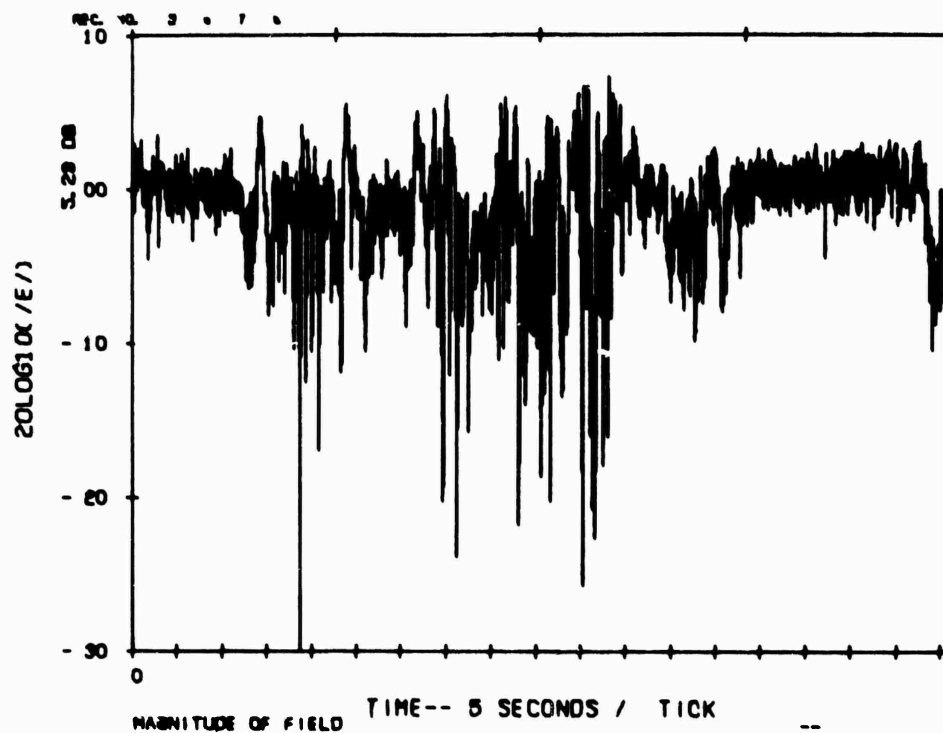
FIGURE 28   AMPLITUDE OF THE FIELD BACK-PROPAGATED 200 km OBTAINED FROM
ESTHER PASS 11 UPLINK PROBE
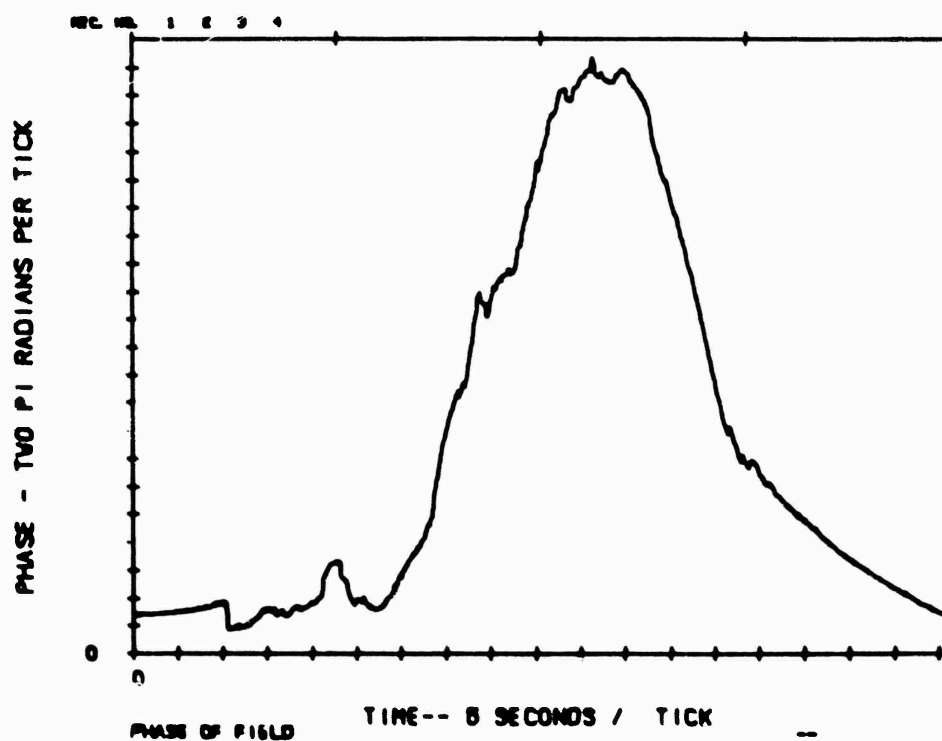
FIGURE 29   PHASE OF THE FIELD MEASURED AT THE GROUND IN ESTHER PASS 11
WITH UPLINK PROBE

131
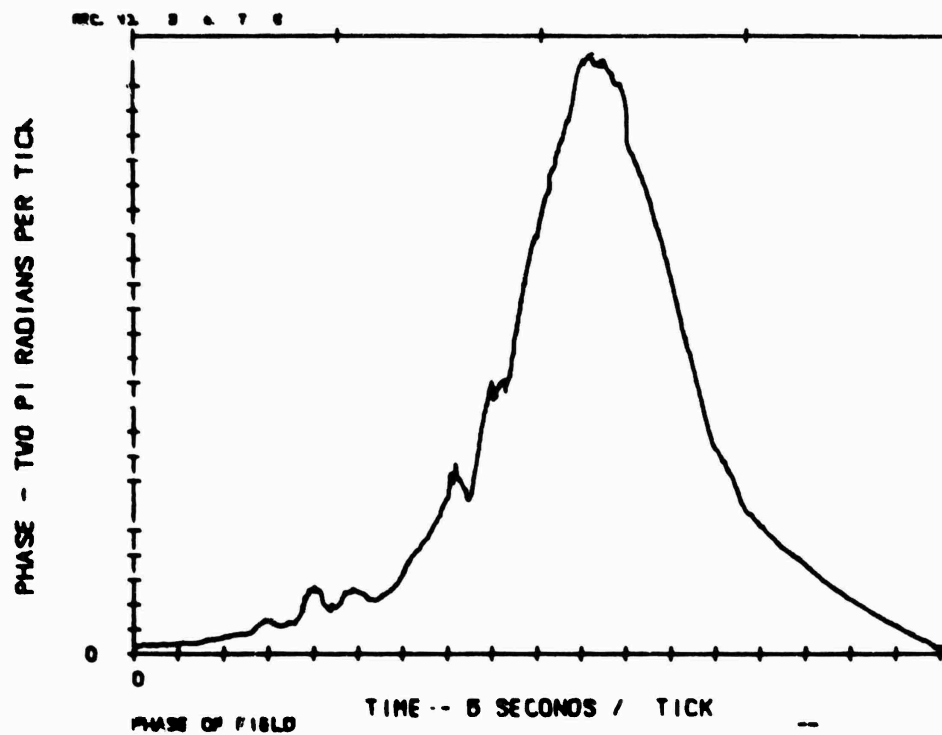
FIGURE 30   PHASE OF THE FIELD BACK-PROPAGATED 100 km OBTAINED FROM ESTHER
PASS 11 UPLINK PROBE
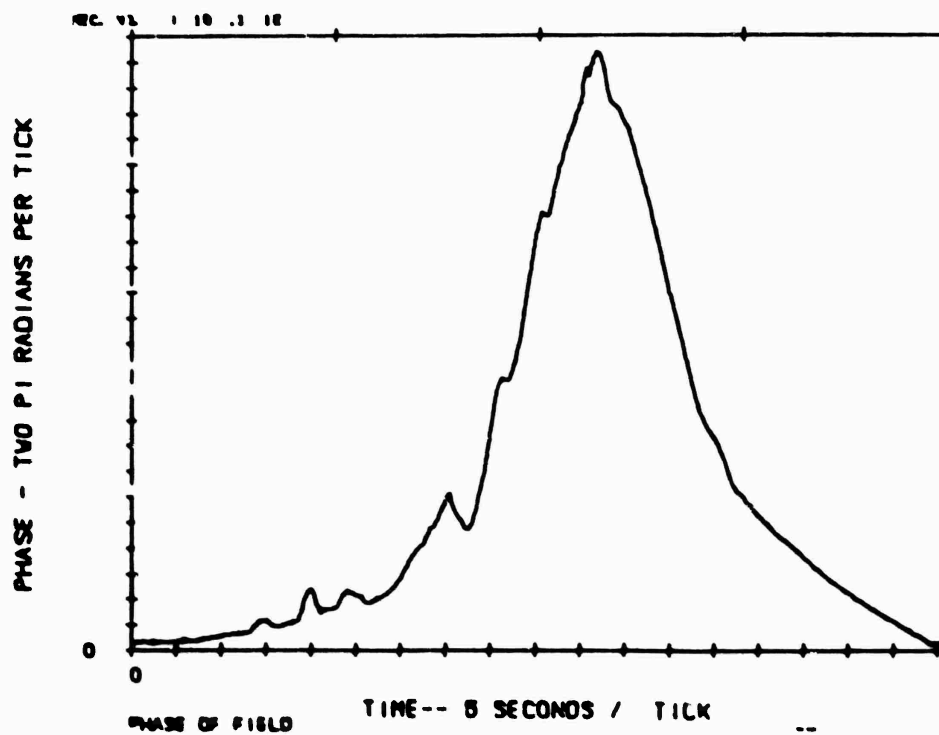
FIGURE 31   PHASE OF THE FIELD BACK-PROPAGATED 140 km OBTAINED FROM ESTHER
PASS 11 UPLINK PROBE
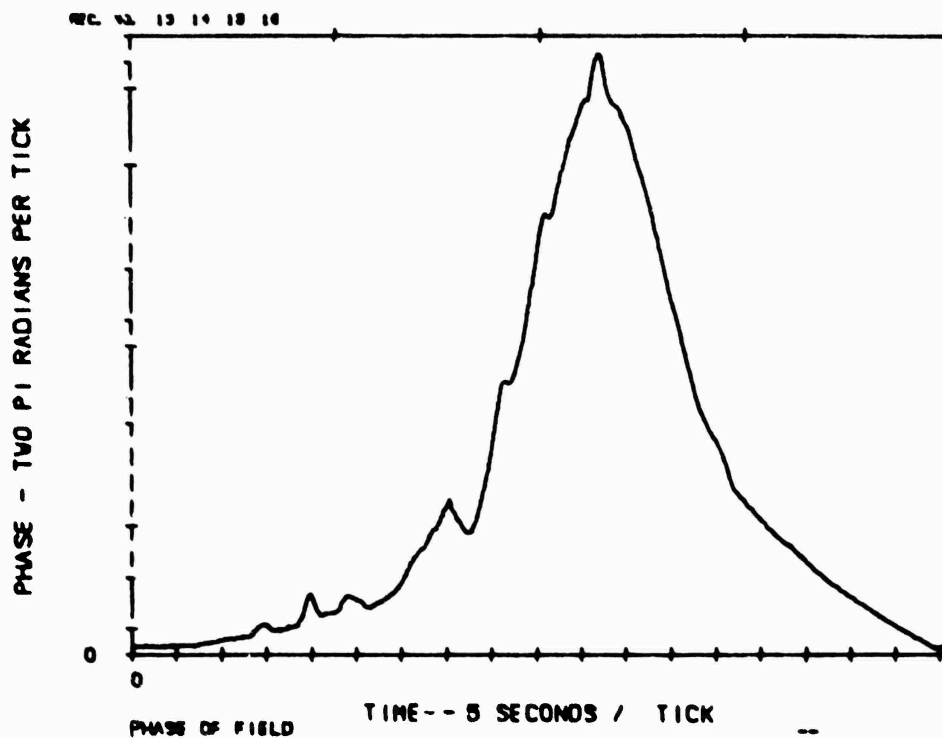
FIGURE 32   PHASE OF THE FIELD BACK-PROPAGATED 150 km OBTAINED FROM ESTHER
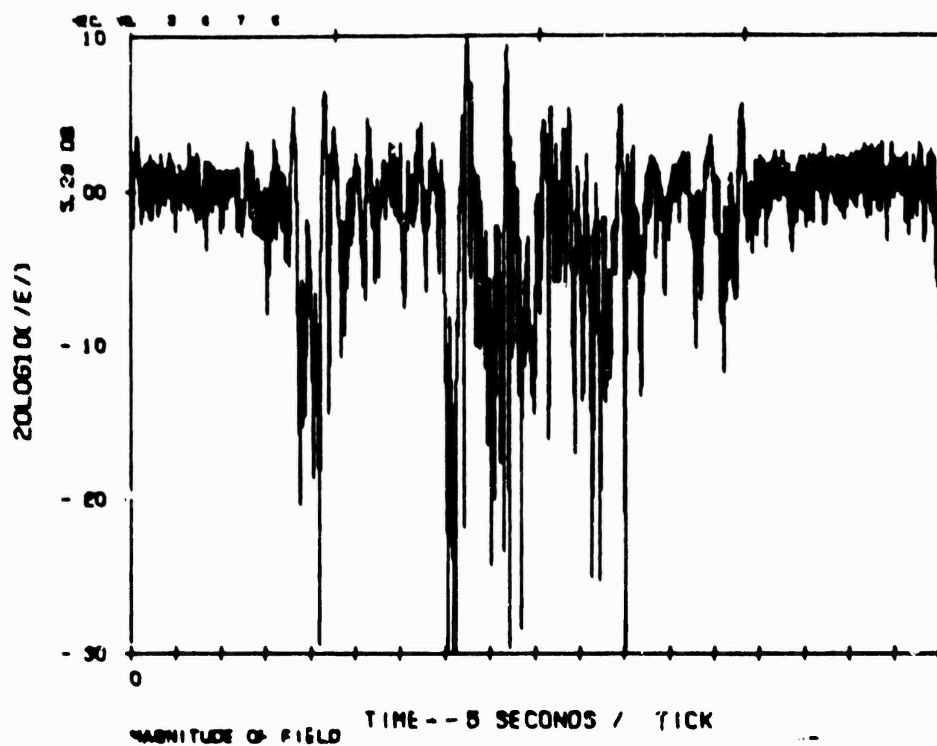PASS 11 UPLINK PROBE
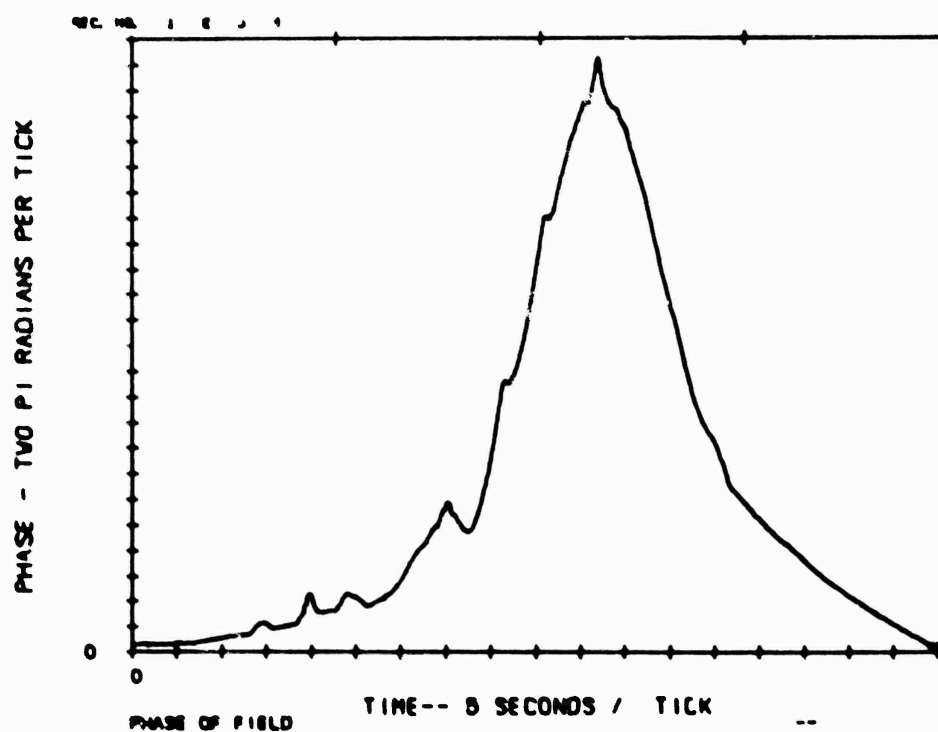
FIGURE 33   PHASE OF THE FIELD BACK-PROPAGATED 160 km OBTAINED FROM ESTHER
PASS 11 UPLINK PROBE

133

FIGURE 34   PHASE OF THE FIELD BACK-PROPAGATED 200 km OBTAINED FROM ESTHER
PASS 11 UPLINK PROBE
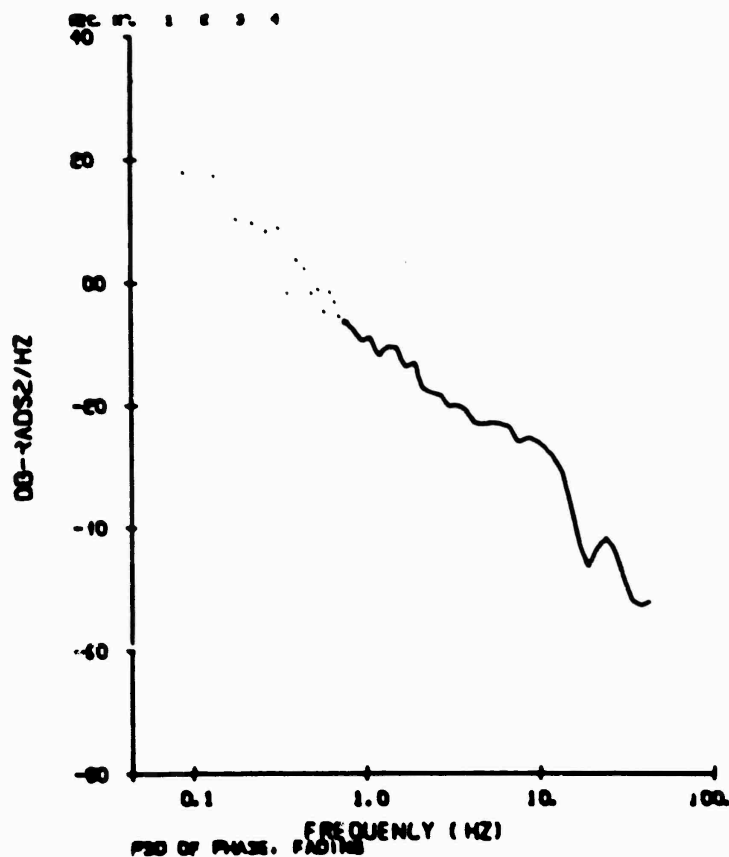
FIGURE 35   POWER SPECTRUM OF THE PHASE OF THE FIELD MEASURED AT THE
GROUND WITH THE UPLINK PROBE DURING ESTHER PASS 11
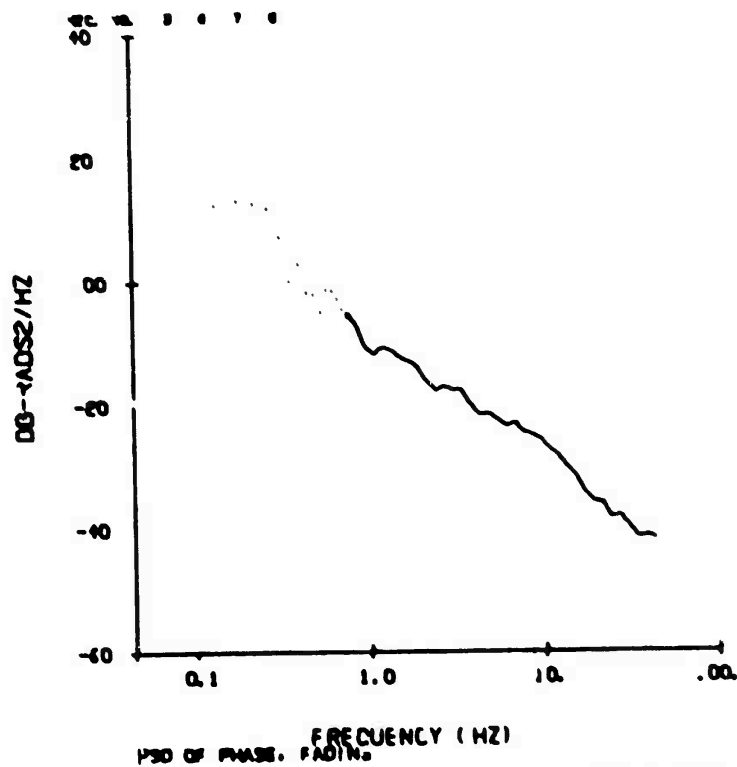
FIGURE 36 POWER SPECTRUM OF THE PHASE OF THE FIELD BACK-PROPAGATED
100 km FROM ESTHER PASS 11 UPLINK DATA
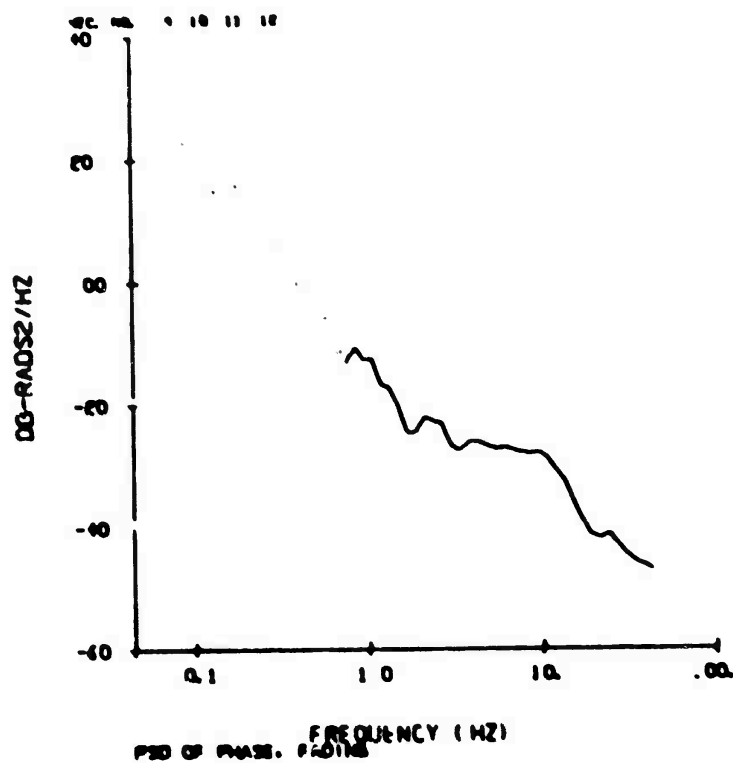
FIGUPE 37 POWER SPECTRUM OF THE PHASE OF THE FIELD BACK-PROPAGATED
140 km FROM ESTHER PASS 11 UPLINK DATA

135
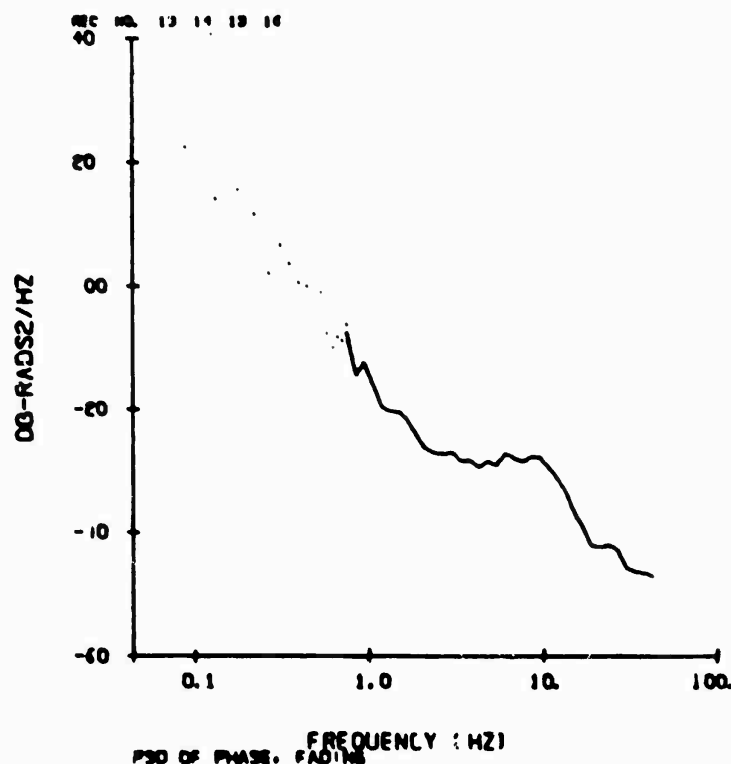
FIGURE 38   POWER SPECTRUM OF THE PHASE OF THE FIELD BACK-PROPAGATED
150 km FROM ESTHER PASS 11 UPLINK DATA
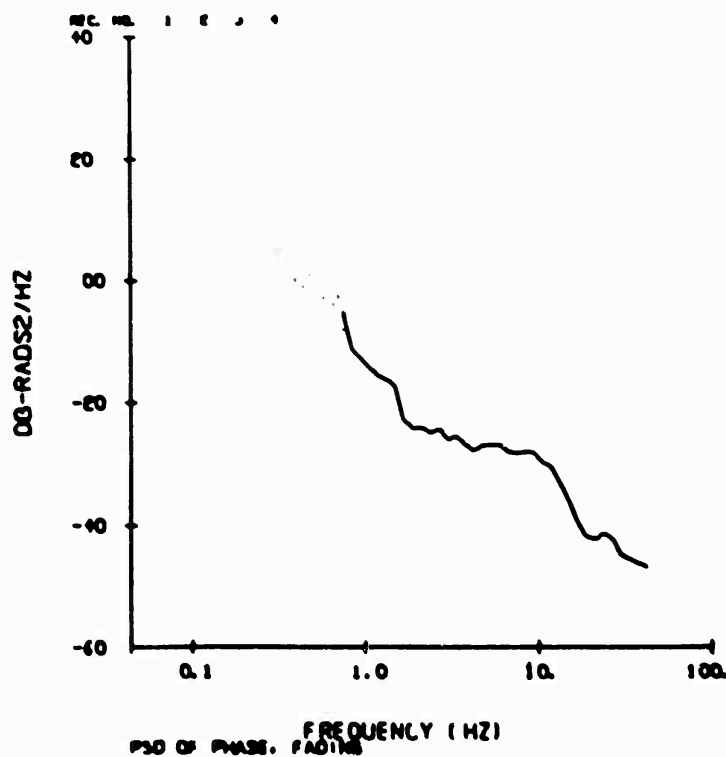
FIGURE 39   POWER SPECTRUM OF THE PHASE OF THE FIELD BACK-PROPAGATED
160 km FROM ESTHER PASS 11 UPLINK DATA

136

in a bin the points themselves are plotted. This method of presentation mechanizes eyeball averaging of spectrum power (at the risk of blurring single-frequency spike phenomena).

Observe that phase spectra at 140, 150, and 160 km are steeper than the phase spectra at the ground. The latter have a 30-to-40-dB/decade roll-off in place of the ≈ 20 dB/decade roll-off observed at the ground. The significant change in slope implies the important fact that back-propagation must be used to get reliable information concerning the behavior of the power spectra of the integrated content.

Comparison of uplink tone and downlink tone-back propagation data shows good agreement. Shown in Figure 41 is the downlink probe phase for ESTHER Pass 18 at the ground and at the back-propagation minimum. Shown in Figure 42 is the uplink back-propagated phase. The agreement between the data is good; corresponding integrated electron content structures can easily be identified. Thus, back-propagation techniques appear to be successful.

VII EVENT ESTHER BACK-PROPAGATED DATA

Back-propagated uplink tone data have been recently obtained for ESTHER. Analysis of this time history of the structure is possible by investigating the behavior of the phase of the back-propagated field.

Preliminary investigation of these data reveals four classes of phase structure (Table 1). Early-time phase structure resembles a Guassian structure, often with one edge steeper than the other (Figure 43). This type of structure was seen until Pass 2 (2332Z), at and beyond which time striations were observed. The striation cloud remained contained in what appeared to be a single cloud until at least 0030Z. By Pass 28 (0113Z), however, a break-up of the region of striation effects was noted. During the period in which the striations remained contained (2332Z to 0030Z and slightly after), two different classes of phase structure were noted. The first class showed well pronounced striations as seen in Passes 6, 8, and 17 in Figures 44, 45,

137

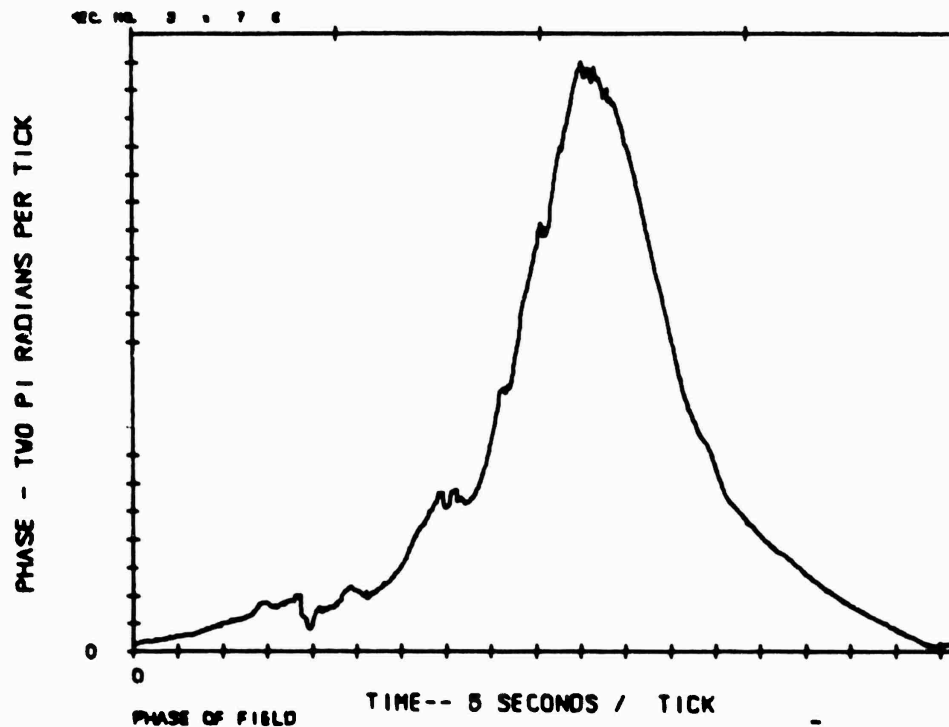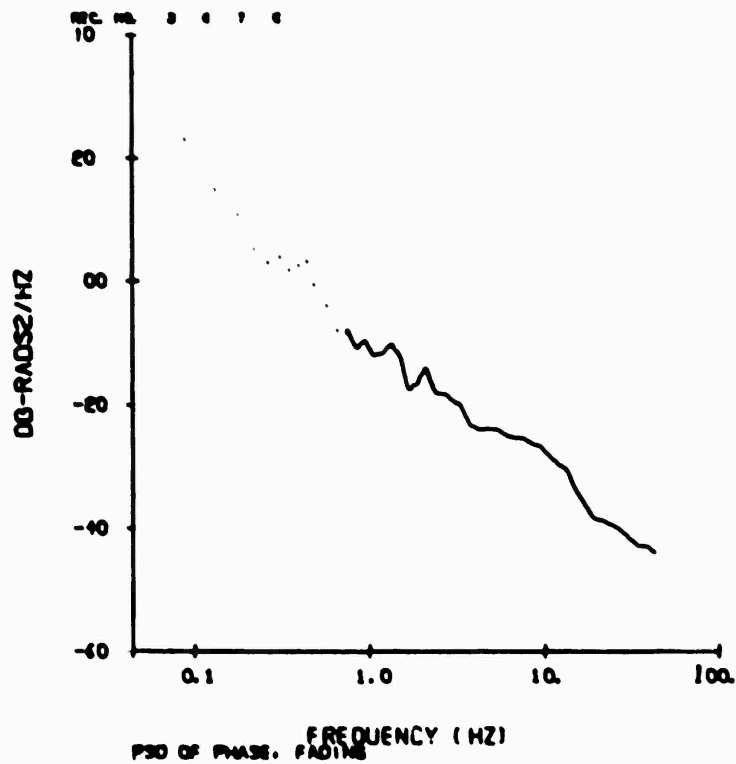FIGURE 40   POWER SPECTRUM OF THE PHASE OF THE FIELD BACK-PROPAGATED
200 km FROM ESTHER PASS 11 UPLINK DATA
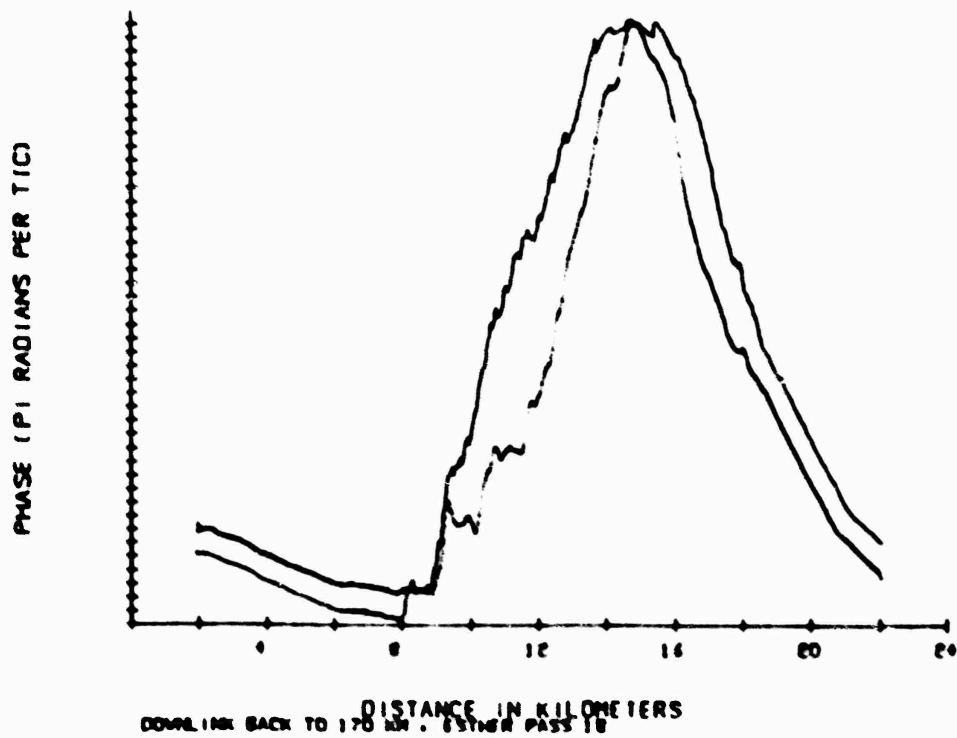
FIGURE 41   PHASE OF THE FIELD MEASURED WITH THE DOWNLINK TONE (solid)
AND BACK-PROPAGATED PHASE AT SCINTILLATION MINIMUM (dotted)
FOR ESTHER PASS 18

138
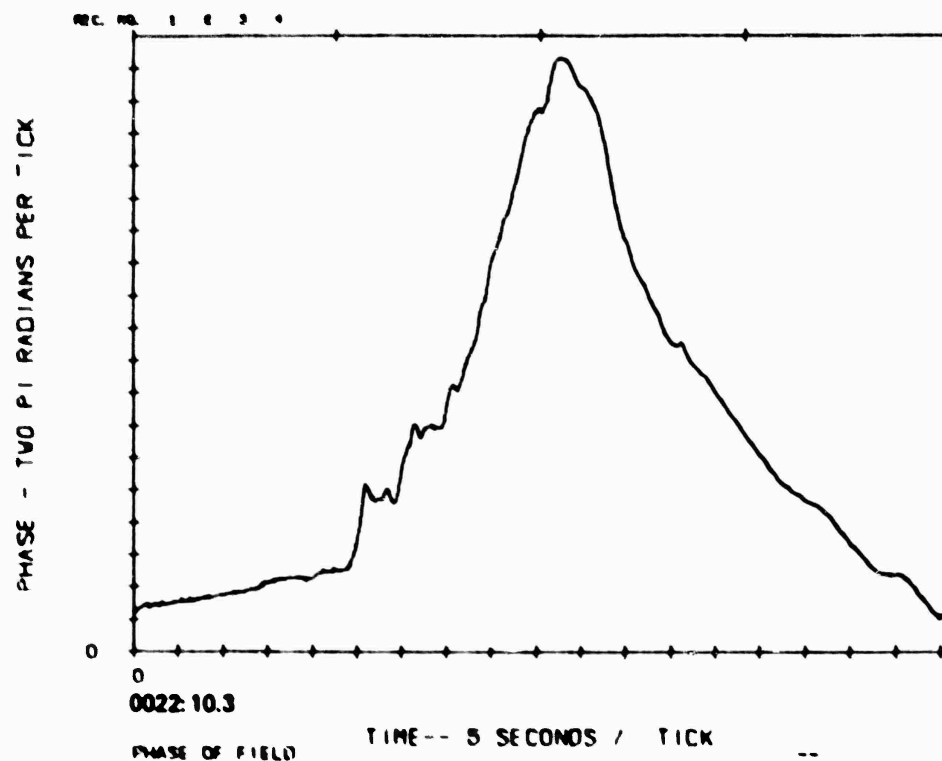
FIGURE 42   PHASE OF THE BACK-PROPAGATED FIELD OBTAINED USING UPLINK DATA
DURING ESTHER PASS 18
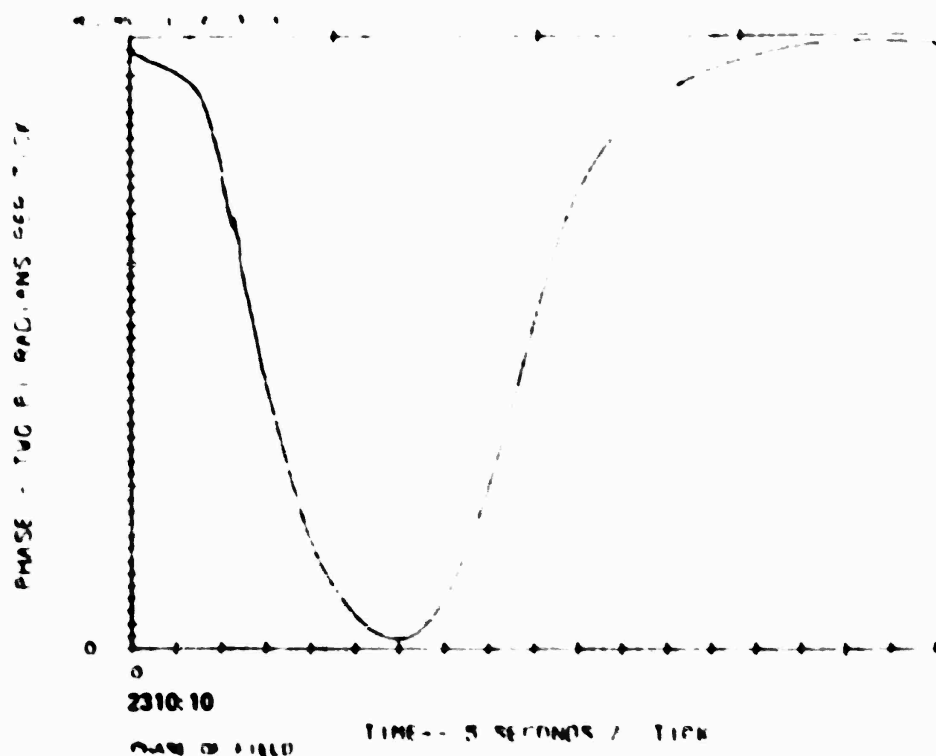
FIGURE 43   A TYPICAL EARLY-TIME BACK-PROPAGATED PHASE (ESTHER Pass 3 Uplink
Data, 2316Z)
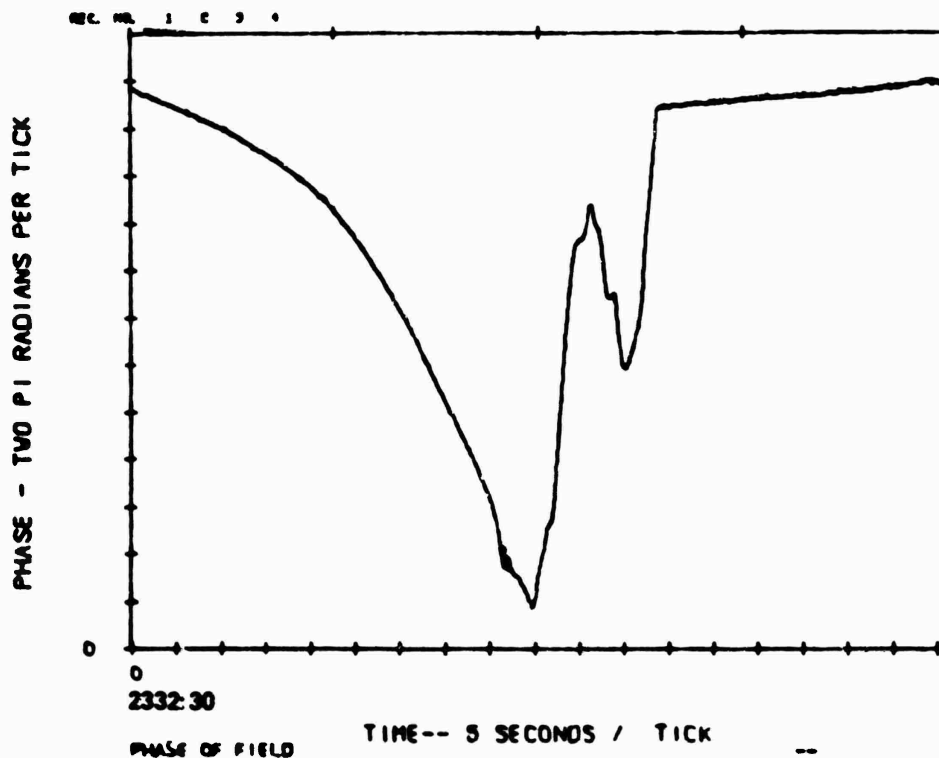
FIGURE 44   CLASS 1 TYPE BACK-PROPAGATED PHASE SHOWING STRONG STRIATIONS
(ESTHER Pass 6 Uplink Data, 2333Z)
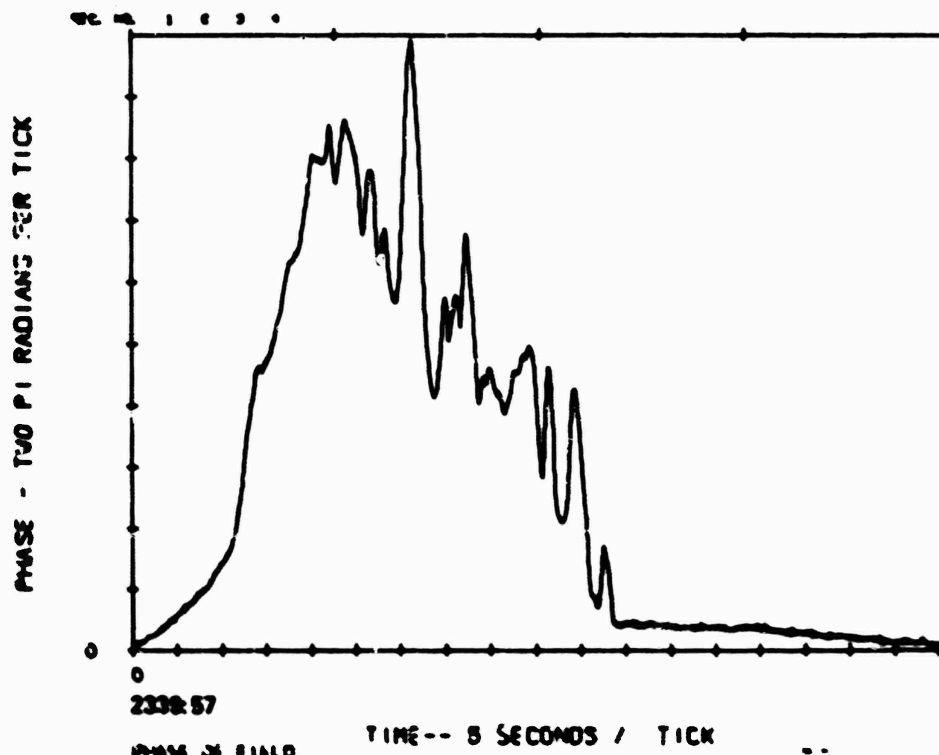
FIGURE 45   CLASS 1 TYPE BACK-PROPAGATED PHASE SHOWING STRONG STRIATIONS
(ESTHER Pass 8 Uplink Data, 2340Z)

140

Table 1

ESTHER PHASE DATA SUMMARY

Type of Phase Structure	Pass Number	Time, Z	Peak Integrated Electron Content (10^{12} el/cm^2)	Phase Power Spectral Density Slope (dB/decade)	Frequency at Which Power Spectral Density is 20 dB Down (Hz)	Propagation Distance at Which S_4 is Minimum (km)	Back-Propagation Distance at Which S_4 is Corrected for Pattern Velocity (km)	Hit-Point Altitude (km)
Early time	3	2316	12	-30	0.12	173	218	-30
Class 1	6	2332	2.7	-35	0.12	161	255	+29
	8	2340	2.5	-55	0.50	149	238	+23
	10	2349	4.3	-30	0.20	145	231	+20
	17	0017	4.0	-30	0.20	181	228	+11
	19	C026	4.1	-30	0.20	173	218	+4
Class 2	7	2336	7.9	-30	0.20	153	193	-5
	9	2345	6.7	-25	0.30	155	195	-12
	11	2353	5.8	-35	0.20	153	193	-20
	18	0022	4.3	-45	0.30	114	182	-16
	19.5	0030	2.6	-50	0.30	164	189*	?
Late time	32	0130	1.8	-40	0.10	137	217	?

*With 26° degree heading correction; without correction it was 262 km.

141

and 46, respectively. The second class of phase structure showed less pronounced striations superimposed upon a triangular shaped background as seen in Passes 7, 9, 11, and 18 in Figures 47, 48, 32, and 42, respectively. Data from late-time passes such as the downlink data for Pass 32 in Figure 49 show breakup of the structure, in this case into three apparent clouds.

The peak phase of the back-propagated cloud gives a measure of the integrated content. Figure 50 shows the time history of this value. Its steady decay could conceivably be associated with a volume expansion of the striated region.

The power spectra of the back-propagated phases seen in Figures 44 through 49, 32, and 42 are shown in Figures 51 through 57, 38, and 58, respectively. Note that no distinct trend is obvious in the behavior of the roll-off slope, as tabulated in Table 1. Slopes with values from 25 to 55 dB/decade are observed.

The back-propagation minimum distance when corrected for aircraft velocity is shown in Table 1. The corrected values are consistent both with the class of feature observed and with the aircraft trajectory altitude on the field line through the track point. This consistency supports the frozen-in assumption used to obtain back-propagation distances.
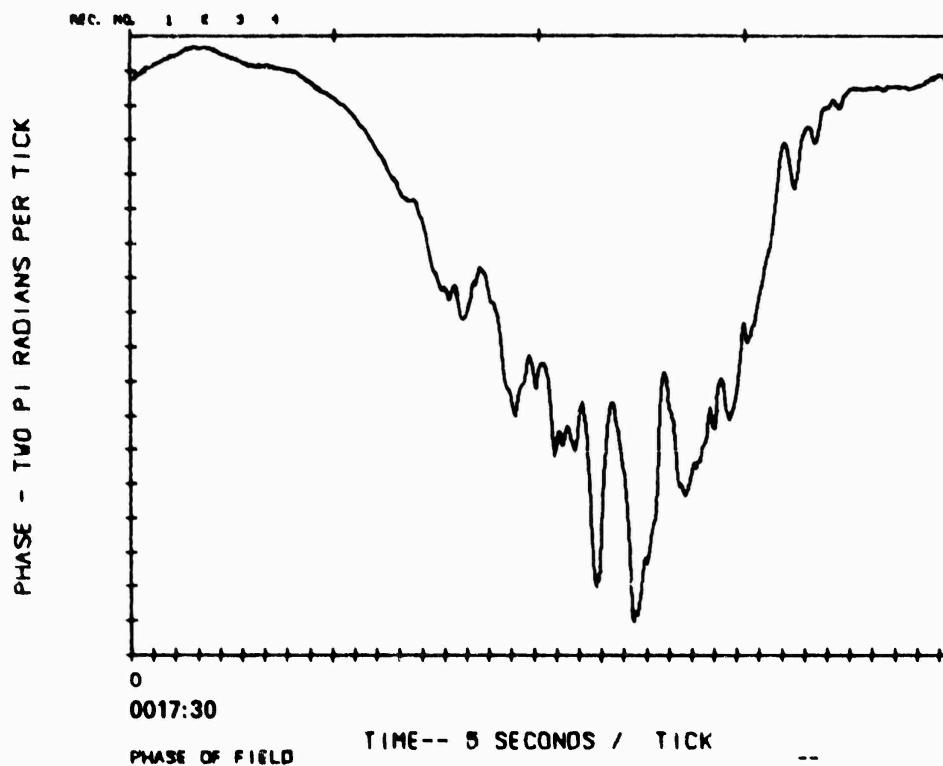
FIGURE 46   CLASS 1 TYPE BACK-PROPAGATED PHASE SHOWING STRONG STRIATIONS
(ESTHER Pass 17 Uplink Data, 0018Z)
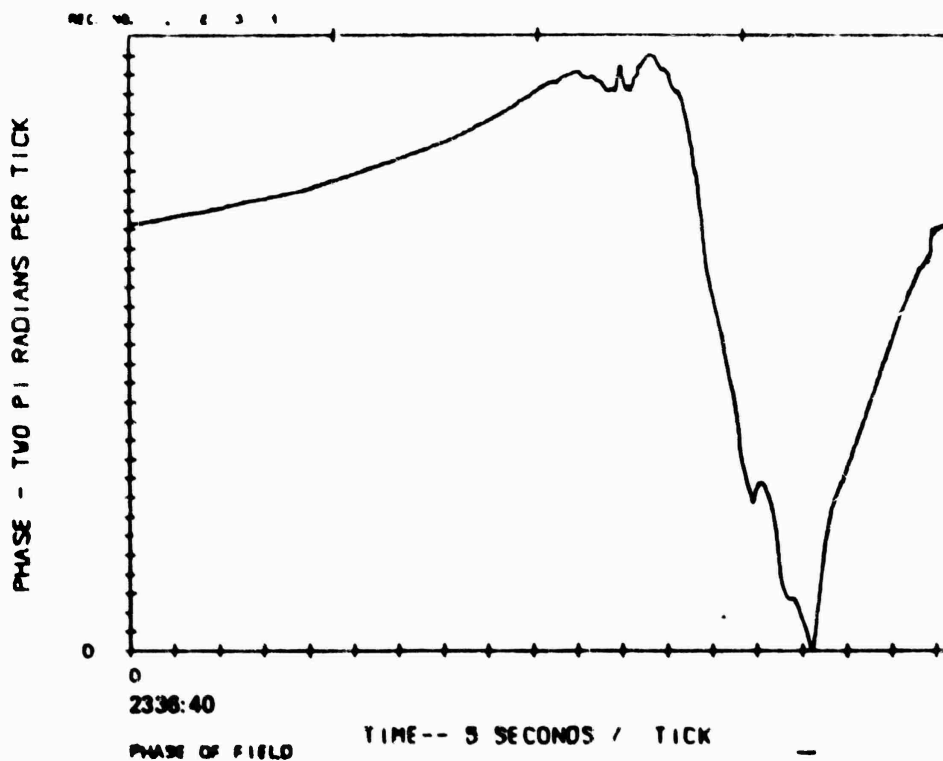
FIGURE 47   CLASS 2 TYPE BACK-PROPAGATED PHASE SHOWING STRONG BACKGROUND
IONIZATION (ESTHER Pass 7 Uplink Data, 2337Z)
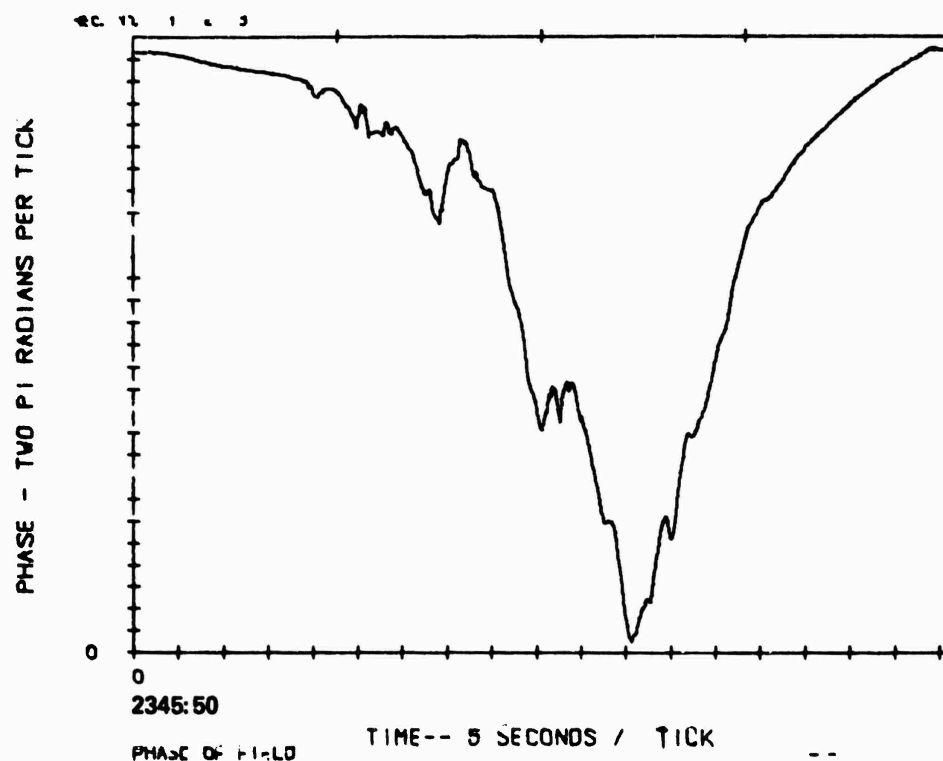
FIGURE 48 CLASS 2 TYPE BACK-PROPAGATED PHASE SHOWING STRONG BACKGROUND IONIZATION (ESTHER Pass 9 Uplink Data, 2346Z)
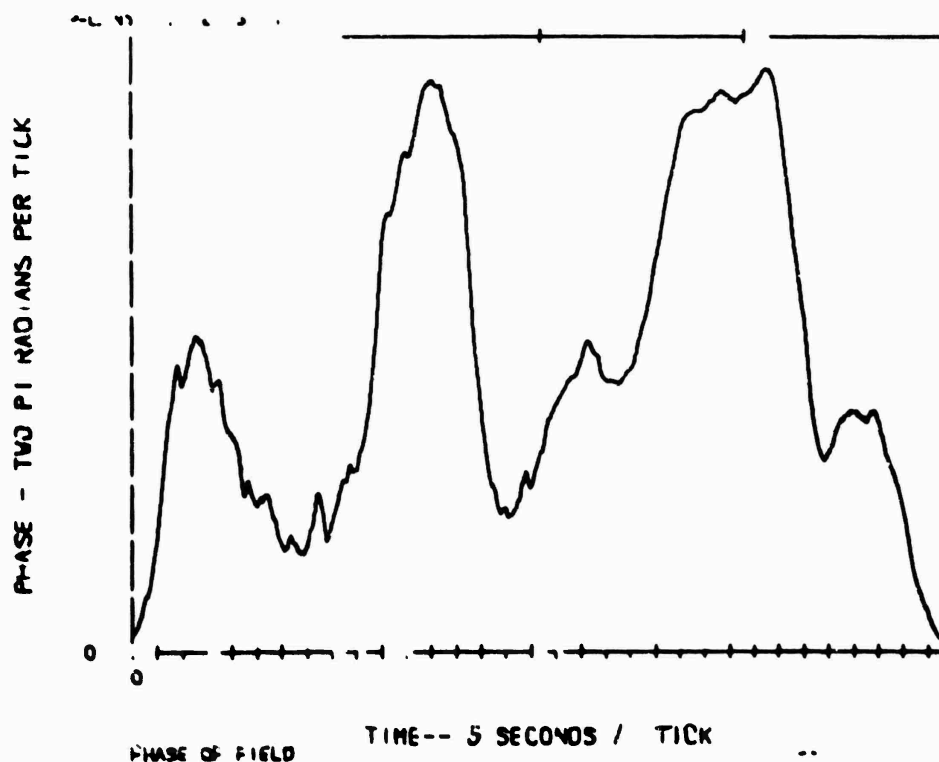
FIGURE 49 LATE TIME BACK-PROPAGATED PHASE SHOWING A BREAK-UP OF THE CLOUD (ESTHER Pass 32 Downlink Data, 0130Z)
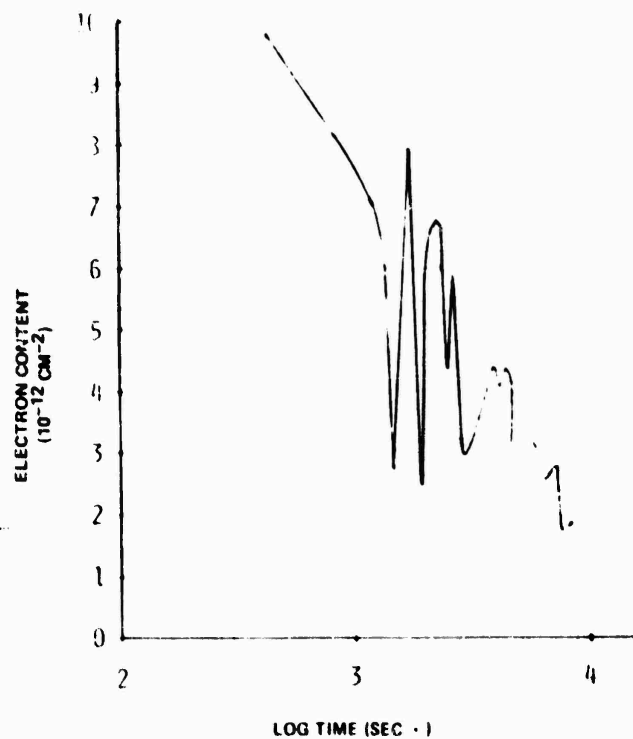
FIGURE 50   PEAK INTEGRATED ELECTRON CONTENT OBSERVED vs TIME
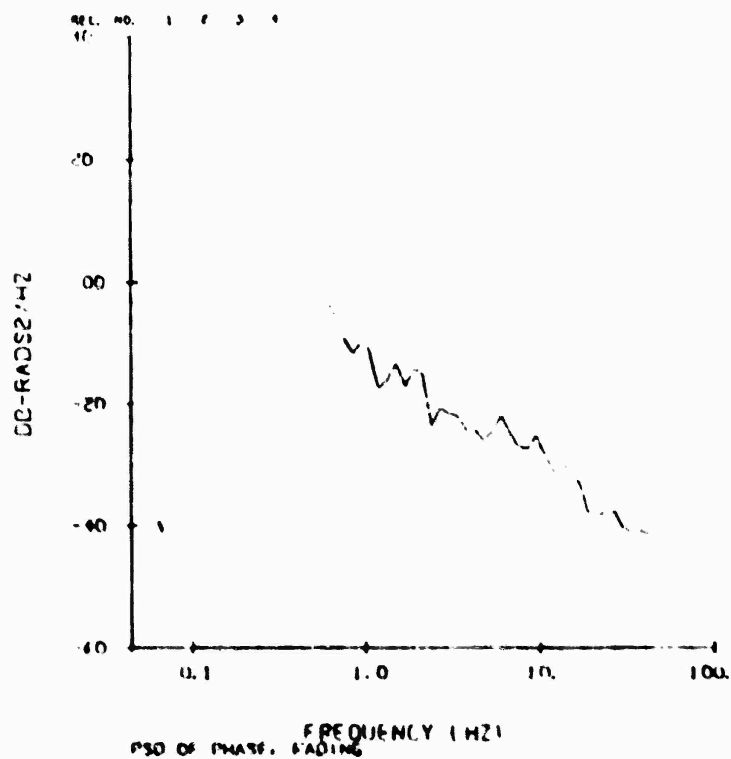
FIGURE 51   POWER SPECTRUM OF THE BACK-PROPAGATED PHASE FOR ESTHER
PASS 3 SEEN IN FIGURE 43

145
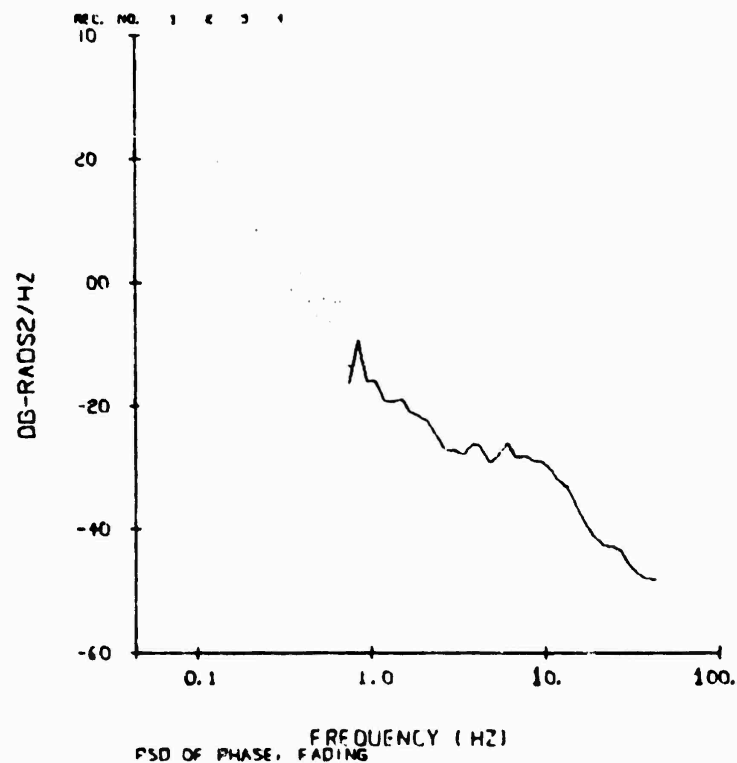
FIGURE 52 POWER SPECTRUM OF THE BACK-PROPAGATED PHASE FOR ESTHER PASS 6 SEEN IN FIGURE 44
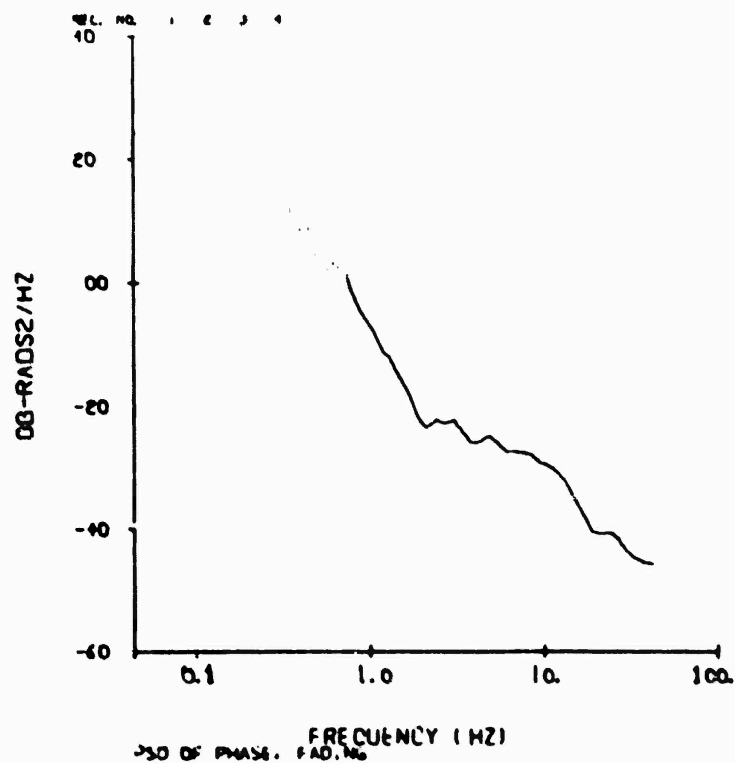
FIGURE 53 POWER SPECTRUM OF THE BACK-PROPAGATED PHASE FOR ESTHER PASS 8 SEEN IN FIGURE 45
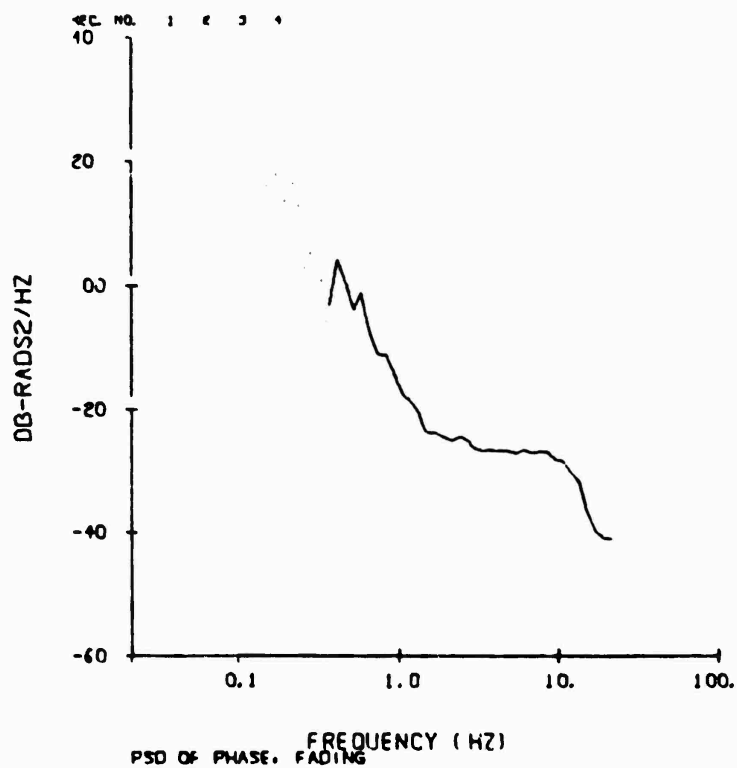
FIGURE 54   POWER SPECTRUM OF THE BACK-PROPAGATED PHASE FOR ESTHER
PASS 17 SEEN IN FIGURE 46
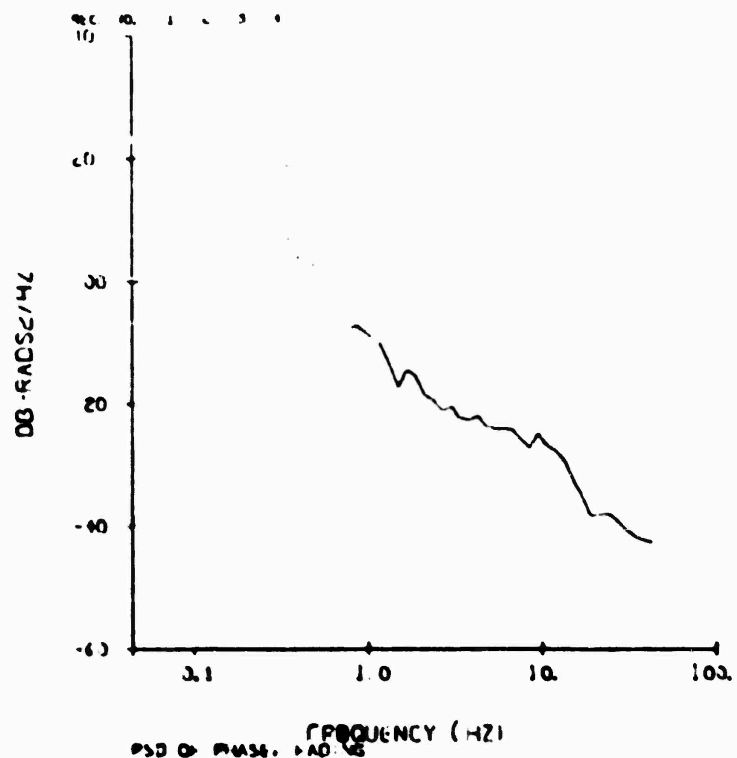
FIGURE 55   POWER SPECTRUM OF THE BACK-PROPAGATED PHASE FOR ESTHER
PASS 7 SEEN IN FIGURE 47

147
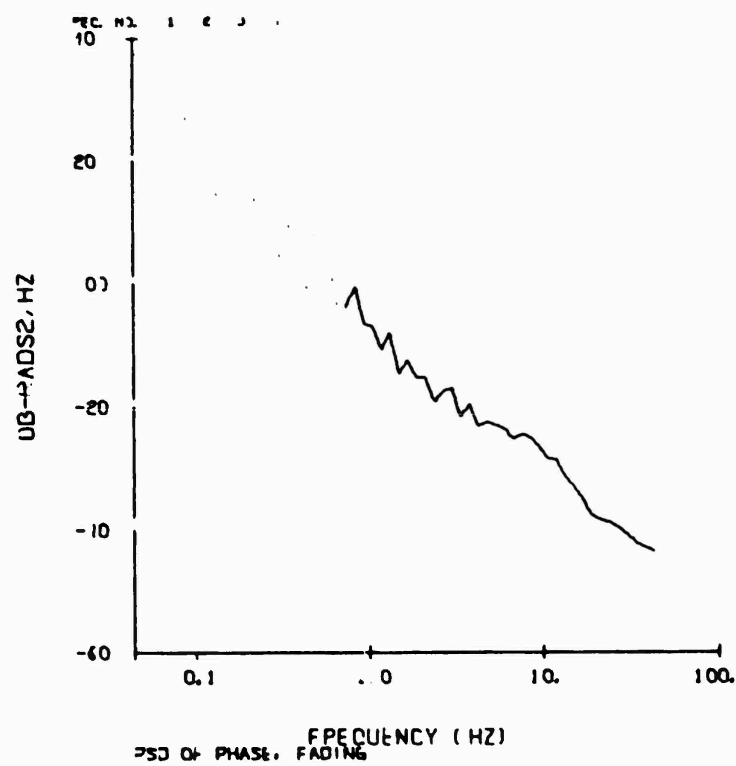
FIGURE 56 POWER SPECTRUM OF THE BACK-PROPAGATED PHASE FOR ESTHER
PASS 9 SEEN IN FIGURE 48
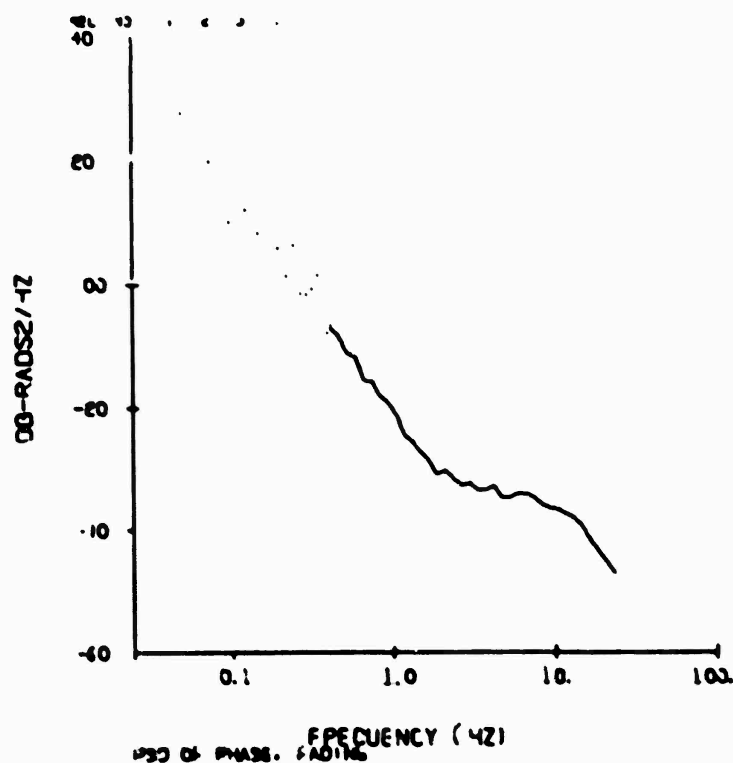
FIGURE 57 POWER SPECTRUM OF THE BACK-PROPAGATED PHASE FOR ESTHER
PASS 32 SEEN IN FIGURE 49
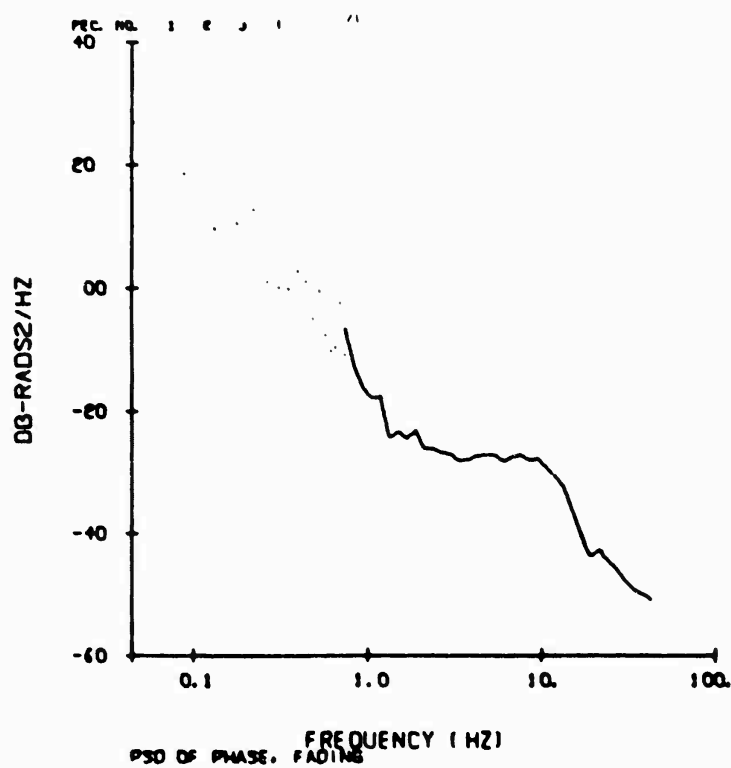
FIGURE 58   POWER SPECTRUM OF THE BACK-PROPAGATED PHASE
FOR ESTHER PASS 18 SEEN IN FIGURE 42

149

UHF RADAR DATA ANALYSIS

V. H. Gonzalez

SRI International
Menlo Park, California

UHF RADAR DATA ANALYSIS

V. H. Gonzalez

SRI International
Menlo Park, California

I INTRODUCTION

One of the objectives of the radar tracking experiment was to acquire electron density data from barium ion clouds so that a description of the electron density distribution in space and time could be given. This paper describes the progress made to date by SRI in the analysis of the acquired data. The general behavior of barium clouds obtained from real-time analysis, such as motion of the ion cloud and variation of maximum electron density as a function of time, has been presented in previous SRI work.[*] Although these results can be reviewed and improved, the effort reported on here consisted of further analysis of the detailed data rather than a refinement of the previous work.

A necessary step before analyzing the data is the calibration of the radar. The calibration procedure is divided into two parts; the first part is the conversion of received signal samples into received power levels (on a relative scale), and the second part is the conversion of the received power levels into electron densities. The first part of this calibration was discussed in detail in an earlier technical report.[*] Previous to recording data, the results of the first part of the calibration were applied in the field, in real time, to the numbers read into

---

[*] V. H. Gonzalez, "Radar Tracking of Ion Clouds," Interim Technical Report 1, Project STRESS, Contract DNA001-76-C-0341, SRI International, Menlo Park, California (July 1977).

the computer. Thus, the recorded detailed data we have now are a measure of power received, in arbitrary units. The second part of the calibration is treated in Section II of this paper, which starts with some basic pertinent formulations and then explains the use of the ionosonde data to obtain a simple functional relation that relates our recorded data (received power) to electron densities in space.

After the calibration procedure is completed, the detailed analysis of the data is begun. The objective of this analysis is to describe the spatial distribution of electron densities at specific times so that correlation with results of related experiments can be made. The related experiments of interest are the probe rocket measurements, the use of the satellite-to-airplane communication link, and the photography. Sections III through V of this paper describe the analysis.

Detailed descriptions of Events ESTHER and FERN are presented in the form of equidensity contours in horizontal planes. The times at which the probe rocket was flown received special attention. Analysis was continued for the FERN ion cloud, to find information about its motion and to correlate the measured electron densities with observable features in photographs.

The spatial description of a Ba-ion cloud as obtained by use of the equidensity contours can be considered merely as a tool to address more significant problems; solutions to these problems in turn would be useful to the understanding of the physical processes that determine the development of the ion clouds.

II RADAR ECHOES FROM FREE ELECTRONS--RADAR CALIBRATION

Consider a point in space, to be called X, and a volume element around it. The radar radiates power P_T, which would produce a power density $P_T/(4\pi r^2)$ at X if the antenna was isotropic. The flux density is modified by the gain of the antenna, $G_T(X)$, in the direction of point X as seen from the radar. Thus, the power density at X is

$$\frac{P_T}{4\pi r^2} G_T(X) \quad . \tag{1}$$

154

If the propagation conditions are not uniform, focusing or defocusing may occur and the power density at X may be modified by a factor, $F(X)$, which is a function of the propagating medium between the radar and the point under consideration [$F(X) = 1$ under uniform conditions]. Thus the power density at X can be expressed as

$$P(X) = \frac{K_T}{R^2} G_T(X) \ F(X)$$

where the constant K_T includes power-transmitting efficiency of the radiating system, the proper physical constants, and the unit conversion factors.

The radar cross section of the electrons in the elemental volume around the point X is:

$$d\Sigma(X) = \sigma_e N_c(X) \ dV \tag{2}$$

where σ_e is the cross section of a single electron and $N_e(X)$ is the electron density at X, uniform within the volume element dV.

The power intercepted and scattered by the element dV is the product of the power density $P(X)$ and the cross section $d\Sigma(X)$. The fraction of the scattered power received by the antenna is

$$\frac{A_{eff}(X)}{4\pi r^2} \ F(X) \tag{3}$$

where $A_{eff}(X)$ is the effective area as a function of the direction of X as seen from the antenna, and $F(X)$ is the same enhancement factor that occurs in the transmitting propagation path (the propagation medium has a reciprocal property).

If receiving gain, $G_R(X)$, is used instead of effective area, then the power received from the element of volume dV is

$$dP_R = K \frac{G_T(X) \ G_R(X)}{R^4} \ F^2(X) \ N(X) \ dV \tag{4}$$

155

where the new constant K includes K_T as well as the conversion factor from effective receiving aperture to gain ($\lambda^2/4\pi$), the efficiency of the receiver, and all of the appropriate numerical constants.

It is at this point that we should introduce a coordinate system for the point X that is appropriate to a phased-array radar. This coordinate system will be the phased-array coordinate system shown in Figure 1, which consists of the two angular coordinates, u and v, and the range coordinate R. In Figure 1, z is the boresight direction (normal to the surface of the antenna array); the angle β is defined as the angle between the line $\overline{AX}$ and the plane x-z, and v in turn is defined as

$$v = \sin\beta \quad .$$

Similarly, α is the angle between the line $\overline{AX}$ and the plane y-z, and u is defined as

$$u = \sin\alpha \quad .$$
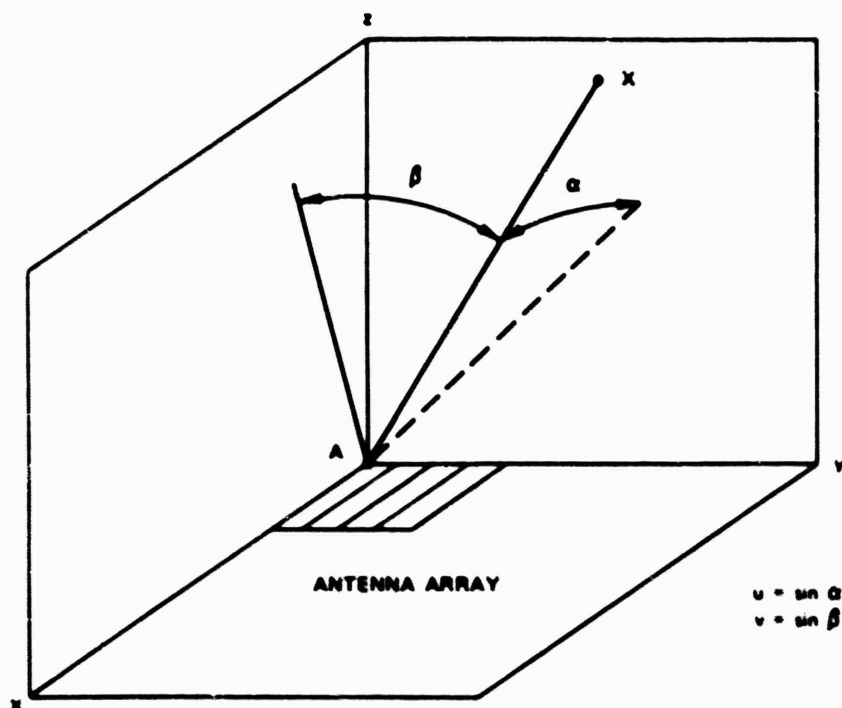
LA-6078-14

FIGURE 1   PHASED ARRAY COORDINATE SYSTEM

156

Calling the angle formed by the line $\overline{AX}$ and the z axis the "off-boresight" angle, δ,

$$\cos\delta = \sqrt{1 - v^2 - u^2} \quad . \tag{5}$$

The volume element becomes

$$dV = \frac{R^2}{\cos\delta} \, du \, dv \, \Delta R \quad . \tag{6}$$

The dimension ΔR is chosen to be equal to $(c\tau)/2$, where c is the velocity of light, and τ is the pulse length. Because ΔR can be included with the other constants, the received power in terms of the radar coordinates becomes, for a given element of volume,

$$dP_R = KN(R,u,v) \, \frac{G_T(u,v) \, G_R(u,v)}{R^2 \cos\delta} \, du \, dv \quad . \tag{7}$$

The gains G_T and G_R can be further expressed in terms of the pointing direction of the beam relative to the boresight, u_0, v_0, δ_0, as:

$$G_T(u,v) = G_{T_0}(u_0, v_0) \, G_{T_1}[(u - u_0), (v - v_0)]$$

$$G_R(u,v) = G_{R_0}(u_0, v_0) \, G_{T_1}[(u - u_0), (v - v_0)] \quad . \tag{8}$$

The specific expressions for G_{T_0} and G_{R_0} are $\cos\delta$; thus

$$G_T(u,v) = \cos\delta_0 \, G_{T_1}[(u - u_0), (v - v_0)]$$

$$G_R(u,v) = \cos\delta_0 \, G_{R_1}[(u - u_0), (v - v_0)] \quad . \tag{9}$$

The integration of dP_R for a given range cell around the angle u_0, v_0 covers a small solid angle. Thus, $\cos\delta \cong \cos\delta_0$ over the region of integration, and a final expression for dP_R becomes:

157

$$dP_R = \frac{K\cos\delta_0}{R^2} N(R,u,v) \; F^2(R,u,v) \; G_{T_1} \; G_{R_1} \; du \; dv \quad . \tag{10}$$

Equation (10) is general enough to include the case where the electron density is not uniform across the beam and also the case where focusing of radiated energy is present.

The simplest case is the one we use for the interpretation of ionosphere measurements and for the calibration of all system constants of the radar. In the ionosphere situation, we can assume that N is uniform across the beam and that focusing does not exist [F(u,v,R) = 1]; then, for a given range:

$$P_R = \frac{K}{R^2} \cos\delta_0 \; N \iint G_{T_1} \; G_{R_1} \; du \; dv \quad . \tag{11}$$

The double integral is a constant, since G_{T_1} and G_{R_1} depend only on $u - v_0$ and $v - v_0$. Thus the integral and the constant K can be lumped into a single system constant, K_S, so that P_R becomes:

$$P_R = K_S \frac{N_e}{R^2} \cos\delta_0 \quad . \tag{12}$$

If the received power is measured using the system noise as the unit, P_R = SNR (because the system noise is virtually a constant value in an array of a few thousand receivers), then the expression above would provide a solution for K_S if values of N_e, R^2, and $\cos\delta_0$ were known. This calibration was achieved by measuring the maximum electron density N_{Max} of the ionosphere. The radar profile provides the value of R and P_R = SNR in the vertical direction, and the ionosonde, which was operated near the AN/FPS-85, provides the value N_{Max}.

Figure 2 shows two ionosphere profiles obtained for Event ESTHER, and Figure 3 is the variation of critical frequency obtained with the ionosonde. The difference between the profiles is caused by horizontal gradients, and the proper profile to use for calibration purposes is the vertical one. The derived values and pertinent units are:

158
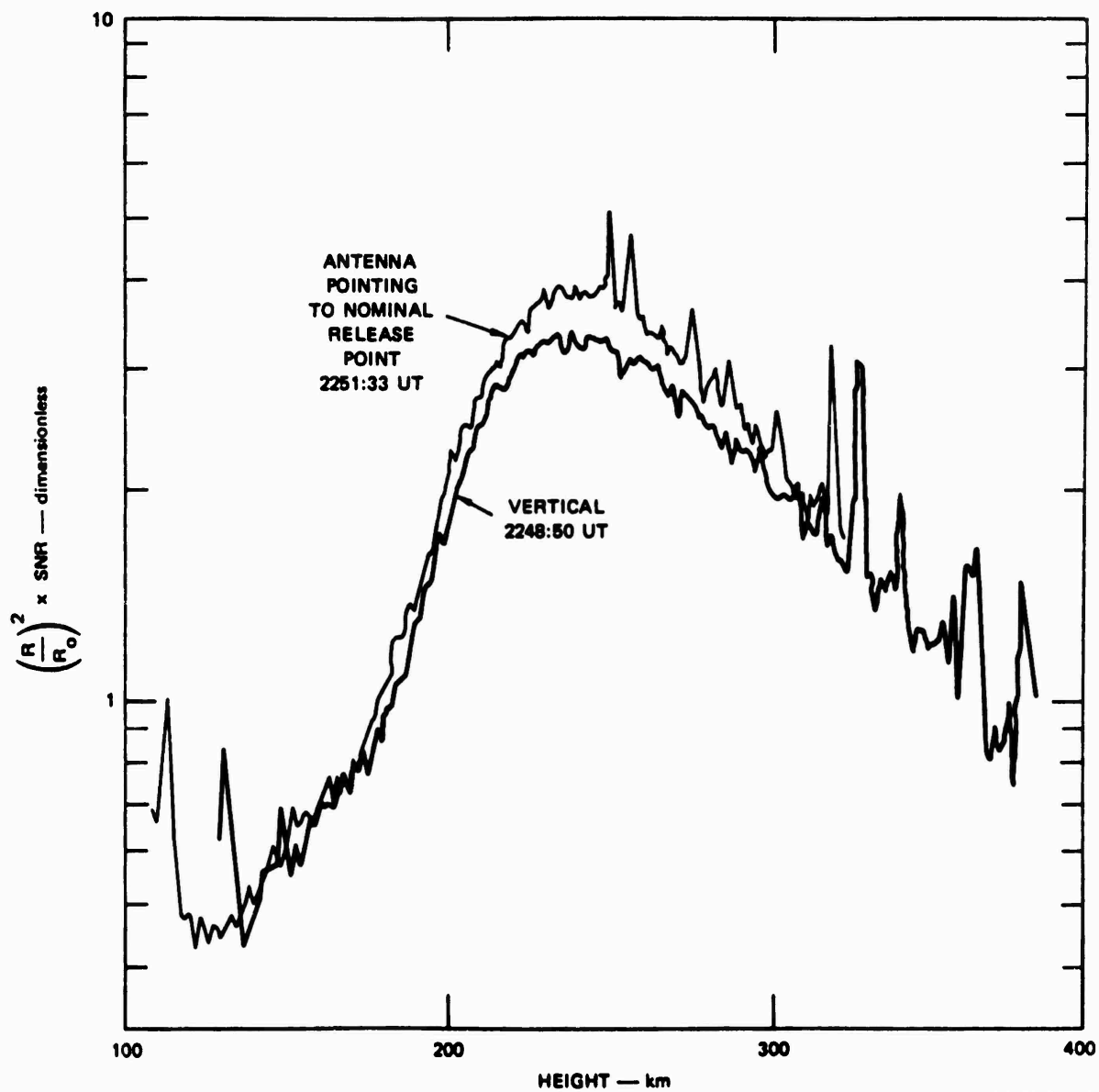
FIGURE 2   IONOSPHERE PROFILES PRIOR TO EVENT ESTHER (R_o = 210 km)

159
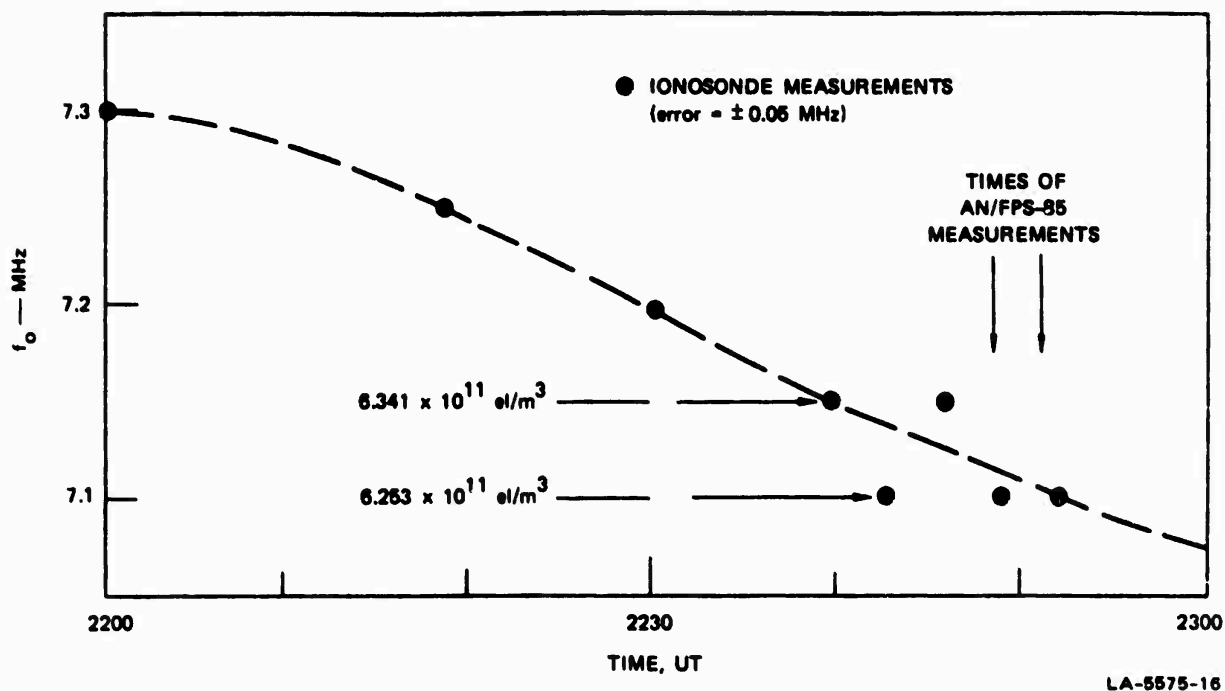
FIGURE 3   F$_o$ VALUES OBTAINED WITH THE IONOSONDE

$$P_R = SNR \text{ (dimensionless)}$$

$$[R] = km$$

$$[N_e] = el/m^3$$

$$K_S = 2.314 \times 10^{-7} \quad . \tag{13}$$

This value of K_S is about 2.8 dB smaller or poorer than that expected during the planning stages of the tracking experiment.

Equation (12), above, is changed to compute electron density from SNR in the following manner:

160

$$N_e = \frac{1.906 \times 10^{11}}{\cos\delta_0} \left(\frac{R}{210}\right)^2 \cdot SNR$$

$$[N_e] = el/m^3$$

$$[R] = km \quad . \tag{14}$$

When there is focusing, or there is nonuniform electron density across the beam, or both, Eq. (10) can be integrated:

$$P_R = K_S \frac{\cos\delta_0}{R^2} \frac{\iint NF^2 G_{T_1} G_{R_1} \, du \, dv}{\iint G_{T_1} G_{R_1} \, du \, dv} \quad . \tag{15}$$

The demoninator has to be integrated only once, while the numerator has to be integrated for each combination of values.

III   DATA ANALYSIS--ELECTRON DENSITY CONTOURS

The radar measurements explored a large portion of the Ba-ion cloud; thus they are able to provide the data base for a spatial description of existing electron densities. The spatial description received considerable attention.

The radar beam was pointed in a very irregular pattern of directions during the tracking of the Ba-ion cloud. Therefore the best way to use the measurements would be to least-square-fit an analytical function with a certain number of adjustable parameters. Unfortuantely, such an analytic function does not exist, and an alternative approach has been used.

We chose constant-electron-density contours at a set of constant heights as the most practical, informative, and useful spatial description of the Ba-ion cloud. This type of description can be easily correlated with two other measurements--rocket probes, and airplane-satellite propagation. The method used to draw a constant-electron-density contour requires a sequence of operations that are briefly described in the following paragraphs.

161

A set of 60 to 80 pointing directions was chosen to make a set of contour maps. The pointing directions were chosen to make a rectangular pattern of tracking (Mode II) and a strobe pattern of tracking (Mode I). Mode II makes measurements evenly spaced throughout the cloud. Measurements made with the strobe tracking (Mode I) was also included because these are measurements with longer integration times and are therefore more accurate than those of Mode II. The total time span of the 60 to 80 measurements is between 2 and 2-1/2 minutes.

The data obtained from each pointing direction are electron densities as a function of range, and these rough numbers are smoothed out in range at the beginning of the process by a 10-point Gaussian convolution filter.

For each height, data points were computed; these data points were the intersection of each beam pointing direction with a horizontal plane (latitude and longitude), and the corresponding electron densities were computed. In this way the problem was reduced to a two-dimensional geometry.

The computation of contours requires the electron density to be an analytic, single-valued function throughout the plane; thus, for a given point in the plane the corresponding electron density has to be interpolated or computed from nearby data points. To achieve interpolation, a circle with a radius of about five times the antenna beam radius was drawn around the given point and all the data points within this circle were used.

The slope parameters of a plane were fitted to the measurements within the circle by a least-squares method that used Gaussian weighting coefficients with an e-folding radius of about twice the beamwidth. Finally, the remaining constant of the plane was computed by a least-squares method that used Gaussian weighting coefficients with an e-folding radius of about 0.8 times the antenna beamwidth; thus the magnitude and the gradient of the electron density were calculated around the given point. The overall procedure may be regarded as an adequate interpolation for our type of data; it was designed to use noisy data points that are irregularly

162

distributed in a plane. That is, the plane contains areas with high density and areas with low-density distribution of data points.

The contours were drawn using a logic that started by searching the plane along two axes for a first point of the chosen electron density. When the first point was found, a search for a second point was made in a small circle around the first. When the second point was found the process was repeated for a third, fourth, and so on. The computation process for the contours produces details that are smaller than a radar beamwidth. Some of these small details result from a combination of measurement error and mathematical artifice; however, the overall results describe the Ba-ion clouds quite well.

IV EVENT ESTHER

A. First Rocket--2329:20 UT (R + 28 min 11 s)

The maximum electron density of the cloud at this time was 7.0×10^{12} el/m^3; thus the three equidensity contours shown in Figures 4 and 5 represent one-half, one-fourth, and one-eighth of the maximum electron density value. The cloud at this time, as seen by the FPS-85, was compact and well defined. Figure 4 shows the position and direction of the probe rocket. The rocket is approaching the ion cloud and it would appear that it is moving toward the densest part of it. However, the dip of the magnetic field compensates for the southward component of the rocket motion, and Figure 5 shows that the probe rocket approaches the one-half contour at H = 175 km without actually penetrating this contour. At 180 km the rocket is actually outside the one-fourth contour.

A preliminary comparison with the curves presented by Baker, Howlett, and Ulwick (these Proceedings) indicates that a good agreement between the radar and rocket probe measurements may be found.

B. Second Rocket--2347:10 UT (R + 46 min 1 s)

The maximum electron density of the ion cloud remained approximately the same as at the time of the first rocket--that is, 7.0×10^{12} el/m^3.
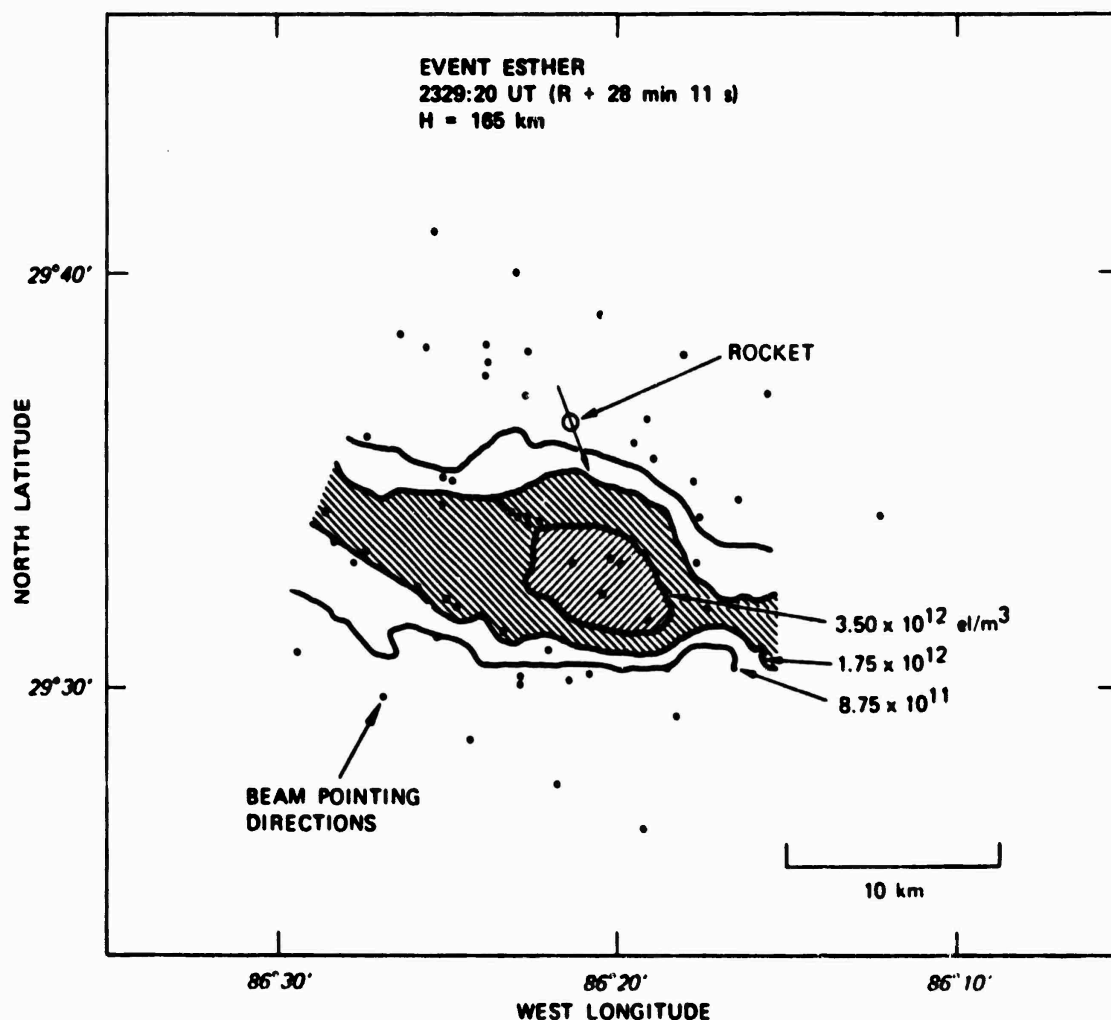
FIGURE 4   EQUIDENSITY CONTOURS ON A HORIZONTAL PLANE AT 165 km —
EVENT ESTHER, 2329:20 UT

From the radar point of view, it was still a well defined cloud that de-
veloped a long tail on the western side, as shown in Figures 6 and 7.

The one-half contour is not appreciably different in cross section
from the equivalent contour at the time of the first rocket, but sur-
prisingly it has a larger width-to-length ratio (rounder) than at an
earlier time. The one-fourth contour, on the other hand, is much longer
than at R + 28 min and assumes the shape of a spoon. The second probe
rocket trajectory, relative to the ion cloud, shares many characteristics
of the first probe rocket trajectory. It almost touches the one-half

164
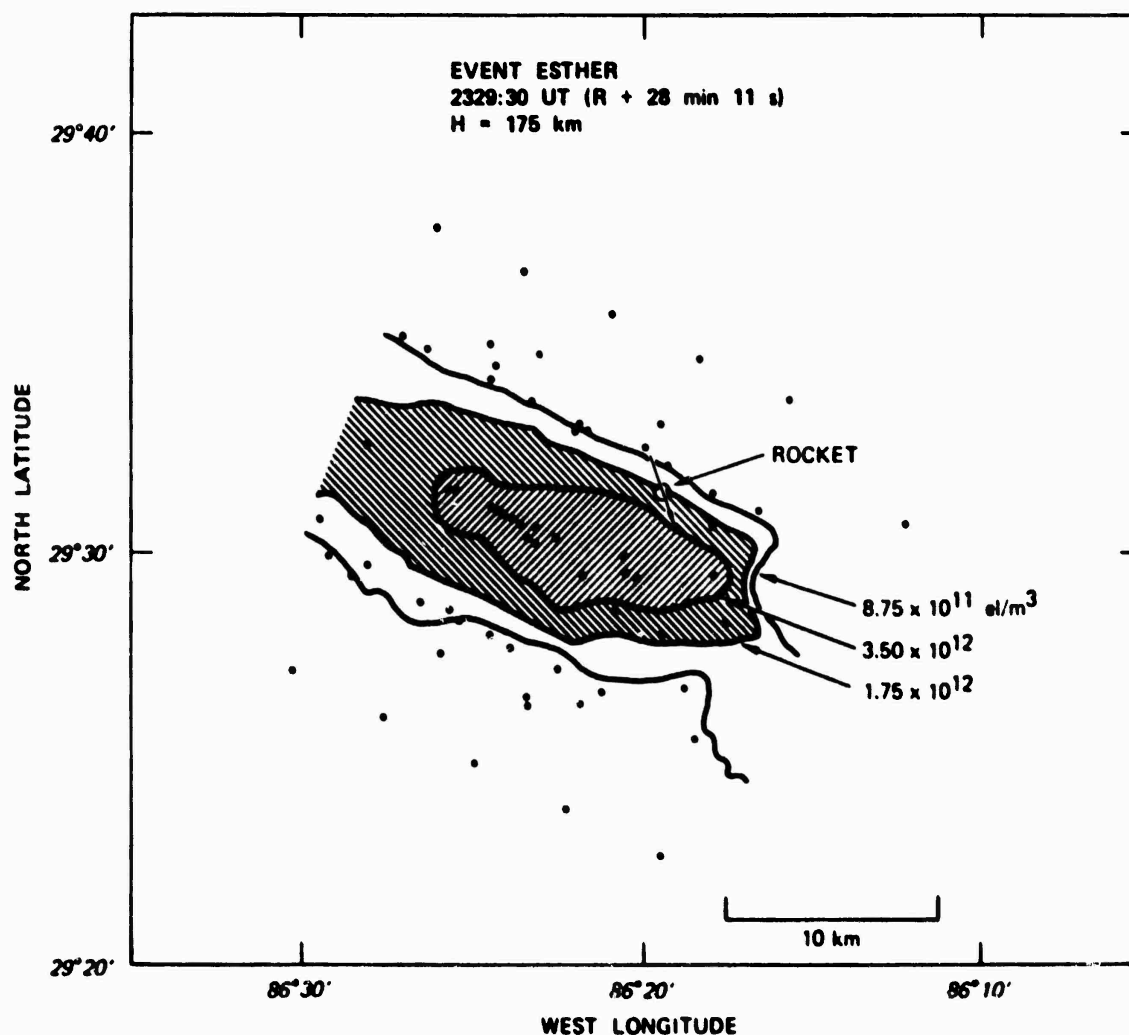
FIGURE 5   EQUIDENSITY CONTOURS ON A HORIZONTAL PLANE AT 175 km —
EVENT ESTHER, 2329:20 UT

contour at H = 160 km, missing the densest part of the ion cloud. The
rocket passes through the trailing or sharp edge of the cloud at about
H = 170 km, and at H = 180 km the rocket is far beyond the trailing edge
of the cloud. It is interesting to note that between H = 170 and H = 180
the rocket probe encountered narrow regions of very high electron density.
The location of these small regions encountered by the rocket corresponds
without doubt to the region where striations developed.

Figures 6 and 7 also show the relation of the transmission experiment
to the ion cloud. In each figure the intersection of the transmission
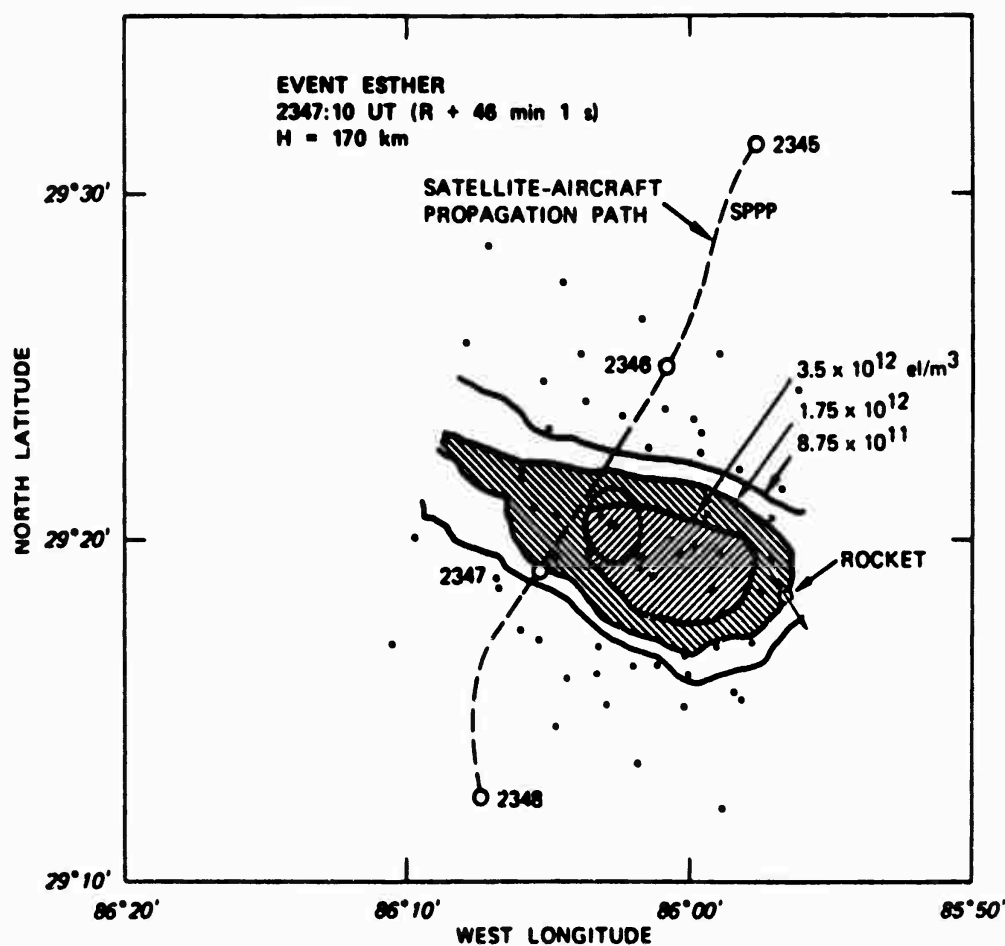
FIGURE 6   EQUIDENSITY CONTOURS ON A HORIZONTAL PLANE AT 170 km —
EVENT ESTHER, 2347:10 UT

path with the horizontal plane at the height of the contours is shown by
the dashed line. Propagation effects were observed between 2346:06 and
2347:18 UT.

The satellite-to-airplane path penetrated the cloud at the time of
onset of propagation effects at an altitude of about 165 km. The raypath
left the cloud at altitude of about 180 km. We see in Figure 7 that the
agreement between the contours derived from radar data and the time of
termination of effects is very good.

166
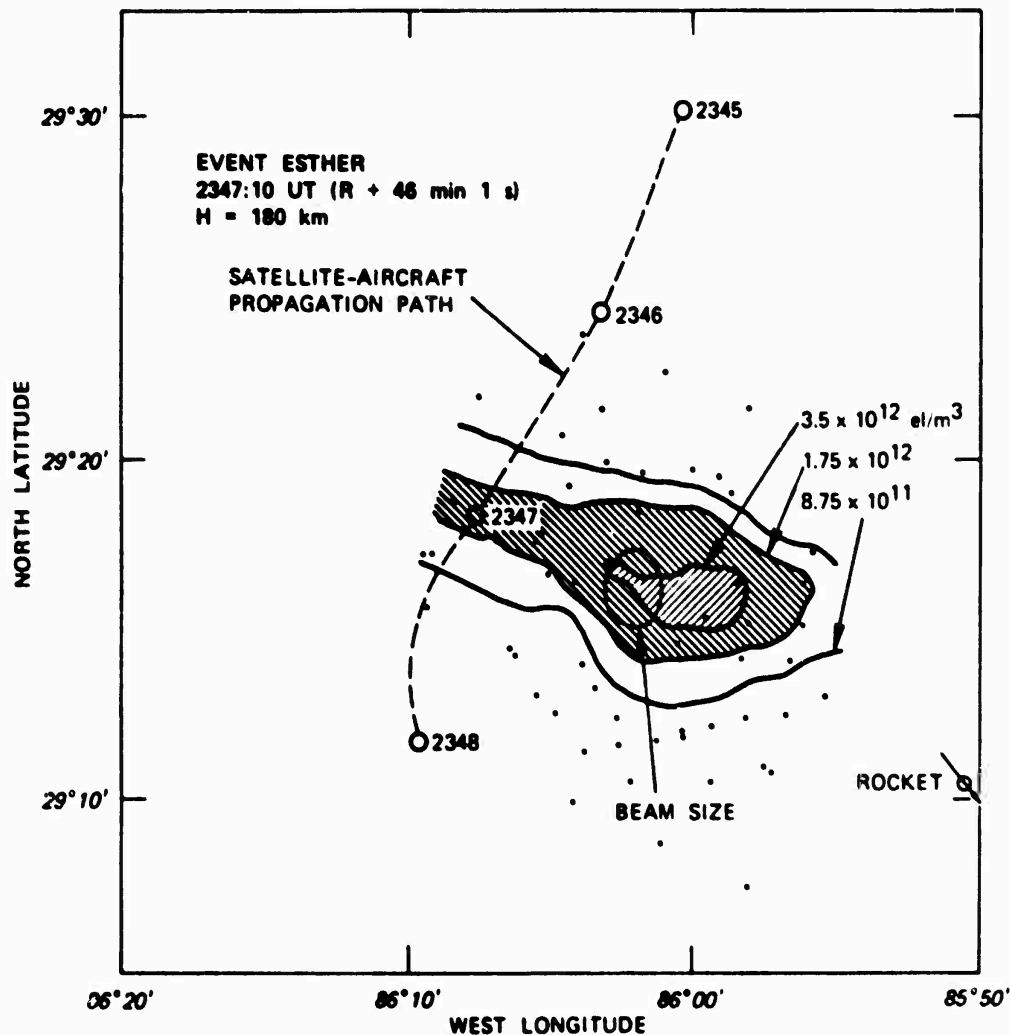
FIGURE 7   EQUIDENSITY CONTOURS ON A HORIZONTAL PLANE AT 180 km —
EVENT ESTHER, 2347:10 UT

C.   Visible Time--0023 UT (R + 1 hr 21 min)

We chose to make a set of contours at a time within the period of
optical coverage that was also interesting for the satellite-to-airplane
communication experiment. This time was 0023 UT. Figures 8 and 9 show
two contour surfaces at altitudes of 160 and 170 km.

The maximum electron density obtained from real-time analysis was
2.4×10^{12} el/m^3, so Figures 8 and 9 show the contours 1.2×10^{12},
0.6×10^{12}, and 0.3×10^{12} el/m^3, again, one-half, one-fourth, and one-
eighth of maximum. These contours show that the ion cloud is very large,
compared to the cloud at the earlier times discussed in the previous
sections.

167
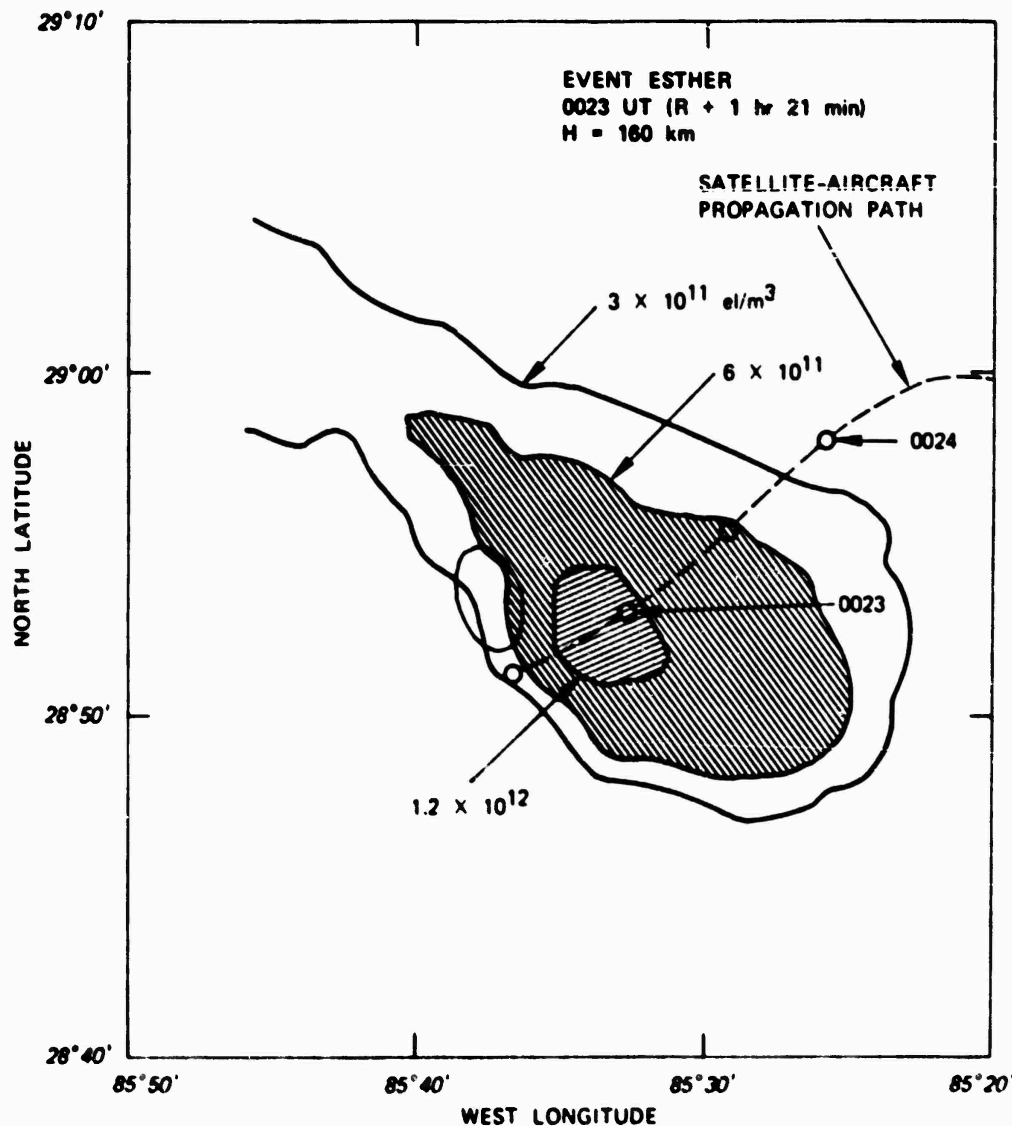
FIGURE 8   EQUIDENSITY CONTOURS ON A HORIZONTAL PLANE AT 160 km —
EVENT ESTHER, 0023 UT

The intersection of the satellite-to-airplane propagation path with
the horizontal planes of Figures 8 and 9 would indicate that propagation
effects should have been observed from about 0022:20 to 0024:00 UT--that
is, the phase shift effects should be maximum for about 100 s at approxi-
mately 0023:00 UT.   ESL observations are not well defined in terms of
start and finish times, but the phase curve shows effects starting at
0022:43 and ending at 0023:38 UT.   These start and finish times corre-
spond to times in the satellite propagation path that are within the
6×10^{11} el/m^3 contour in Figures 8 and 9.
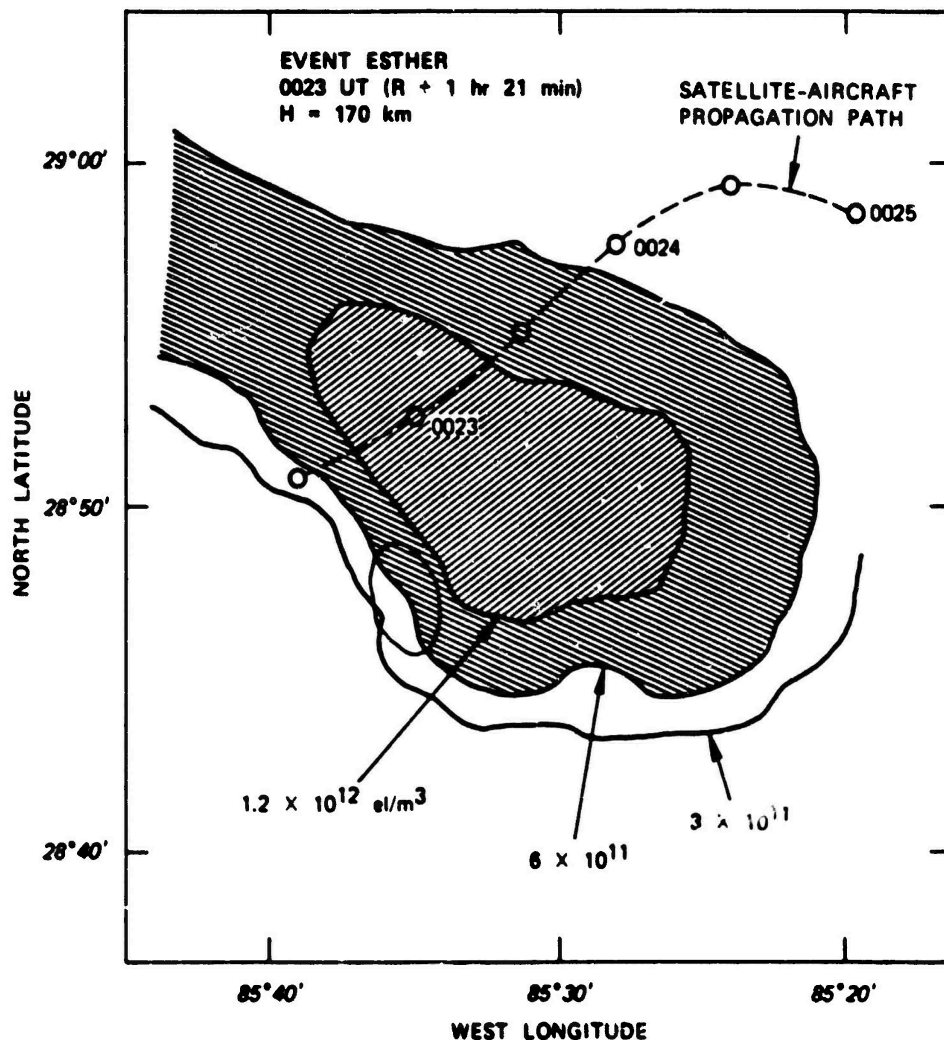
FIGURE 9   EQUIDENSITY CONTOURS ON A HORIZONTAL PLANE AT 170 km —
EVENT ESTHER, 0023 UT

D.   Vertical Electron-Density Distribution

At the time the contours shown in the previous sections were calcu-
lated, the maximum electron density corresponding to each height was also
calculated. Figure 10 shows the vertical electron-density distribution
obtained every 5 km, for the three periods of time that were examined in
detail.

The radar beam was not pointed along the magnetic field, so the
densest field-aligned part of the cloud was not sampled at all heights,
and that seems to be the reason for the apparent discontinuities in the
profile corresponding to R + 46 min.

169
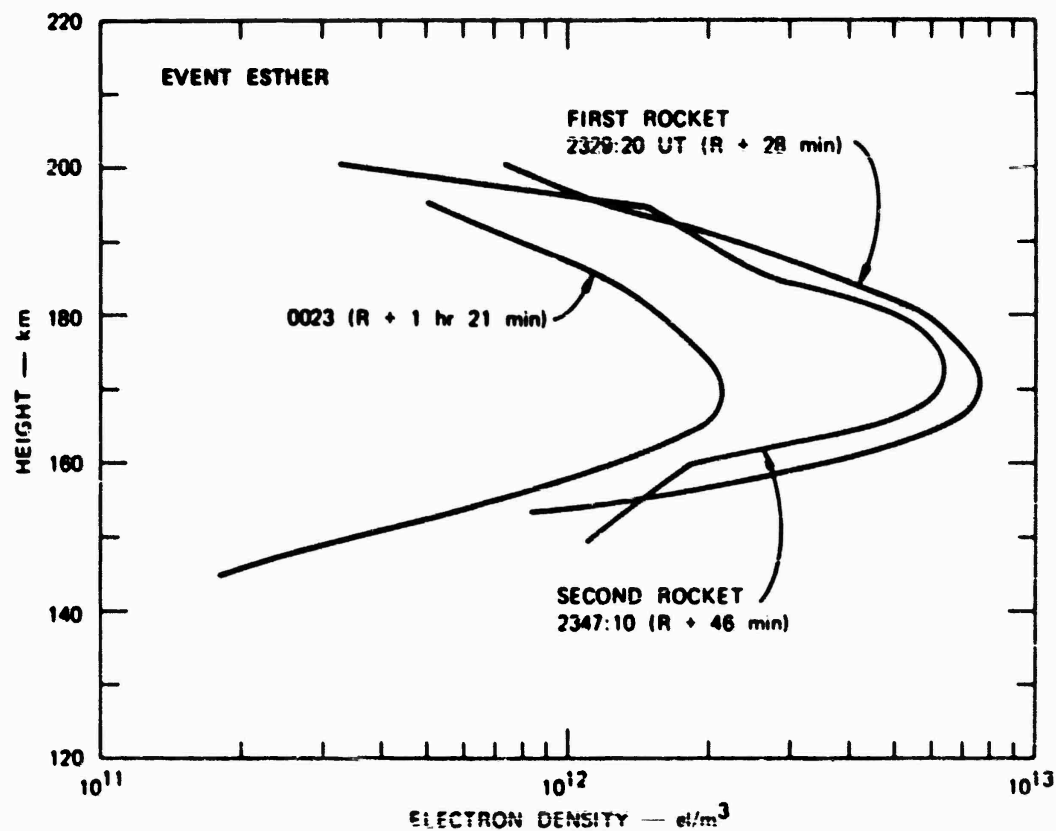
FIGURE 10   VERTICAL ELECTRON-DENSITY DISTRIBUTION — EVENT ESTHER

The altitude of the center of the ion cloud changed greatly during the first 28 minutes, from 189 km at release time to 170 km at R + 28 min, but the change between R + 28 min and R + 1 hr 21 min is very small (less than 2.5 km). The center of the cloud even seems to rise somewhat between R + 28 min and R + 46 min, but this change of altitude is less than the altitude variation of data points (5 km) obtained to construct the curves of Figure 10.

The vertical spread of electron density cannot be meaningfully compared between R + 28 min and R + 43 min because of the discontinuity in the vertical profile at R + 43 min. However, the vertical distribution at R + 1 hr 21 min is broader than the other two distributions. The widths of the vertical profile (R + 1 hr 21 min) at one-half and one-fourth of

170

the maximum electron density are consistently larger than the widths of the other two curves at corresponding densities.

V EVENT FERN

A. First Rocket--2327 UT

The maximum electron density of the ion cloud obtained in the field at this time was not a well defined quantity because the measurement set had a spread of points from 5.0×10^{12} el/m^3 to 9.6×10^{12} el/m^3. If the latter number is chosen, the contours drawn in Figures 11 and 12 correspond to one-half, one-fourth, one-eighth, and one-thirty-second of the maximum (the one-sixteenth value is missing in the sequence).

The contours presented in Figure 11 at an altitude of 150 km (altitude of the cloud as given by the real-time tracking results) show a compact and well defined cloud whose maximum electron density is approximately 4.4×10^{12} el/m^3. The rocket position and horizontal motion seems to indicate that the rocket is under the densest part of the ion cloud and that probably it has already missed the interesting part.

As we draw contours at higher altitudes, the combination of magnetic field dip and rocket trajectory indicates that the probe will move along a surface of constant electron density from west to east and emerge at the front of the ion cloud.

The contours of Figure 12 at an altitude of 175 km completely change the interpretation deduced from Figure 11. The equidensity contours open on the eastern side of the cloud, and very high electron densities appear. In Figure 12 (H - 175 km), the rocket is inside the 2.4×10^{12} el/m^3 contour, and at an altitude of H - 185 km (contours not shown in this paper) the contour 4.8×10^{12} el/m^3 expands up to the probe trajectory.

The electron densities encountered by the rocket, on the other hand, reach a maximum at about 150 km. Because of this discrepancy, it is useful to make a comparison between the electron densities measured in situ and the electron densities that, according to the radar data, should have been measured. This comparison is shown in Figure 13. The electron

171
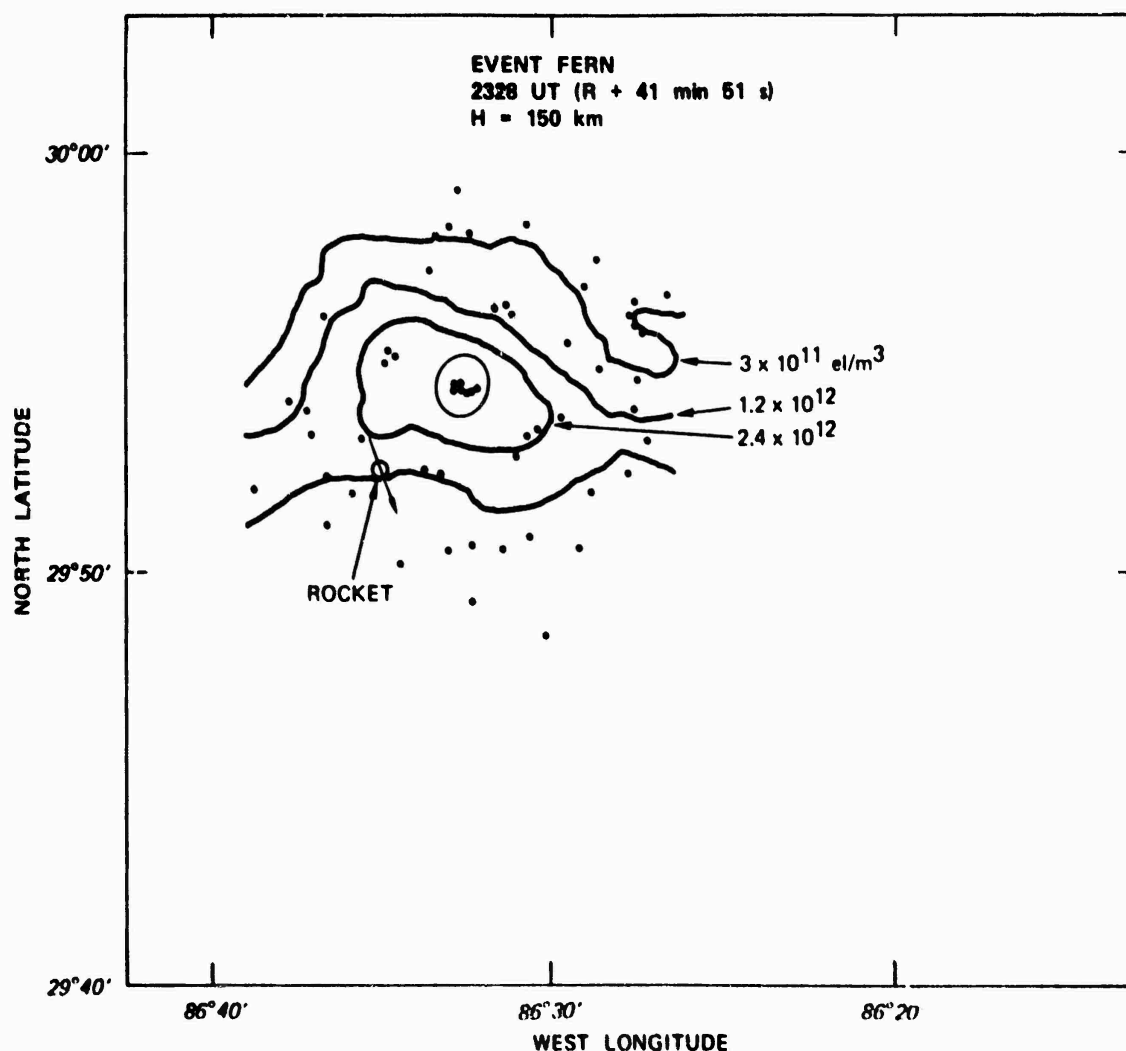
FIGURE 11   EQUIDENSITY CONTOURS ON A HORIZONTAL PLANE AT 150 km —
EVENT FERN, 2328 UT

densities of both sources agree very well up to an altitude of 160 km.
Above 160 km the rocket data show irregular variations in electron den-
sities at levels below 10^{12} el/m^3. The radar data, on the other hand,
show increasing electron density, and the ratio between the two densities
reaches a maximum of seven at 185 km.

The difference between the two measurements is attributed to a focus-
ing effect that occurs when the EM energy travels along and nearly parallel
to the striations of the Ba-ion cloud. This anomalous type of propagation

172
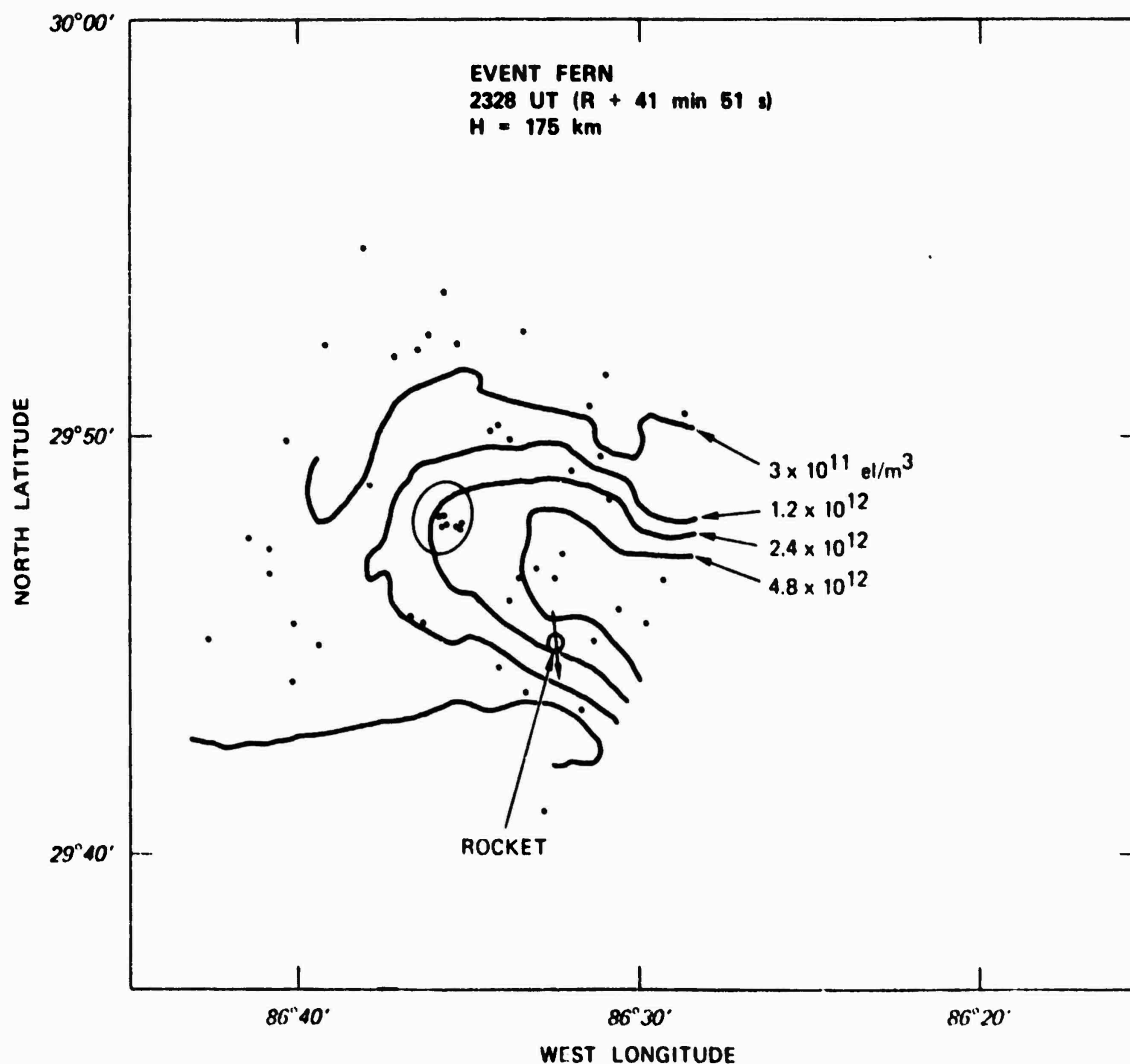
FIGURE 12   EQUIDENSITY CONTOURS ON A HORIZONTAL PLANE AT 175 km —
EVENT FERN, 2328 UT

has been observed in the past, during the SECEDE experiments, when a Ba-
ion cloud was near the magnetic zenith of the AN/FPS-85. The presence
of focusing at the time of SECEDE was inferred from the fact that the
measured returns showed an unreasonable increase in electron densities.
The STRESS experiment, on the other hand, shows a comparison of radar
data with local measured electron densities, and the results might be
regarded as solid experimental evidence that an apparent increase in elec-
tron density due to a focusing effect does in fact exist.
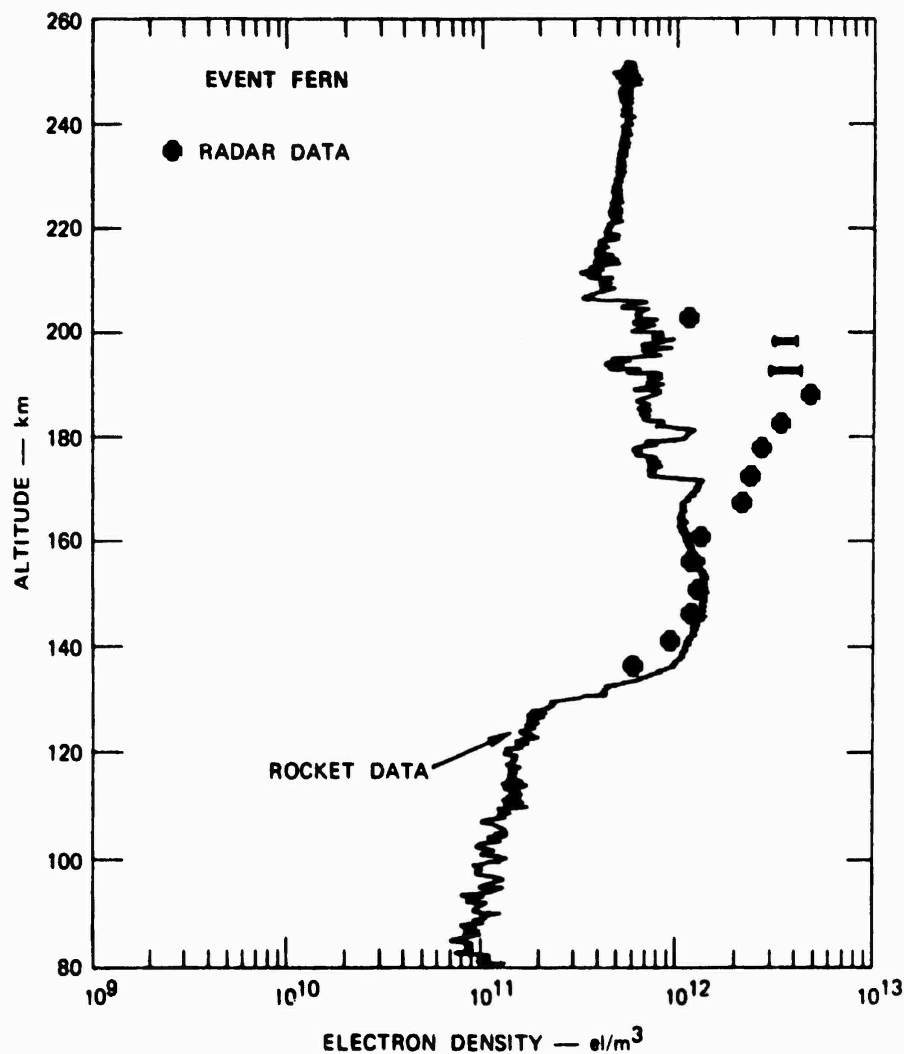
FIGURE 13 COMPARISON OF ELECTRON DENSITIES MEASURED BY THE PROBE ROCKET
AND THE RADAR, ALONG THE ROCKET TRAJECTORY — EVENT FERN

The ion cloud at the time of the rocket flight has developed stria-
tions, as shown by the rocket data in the southern and eastern side of
the Ba cloud (see Figures 11 and 12). The radar is located north and
slightly east of the cloud, and to make measurements within the 4.8×10^{12}
el/m^3 contour at an altitude of 175 km (Figure 12), the radar beam travels
through and nearly parallel to the striations at lower altitudes (140 to
160 km). As a result, the factor F^2 in Eq. (15) acquires large values
over a rather wide portion of the barium cloud.

174

The mechanism by which propagation parallel to field-aligned structure produces focusing has not at this point been described in detail. An understanding of its nature is expected to yield useful information about the gradients existing in the striations. It is interesting to note that propagation through a smooth cloud would produce the opposite effect--that is, the smooth cloud acts as a divergent lens.

B. Vertical Electron Density Distribution

Event FERN was examined in detail at the time of the first probe rocket and at two other times--R + 1 hr 9 min and R + 1 hr 46 min. The vertical electron-density distributions obtained are shown in Figure 14. The data must be regarded with some caution because of the problems encountered during the tracking of Event FERN.
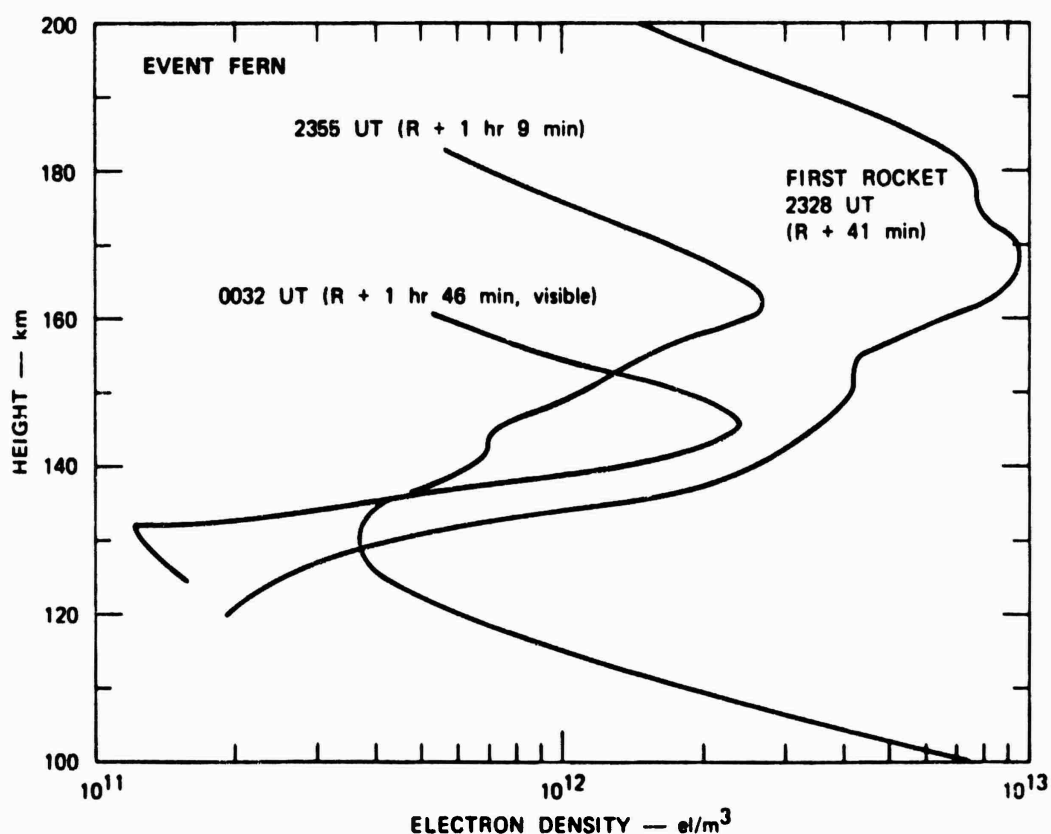
FIGURE 14   VERTICAL ELECTRON DENSITY DISTRIBUTION — EVENT FERN

175

The vertical profile at R + 41 min, as discussed in the previous section, is influenced by focusing, and the maximum electron density might not actually be as large as 9×10^{12} el/m^3, as indicated in Figure 12. The profile at R + 1 hr 9 min is taken when the body of the ion cloud is in the magnetic zenith; however, the striated part of the cloud is east of the magnetic zenith so that the profile of Figure 14 is probably correct. The profile obtained at R + 1 hr 46 min is not affected by focusing; on the other hand, the radar scanning may have been a region of the cloud that did not contain the highest electron density. The contour maps obtained at this later time describe the center part of an S-shaped cloud. The vertical distribution shown in Figure 14 shows a narrow vertical extent of the cloud that might be described as pancake-shaped.

The three altitudes corresponding to the peak electron densities are plotted as a function of time in Figure 15 and compared to the time variation of the tracked point obtained in real time. It should be recalled that soon after the release, the cloud track was established smoothly; however, after 20 or 30 minutes, strong echoes appeared at low altitudes which, combined with the fast downward velocity and the approach of the cloud to the magnetic zenith, made the operator doubt the quality of the track. The altitude of the cloud was then manually reset at R + 56.5 min and the track was reestablished. In spite of this, the strong echoes at low altitudes persisted and the real-time feedback was not good enough to provide confidence that the track was free from contamination. Thus, the radar was manually reset at various times, following different criteria.

The altitudes at 2355 and 0032 UT obtained from data of Figure 14 and shown in Figure 15 are consistent with the later time history of the tracked point. The altitude at 2327 UT is inconsistent with all the other data of Figure 15, and the altitude of the maximum point on the plot might be caused by focusing effects.

One possible explanation for the development of FERN is that the release split in two parts, with one part descending very fast to E-layer altitudes and a second part remaining at an altitude of over 170 km for at least one hour.

176
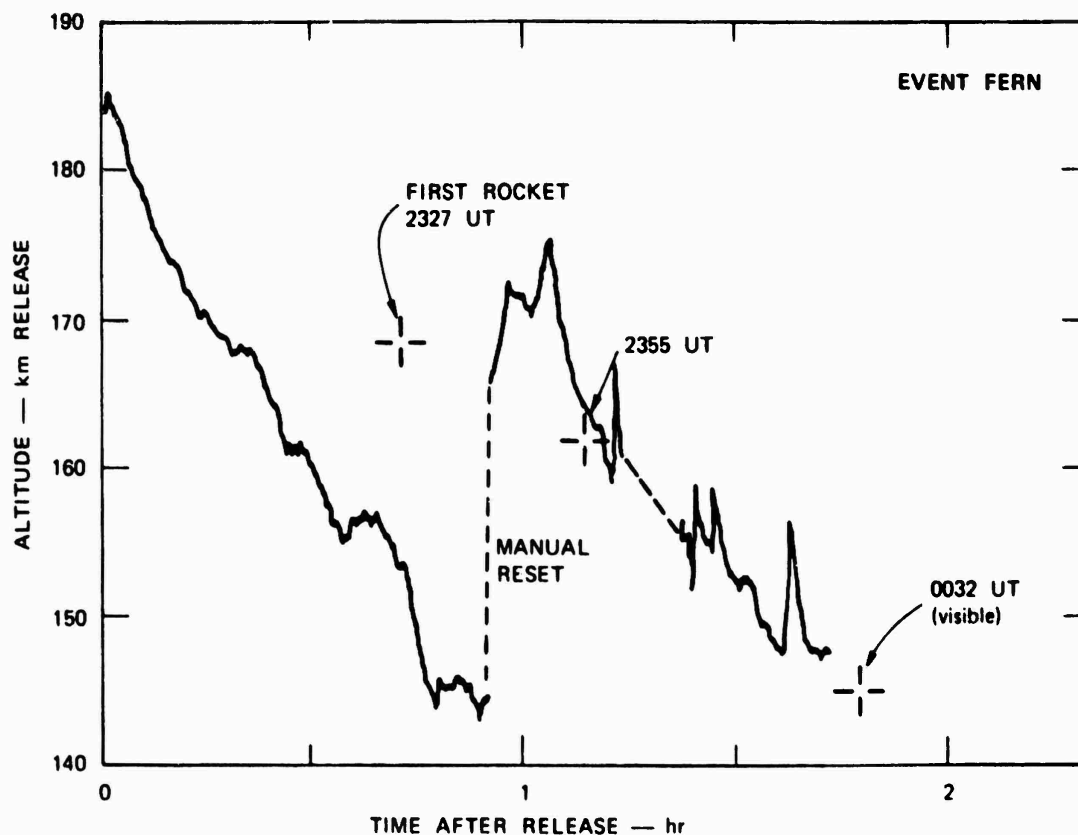
FIGURE 15   ION CLOUD ALTITUDE vs TIME OBTAINED IN REAL TIME — EVENT FERN

The existence of the fast-falling portion of the cloud is supported by the ionosonde data, which show an echo approaching the radar with a velocity that is consistent with the first portion of the real-time curve of Figure 15. The second portion of the ion cloud which later became visible, would be related to the height variation between R + 58 min and R + 2 hr.

The electron density profiles of Figure 14 also show electron densities below 130 km at R + 1 hr 9 min. This portion of the electron density profile is shown dashed to emphasize the doubtfulness of this result. Radar returns corresponding to low altitudes were received, and examples are shown in Figure 16. Whether these close range echoes are related to the mechanism of incoherent scatter is not known at this time, and the cause of their presence is a problem that should be examined. A portion of the FERN ion cloud falling to E-layer altitudes is the only explanation that would support high electron densitites at altitudes below 130

177

EVENT FERN

R + 1 hr 30 min 56 s

1 hr 30 min 45 s

1 hr 0 min 6 s

1 hr 0 min 0 s

0 hr 50 min 5 s

0 hr 50 min 3 s

IONOSPHERE

10 dB

150   200   250   300   350   400
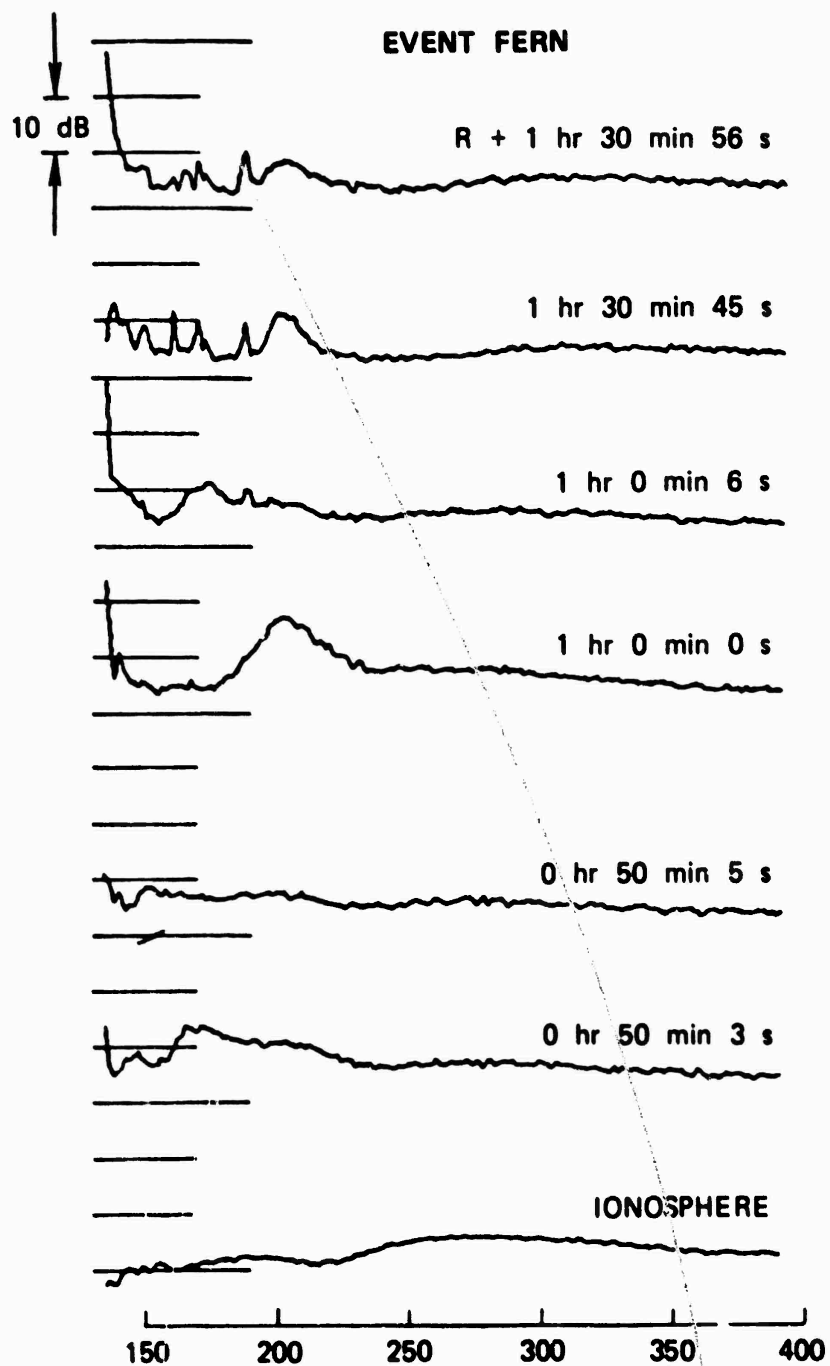
FIGURE 16   SAMPLE RADAR RETURNS OBTAINED AT VARIOUS TIMES — EVENT FERN

178

km; however, it would be interesting to see if the high electron densities obtained by the incoherent-scatter interpretation are maintained at a height of 100 km when the loss processes are taken into consideration.

C. Motion of the Ion Cloud

Event FERN was the only release of the STRESS series that caused confusion in real-time tracking in the field. After the first 30 minutes it was difficult to determine whether the radar was tracking the ion cloud properly of not. It is of interest then to reconstruct the motion of the ion cloud. If it divided in two sections, the section that stayed at high altitudes and later became visible is the one of interest to us.

To find the motion of the barium cloud we constructed contours of the scanned part of the cloud at a few different altitudes about every 5 minutes, and then we superimposed the contours to find the overall extent of the cloud and its motion. Figures 17 and 18 are two examples that illustrate the procedure followed and the problems encountered.

Figure 17 shows the contours obtained at 0018 UT and 150 km. The measurements, in the 2 minutes of data used for these contours, were taken in a region fairly close to the densest part of the Ba-ion cloud. Figure 18, on the other hand, uses data from a period in which manual reset was being done. Data were taken first in the rectangular pattern shown in the upper left-hand side of the picture and then the radar was pointed to the area in the lower right hand-side where more measurements were made.

When Figures 17 and 18 are overlaid on each other, even though the contours look different a good agreement is found if the 2.4×10^{12} el/m^3 contour of Figure 18 is shifted to the middle of the corresponding contour in Figure 17. With a small rotation, most of the 1.2×10^{12} el/m^3 contour of Figure 17 can be made to agree with the corresponding contour of Figure 18. Thus the shift, the rotation, and the time between the contours are the means we used to investigate the motion of the ion cloud. The rotation is clockwise when looking down to the surface of the earth and it is a feature continuously observed between 0018 UT and 0100 UT.

179
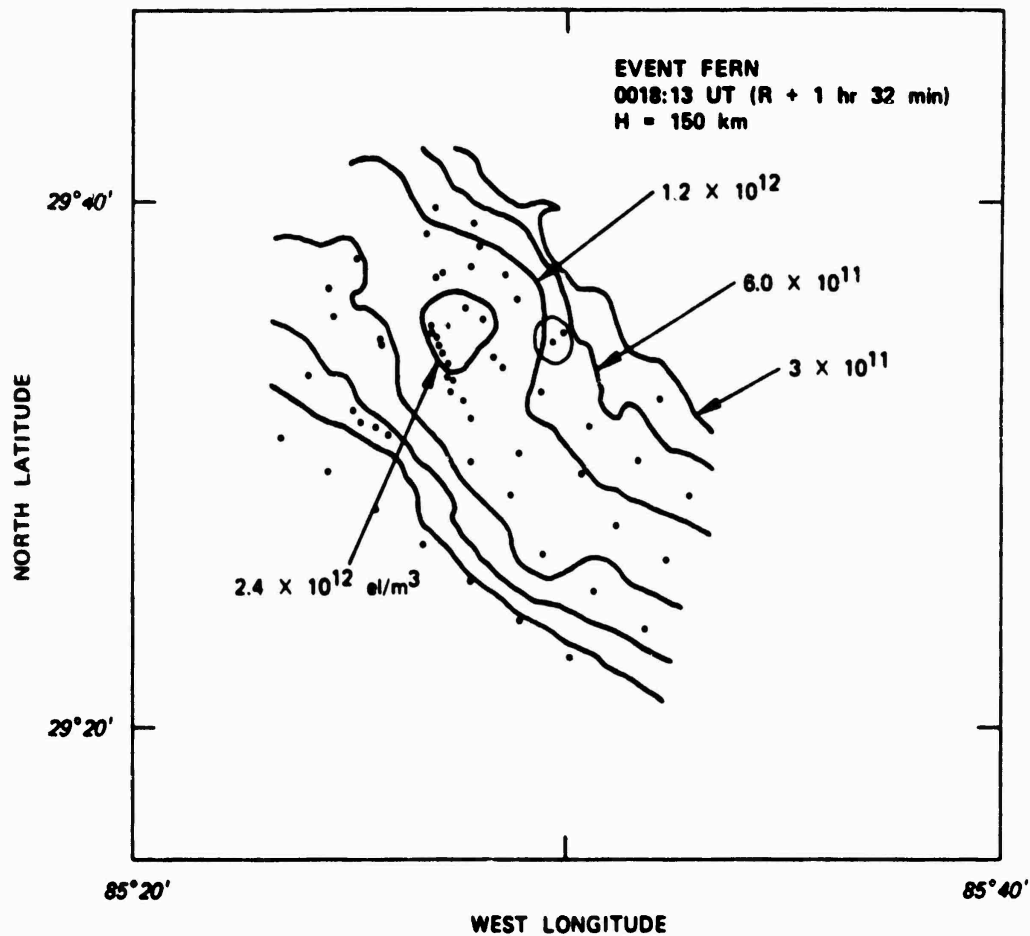
FIGURE 17 EQUIDENSITY CONTOURS AT 150 km — EVENT FERN, 0018 UT

Figure 19 summarizes the motion of the FERN ion cloud obtained from this analysis for the altitude of 145 km. The magnetic field line through the release point was traced to 145 km, so we can see that the motion of the Ba-ion cloud across the magnetic field was to the east and to the south. Any northward component is due to a sliding of ionization down the magnetic field lines.

D. Correlation with Photography (0031:40 UT)

The correlation of radar measurements with photography is interesting in itself, and in the case of FERN it has the additional interest of revealing which part of the ion cloud was being observed at any given time.
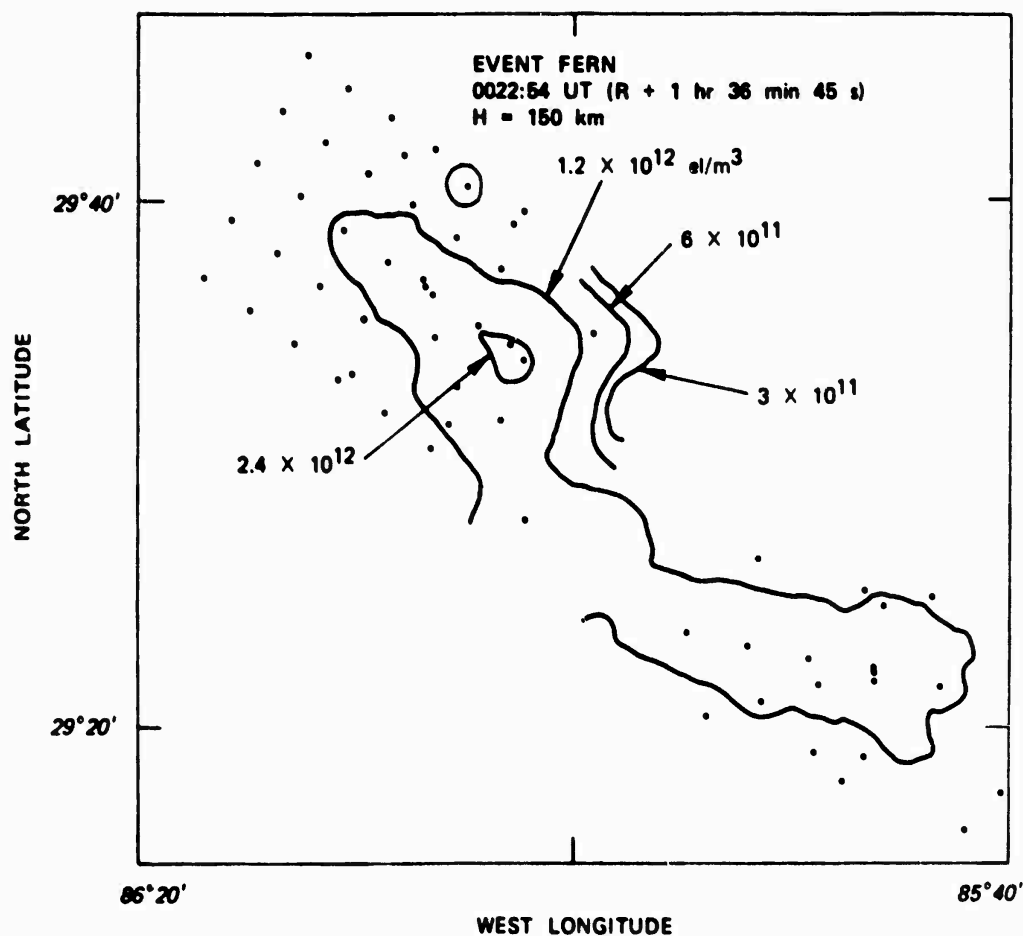
FIGURE 18   EQUIDENSITY CONTOURS AT 150 km — EVENT FERN, 0023 UT

The correlation was done through the technique of obtaining contours of constant line-integrated electron density along the radar beam and also contours of the maximum electron densities encountered along the radar beam.

Figure 20 shows the correlation of a picture of the FERN cloud taken by TIC from C-6 at 2331:40 UT with line-integrated electron density contours. The small open circles in this picture represent the stars used to position the overlay on the picture itself. The large open circles represent the approximate size of the radar beam, and the dots are the points to which the radar was pointed in the set of measurements used for the contours.

181
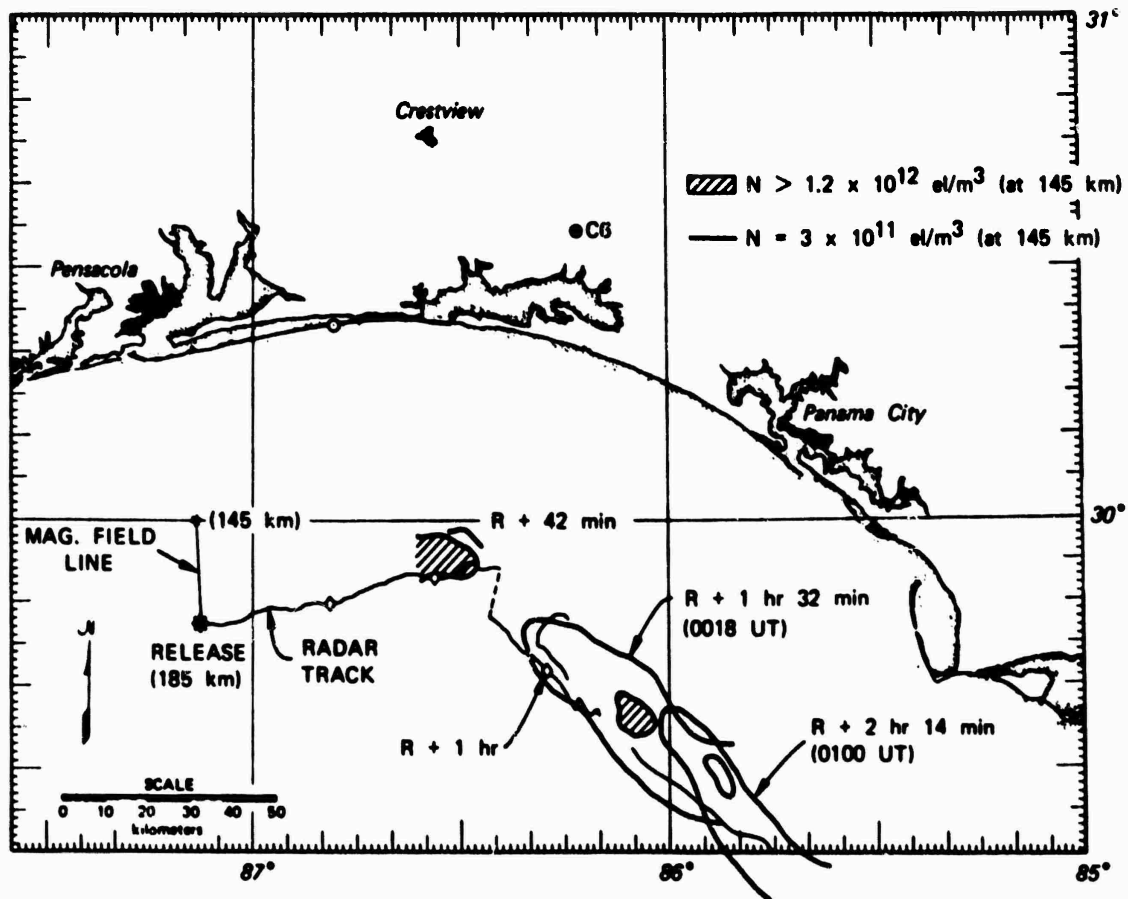
FIGURE 19   RECONSTRUCTED MOTION OF ION CLOUD GIVEN BY EQUIDENSITY CONTOURS COMPARED WITH REAL TIME RADAR TRACK — EVENT FERN

The contours of 2×10^{16} el/m^2 follow very well a large structure of the ion cloud that extends to the lower left-hand side of the picture. This is the eastern portion of the cloud (lower left-hand side), where the sun was already setting. The small portion of the 4×10^{16} el/m^2 contour has the appearance of being a portion of a contour that would encircle the brightest part of the cloud.

Figure 21 shows the maximum electron density contours associated with each pointing direction, and the resulting contours are similar to those of Figure 20. The four contours below the maximum density contour of Figure 20 agree in great detail with the corresponding contours of Figure 21.

182
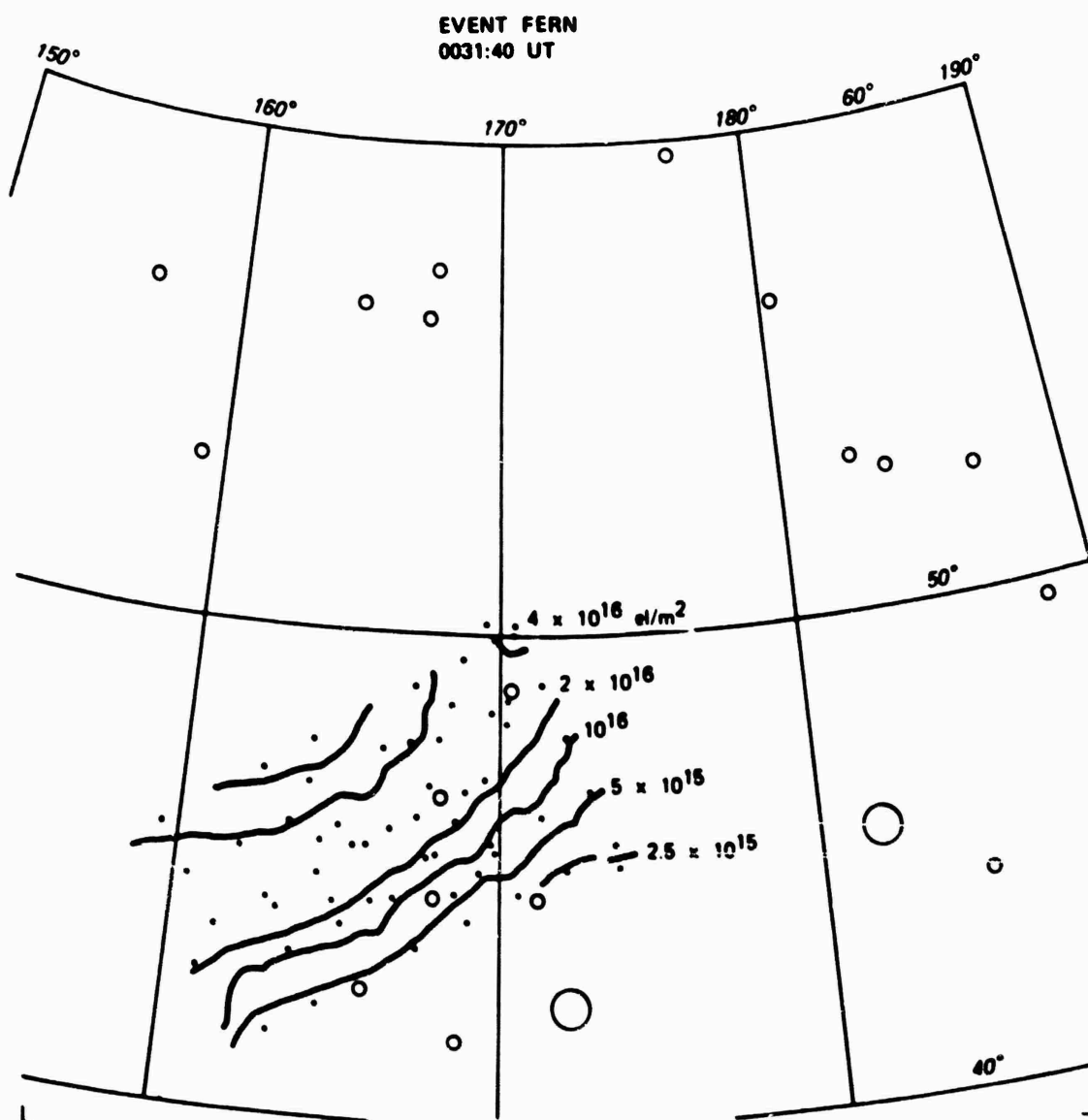
FIGURE 20   CORRELATION OF RADAR MEASUREMENTS WITH PHOTOGRAPHY —
EVENT FERN.   Radar measurements are given by line-integrated electron
density contours.
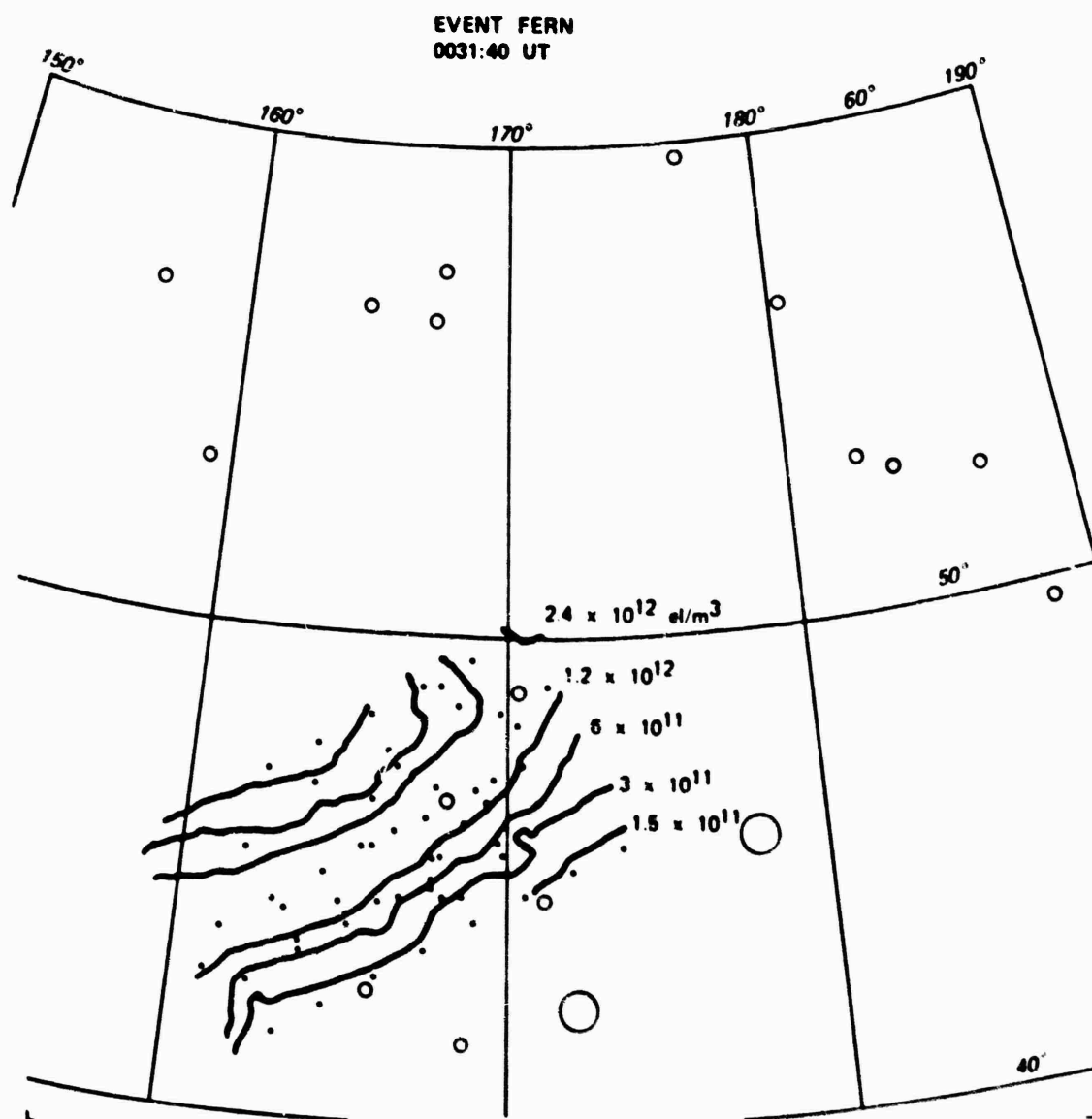
FIGURE 21   CORRELATION OF RADAR MEASUREMENTS WITH PHOTOGRAPHY —
EVENT FERN. Radar measurements are given by equidensity contours of
maximum electron density encountered along line of sight.

184

The upper portions of the contours, however, have an important difference: they have the same shape but they are displaced by a factor of 2. For instance, the lower portion of the 10^{16} el/m^2 contour agrees with the 6×10^{11} el/m^3 contour, and the upper portion of the 10^{16} el/m^2 contour agrees with the 3×10^{11} el/m^3 contour. Thus we may say that the part of the cloud below the bright center structure has a depth of the order of 17 km, where the part of the cloud above the bright center structure has a depth of the order of 34 km.

VI   SUMMARY

At present the radar data analysis is not completed, and this paper constitutes only a progress report. We have developed the tools to make three-dimensional descriptions of the ion clouds by stacking a series of equidensity contours at various altitudes. This model will be useful to correlate the radar measurements with other related measurements (rocket and satellite-airplane transmission) so we can understand and interpret all the results from a better perspective. For instance, we were able to define the trajectories of the ESTHER probe rockets in relation to the ion cloud, so their measurements can be put to very effective use. The same understanding can be attained in Event FERN, except that in this case the comparison obtained will also be helpful in interpreting an anomalous type of propagation encountered by the radar.

Thus, the interpretation of radar data coordinated with related experiments will provide detailed descriptions of the ion cloud at specific times, which in turn will be helpful to theoreticians in understanding the development of the ion clouds. Further usefulness is expected to be found by system-oriented efforts such as the satellite-airplane experiment, which will benefit from a detailed description of the propagating medium.

The radar data, through the use of the equidensity contours obtained, can also provide understanding of the development in time of features of the ion clouds--for example the motion of the main portion of the FERN

185

ion cloud. Thus method can also provide a description of the splitting
of the cloud through analysis of data in the first 30 minutes of the
cloud's life.

The evolution of size, length, and thickness along and across the
magnetic field is interesting because it will yield a clue to the winds
and electric fields present, particularly in the cases in which the re-
lease was done before twilight when optical observations were not pos-
sible.

Late-time cloud development is also a matter of interest because for
the first time we now have radar observations of the size of the clouds
and the electron densities present.

The correlation of line-integrated electron density contours with
photography lends a great deal of confidence in the approach employed in
the radar data analysis and in the interpretation of the data, and it
might be developed into a yardstick useful to quantitative analysis of
optical data.

ANALYSIS OF IONOGRAMS

N.J.F. Chang

SRI International
Menlo Park, California

ANALYSIS OF IONOGRAMS

N.J.F. Chang

SRI International
Menlo Park, California

ABSTRACT

Anomalous radar returns seen on ionograms following iono-
spheric barium releases are analyzed to determine their origin
and their interpretation. Two types of echoes are identified;
one type originates from the barium cloud and the other type
from layers formed by the descent of barium ions into the E-
region. A review is made of sporadic-E literature because
some of the explanations of the origin and reflection mecha-
nisms proposed for sporadic-E appear to be applicable to barium
echoes. Data from past barium releases were also reviewed to
supplement the STRESS data base. The findings indicate that
reflection from an overdense layer or target is not the cause
of the barium-associated returns. Thus, the maximum frequen-
cies of the returns cannot be interpreted as a maximum plasma
frequency. Gradient reflection and scatter from weak or strong
irregularities are both plausible mechanisms for both types of
echoes. The characteristics of the E-region returns and their
likely cause (compression due to wind shear) suggest that these
layers are thin with sharp boundaries and a rough underside.

I INTRODUCTION

A. General

This paper describes the results obtained from operation of an iono-
sonde during the Pre-STRESS and STRESS experiments conducted at Eglin,
Florida during the winter and spring of 1976/1977. The analysis is di-
rected at interpretation of anomalous returns seen on ionograms obtained
after each barium release. These returns are shown to originate from
the barium ion cloud and from layers created from barium ions migrating
to the E-region.

The nature of radio waves reflected or scattered from barium layers
is examined in light of sporadic-E theories and experimental results.
In addition, mechanisms proposed for the generation of sporadic-E layers
are assessed to determine their applicability to barium layers.

B. Background

On 1 December 1976 and during February and March 1977, six iono-
spheric barium releases were made, each on one of the six late afternoons
or evenings near Eglin AFB, Florida. The releases were made for the pur-
pose of generating a region of structured ionization that would occlude
transmissions between an aircraft and a synchronous satellite. These
experiments, sponsored by the Defense Nuclear Agency (DNA) in cooperation
with the Air Force Electronics System Division (ESD) and the Air Force
Avionics Laboratory (AFAL), were conducted to evaluate satellite communi-
cation links under conditions that simulate many aspects of a post-nuclear-
burst environment.

An integral part of the experiment was the FPS-85 radar operating
in an incoherent-scatter mode. This instrument was tasked to track the
ion cloud (in order to properly position the aircraft with respect to
the satellite and ion cloud) and to provide diagnostic information on
electron densities within the cloud.

In support of the FPS-85 radar, SRI operated a vertichirp ionosonde
to provide $f_o F2$ measurements for calibration of the FPS-85 radar. Addi-
tional objectives of the vertichirp radar were to obtain electron density
profiles of the background ionosphere (used to calculate ambient Pedersen
conductivities for the six barium releases), and to serve as a real-time
monitor of the state of the ionosphere. Unfortunately, virtually no
ionospheric data were obtained below 200 km, so it has not been possible
to calculate the desired conductivities.

It is not known why ionospheric returns, which would normally origi-
nate from the E-region in the late afternoon or evening, are absent below
200 km. However, a number of possible reasons can be cited: (1) In the
evenings the noise background was fairly high between the lower-frequency

190

limit of the sounder and about 1 or 2 MHz, thus obscuring any ionospheric returns that might have existed in this frequency range; (2) although the lower-frequency limit of the vertichirp was 0.5 MHz, on most ionograms the actual limit appeared to be about 2 MHz; (3) the sensitivity of the vertichirp at low frequencies was poor; and/or (4) E-layer critical frequencies were below the lower limit of the system.

Ionospheric returns below 200 km were also absent during SECEDE II and HAPREX, which required assuming a density model for that region in order to generate Pedersen conductivities. This exercise was not repeated here because actual E-region data can be obtained from the FPS-85 radar or the rocket probe measurements. In addition, since the conjugate ionosphere is believed to play at least as important a role in cloud dynamics as does the sunlit ionosphere, it made little sense to calculate conductivities from an E-region model when no conjugate measurements were made.

In terms of its primary objective--obtaining f_oF2 values for the FPS-85 radar--the vertichirp operated successfully on all six Pre-STRESS and STRESS releases. On BETTY, equipmental problems caused a loss of data shortly after release (0002 UT) until the problem was corrected at 0100 UT). Good data, however, were obtained prior to the vertichirp outage and after 0100 UT.

A somewhat unexpected bonus of the vertichirp operation was the observation of intense and persistent E- and F-region returns that are believed to originate from the barium ion cloud because of their occurrence in approximately the same time and range space as the cloud. Table 1 summarizes the barium signatures seen on the Pre-STRESS and STRESS ionograms. Intense E- and F-region echoes were observed on Event FERN. The E-region echoes were particularly strong, indicating returns from frequencies as high as 18 MHz. For the other three releases (CAROLYN, DIANNE, and ESTHER) weak F-region traces lasting several minutes were observed. No barium-associated echoes were observed for Event BETTY because of an untimely equipment failure during the period when returns from the barium cloud would have occurred. When the vertichirp resumed operation at R + 68 min, a weak sporadic layer was observed between 2 and 4 MHz. Although the association of this trace with the barium cloud

191

Table 1

SUMMARY OF BARIUM SIGNATURES SEEN ON PRE-STRESS AND STRESS IONOGRAMS

Event	First BA Echo	Last BA Echo	Duration (min)	Maximum Frequency (MHz)	Remarks
ANNE	R + 13.7 min (2321 UT)	R + 97.7 min (0048 UT)	84	15	Strong, continuous F-region echoes
BETTY	No data	No data	No data	No data	
CAROLYN	R + 17.8 min (0012 UT)	R + 29.8 min (0024 UT)	12	10	Weak F-region echoes
DIANNE	R + 44.9 min (0046 UT)	R + 72.9 min (0114 UT)	28	9	Weak F-region echoes
ESTHER	R + 17.8 min (2319 UT)	R + 20.8 min (2322 UT)	3	10	Weak F-region echoes
FERN	R + 12.8 min (2259 UT)	R + 213.8 min (0220 UT)	201	18	Strong, continuous E- and F-region echoes

192

cannot be ruled out, we believe that this signature was not related to the barium cloud because ionograms on several non-release days had similar echoes at similar times. We feel, however, that had the vertichirp been operational throughout the times of interest F-region returns from BETTY would have been observed.

Although barium echoes were also observed during other barium release series (SECEDE II and III), the STRESS results were particularly interesting for the following reasons: (1) The returns for FERN showed a clear downward migration of the reflecting layers, thus implying that Ba ions moved down to the lower E-region; and (2) the maximum frequency of the E-region returns for FERN was 18 MHz at R + 81 min. The significance of these results is not clear, since it is difficult to accept critical frequencies this large at late times.

Previous reports of barium-associated returns on ionograms [1-5] for the most part described the observations but made no attempt to explain the nature of the reflecting layers or the significance of the returns. Thus, the questions raised concerning the nature of the reflecting layers (image or Ba ions) and the interpretation of the critical frequencies have not hitherto been addressed.

This paper will be concerned primarily with the interpretation of the barium-related returns seen on the ionograms. Of particular interest are the interpretation of the barium returns in terms of peak densities, the origin of the apparent barium-cloud-related sporadic-E echoes, and the possible interaction of the barium cloud with underlying layers. Since the barium returns bear such a close resemblance to sporadic-E returns, a review of the literature (Section II) was conducted to determine the relevance of previous work to the present study. It was found that the mechanism believed responsible for midlatitude sporadic-E (compression of metallic ions by horizontal wind shears) plays a major role in creating the reflecting Es layers seen on the ionograms. Furthermore, wind shear may have played a role in Event FERN. In addition, the nature of sporadic-E reflection of radio waves appears to be applicable to the Ba traces. These results will be discussed in Section III, with the summary and conclusions following in Section IV.

II REVIEW OF MIDLATITUDE SPORADIC-E LITERATURE

Sporadic-E is a term used to describe a distinctive trace on iono-
grams in the 90-to-120-km height regime. At midlatitude these traces,
characterized by a relatively height-independent echo of a transient
nature, are normally quite distinct from the E-region returns. At times
the maximum frequency returned from sporadic-E layers can be much greater
than the returns from any of the other layers. Sometimes the sporadic-E
layer is opaque and partially or completely blankets anything above it.
On other occasions the upper layers appear to be unaffected by the under-
lying sporadic-E layers. Retardation near the maximum frequency of the
Es trace is sometimes present, implying that the layer is relatively thick
with a well defined peak electron density. On other occasions the trace
is narrow and shows no retardation, suggesting reflection from a thin layer
or from a sharp boundary. Sometimes magnetoionic splitting at the low-
frequency end of the trace may be visible; usually there is none.

Attention herein is primarily directed at midlatitude sporadic-E
because both its origin and reflection mechanism potentially apply to
the interpretation of barium echoes. Two other categories of sporadic-E
exist--auroral and equatorial. However, the physical phenomena generally
associated with these--auroral partical precipitation and scattering by
plasma waves in the electrojet, respectively--do not appear to be germane
to this discussion. These two types will not be considered here.

Sporadic-E has been a popular topic of research for many years, and
hundreds of theoretical and experimental papers and reports currently
exist. There have been numerous seminars and conferences on the subject,
and three have led to special issues of Radio Science being devoted to
the papers presented.[6-8] These issues, as well as a book edited by Smith
and Matsushire,[9] a review by Whitehead,[10] and most recently a comprehen-
sive report by Miller and Smith[11] serve as an ideal starting point for
the uninitiated reader.

The number of different explanations and theories on the origin,
generation mechanism, and scattering mechanism responsible for Es indi-
cates the complexity of the subject. In spite of all this interest,

however, many features of sporadic-E layers remain unexplained. It has only been within the last ten years that a theory regarding the origin of midlatitude sporadic-E layers has gained general acceptance. This is the wind-shear theory originally proposed by Dungey[12,13] and developed by Whitehead,[14] Axford,[15] and MacLeod.[16] The theory is consistent with many of the observed features of Es and is now believed to explain at least some of the observed Es traces.

The wind-shear model contends that long-lived metallic ions from ablating meteors are compressed into thin layers by the combined action of the horizontal neutral wind and the geomagnetic field. Specifically, in the lower E-region, where the ion-neutral collision frequency exceeds the ion gyrofrequency, the ions are effectively moved by the neutral particles. As the ions move they are subject to a Lorentz force that acts perpendicular to both the predominantly horizontal neutral wind and the geomagnetic field. Thus, the ions can acquire a significant vertical component of motion while the electrons are dragged along by the polarization fields. Often large vertical shears exist in the neutral wind and these in turn lead to vertical shear of the ion motion. The resulting convergence and divergence of the ion flow can produce a net flow of ionization into a region and thus cause an enhancement of ion density. (Correspondingly, however, when there is a net flow out of the region there is a depletion of ion density.) Because metallic ions have a long lifetime in the lower E-region, the density of the enhanced layers will increase (or decrease) with time.

Other mechanisms--instability and turbulence--have been suggested as an alternative to the wind-shear theory, but these do not appear as applicable to midlatitude sporadic-E. Also, in terms of application to barium-associated E-region returns, the wind-shear theory appears the most attractive and will be discussed in Section III.

Since ionograms probably provide the bulk of sporadic-E observations, much effort has been directed toward providing an explanation of these signatures. The interpretation of two parameters--f_bEs and f_tEs--that are used to describe the appearance of sporadic-E echoes on ionograms, is of particular interest. The first term (f_bEs, the blanketing frequency)

135

is used to specify the frequency of a partially transparent sporadic-E layer, above which the upper layers are visible and below which the upper layers are obscured. The second term (f_tEs, the top frequency or sometimes the critical frequency) specifies the highest frequency returned from the layer.

These parameters can be related to peak densities in the layer if certain assumptions regarding the reflection medium are made. Two models have been proposed:[17,18]

(1) Thin-layer model, in which gradient reflection from thin horizontially stratified layers is responsible for the Es trace.

(2) Patchy-layer model, in which reflection or scatter from irregularities embedded in the layer are responsible for the Es returns.

Each of these models and variations of them have been tested against observations, and each is capable of explaining certain features of Es.

The thin-layer model attributes reflection to the large electron-density gradients that characterize the vertical profile of Es layers revealed by rocket flights. Reflection coefficients, calculated from a full-wave solution of the wave equation, indicate that gradient reflection can produce Es returns of sufficient strength to be seen on the typical ionogram.[17,18] Miller and Smith[11] found, however, that the range of partial transparency observed (difference between f_bEs and f_tEs) cannot be explained by gradient reflection from the profile associated with the particular sporadic-E layer.

The patchy-layer model features dense blobs of ionization embedded in a background of lower electron concentration. The peak density of these blobs corresponds to f_tEs, the maximum frequency of the sporadic-E reflection, and therefore signals incident on them with frequencies below this value are totally reflected. The blanketing frequency, f_bEs, on the other hand, corresponds to the minimum uniform electron density in the background. Radio waves with frequencies exceeding this value are able to penetrate the layer and be reflected from a higher layer.

A variation of the patchy-layer model envisions small-scale irregularities in the vertical electron density distribution. Energy is returned from these layers as described by the scattering theory of Booker and Gordon,[19] and Gordon.[20]

While there are sufficient theories and observations of sporadic-E against which to test these models, existing observations of barium echoes are not of sufficient quality to permit similar comparisons. Nevertheless wind-shear theory and the reflection models discussed above can be used in Section III to aid in the interpretation of the data.

III ANALYSIS OF PRE-STRESS AND STRESS IONOGRAMS

Observation of traces on ionograms that appear to be associated with barium release is not new. Such effects were probably first recorded by investigators from the Max-Planck Institute in the late sixties.[21] Similiar effects were also reported during SECEDE II and III, and more recently in the STRESS program.

During SECEDE III, conducted in Alaska during March 1969, nine barium releases of various yields were made ranging from 2.4 kg to 96 kg. Although two Ba canisters were released at different heights on each of the first three days of the test series, these multiple releases will be counted as a single event. Thus, there were six events.

Ionograms taken at College, Alaska showed traces that are attributable to reflection or scatter from the ion cloud for three of the six events. These traces, for the most part, occurred at a virtual height of 200 km, in agreement with the slant range to the cloud from the ionosonde. The echoes lasted a few minutes and were first observed roughly ten minutes after release. In addition, the frequency extent of the echoes was typically less than 1 Hz except for the large 96-kg release, which had a frequency extent from 4 to 8.5 MHz.

Three of the events apparently did not produce any noticeable echoes
on ionograms, but propagation conditions or the yield of the release were
judges responsible.[1,5]

During SECEDE II, conducted in Florida in 1971, six 48-kg barium re-
leases were made. Each of these produced clear ionospheric effects and
in fact on three releases the resulting E-layer was sufficiently dense
that the upper layers were blanketed. Since f_oF2 at the time of blanket-
ing was in the 4-to-5-MHz range, a lower estimate of the peak electron
concentration in the cloud is 2×10^{11} el/m^3. The onset of blanketing
occurred typically about 100 minutes or more after the release, and the
duration was a few tens of minutes.

With the exception of the times when the F-region was blanketed by
the underlying Eb-layer, SECEDE II ionograms showing returns from the
barium cloud are quite similar.* In general, they have the following
characteristics: (1) The onset of barium echoes occurred about 2 to 10
minutes after release; (2) mixed-mode echoes† were generally the first
evidence of the barium cloud; (3) multiple echoes separated by 10 to 20
km were typical as the trace developed; (4) Eb or Fb traces‡ were gen-
erally very thin, but on occasion they were as much as 50 km thick; (5)
retardation or magnetoionic splitting was not observed; (6) partial blan-
keting of the upper layers was not evident on the ionograms inspected
even prior to and following the passage of the blanketing layer, thus
suggesting a layer of limited horizontal extent; (7) ionograms for OLIVE
showed the virtual range decreasing at a rate of about 14 m/s. This

---

*These conclusions were based on inspection of available SECEDE II iono-
grams published in reports. The results, however, pertain primarily to
OLIVE, since this is the only event for which a complete set of iono-
grams was available.

†Mixed-mode echoes identify returns from a propagation path that includes
some combination of traverses between the ion cloud, the ionosphere, and
the icnosonde. This indirect route leads to a longer path and thus this
type of returns can be distinguished from the direct path between the ion
cloud and the ionosonde.

‡For brevity, barium-associated traces on ionograms will be designated as
Fb or Eb if they occur at F- or E-region heights, respectively.

198

value was consistent with radar measurements at 10 MHz, which indicated a descent of 17 m/s during the first hour.

Although not as striking as the SECEDE results, the STRESS iono-grams exhibit approximately the same behavior as summarized above, with the following exceptions: (1) There is a hint of magnetoionic splitting near 6 MHz, and a hint of retardation at the high-frequency end of the F-region trace in ANNE at 2338 UT; (2) the first evidence of the barium echo generally occurred later (in the 10-to-20-minute time frame) than in SECEDE; and (3) blanketing of the upper layers was not observed for any of the releases.

Figure 1 illustrates some of the salient features that are discussed in this section. This figure shows ionograms taken shortly after the FERN release and during a particularly interesting period when the F-region trace developed and subsequently moved down to the lower E-region. FERN was released at 2246:09 UT, with apparently no effect evident on iono-grams taken at 2247 and 2250 UT. The first evidence of the barium re-lease occurred at 2253. At this time a faint trace appeared below the F-layer trace at about 4 MHz. The intensity and frequency extent of this trace increased in each subsequent ionogram and by 2309, or R + 23 min, it was clearly visible. At this time the trace developed a "nose" at the low-frequency end and showed a slight amount of frequency dependence at each end of the return.

The minimum virtual height of the Fb trace at 2309 was 185 km. In the next sequence of seven ionograms, covering a time period of 23 min, this trace decreased in intensity and frequency extent while descending to 130 km. At 2332 the Eb returns occurred primarily between 2 and 4 MHz, but near 8 MHz there was a hint of Fb returns at a height of 200 km.

Starting from 2335 the Eb trace continued to descend, but its fre-quency extent increased until at 0007 UT the maximum frequency returned was 18 MHz. The layer reached a minimum altitude of about 105 km at 0025 UT, and after this time the minimum height of reflection started to increase with time such that by 0203 UT it was at a height of 135 km.

The above scenario suggests a number of important questions: (1) What significance can be attached to the maximum frequency returned from the Eb or Fb layers? (2) What is the nature or origin of the reflecting layers? (3) What is the reflection or scattering mechanism? (4) What is the cause of the echo intensity variation with time? These questions will be addressed in the remainder of this section.

A. Nature of the Reflecting Layers

The contention that F-region traces of the type depicted in Figure 1 result from the barium ion cloud rests on the assumption that these traces originate in a time and range space similar to that of the ion cloud, and upon the uniqueness of these returns. That is, these signatures are not normal ionospheric returns, and were never observed on non-release days.

In FERN the downward migration of the reflecting layer from a virtual height* of 200 km to 115 km over a 60-min period is taken as evidence that barium ions do descend to the lower E-region and are the cause of the Eb-returns.† The possibility of barium ions descending to the lower E-region and forming layers that reflect incident radio signals has been suggested in the past.[22,23] The opinions of these authors were based primarily on ionograms and HF radar data indicating that typically the reflecting layer approached the observer, reached a minimum range, and then receded from the observer. While a descending Ba layer that reaches a minimum height of approximately 110 km and subsequently passes away from the observer would be consistent with observations, an equally plausible model is that the returns are due to reflection from an E-layer enhancement induced by the F-region cloud. Motion of this enhancement overhead would be consistent with the range-time history observed.

---

*The virtual-height label used on ionograms is correct only for a vertical propagation path. For off-vertical paths the term range or group path should be used. Our use of the term is only in reference to the label on the ionograms and does not imply any specific propagation path.

†The cause of radio-wave reflection is actually the electrons that are dragged along by the polarization fields.
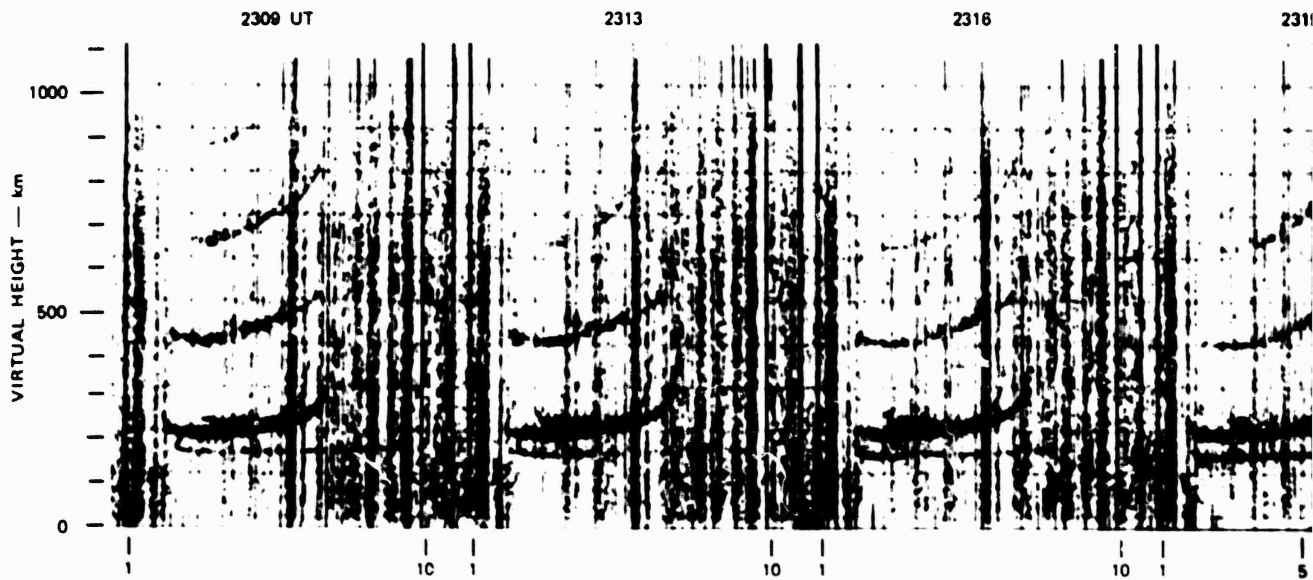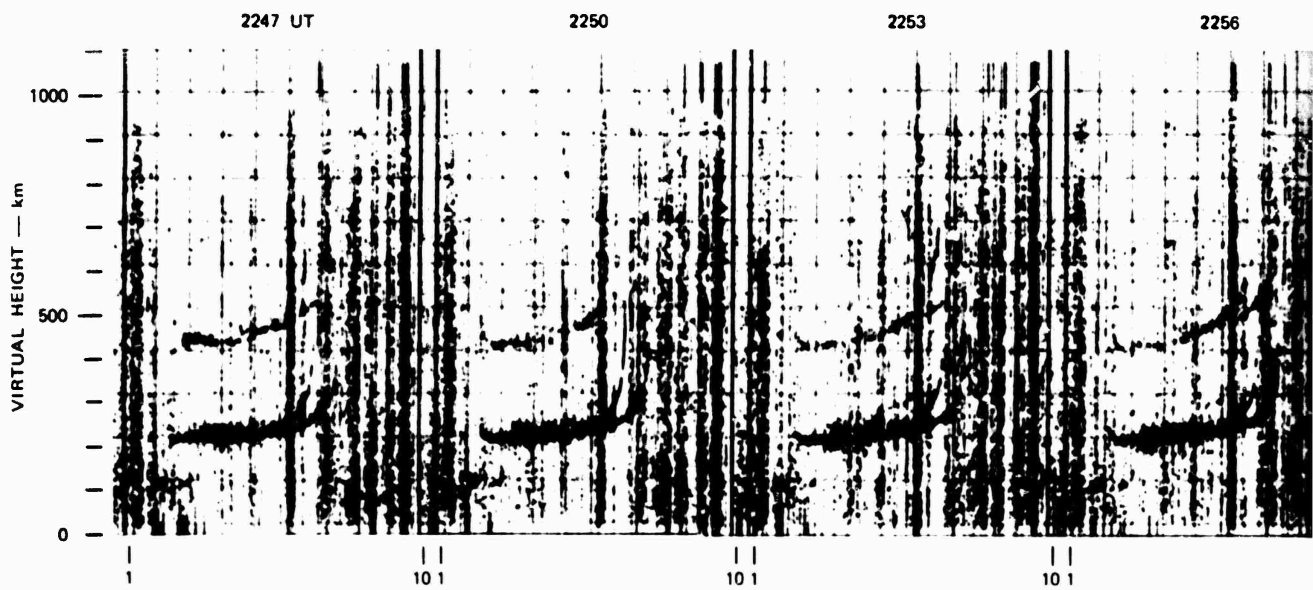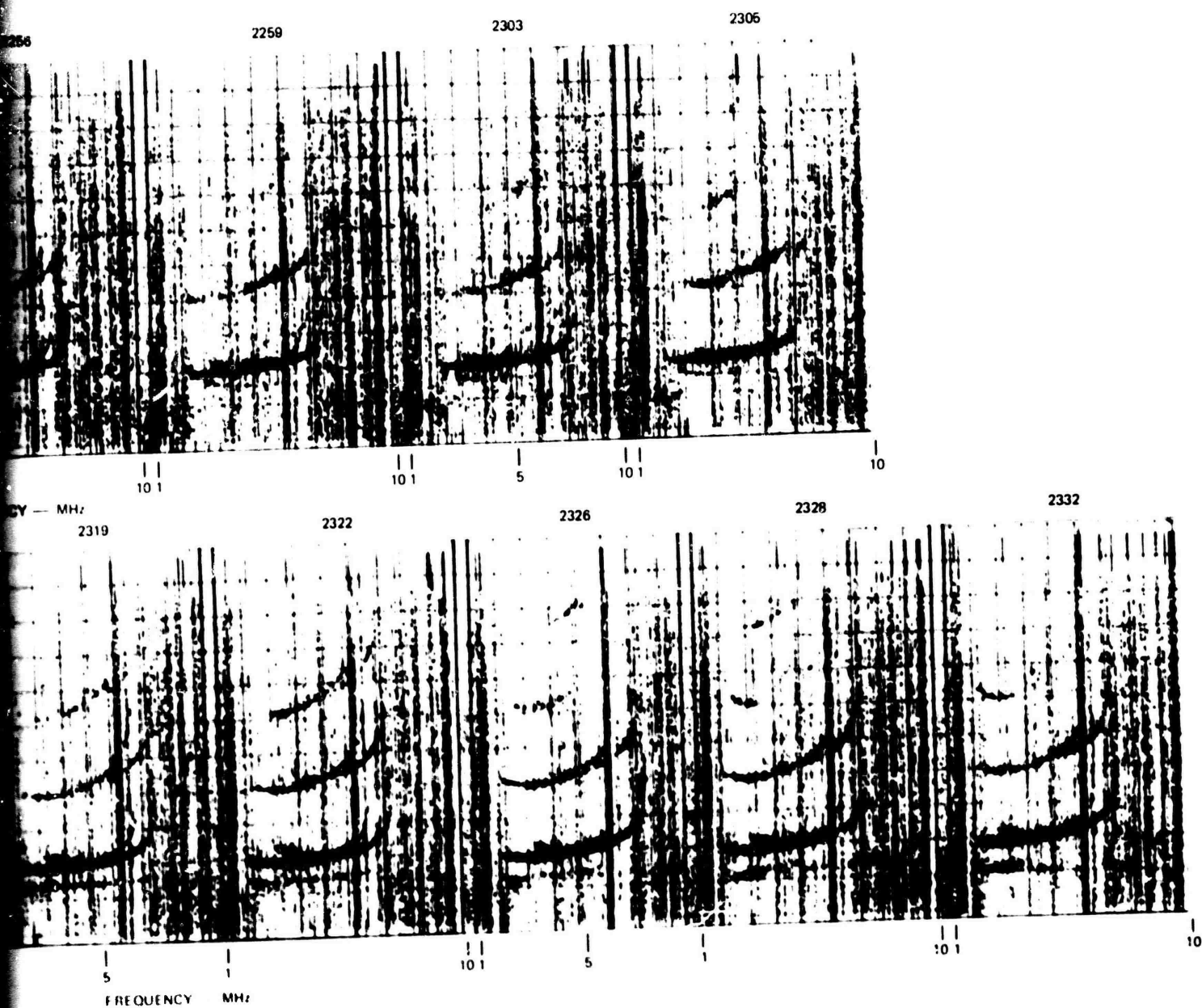
FIGURE 1   SEQUENCE OF IONOGRAMS FOR
EVENT FERN SHOWING THE
MIGRATION OF THE REFLECTION
LAYER FROM THE F-REGION TO
THE LOWER E-REGION

2335 UT   2338   2342   2346

VIRTUAL HEIGHT — km

1000

500

0

1   10 1   10 1   10 1

FREQUENCY — MHz

0001 UT   0007

VIRTUAL HEIGHT — km

1000

500

0

1   10   15   1   10   15

FREQUENCY — M

2346   2350   2355

FREQUENCY — MHz

0014   0020

FREQUENCY — MHz
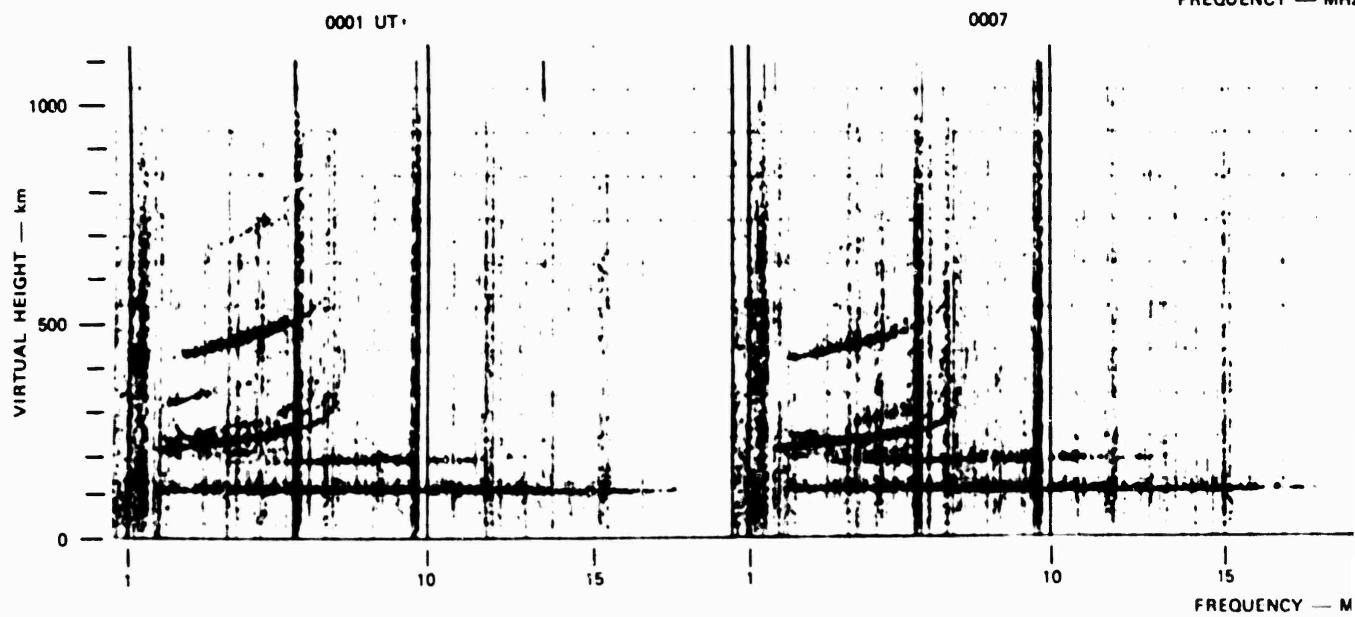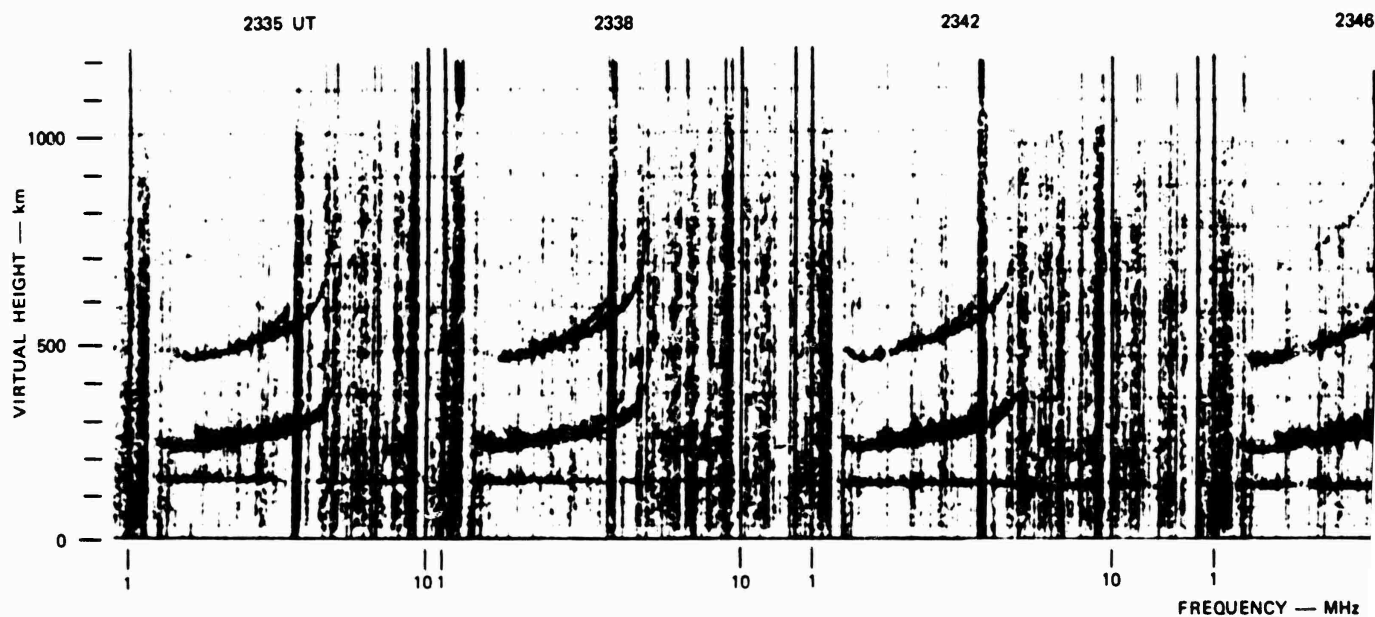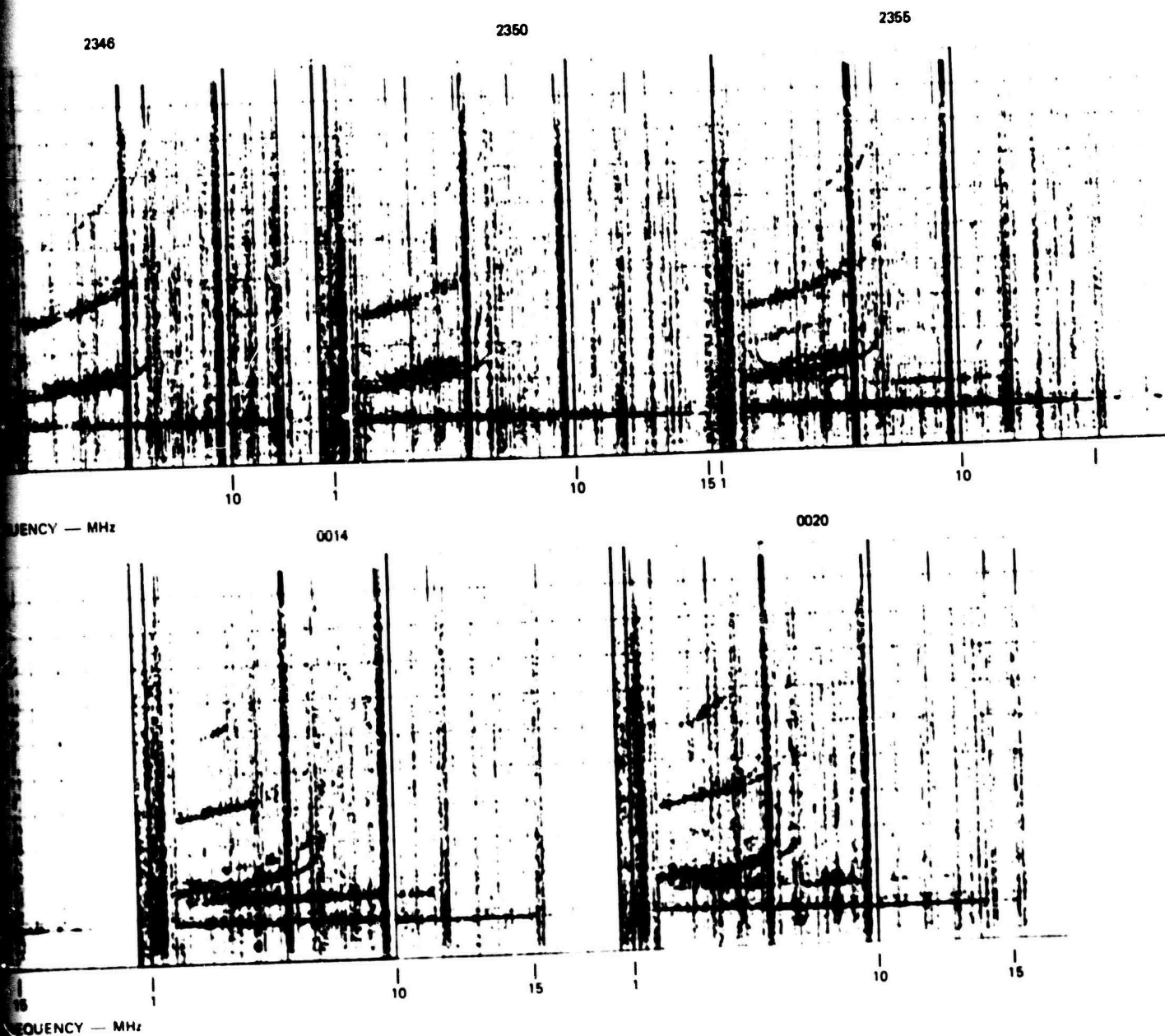
FIGURE 1   (Concluded)

A firm position on these two models was not taken during the SECEDE program, apparently because arguments could be made in favor of either one. We feel, however, that the FERN ionograms show conclusively that barium ions do descend to the lower E-region and are the cause of the Es return. This conclusion is further supported by the FPS-85 radar measurements and by the SECEDE II data.

Furthermore, the development of the echo as the layer descends suggest that the ions are compressed into thin layers, with a corresponding increase in cross section. Such behavior is consistent with that predicted by wind-shear theory. Thus, the Eb trace in FERN is a graphic example of how a sporadic-E layer is created by the compression of metallic ions, and gives support to wind shear as the probable mechanism of Eb returns or sporadic-E.

1. Migration of Barium Ions to the Lower E-Region

Figure 2 shows the range-time history of barium echoes observed during FERN. This figure shows that the barium cloud, released at an initial range of 221 km from the ionosonde, separated into two parts that drifted toward the observer at different rates. One part, which we shall designate the secondary cloud, approached the radar at about 24 m/s during the first 60 min, reached a minimum range of 105 km at R + 104 min, and then receded at about 11 m/s.

The quality of the Fb returns was poor during the first 60 min and considerable scatter can be seen in these range points. After R + 60 min, however, the Fb trace became quite distinct (see Figure 1), so greater confidence can be placed in these points. Because of the scatter the early behavior of the layer causing the Fb returns is uncertain, but based on the known range of the cloud at release (221 km) and the range of the layer after R + 60 min it is clear that this part of the cloud also approached the ionosonde, but at a slower rate.

The descent of a portion of the FERN ion cloud into the E-region is also supported by the FPS-85 measurements shown in Figure 3. During the first 60 min the radar tracked a portion that began near the release
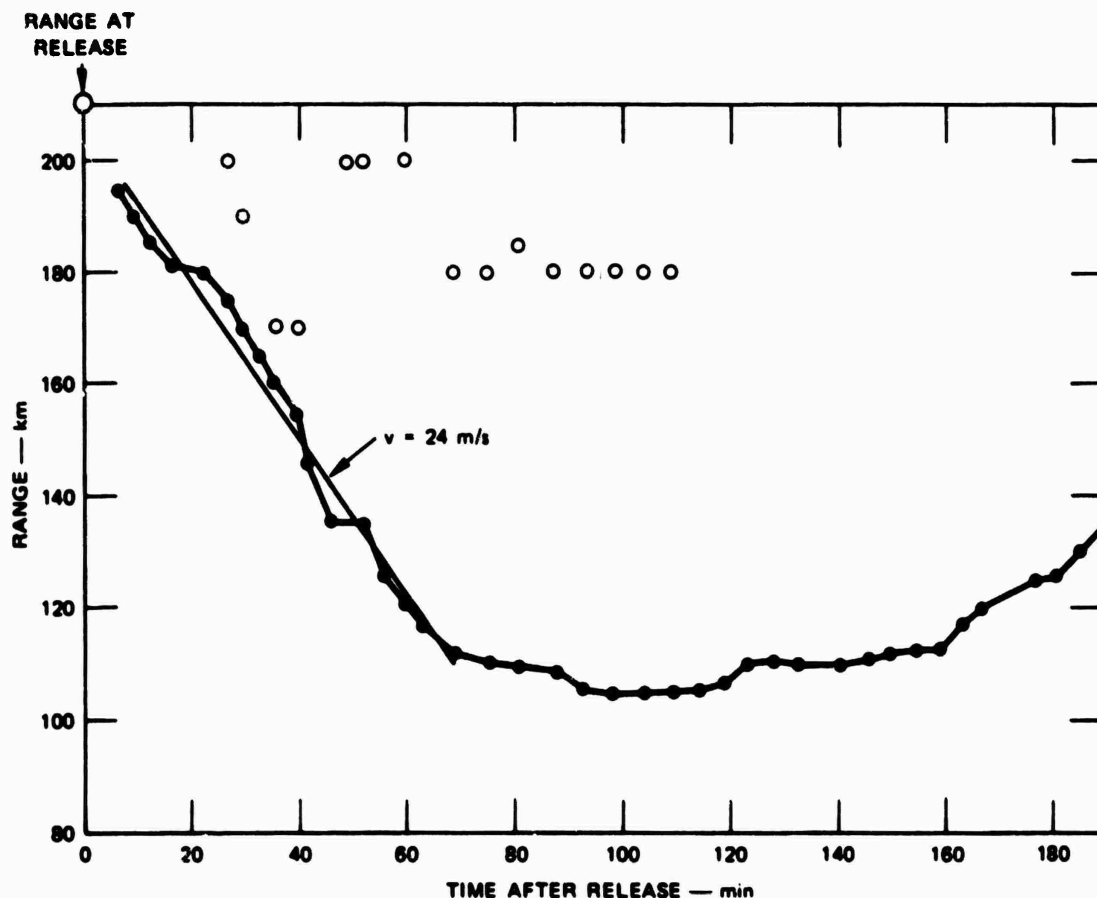
FIGURE 2   RANGE-TIME HISTORY OF BARIUM ECHOES FOR EVENT FERN

height and fell to 143 km. At approximately R + 55 min the radar switched
to another part (we shall call this the main cloud, since it is this cloud
that later became visible), which at that time had descended to 172 km.
If we assume a uniform rate of descent for this target we find that its
descent rate over the first 60 min is about 4 m/s, compared to 12 m/s for
the secondary cloud. After R + 60 min, however, the main cloud also
showed a rapid descent until R + 100 min, when the radar was no longer
able to track the cloud.

Before proposing a model that appears to be consistent with the
vertichirp and FPS-85 data, let us digress and consider how ions move in
a magnetic field. Above about 130 km, and especially so at greater alti-
tudes, collisions between barium ions are infrequent compared to the ion

206
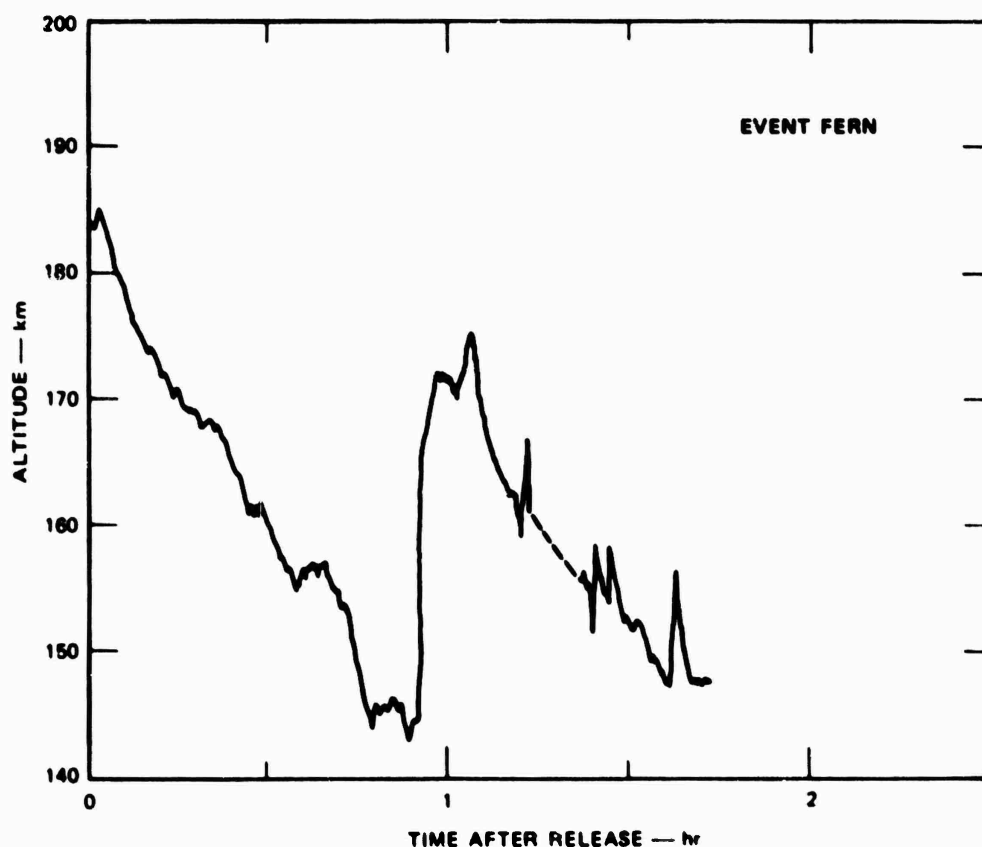
FIGURE 3   ALTITUDE OF ION CLOUD AS A FUNCTION OF TIME — EVENT FERN

gyrofrequency. Hence, to first order, barium ions can freely move only in the direction of the magnetic field. When barium ions are released in sunlight at 185 km they quickly become ionized, forming a spherical cloud. This initial shape is distorted by gravity, the ambient electric field, and/or by the neutral winds.[*] Because of the magnetic-field constraint, only a northward component of the neutral wind, a westward component of the electric field, or gravity is effective in causing a vertical motion of the barium ions.

Since it is known from optical and radar data that only a portion of the FERN cloud descended into the E-region, the mechanism driving

---

[*]Ambipolar diffusion is neglected in this discussion because it occurs roughly equally in both directions parallel to the magnetic field. Hence, to first order, it does not displace the cloud, taken as a whole.

the ion cloud down the field lines must also be capable of causing this
separation. This division of the cloud can only be explained by a verti-
cal wind shear. If gravity is neglected, the observed vertical motion
of 12 m/s requires a neutral wind with a northward component of at least
12/sin(60 = 14 m/s. Although winds of this magnitude and even larger are
known to exist at the altitude of the barium release, little is known
about the nature of wind shears above about 160 km. We offer the behavior
of FERN as evidence that significant wind shears do exist above 180 km.

The model that appears to be consistent with the ionosone and FPS-
85 measurements discussed above is the following: Shortly after release,
wind shear caused the lower portion of the ion cloud to separate from the
main cloud. Both clouds drifted eastward at about 23 m/s due to an am-
bient $\vec{E} \times \vec{B}$ force (see Figure 4). The upper part of the ion cloud (main
cloud), which was unaffected by the neutral wind, had an additional down-
ward motion due to gravity. This descent rate, given by the ratio of the
acceleration of gravity to the barium-ion collision frequency, is about
6 m/s at 180 km, a value consistent with the implied descent rate of 4
m/s in Figure 3. The lower part, however, descended at a faster rate--
12 m/s--because of gravity plus an additional contribution due to a north-
ward component of the neutral wind.

A common eastward motion due to $\vec{E} \times \vec{B}$ was postulated for both
clouds because it is known that the ambient electric field does not vary
with height. Figure 3, however, indicates that the secondary cloud shows
an additional northward motion while the main cloud shows a southward
motion. The resulting horizontal component toward the ionosonde plus the
vertical motion indicated by Figure 2 for the secondary cloud is consis-
tent with the 24-m/s range rate shown by Figure 2.

The main cloud appeared at a constant range from the ionosonde
after R + 70 min because its northward motion due to the descent of the
ions down the field lines is compensated for by the southward motion of
the cloud due to $\vec{E} \times \vec{B}$ forces (see Figure 3). Apparently, as the main
cloud slowly descended, primarily due to gravity, it encountered a strong
northward neutral wind, which cause the descent rate shown in Figure 3.

208
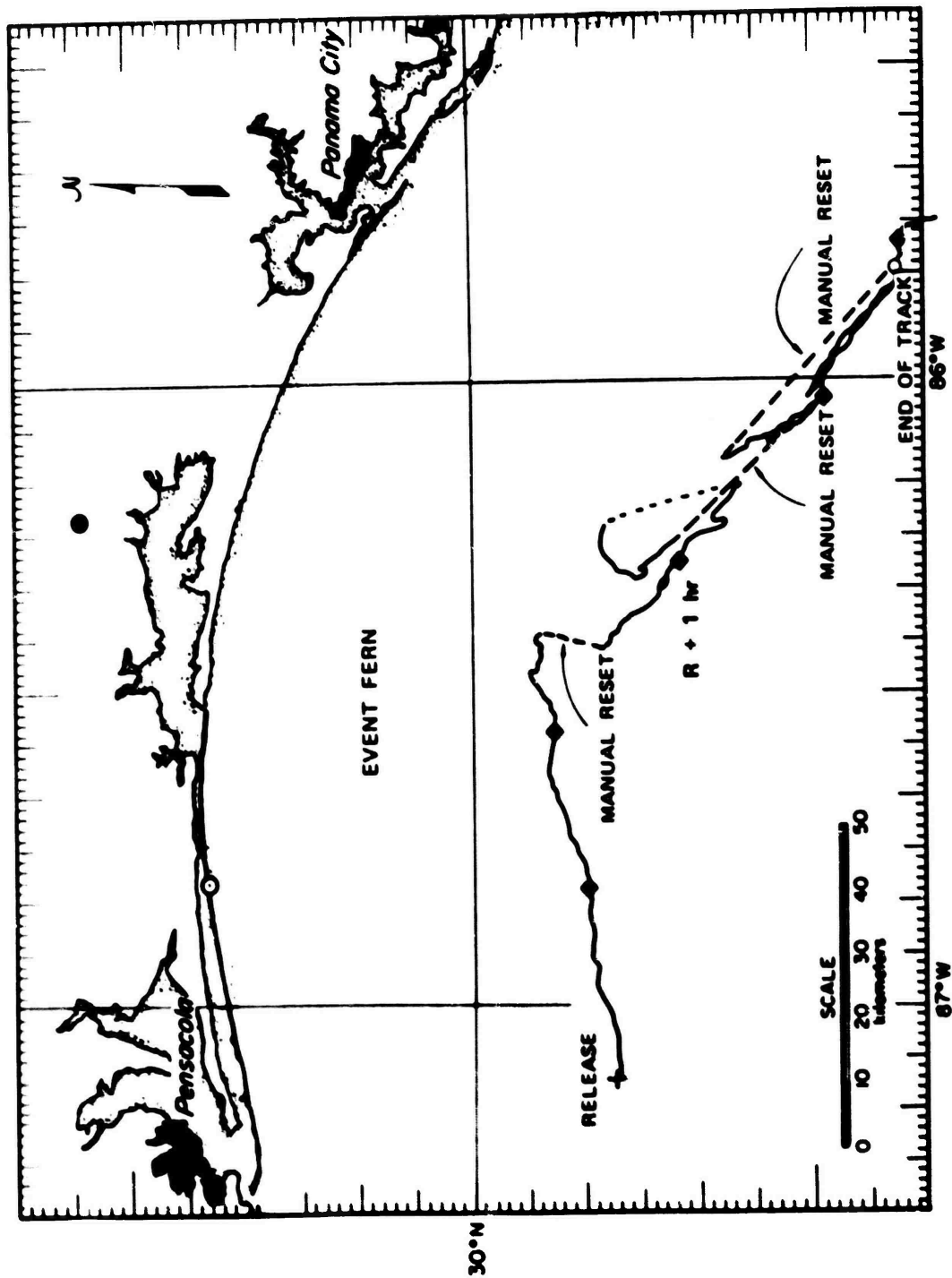
FIGURE 4   MOTION OF ION CLOUD WITH 20-MINUTE MARKERS — EVENT FERN

2. Interaction Between E- and F-Region Caused by Barium Releases

The interaction of an F-region barium cloud with the underlying E-region was pointed out by Haerendel, Lust, and Rieger.[24] These investigators proposed that at F-region heights an ion cloud driven by an ambient electric field will become polarized because of charge separation arising from the difference in mobility between electrons and ions. This polarization field will in turn be neutralized by current flow along the equipotential magnetic field lines. These currents are carried by electrons due to their higher mobility along the field lines, while down in the E-region, due to high Pedersen conductivity of the ions, the horizontal currents are largely carried by the ions.

The situation in the F-region, depicted in Figure 5, is that as the ions move away from the electrons in the barium cloud the polarization field created is neutralized by electrons arriving from the underlying E-region. The electrons, on the other hard, at the rear of the cloud flow down the field lines and tend to cause a local increase in electron density there. Below the front of the cloud there is a local increase of positive charges.

Experimental verification of the E-region interaction of ionospheric barium releases has been attempted with some success by Stoffregen,[26] although his efforts were somewhat inconclusive due to the possibility of auroral contamination in his measurements. At any rate, Stoffregen observed that within the first minute of release photometric measurements near the foot of the magnetic field line passing through the barium cloud reveal a rapid buildup of 5577-Å emissions that reaches a maximum and then decreases to the background level. The duration of the event was generally only a few tens of seconds, with maximum intensity occurring about 10 s after the barium release. Apparently because the degree of interaction is proportional to the peak density of the ion cloud, the E-region effect rapidly decreases as the ion cloud diffuses. Hence, observation after the first minute or so does not produce measurable results.[26]
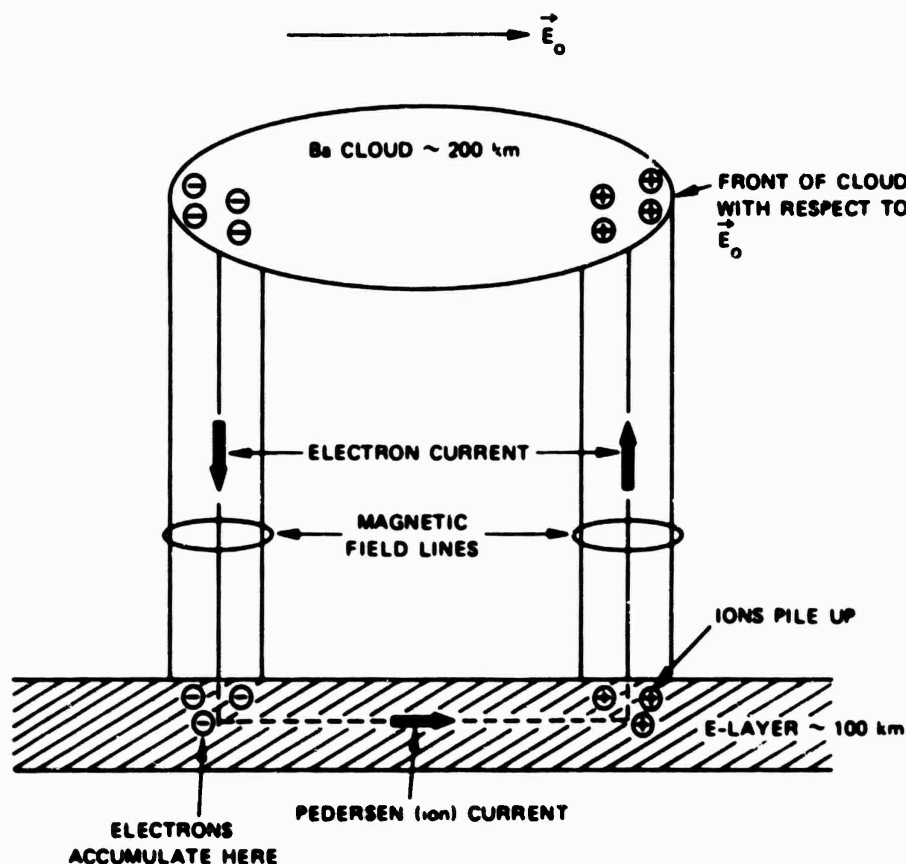
FIGURE 5 SCHEMATIC PICTURE SHOWING HOW AN F-REGION BARIUM CLOUD
INTERACTS WITH THE UNDERLYING E-REGION THROUGH THE
EQUIPOTENTIAL GEOMAGNETIC FIELD LINES

Although the SECEDE and STRESS series utilized barium releases with larger
yields than these reported by Rieger et al.[21] of the Max Planck Institute,
and hence would be expected to produce larger and longer E-region effects,
there were no experiments (optical or radio) to observe these interactions
in either the SECEDE or the STRESS programs. Thus, except for papers by
Mende[25,26,27] and by Landshoff[28] which described the possible E-region
effects of an F-region barium release there has been no recent effort,
experimental or theoretical, on the topic.

The interest in E-region interaction is due to its part in the
overall understanding of barium-cloud development. In addition, if the
E- and F-region are in fact coupled together by the equipotential geomag-
netic field lines, small-scale irregularities that are produced in the

211

E-region by turbulence can be projected into the F-region cloud and can thus be the cause of small-scale structure.[29-31]

In summary, we have found on ionograms no evidence of E-region enhancement produced by coupling between the E- and F-region via the geomagnetic field lines. This lack of results, however, does not rule out the possibility that this interaction might have gone unnoticed because experiments were not optimized to detect the effect of E-region enhancement.

B. Reflection of Radio Waves by Barium Ionization

Perhaps two of the most puzzling features of sporadic-E returns and indeed of ionospheric returns from barium releases are the frequency extent of the traces and the maximum frequency reflected. Often the latter value is much greater than the critical frequency of the F-layer, and, if converted to a peak electron concentration with the formula $f_c^2 = 80.1\ N$, it results in an unrealistically high value. (f_c is the critical frequency of the layer in Hz, and N is the peak density in el/m^3.)

For example, if the 15-MHz maximum frequency observed for Fb in ANNE at R + 47 min is interpreted as a critical frequency, the resulting peak density of the layer would be $3 \times 10^{12}\ el/m^3$. If density decays as $t^{-1/2}$, as required by ambipolar diffusion along the geomagnetic field lines, an initial peak density of $2 \times 10^{14}\ el/m^3$ would be required. This value is about an order of magnitude greater than that generally accepted for a 48-kg barium release at 185 km altitude.

The proper interpretation of barium-associated returns seen on ionograms rests on knowledge of the physical nature of the reflecting layer and in particular on whether radio signals are reflected or scattered from the layers. As we shall see, a definitive answer to this question cannot be given because the available data appear to be consistent with at least two different models.

A key parameter in any discussion of radar target characteristics is the radar cross section (RCS) of the target. This quantity is derived from the system constants of the radar (antenna gain, frequency, etc.)

212

and from measured parameters (range and received power). Unfortunately, while the vertichirp does provide range measurements (virtual height as a function of frequency), it was not configured to provide amplitude information. Thus, with the receiver set on AGC (automatic gain control) and with no provisions made to record the AGC voltage or to calibrate the intensity of the ionograms, it is now only possible to make a crude estimate of the strength of the barium-associated returns.

Laboratory measurements made after the completion of the STRESS experiments showed that the vertichirp sounder is able to measure a signal level of approximately -140 dBm over the range of frequencies used. To convert this signal to a minimum radar cross section we use the radar equation

$$P_R = \frac{P_T G^2 \lambda^2 K L \sigma}{(4\pi)^3 R^4}$$

where

P_R = Received signal strength

P_T = Transmit power (8 watts)

G = Antenna gain (3 dB)

λ = Wavelength (30 m at 10 MHz)

K = Modulation factor (-13.5 dB)

L = Two-way absorption and other losses (-3 dB)

σ = Radar cross section (RCS)

R = Range of the target (200 km).

Several of the numbers in the above list, the antenna gain, the D-region absorption and other losses, and the measured signal strength are not known, and estimates were made. The modulation factor, K, results from gain weighting used in the transmitter and receiver and from the duty cycle of the transmitted signal. Thus, at a frequency of 10 MHz the RCS of the barium cloud is

213

$$\sigma(\text{dB m}^2) = P_R(\text{dBm}) + 187 \text{ dB} \quad .$$

Using the laboratory measurement of -140 dBm for P_R we conclude that under ideal conditions the vertichirp should be able to detect the cloud if it has an RCS of at least 47 dB relative to 1 m^2, or 5×10^4 m^2.

Measurements of barium-cloud radar cross section in the 5-to-10-MHz range during SECEDE II and III indicate that the cross section of a typical 48-kg cloud reaches a peak of about 10^6 m^2 shortly after release and decays to about 10^5 m^2 in about 10 to 15 min. The RCS is not well behaved, and 5-to-10 dB excursions in a one-minute period can occur. Nevertheless, during the first 10 min following release, 2 to 3×10^5 m^2 appears to be a representative RCS. Late-time data when the ion cloud is fully striated apparently do not exist, but in view of the strength of the late-time echoes seen in Event ANNE, the RCS must remain above 10^5 m^2 for tens of minutes.

Cross sections for the layers causing the E-region returns are not available, but based on their appearance on the ionograms we estimate that the received signal power is comparable for echoes from both E- and F-regions. Because of the range dependence in the radar equation, however, the RCS of the layer at 100 km can be a factor of 16 less than the RCS of a layer at 200 km and still have the same received power. Thus, the minimum detectable cross section at 100 km is about 3×10^3 m^2.

Before we address the question of the reflection mechanism to be associated with the F-region returns we first note some of their characteristics:

(1) The first evidence of barium echoes occurs some time after release. During SECEDE II barium echoes were observed about 2 to 10 min after release. During STRESS, echoes occurred in the 10-to-20 min time frame.

(2) The first echoes observed were either direct or mixed-mode echoes.

(3) Retardation or magnetionic splitting was generally not evident on barium returns. The traces were typically very thin and show little or no range dependence with frequency.

214

(4) When the echoes were first observed they tended to be
     weak, but they typically increased in intensity with
     the passage of time.

From these observations we conclude that the returns were not due to
overdense or total reflection. The reasons are as follows: HF radar mea-
surements show that maximum cross section occurs a few minutes after re-
lease. Hence, if overdense reflection was responsib .or the Fb traces
the strongest returns would occur one or two minute after release, with
intensity decreasing with time. The opposite trenc s observed.

Gradient reflection and scattering, either from cense blobs or weak
irregularities, are two mechanisms often proposed to explain sporadic-E
echoes. In applying these models to barium echoes we find that signal
intensity does not permit a clear choice, since both mechanisms can lead
to returned signals with comparable radar cross sections.

In terms of signal characteristics we expect gradient reflection to
result in thin, discrete echoes, whereas scattering should lead to dif-
fused returns that may at times have appreciable range depth. Since ex-
amples of both types of echoes can be found in the data, a clear choice
between the two models cannot be made.

Thus we conclude that gradient reflection and scatter are viable
mechanisms for the origin of Fb echoes. Because of the large minimum
detectable RCS (5×10^4 m^2) of the vertichirp, the release and initial
development of the barium cloud is not visible to the ionosonde. Only
when the cloud has expanded and perhaps formed sheets of sufficient cross
section at the correct orientation to the ionosonde is the cloud detected.
The ion cloud is highly aspect-sensitive and at times a mixed-mode echo
is observed because its path presents a larger cross section than the di-
rect path.

The characteristics of the E-region echoes observed during FERN are
quite similar to those summarized for the Fb returns with the following
additions:

(1) Blanketing of the upper layers was not observed for any
     of the STRESS releases. Blanketing occurred on three of
     the six releases in SECEDE II.

215

(2) FERN showed a clear descent of the echoing layer from the F-region to the lower E-region. This trace started as a weak return but later became very intense.

Blanketing was not observed during FERN, possibly because the layer density was too low, or because the layer did not pass directly overhead. The layer's peak density is not well known, but the SECEDE II results suggest that 3×10^{11} m^2 (5 MHz critical frequency) is possible even 100 min after release. Since the lack of partial blanketing for any event implies a rather limited horizontal extent for the Eb layer we conclude that the peak density region of the FERN Eb layer probably did not pass over the ionosonde.

The strength of the FERN Eb returns and their time characteristics suggest that the returns are due to thin layers with high gradients. The underside of these layers, however, cannot be smooth; if they were, returns would not be possible unless these layers were directly overhead. The best model for the Eb layers seems to be a thin, rough layer with high gradients.

IV CONCLUSIONS

Analysis of ionograms obtained during the Pre-STRESS and STRESS program in concert with other pertinent data and sporadic-E theories yield the following observations and conclusions:

(1) Characteristics of barium-associated ionosonde traces

    (a) F-region echoes (Fb echoes)

        • Evidence of barium cloud first occurs some time after release. During SECEDE II, barium echoes were observed about 2 to 10 min after release.

        • The first echoes observed were either direct or mixed-mode echoes.

    (b) E-region echoes (Eb echoes)

        • FERN showed a clear descent of the echoing layer from the F-region to the lower E-region. This E-region trace subsequently became very intense, reached a minimum range of 105 km, receded, and then faded out.

216

- Blanketing of the upper layers was not observed during any of the STRESS releases. Blanketing occurred in three of the six SECEDE II releases.

(c) E- and F-region echoes

- Retardation and magnetoionic splitting were generally not observed. The traces were typically very thin and showed little or no range dependence with frequency.

- When the echoes are first observed they tend to be weak, but they typically increase in intensity with time.

(2) Nature of the layers responsible for the barium-associated returns

(a) The direct and mixed-mode returns in the F-region originated from the barium ion cloud.

(b) Mixed-mode echoes are due to the aspect-sensitive nature of the ion cloud.

(c) In the E-region the returns are from layers of barium ions that separate from the main cloud and descend to the E-region through the combined action of gravity, a northern component of the neutral wind, and/or a westward component of the electric field.

(d) Once the barium ions descend to the E-region they are compressed into thin layers, with a corresponding increase in cross section.

(3) Reflection or scattering mechanism responsible for the echoes

(a) The nature of the reflection layer can be best described as a thin layer of barium ions with sharp upper and lower boundaries.

(b) Gradient reflection is the most likely mechanism, but other possibilities such as scattering from weak irregularities or from dense blobs cannot be ruled out.

(c) Reflection is not specular, so maximum frequency observed for the layer cannot be interpreted as a critical or a maximum plasma frequency.

(4) Coupling of E- and F-region. E-region interactions with the F-region cloud through electro-dynamic coupling via the equipotential field lines are not supported by the data.

217

REFERENCES

1. G. N. Oetzel and N.J.F. Chang, "Analysis of SECEDE III HF Data," RADC-TR-69-412, Contract F30602-68-C-0076, Stanford Research Institute, Menlo Park, California (November 1969).

2. J. J. Simons, "Event OLIVE--Ionosonde Late-Time Observations (U)," (Report Unpublished).

3. J. J. Simons, "Preliminary Ionosonde Observations during SECEDE II (U)" (Report Unpublished).

4. R. Baender, "Vertical-Incidence-Sounder Observations During SECEDE II (U)" (Report Unpublished).

5. N.J.F. Chang, "SECEDE II Ionograms Revisited (U)" (Report Unpublished.

6. Radio Science, Vol. 10, No. 3, Special Issue: "Recent Advances in the Physics and Chemistry of the E Region" (March 1975).

7. Radio Science, Vol. 7, No. 3, Special Issue: "Papers Presented at Third Seminar on the Cause and Structure of Temperature Latitude Sporadic E" (March 1972).

8. Radio Science, Vol. 1, Special on Sporadic-E (February 1966).

9. E. K. Smith, Jr. and S. Matsushite, Eds., Ionospheric Sporadic E, (The MacMillan Co., New York, New York, 1962).

10. J. C. Whitehead, "Production and Prediction of Sporadic E," Rev. Geophys. Space Phys., Vol. 8, pp. 65-144 (1970).

11. K. L. Miller and L. G. Smith, "Midlatitude Sporadic-E Layers," Aeronomy Report No. 76, IULU-ENF 76 2507/, University of Illinois, Urbana, Illinois (December 1, 1976).

12. J. W. Dungey, "The Influence of the Geomagnetic Field on Turbulence in the Ionosphere," J. Atmos. Terr. Phys., Vol. 8, pp. 39-42 (1956).

13. J. W. Dungey, "Effect of a Magnetic Field on Turbulence in an Ionized Gas," J. Geophys. Res., Vol. 64, pp. 2188-2191 (1959).

14. J. D. Whitehead, "The Formation of the Sporadic-E Layer in the Temperate Zone," J. Atmos. Terr. Phys., Vol. 20, pp. 49-58 (1961).

15. W. I. Axford, "The Formation and Vertical Movement of Dense Ionized Layers in the Ionosphere due to Neutral Wind Shears," J. Geophys. Res., Vol. 68, pp. 969-779 (1963).

16. M. A. MacLeod, "Sporadic E Theory, I. Collision-Geomagnetic Equilibrium," _J. Atmos. Sci._, Vol. 23, pp. 96-109 (January 1966).

17. C. A. Reddy, "Physical Significance of the Es Parameters FbEs, fEs, and FoEs, 2. Causes of Partial Reflections from Es," _J. Geophys. Res._, Vol. 73, pp. 5627-5647 (1968).

18. C. A. Reddy and M. M. Rao, "On the Physical Significance of the Es Parameters FbEs, and FoEs," _J. Geophys. Res._, Vol. 73, pp. 215-224 (1968).

19. H. G. Booker and W. E. Gordon, "A Theory of Radio Scattering in the Troposphere," _Proc. IRE_, Vol. 38, pp. 401-412 (1950).

20. W. E. Gordon, "Incoherent Scattering of Radio Waves by Free Electrons with Applications to Space Exploration by Radar," _Proc. IRE_, Vol. 46, pp. 1824-1829 (1958).

21. E. Rieger, J. Foppl, G. Haerendel, L. Haser, J. Loidl, R. Lust, F. Melzner, B. Meyer, and H. Neuss, Final Report on Experiment R-33 in ESRO-Payload S04, Max Planck Institute Fur Aeronomie, West Germany (January 1968).

22. G. D. Thome, "The OLIVE Working Group--A Summary of Findings" (Report Unpublished).

23. S. B. Mende, "Estimate of Induced E-Region-Irregularity Enhancement (U)" (Report Unpublished).

24. G. Haerendel, R. Lust, and E. Rieger, "Motion of Artificial Ion Cloud in the Upper Atmosphere," _Planet. Space Sci._, Vol. 15, pp. 1-18 (1967).

25. W. Stoffregen, "Electron Density Variation Observed in the E-Layer Below an Artificial Barium Cloud," _J. Atmos. Terr. Phys._, Vol. 32, pp. 171-177 (1970).

26. S. B. Mende, "Observation of Current System and Striation Formation Mechanism (U)" (Report Unpublished).

27. S. B. Mende, "Generation of Secondary Irregularities by Motion of Ion Clouds (U)" (Report Unpublished).

28. R. K. Landshoff, "Interactions Between the Barium Bloud and the E Layer (U)" (Report Unpublished).

29. G. C. Reid, "The Formation of Small-Scale Irregularities in the Ionosphere," _J. Geophys. Res._, Vol. 73, pp. 1627-1640 (1968).

30. H. J. Volk and G. Haerendel, "Striations in Ionospheric Ion Clouds, 1," _J. Geophys. Res._, Vol. 76, pp. 4541-4559 (1971).

31. K. H. Lloyd and G. Haerendel, "Numerical Modeling of the Drift and Deformation of Ionospheric Plasma Clouds and of Their Interaction with Other Layers of the Ionosphere," J. Geophys. Res., Vol. 78, pp. 7389-7415 (1973).

TV TRACKING SYSTEM

R. D. Hake, Jr.   N.J.F. Chang

SRI International
Menlo Park, California

TV TRACKING SYSTEM

R. D. Hake, Jr.   N. J. F. Chang

SRI International
Menlo Park, California

ABSTRACT

A three-site television-aided tracking network was con-
structed and fielded for the STRESS series of barium releases.
The TV network acquired the barium-ion clouds as early as times
corresponding to a 3° solar depression angle and maintained track
until the sun set on the cloud 40 to 45 minutes later. The
differences between cloud tracks generated by this television
network and by an incoherent-scatter radar that had also tracked
the clouds could be ascribed to the two systems intentionally
focussing on different regions of the amorphous ion cloud. Op-
erating experience of the TV-tracking system showed that the
most useful tracking procedure for experiments such as STRESS,
though not necessarily the most accurate, was a single-site
track that uses an empirical model for the cloud altitude after
release. Projection of the second DIANNE rocket probe trajec-
tory onto cloud photographs from various ground stations showed
that the rocket did not encounter the region of peak electron
density in its passage through the cloud. The radar-derived
electron density profiles could be related to specific ion-
cloud features for Event ESTHER, but not for Event FERN.

I SYSTEM DESIGN AND CONSTRUCTION

A. Background

The overall design of the TV-track system was based on a similar
system[1] used by the University of Alaska during the SECEDE-II series of
barium releases conducted at Eglin AFB during early 1971. In the SECEDE-
II series, the TV system's primary purpose was to generate a cloud-track

that was used in real time to vector a photographically instrumented
aircraft to the foot of the magnetic field line passing through the cloud.
The successful operation of that TV system established a high degree of
confidence in optical tracking systems in general. The problems en-
countered during that system's real-time operation were extremely useful
in establishing the successful netting philosophy for the STRESS releases.

B.   Siting, Netting, and Hardware

It was decided to again establish TV-track observing sites at three
locations, to provide redundancy in the cloud-triangulation procedure,
as well as to provide a backup capability in the event of cloud cover
obscuring one site. No reason was found to change the locations from
those used during SECEDE-II. Those sites are separated by baselines of
nearly 100 km, appropriate to high-resolution triangulation from a 200-km
range to the releases. The TV-track sites, located at Tyndall Air Force
Base site 9702, Eglin AFB site C-6, and the Barin Field Naval Air Station,
are shown in Figure 1 along with other elements of the STRESS experiment
matrix.[2] Also shown in Figure 1, are a generalized box model of a barium
cloud (assumed to be centered at 185 km altitude) and the positions of
the ground shadow of that cloud appropriate to the pre-STRESS and STRESS
tests.

Note that the C-6 TV site was collocated with the FPS-85 Space Track
Radar, which was used to perform the radar track[3] of the ion clouds by
incoherent-scatter techniques. Site C-6 was established as the principal
site of the TV net, containing the triangulation computer and functioning
as the liaison with the balance of the STRESS experiment. Under normal
operating conditions, the TV-derived ion-cloud position was relayed to
the FPS-85 radar installation by means of acoustic-coupled phone lines.
The FPS-85 computer then projected the cloud position down the satellite
line of sight with the same algorithms used to generate a cloud shadow
from the radar-derived cloud position. The TV-derived cloud and cloud-
shadow positions were then relayed to the various STRESS users by per-
sonnel inside the FPS-85 building. The primary cloud-data user was the
aircraft controller, located at CERTS on the Eglin main base. Secondary
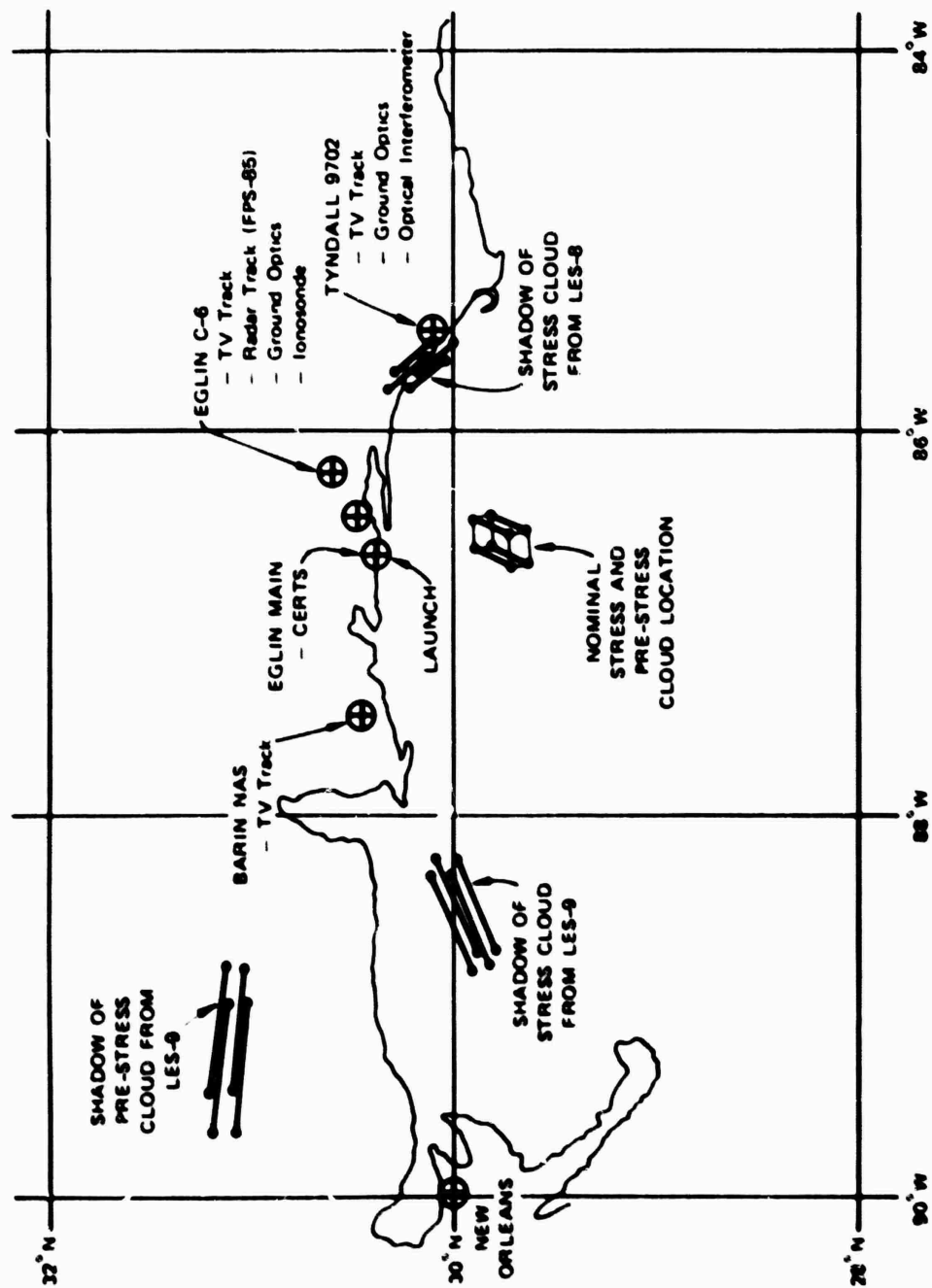
FIGURE 1 PROJECT STRESS: INSTRUMENT, CLOUD, AND SHADOW LOCATIONS

225

users were personnel associated with the probe rockets at the launch site, and the optical interferometer at Tyndall site 9702.

A low-light-level TV camera [Cohu Model 4410, Silicon-Intensified-Target (SIT) camera] was mounted at each site on a motor-driven platform with remote controls for setting azimuth and elevation. Azimuth and elevation readouts were digitized to 14-bit accuracy for display and for input to the central triangulation computer at Site C-6. The digital look-angle data were transmitted from the "wing" sites (Tyndall and Barin) to the TV-net central computer at C-6 on commercial phone lines by means of acoustic couplers. The central computer (HP-2100) performed the triangulation of the cloud position using data from one, two, or all three of the sites according to selection procedures and algorithms discussed in Section II-C, below. It then computed the look angles of this theoretical cloud location as seen from each site, and transmitted these angles back to each site along the same phone lines used for the data input. The look-angle data, along with an electronically generated boresight reticle, was stored in a matrix memory device at each site. The contents of the matrix memory were continuously mixed with the video from the camera and displayed on the monitor screen. The operator was thus provided with video imagery of the cloud, overlaid with a boresite and the computed cloud position as seen from his site. In addition to its own boresight, the C-6 TV monitor displayed the central portions of the Barin and Tyndall boresight overlays.

The TV tube in the Cohu cameras was an RCA SIT vidion with a 16-mm format. The cameras were equipped with f/0.95, 50-mm-focal-length lenses (Schneider "Xenon" Model CM120), giving a TV field of view of roughly 10.5° (vertical) by 14° (horizontal). A narrowband interference filter (26.5 Å full-width at half maximum, 4563 Å peak wavelength, 58% peak transmission) was used to isolate the 4554-Å line and enhance the visibility of the ion cloud when viewed against the bright twilight sky. These filters could be manually placed over the TV-camera lenses, and permitted acquisition of the cloud 5 to 10 minutes earlier than would otherwise have been possible. By blocking out the light from the neutral

226

cloud, the ion filters also helped in identifying the early development of structure in the ion cloud.

Figure 2 is an example of the video imagery available at each site; these pictures were taken from Event DIANNE at 0034 GMT (R + 32 min, 50s). The sequence of bars and dots across the top of each screen is a time code, which was also stored and updated in the matrix-memory device. The length of the lower bar in the time code increased one step at the change of the minute and an upper bar (absent in this case) showed the hour. In the Tyndall screen, the computed cloud position is the short bar just to the lower left of the ion-cloud luminosity. The boresight reticle is the group of two short and two long bars near the center of the screen. In the Barin screen, the boresight reticle and computed cloud position (short bar touching the left-hand bar of the reticle) are visible, along with a burn spot on the T' camera tube (central dark blotch), and spurious bits injected into the matrix memory by interference on the C-6/Barin data-line phone connection (long bar just to the left of the burn spot). In the C-6 screen, the boresight reticles and computed cloud positions from Tyndall and Barin are overlaid onto the lower left and right (respectively) corners to show the scientific director at C-6 the magnitude and sense of the tracking discrepancies at the two wing sites.

Each site operator was responsible for maintaining a steady track on the relevant portion of the ion cloud as it evolved in time. The scientific director viewed the C-6 display, and received information orally from the wing-site operators concerning the gross structure of the cloud as seen from their site. The scientific director then determined, on the basis of this information from the wing sites, visual imagery of the cloud as seen from C-6, and the visual overlay of the boresight/computer-track-point discrepancies at all sites, whether each site should maintain track on their chosen part of the cloud or should shift emphasis to a different portion of the cloud. This real-time feedback was quite necessary because of the differing appearance of the diffuse, geometrically complex barium clouds from the three widely separated points of view.

227

(a) C-6 VIEW

(b) TYNDALL VIEW

(c) BARIN VIEW

FIGURE 2   TV IMAGERY OF EVENT DIANNE AT 0034 UT (R + 32 min, 50 s) AS RECORDED ON VIDEO TAPE AT THE THREE TV-TRACK SITES

II SYSTEM OPERATION

This section of the report contains a brief description of the operation of the TV net during each of the six releases and the cloud-position tracks obtained during the operations. The figures in this section show the ground projections of the TV and radar cloud-track points for Events ANNE through FERN. The TV-track data are given as heavy lines with 10-minute markers; the radar-track data are given as light lines with 20-minute markers.

Table 1 summarizes the temporal data for the six releases. Notice that the progression of release time was from late to early. ANNE was released at 96° SDA when the experience of SECEDE showed that the sky was dark enough to permit a continuous optical track following the release. Succeeding releases were made progressively earlier, so that the clouds could be documented during the twilight optical window at progressively later stages in their evolution. As the series progressed, the TV net acquired the cloud at earlier times, and consistently acquired the later clouds at about an SDA of 3°. The track duration in most cases was about 40 minutes.

A. Pre-STRESS Event ANNE

Water clouds were present at all three sites during Event ANNE, which interfered with the TV imagery to varying degrees. At Barin, the barium cloud was obscured almost completely by overcast, being discernible only during the flash as the barium was released, and for a few intermittent periods of seconds at later times. The deletrious effect of the overcast at Barin was compounded by the fact that the barium cloud was within a few degrees of the nearly full moon. The overcase was considerably thinner at C-6 and Tyndall, where the release was clearly observed and the barium cloud position was obscured only intermittently. The cloud track was generated by two-station tracking from C-6 and Tyndall. Track was initiated immediately after release and continued for about 30 minutes before the cloud began to fade. The cloud was finally lost from the C-6 site at R + 35, and from Tyndall somewhat earlier.

229

Table 1

SUMMARY OF STRESS TEMPORAL DATA FOR TV-TRACK SYSTEM

Event	Date	Time of SDA* = 6°, GMT	Release Time, GMT	Interval by Which Release Preceded SDA 6° (minutes)	TV-Net Acquire		TV Loss of Track, GMT (Time After Release)	Track Duration (minutes)	Last View of Cloud, GMT
					Time, GMT (Time After Release)	SDA (deg)			
ANNE	12/1-2/76	2312	2311:42	0	2311 (R+0 min)	6	2341 (R+30 min)	30	2343
BETTY	2/26-27/77	0006	2352:27	13	0003 (R+11 min)	5.3	0040 R+48 min)	37	0040
CAROLYN	3/2-3/77	0009	2354:10	15	0000 (R+6 min)	4	0040 (R+46 min)	40	0042
DIANNE	3/7-8/77	0012	0001:08	11	0001 (R+0 min)	3.5	0042 (R+41 min)	41	0045
ESTHER	3/13-14/77	0016	2301:09	75	0002 (R+61 min)	2.8	0044 (R+103 min)	42	0047
FERN	3/14-15/77	0017	2246:09	91	0004 (R+78 min)	3.2	0046 R+120 min)	42	0052

*SDA = solar depression angle, referenced to Site C-6.

Post-event analysis of the TV-track data summarized in Figure 3, showed that the two-station solution agreed reasonably well with the FPS-85 radar track. The TV-track data sent to the FPS-85 was misinterpreted within the FPS-85 computer; the latitudinal and longitudinal displacements from the reference location were interchanged. This resulted in the optically derived cloud-shadow locations being considerably in error. The aircraft followed the optically derived shadow and gathered no data for the first 27 minutes of cloud life. Fortuitously, the true cloud shadow and the shadow derived from the interchanged data crossed paths at that time and the aircraft began acquiring data. Shortly afterward, the sun set on the cloud and the aircraft was directed to follow the radar-derived cloud track.

A further difficulty during Event ANNE was the occurrence of large and apparently random excursions of the shadow on the ground, making it difficult for the aircraft to intercept the optically derived cloud shadow. This problem was traced to the random altitude excursions of the two-station C-6 and Tyndall solution as the two sites tracked the cloud. These altitude excursions were magnified in projecting the cloud location down to the shadow location, and the subsequent erratic behavior of the shadow prevented the air traffic controller from accurately directing the aircraft to intercept the cloud shadow. The solution to this problem was to allow the triangulated cloud position to assume any altitude, but to translate that position along the earth's magnetic field lines to a smoothly varying cloud-center altitude before generating a cloud shadow. Figure 3 shows that the TV-track point was significantly east of the radar-track point. This was caused by the TV net choosing to track a portion of the ion cloud close to the head of the cloud (also called the hard edge or trailing edge); the radar, however, automatically gravitated toward the most dense part of the cloud (integrated over the radar-beam volume). This discrepancy was accepted as a genuine difference between the two methods of tracking, and no attempt was made to force a common track point for the two systems for the later events.
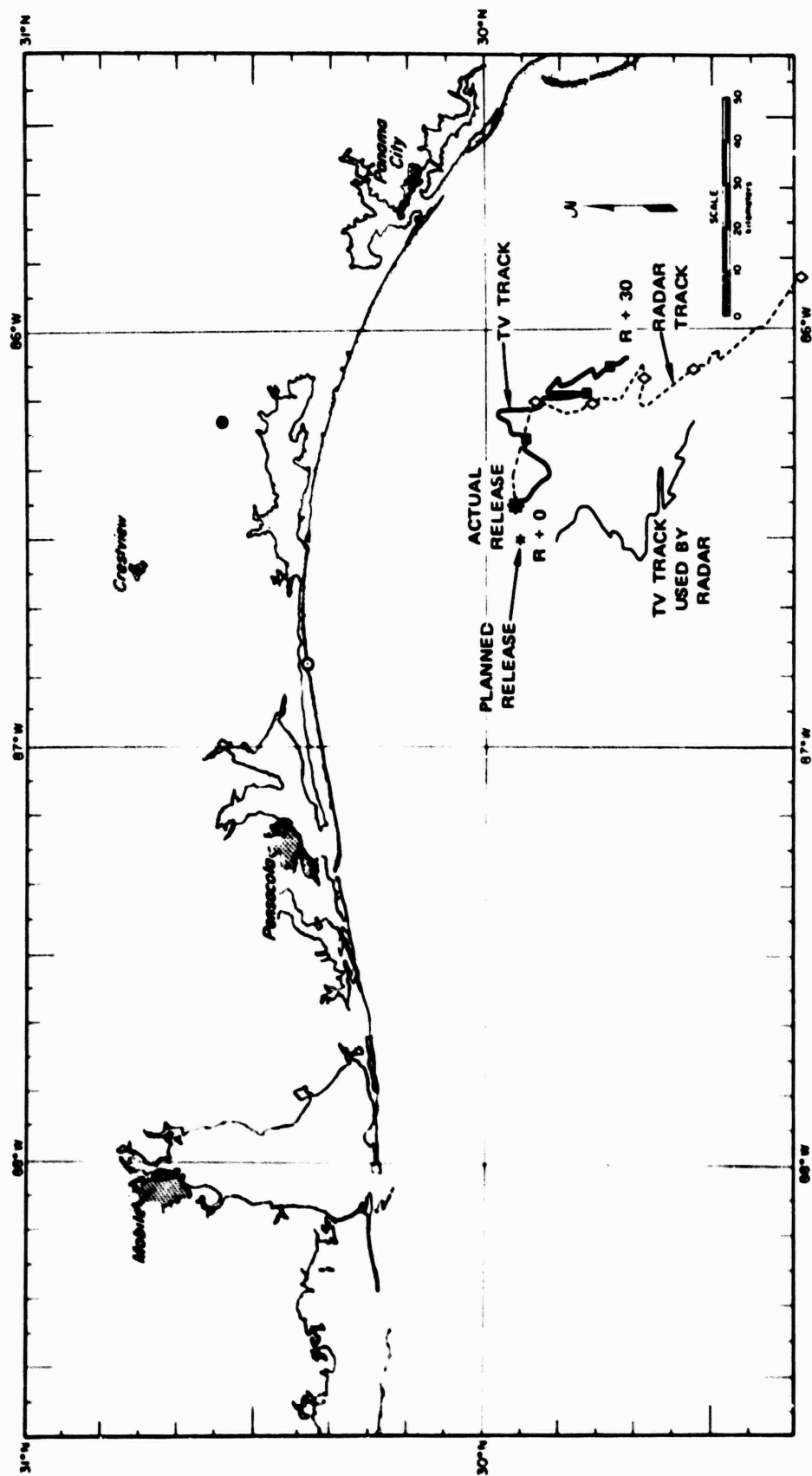
FIGURE 3   TV AND RADAR TRACKS OF ION CLOUD — EVENT ANNE

In summary, the TV-track system performed during Event ANNE in a manner that revealed several problems with the system and its use, but showed no major obstacles to its successful use in STRESS per se.

B. STRESS

1. Event BETTY

Event BETTY also occurred under less-than-optimum sky conditions, with light overcast at Tyndall and C-6, and light to heavy overcast at Barin. The actual release was not observed on any of the TV systems, because it occurred considerably to the south of the anticipated location. Event BETTY was the first barium-ion cloud to be released at a solar depression angle (SDA) of less than 6°, and hence required adapting to the brighter sky-background conditions. C-6 was the first TV site to acquire the cloud, at R + 11 min. A single-site track was initiated at that time, with the cloud altitude being fixed at 185 km (the empirical-model software for cloud-altitude falling as a function of time was not operational for Event BETTY). Most of the early cloud track was generated by the C-6 single-site track because Tyndall and Barin had only intermittent views of the cloud. Barin had a rain shower at about R + 26 min, for which the equipment had to be covered, and the Barin site was generally useless during the entire event. Tyndall visibility improved substantially near R + 35 min and a two-station track was used for the next 10 min. Site C-6 became completely overcast at R + 46 min, shortly before the sun set completely on the cloud as observed from Tyndall at R + 48 min.

The track of Event BETTY, shown in Figure 4, is much smoother than the ANNE track; it shows the track-smoothing effect of the empirical-height solution (for BETTY the empirical-height solution placed the cloud at a constant altitude of 185 km). The radar lost the cloud just after release and did not reacquire it until R + 40 min, a time period indicated by the light dashed line in Figure 4. Since the dashed line is only an extrapolation between two known radar locations, the disagreement between it and the TV track is not judged to be significant. The nonuniform

233
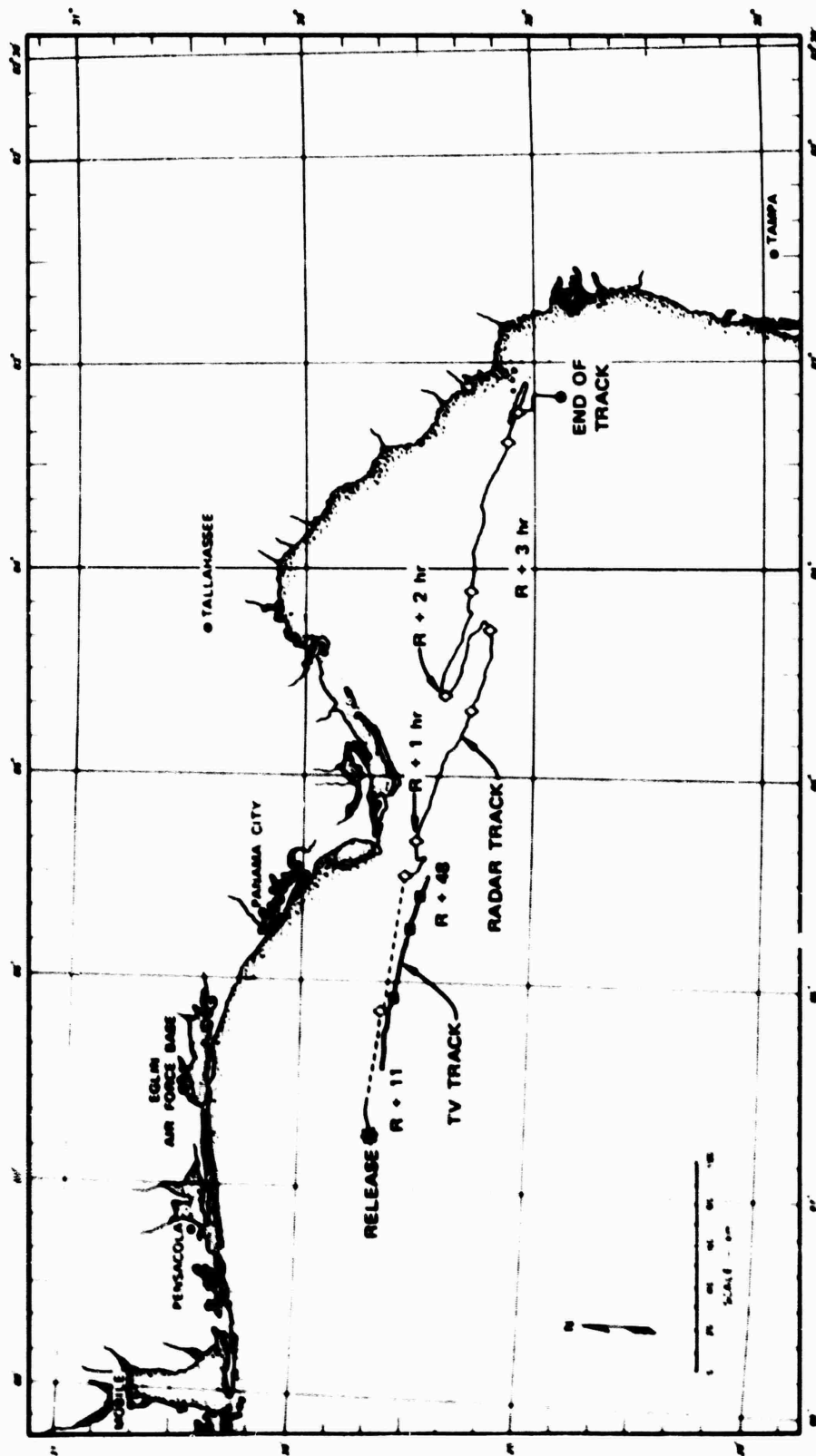
FIGURE 4 TV AND RADAR TRACKS OF ION CLOUD — EVENT BETTY

cloud velocity indicated by the differing distance between 10-minute marks on the TV track was caused by changing the portion of the ion cloud tracked by the TV net.

The TV-track data used by the FPS-85 was again in error, because two of the 32 coaxial cables connecting the TV-interface unit to the FPS-85 computer were interchanged during the experiment setup. This problem was identified during post-event data analysis, and was corrected by arranging to leave the interface unit connected to the computer for the remainder of the STRESS test window. The problem had not been detected before the release because last-minute changes in the release scenario necessitated foregoing some of the normal consistency checks between the FPS-85 and TV-track computers.

2. Event CAROLYN

Visibility at Tyndall and C-6 was quite good for most of Event CAROLYN, but Barin's view of the barium-ion cloud was somewhat degraded by cirrus. The actual release was seen by all sites and the ion cloud itself was first acquired by the Tyndall site at R + 6 min, followed by C-6 at R + 8 min. A two-station track was maintained until R + 30 min when the ion cloud became sufficiently distinct through the cirrus at Barin that a three-site track could be initiated. Low-altitude cumulus obscured the C-6 view of the ion cloud at R + 42 min, shortly before the TV track was terminated by the sun setting on the cloud. The cloud faded from view at Tyndall at approximately R + 49 min. The southern edge of the ion cloud passed through the Tyndall magnetic zenith at ~R + 42 min, providing a magnificent view of some very narrow (N-S) and extremely long (E-W) sheets.

CAROLYN was a well behaved ion cloud in the sense that a fairly well defined group of striations formed at the head (trailing edge) of the cloud and maintained their identity as the cloud drifted to the east. Since this striation group was easily identifiable from all sites, and unquestionably the most interesting part of the cloud from a STRESS point of view, the TV track job was made considerably easier.

235

The TV track for Event CAROLYN, shown in Figure 5, agrees quite well with the radar track. Since the radar track point automatically gravitated to the highest-average-electron-density portion of the ion cloud, this agreement shows that during the optical lifetime of this well behaved event the striated head of the cloud must have retained a high average electron density. The TV-track software and all interfaces worked well during Event CAROLYN, resulting in an optical track that was quite smooth and usable by the aircraft controller.

3. Event DIANNE

Skies over all three TV sites were reasonably clear throughout the entire release. The release was again seen by all sites, and by this time, the site operators were sufficiently well experienced in finding the rather amorphous early cloud that the ion cloud was kept in continuous track following the release. The initial cloud track was a two-station (Tyndall and C-6) track. At R + 14 min, the skies became dark enough over Barin to make that site view useful and a three-station track was initiated. The optical track continued until R + 41 min; the cloud was lost from view around R + 44 min.

Event DIANNE was not a well behaved ion cloud. It developed a kink near the midpoint, starting at about R + 16 min. The striations at the head (trailing edge) of the cloud moved out of the main body of the cloud much faster than in the previous releases, resulting in a rather tenuous bunch of striations with an ill-defined center. An attempt was made to keep the TV-track aim point within the striated region at the head of the cloud, and closer to the unstriated main body from which the striations were emerging than to the lead striation. The tracking situation was further confused when a second striated region developed behind the kink, well away from the head of the cloud. This second group of striations was ignored in picking the TV-track target.

The TV-track cloud position, shown in Figure 6, was well behaved during Event DIANNE, with the empirical height solution providing the smoothest track of any of the STRESS releases. Unfortunately, the FPS-85 computer went down at around R + 20 min, and the restart procedure

236
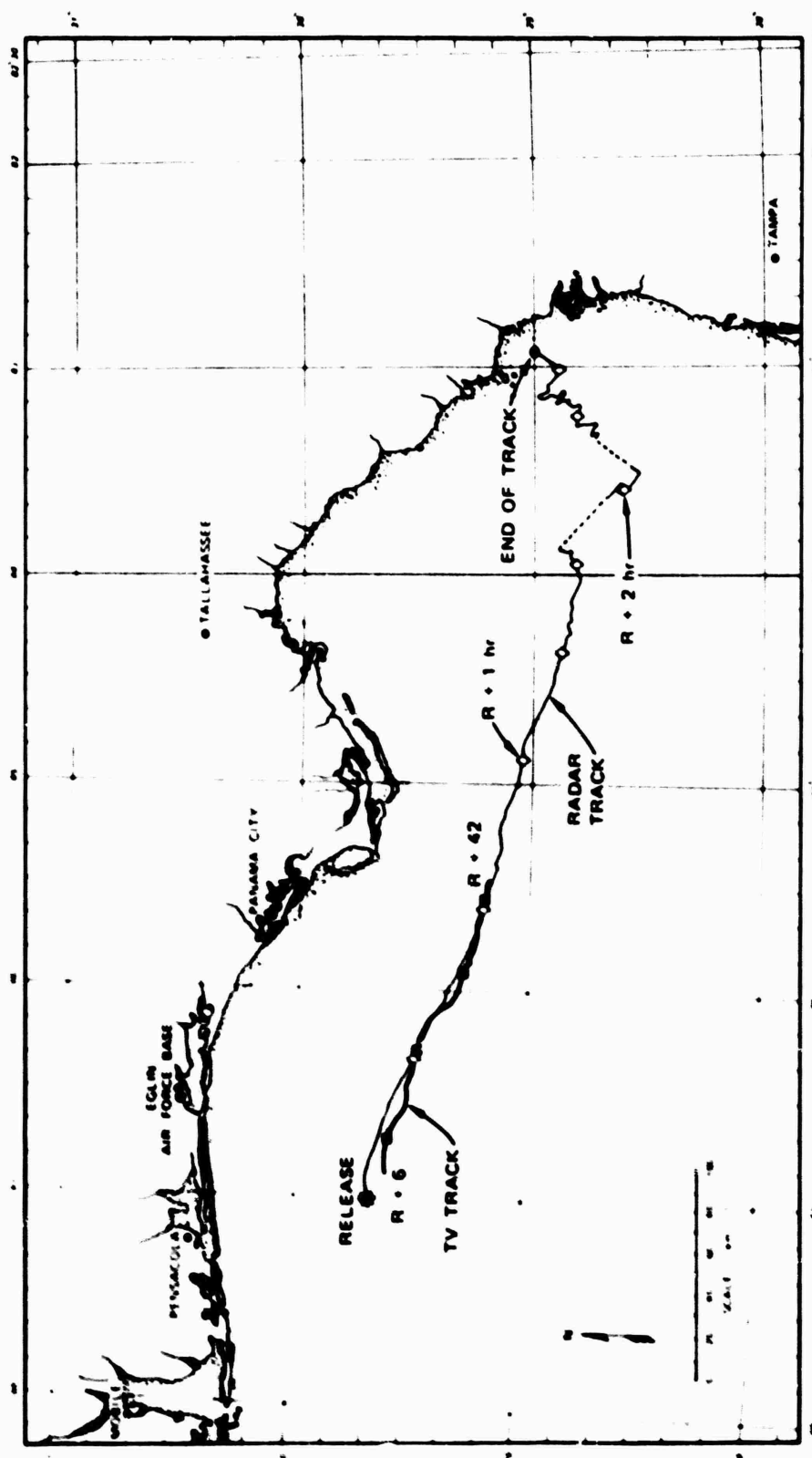
FIGURE 5 TV AND RADAR TRACKS OF ION CLOUD — EVENT CAROLYN

237
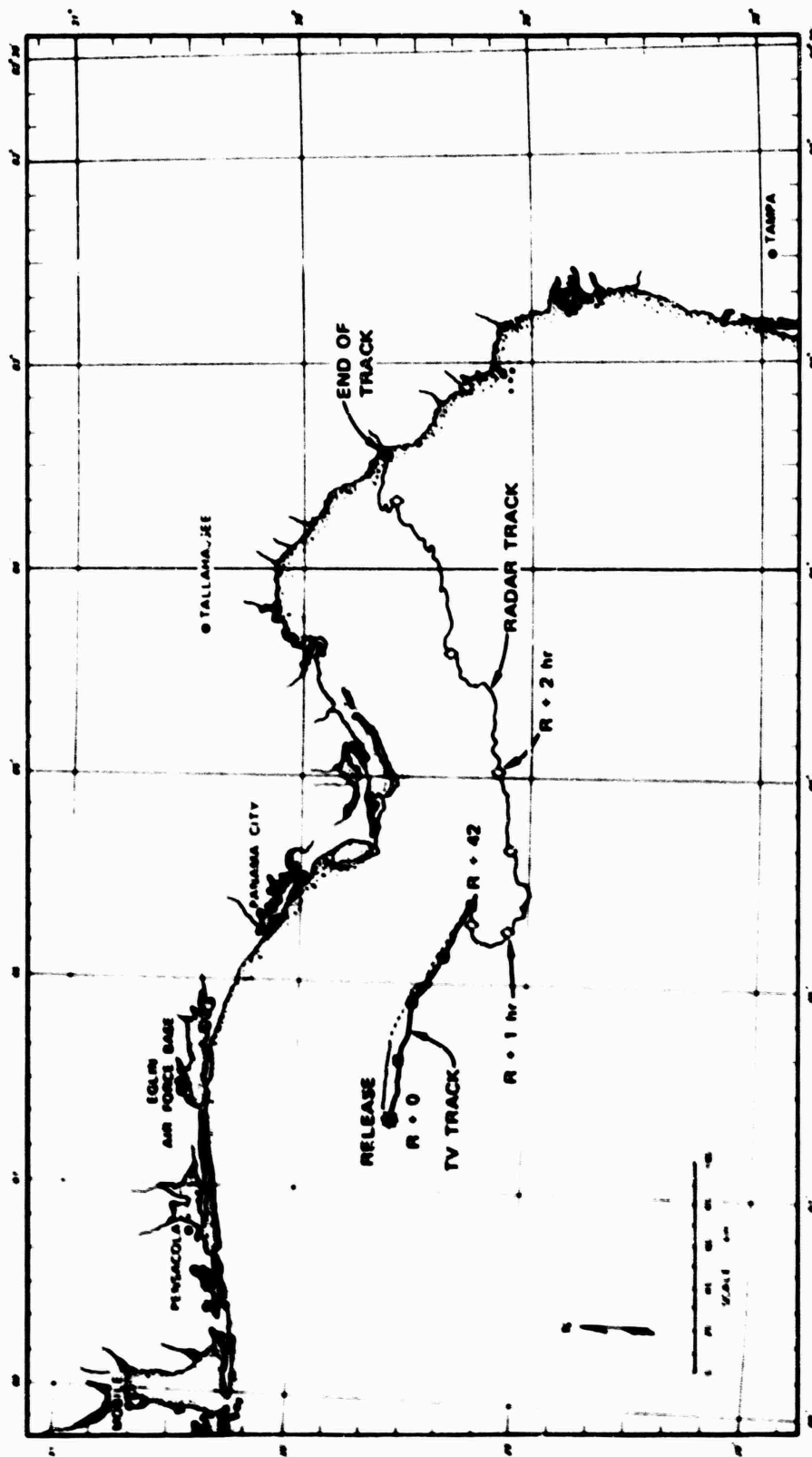
FIGURE 6   TV AND RADAR TRACKS OF ION CLOUD — EVENT DIANNE

introduced an erroneous coordinate-system zero into the software that handled the TV-track data. The TV-track data given to the aircraft controller were thus invalid after R + 20 min. At R + 38 min, when the radar came back on line (following a computer failure), it was reset to the optical track point. The radar track then moved west, not because the cloud was moving west, but because the radar was automatically seeking the region of highest average electron density. The radar settled down and began a reasonably smooth eastward motion at a point considerably to the west of the extrapolated optical track. This shows that the center of the striated region tracked optically was not the region with the highest average density for DIANNE.

4. Event ESTHER

ESTHER was the first of the two clouds released considerably before sunset. By the time the ion cloud became visible it was almost completely striated, and turned out to be a rather good object to track. There was a well defined group of striations that maintained their identity, both collectively and individually, as the cloud drifted to the southwest.

Skies were quite clear throughout the event at Tyndall and C-6. There was a high, thin overcast at Barin, however, which resulted in the Barin picture being consistently fuzzy, with none of the well defined structure seen at Tyndall and C-6. TV-track software, the FPS-83 interface, and the FPS-85 computer all worked well during Event ESTHER.

The track of Event ESTHER, shown in Figure 7, portrays the later stages of another well behaved ion cloud, with the radar track being quite smooth during the optical-cloud lifetime. The initial eastward bias of the optical track is caused by the eastern end of the cloud having the greatest contrast in the early twilight, and thus appearing as the best target to an optical system.

The occasional discontinuities in the optical track occurred because of a decision to change emphasis to a different part of the cloud, as the entire cloud became visible. The optical track moves closer to

239
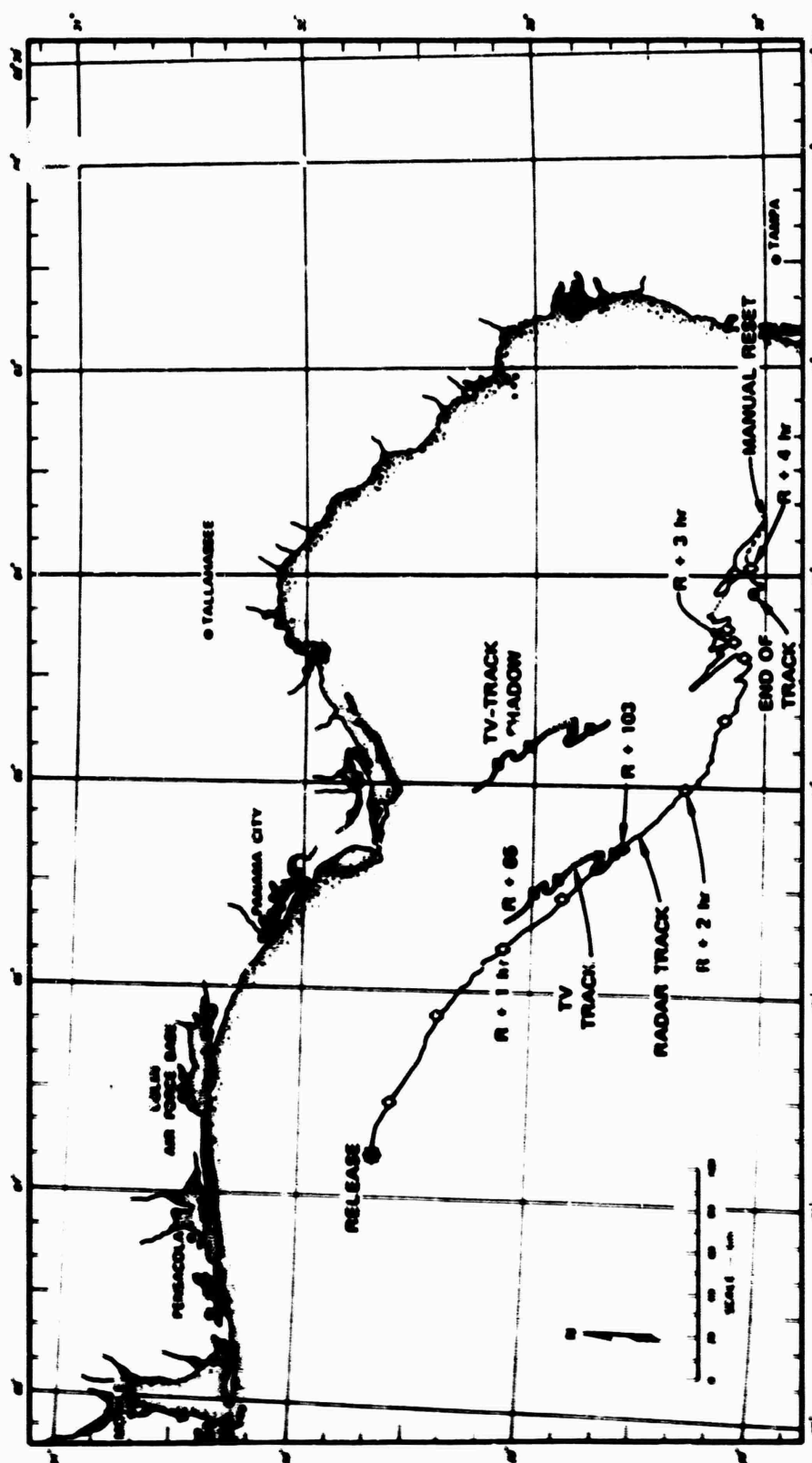
FIGURE 7 TV AND RADAR TRACK OF ION CLOUD — EVENT ESTHER

that of the radar as the overall structure of the cloud becomes more apparent in the darkening sky. In the case of ESTHER, where LES-8 was the transmitting satellite (as opposed to LES-9 for releases ANNE through DIANNE), it was convenient to give the optically derived cloud-shadow track on the same plot, as indicated by the line marked "shadow."

5. Event FERN

Event FERN was much like Event ESTHER insofar as TV-track system operation was concerned. All sites were clear, the cloud was well striated as it became visible, and the Barin view of the cloud was marginally useful. Again, all TV hardware and software worked well and a solid track was maintained from R + 78 to R + 120 min. The cloud was no longer perceptible by R + 126 min.

An attempt was made to center the TV track, shown in Figure 8, on the eastermost area of structured luminosity. It was noticed that, as in the case of ESTHER, the TV track was east of the radar track, but it was assumed that the discrepancy was again caused by different, but equally valid, portions of the cloud being tracked. However, when the aircraft was directed to intercept the cloud shadow generated from the optical track (at about R + 70 min when the radar temporarily lost track on the cloud), the magnitude of the cloud-generated interference effects was observed to decrease markedly. We now believe this is because the TV net was tracking not the head of the main ion cloud, but the eastern end of the ion bridge,[*] which had had sufficient time since release to form striations of its own. This belief is based on the low density of that region as observed by the aircraft, and on the noticeably earlier fading of that region when compared to the main cloud region (implying a significant difference in altitude, and hence a different origin).

Figure 9 is a montage of three views of the cloud as seen from C-6 over a 90-s time span. Region A is the part of the ion cloud upon

---

[*]The term "ion bridge" denotes the nebulous region of barium ionization left by the neutral cloud as it is blown eastward of the main ion cloud. It is produced by photodissociation of BaO, followed by photoionization of the barium, and has a much lower ion density than the main ion cloud.

241
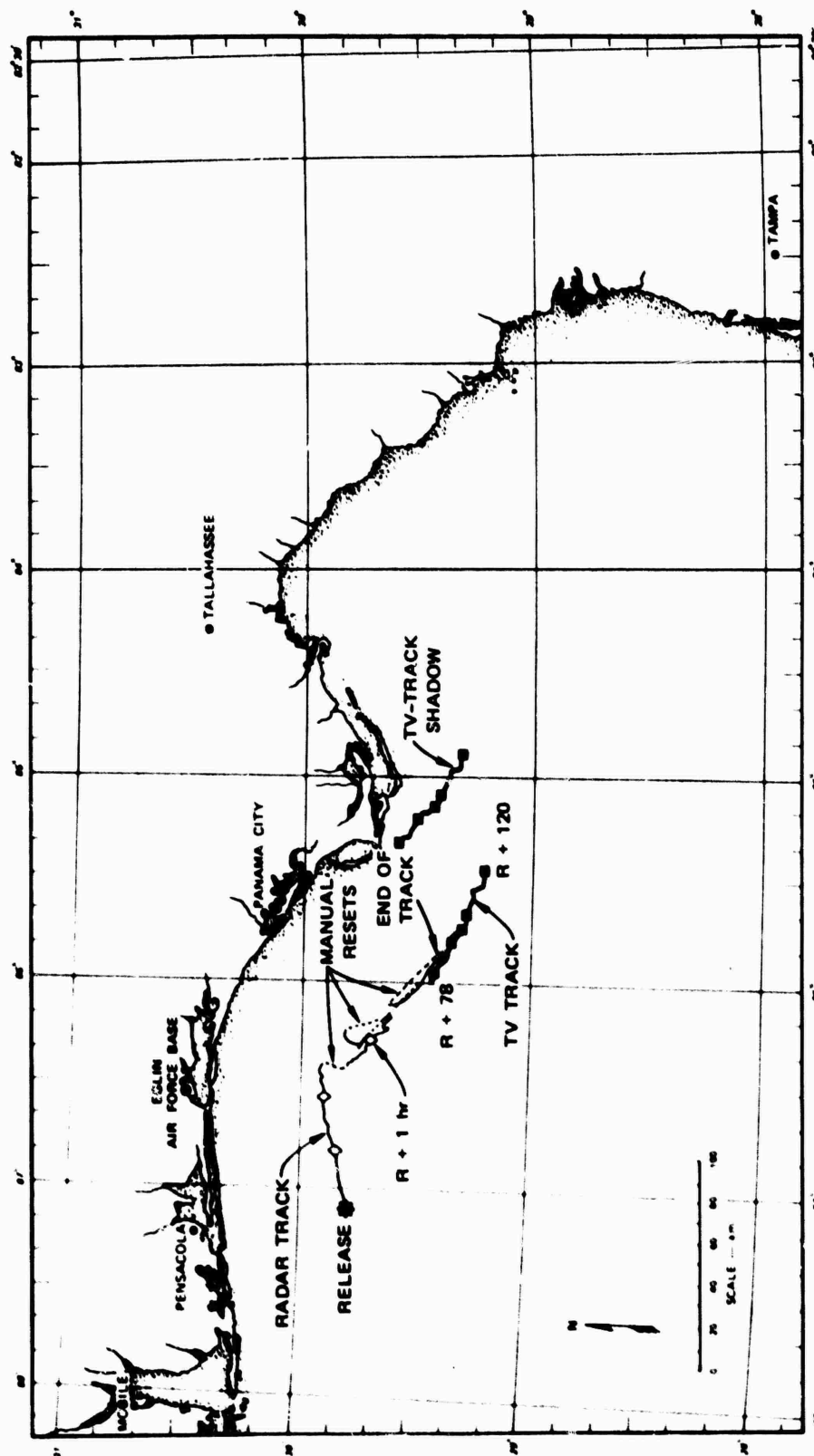
FIGURE 8   TV AND RADAR TRACK OF ION CLOUD — EVENT FERN

242
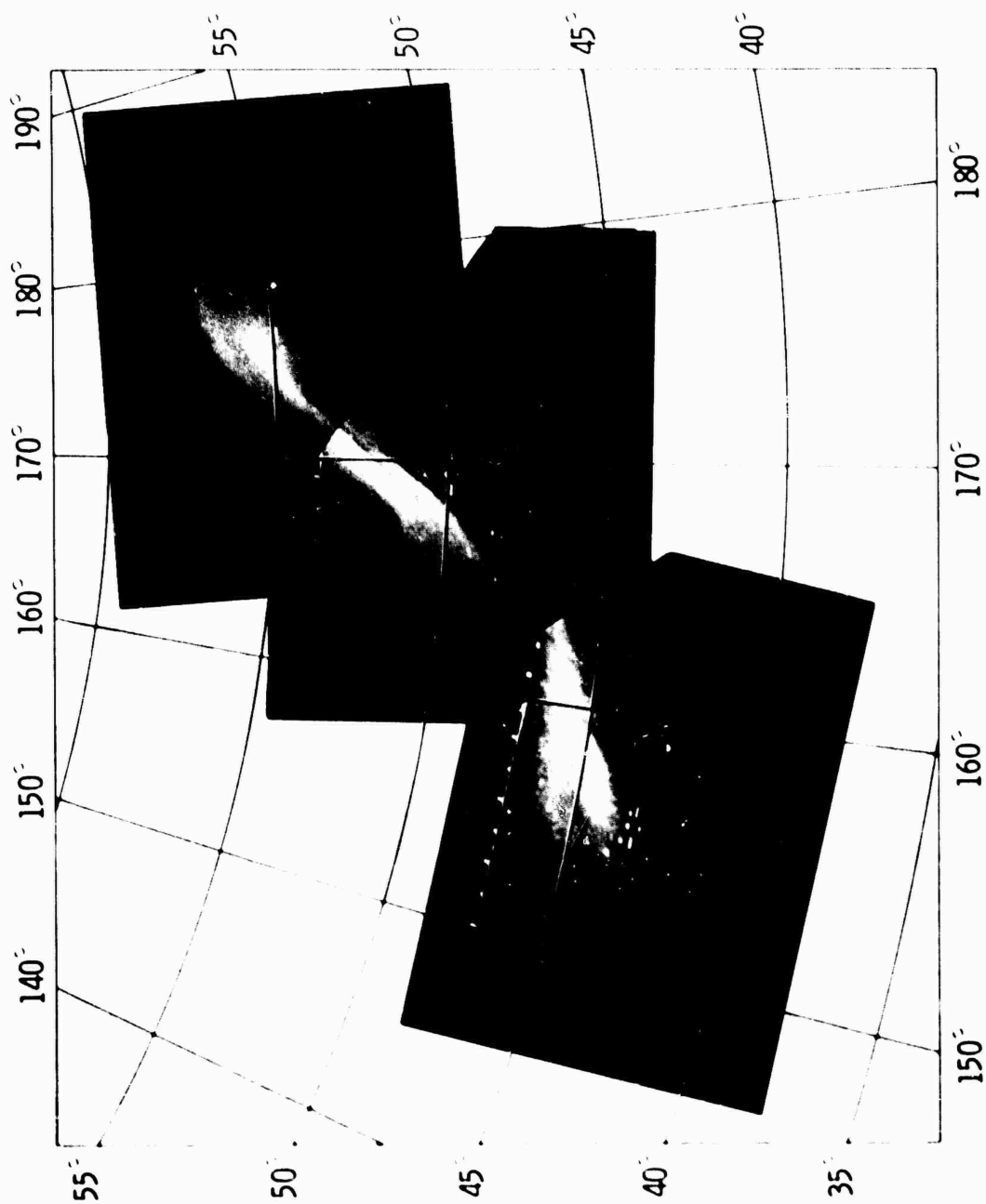
FIGURE 9   MONTAGE OF TV VIEWS OF FERN, AS SEEN FROM SITE C-6 DURING THE 0046-TO-0047:30 TIME PERIOD
(R + 120 min to R + 121 min, 30 s)

which the TV net focussed while tracking the cloud. Region B is assumed to be in the main ion cloud and is the portion of the cloud tracked by the FPS-85. Note that the azimuth and elevation lines in Figure 9 are only approximate, since the montage was created by overlaying TV pictures generated over a 90-s time period.

III COMPARISON OF OPTICAL AND RADIO DATA

To aid in the interpretation of optical and radio data, overlays of azimuth and elevation were generated for selected barium cloud photo-graphs.[*] These overlays were generated by a computer program that used the right ascension and declination of the stars, the location of the viewing station, the time and date of the photographs, and the location of three reference stars in some convenient cartesian-coordinate system appropriate to the pictures. With these inputs, a full-size computer plot was generated for each photograph showing the positions of the stars in the field of view along with lines of constant azimuth and curves of constant elevation referenced to the viewing station.

The accuracy of the overlays was judged by comparing the computer-generated star locations with those in the photographs. In all cases considered in this section, the computer-generated star positions agreed with the actual ones in the photographs to within 0.1% in angular posi-tion. This accuracy was sufficient for our purposes and since photo-graphic paper stretch can introduce errors of this magnitude, no attempt was made to further refine the overlays.

The photographic overlays and the parameters used in generating them provided the means of plotting radar or TV pointing directions (azimuth and elevation) on selected pictures of the barium cloud. The trajectory of the probe rocket viewed from different photographic sites was expressed in terms of azimuth and elevation from the site of interest and plotted

---

[*] The photographs used in this section were graciously provided by Tech-nology International Corp.

on the overlays. With these variables plotted, it is possible to better appreciate the relationship between measurements made by the various radio sensors and our physical view of the barium ion cloud gained largely through optical data.

Two types of radar-derived density data are presented in this section. One type is a plot of electron density (analogous to barium ion density because of charge neutrality) as a function of range for a particular radar pointing direction and time. These plots typically represent at least a 1-s average over 40 pulses. The background ionosphere has been removed, so that what is shown is the excess ionization above the normal ionosphere contributed by the barium ion cloud.

The second type of radar data shows fluctuations in electron density as a function of range for a particular radar look angle and time. These curves were generated by subtracting a "smooth" profile from the unfiltered cloud profiles mentioned above, and show structure related to striations within the ion cloud. Because the procedure used in calculating the fluctuations involves a difference between large quantities, it was particularly error-sensitive and random noise-like peaks can appear. To minimize this type of noise, fluctuations for ESTHER were averaged over four records. FERN, however, was plagued with propagated noise that could not be removed by averaging. Thus, fluctuations for FERN are unaveraged. In either case, the peaks were considered significant only if they persisted over a number of records and if they changed in range with antenna motion.

The "point" tracked by the TV-track operator is also shown in each picture. Comparison of the TV-track point and radar measurements shows how successful the TV-track system was in locating and tracking the region of maximum electron density within the ion cloud. In addition, the juxtaposition of radar measurements with the ion cloud gives a guide in the interpretation of the radar data in terms of our physical picture of the cloud.

245

A. Event DIANNE

Figure 10 shows how Event DIANNE appeared from C-6 around the time
of the second rocket probe (51-2). In the first frame of the montage the
dimensions of the ion cloud are about 10° in azimuth and about 7° in
elevation. Over the next nine minutes the western part (right-hand side)
of the cloud develops a kink but otherwise remains approximately station-
ary in angular position. The eastern part, however, moves toward the
east as striations are "pulled" from the ion cloud.

There is a noticeable decrease in the vertical extent of the ion
cloud with time, and by 0039:09 UT the cloud encompasses only about 4°
in elevation. (Note that this shrinkage occurs in spite of the increas-
ing camera exposure time for each successive frame. This can be deter-
mined by noting that many more stars are visible in the last frame of
Figure 10). Two reasons can be cited for the decrease in vertical extent
of the ion cloud: First, the general downward motion of the top of the
ion cloud is due to the southward drift of the cloud (see Figure 6).
Second, the actual "bottom" of the ion cloud is not visible at late times
because the sun is not illuminating it. Thus, in the last frame of
Figure 10 the ion cloud probably actually extends below 45° elevation.

Views of DIANNE as it appeared from Tyndall are presented in Figure
11. Each of these four pictures was taken at approximately the same
time as its counterpart in Figure 10. As already mentioned in the dis-
cussion of Figure 10, the striated portion of the cloud moved eastward,
and this is also evident in Figure 11. (Compare the upper left portion
of the ion cloud at 0030:35 and at 0038:58.)

In the first and last frame of Figure 10 the regions probed by the
FPS-85 radar are identified by a series of points and lower-case letters.
The projections of these points along the radar line of sight are shown
in Figure 11 (frames at 0030:35 and at 0038:58) as a series of connected
points. The letter identifies the particular point in Figure 10 that was
projected and the number next to the extreme right point in each projec-
tion specifies the radar range in kilometers. Range increases in 5-km
increments toward the left. The approximate position of maximum electron

246
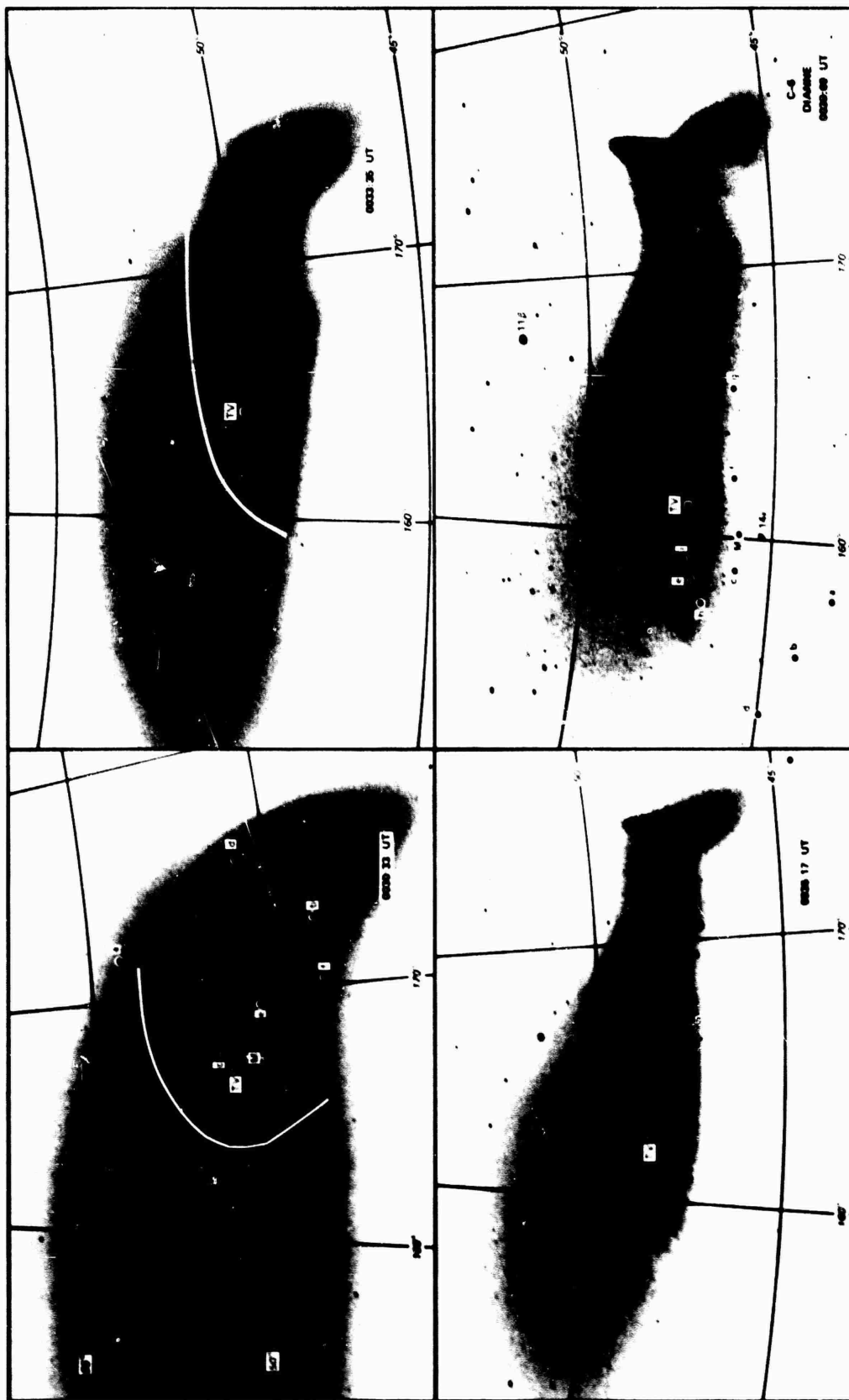
FIGURE 10 VIEWS OF EVENT DIANNE FROM C-6 AROUND THE TIME OF ROCKET PROBE 51-2. The point marked TV represents the boresight of the TV camera at the indicated times. Points identified with letters are where the FPS-85 made measurements around the picture times. Refer to Figures 12 and 13 for the pointing directions of these points, times of the measurements, and the measured profiles.

247

FIGURE 11 VIEWS OF EVENT DIANNE FROM TYNDALL AROUND THE TIME OF ROCKET PROBE 51-2. The point marked TV represents the boresight of the TV camera at the indicated times. Projections of the radar line of sight for the points in Figure 10 are shown as a series of connected data points. Range increases from right to left, with the radar range to the first point as indicated. The large point on each projection represents the approximate position of peak electron density.

density measured by the FPS-85 radar along each look angle shown is identified by the large point on each projection. Electron density profiles corresponding to the lettered points of Figures 10 and 11 are shown in Figures 12 and 13.

As an example of the relationship between Figures 10 through 13, consider point "c" in the first frame of Figure 10. Reference to Figure 12 shows that this profile was taken at 0029:56.3 with the radar pointed at an elevation of 51.61° and an azimuth of 167.63°. The peak density measured was 18.8×10^{12} el/m^3 and occurred at a range of 229 km. The projection of this line of sight on the Tyndall view is shown in the first frame of Figure 11 as the line labeled "c."

In Figures 10 and 11 the point on the ion cloud where the operator was boresighted is identified by a square symbol and the letters TV. No TV symbol is shown in the Tyndall view at 0038:58 (Figure 11) because the point (63.3° elevation, 192.2° azimuth) fell outside the camera's field of view.

From approximately 0031 to 0039 UT no radar data were available due to a power outage. Unfortunately, this loss of data overlaps the flight of the second DIANNE probe. With the data that are available, however, it is possible to infer what would have been measured by extrapolation. These extracted values can then be compared with the rocket measurements.

The maximum density measured by the FPS-85 radar around 0030:33 UT for DIANNE was 40.3×10^{12} el/m^3. This occurred at an elevation of 50.43°, an azimuth of 167.34°, and a range of 208 km. This point is labeled M in Figure 10. Thus, at this time, tracking the steep edge of the cloud from which striations originate is a reasonable procedure to use in order to locate and follow the maximum density region of the ion cloud.

Some idea of the density distribution of the ion cloud can be gained by studying Figures 10 and 12. Note that point "a", which lies above the ion cloud, reveals essentially the background density. Points "d" and "f", on the other hand, which lie near the edge of the ion cloud, have a correspondingly low peak density. In the core of the cloud (b,

249
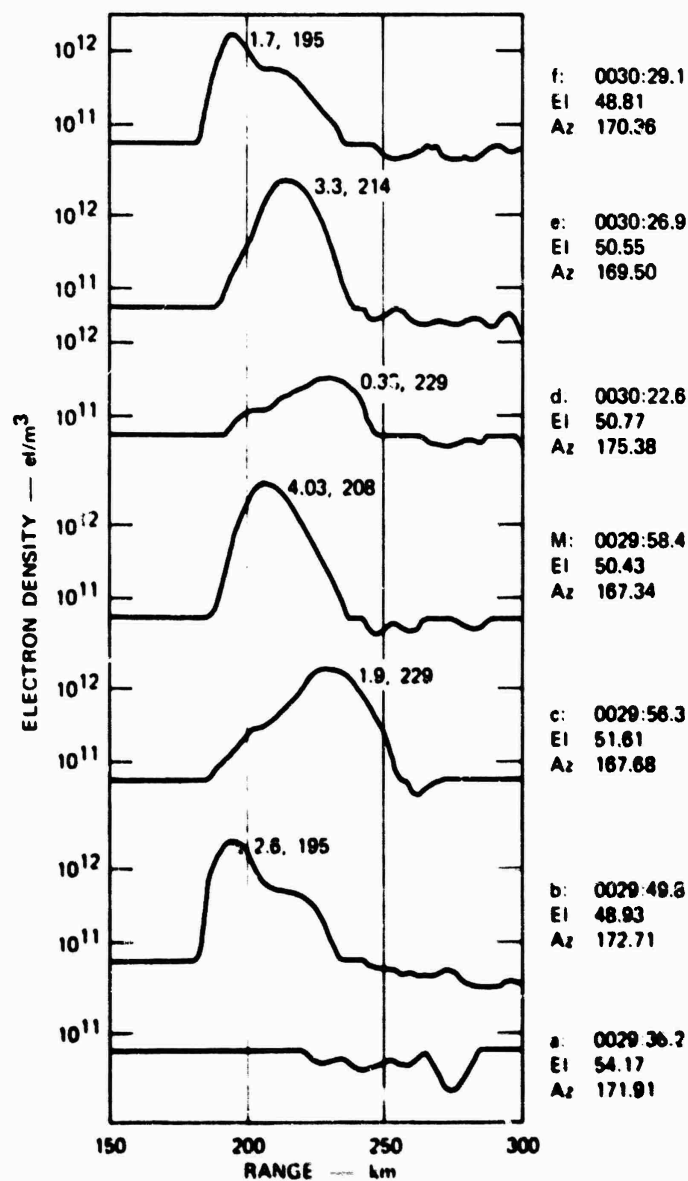
FIGURE 12   SELECTED ELECTRON DENSITY PROFILES FOR DIANNE APPROPRIATE TO
0030:33 UT IN FIGURE 10 AND 0030:35 UT IN FIGURE 11. The pair of
numbers next to each peak represents the peak electron density in units of
10^{12} el/m^3 and the range to this point in kilometers. Time and appropriate
pointing direction are also indicated.
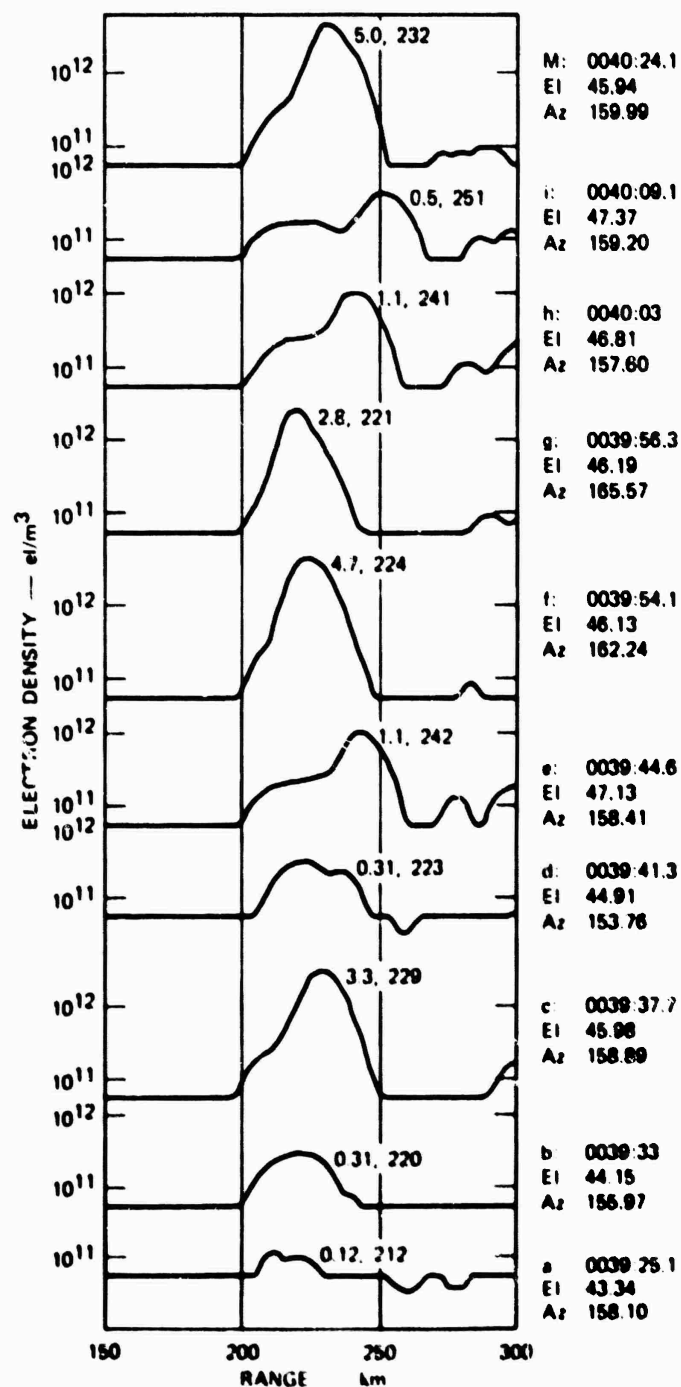
FIGURE 13 SELECTED ELECTRON DENSITY PROFILES FOR DIANNE APPROPRIATE TO 0038:58 UT IN FIGURE 10 AND 0039:09 IN FIGURE 11. The pair of numbers next to each peak represents the peak electron density in units of 10^{12} el/m^3 and the range to this point in kilometers. Time and approximate pointing direction are also indicated.

251

c, e, and M), relatively high densities are recorded. At the time of
this photograph the sun was illuminating the entire ion cloud and hence
the radar measurements appear to be consistent with optics.

At 0039:09 the sun had set on the bottom portion of the ion cloud
and photographs now give a mistaken impression of the actual extent of
the ion cloud. For example, although points b and d appear to lie en-
tirely outside of the ion cloud in the last frame of Figure 10, the
radar measurements shown in Figure 12 indicate that some density (albiet
a low figure) is measured. In fact, around this time, the maximum den-
sity measured was 49.6×10^{12} el/m^3. This point is labeled M and lies
outside of the visible portion of the ion cloud.

Six probe rockets were launched during STRESS to provide in-situ
electron density measurements of the ion cloud. Although all six probes
launched during DIANNE, ESTHER, and FERN (two probes for each barium
release) apparently penetrated the volume of the ion cloud, the penetra-
tion generally occurred at times of poor or no optical coverage. The one
exception was the second probe launched during DIANNE, probe flight 51-2.
This probe entered the cloud around 0034:30 and measured a peak density
of 1.4×10^{12} el/m^3 at a height of 182.71 km. Although the FPS-85 was
inoperative at this time because of a power failure, we estimate from
measurements before and after the power failure that the peak density
within the ion cloud was at least 4×10^{12} el/m^3.

To determine the region probed by the rocket, consider its flight
as viewed from C-6, Grayton Beach, and Tyndall. Six points on the rocket
trajectory are shown in each frame of Figure 14. The point identified
with a "square" is the position of the probe when it first encountered
an increase in ionization above the normal background ionosphere. The
other points starting from this origin locate other significant features
along the rocket path, as summarized in Table 2.

In order for the trajectory points shown in Figure 14 to lie within
the volume of the ion cloud defined by the photograph they must appear
to be superimposed upon the image of the cloud from all three sites.
We emphasize, however, that the actual extent of the ion cloud cannot be

252
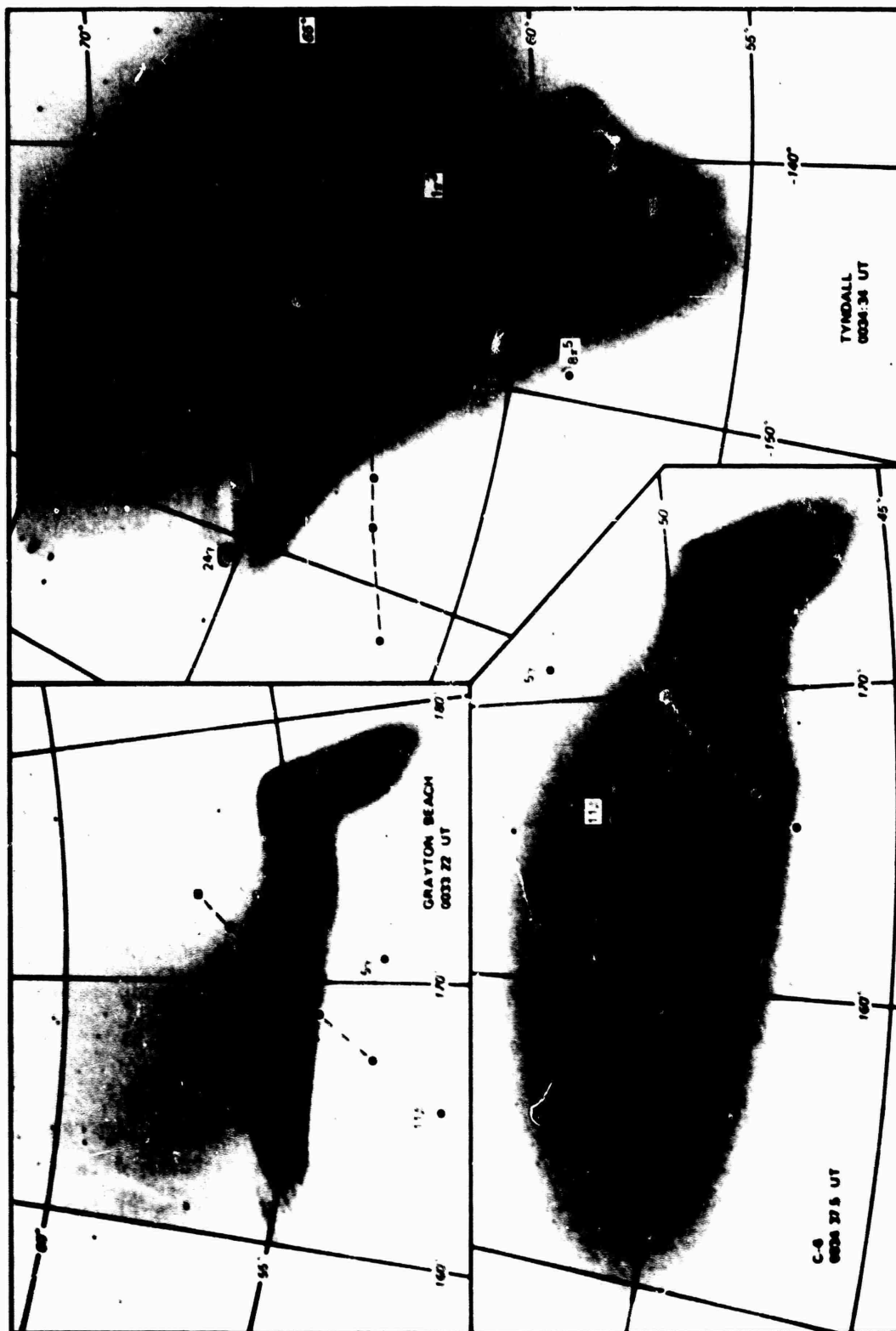
FIGURE 14 EVENT DIANNE: MONTAGE OF PHOTOGRAPHS SHOWING THE TRAJECTORY OF ROCKET PROBE 51-2
ABOUT THE TIME SIGNIFICANT IONIZATION ABOVE THE BACKGROUND WAS MEASURED. Cloud entry
was at the position identified by a black square.

Table 2

SUMMARY OF SIGNIFICANT POINTS
ALONG TRAJECTORY OF PROBE 51-2

Point	Time, UT	Height (km)	Remarks
1	0034:30.6	171.41	Cloud entry
2	0034:35.6	175.07	
3	0034:40.6	178.51	Sheet entry
4	0034:46.6	182.33	Peak density
5	0034:50.6	184.71	Sheet exit
6	0034:59.6	189.52	Cloud exit

sharply delineated and that the photographic extent of the cloud is a
function of exposure time and geometry. That is, the pictures may show
regions of high illumination and not necessarily regions of high electron
densities. Nevertheless, it is useful to interpret the rocket probe data
in terms of its position with respect to the photographs.

An examination of the Tyndall view shows immediately that points
4, 5, and 6 lie outside the visible cloud. A similar conclusion can be
drawn for points 1 and 2 from the Grayton Beach photograph. Although we
can conclude that point 3 probably lies in the cloud, this conclusion is
weakened by the proximity of the point to the top edge of the cloud in
the Grayton Beach photograph. In fact, since maximum density is measured
at point 4, which clearly lies outside of the cloud, we conclude that
probe 51-2 did not penetrate the volume of the ion cloud as defined in
Figure 14. Thus, there is no inconsistency in the lower electron density
measurement made by the probe in comparison with the FPS-85 measurements.

B. Event ESTHER

ESTHER was an important event because of the transmission effects
that it produced. Both rocket probes recorded highly structured data,
but unfortunately no optical data are available during the time of the
probes. Figure 15 shows Event ESTHER at a time (0035 UT) when photo-
graphic and radar data were particularly good. In addition this time is
of interest because strong fading was encountered by the aircraft.
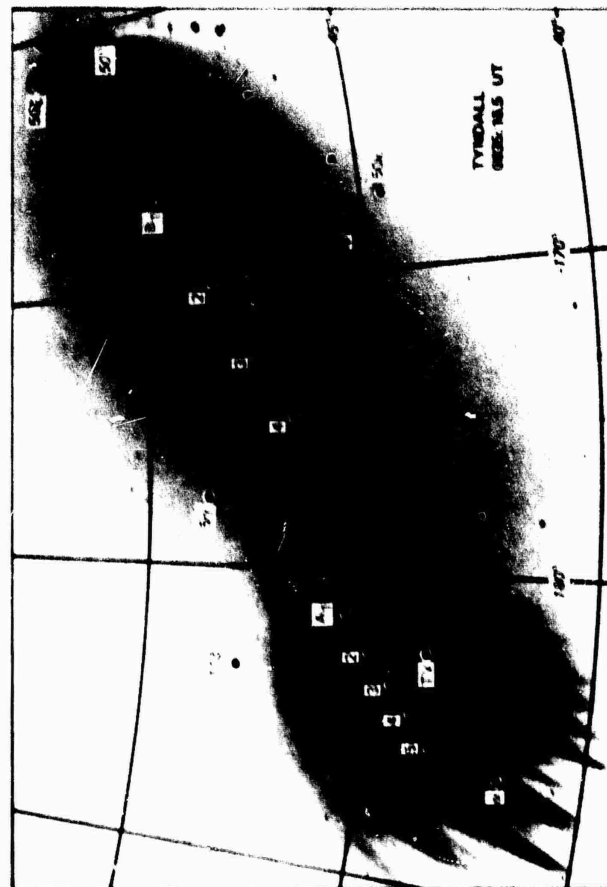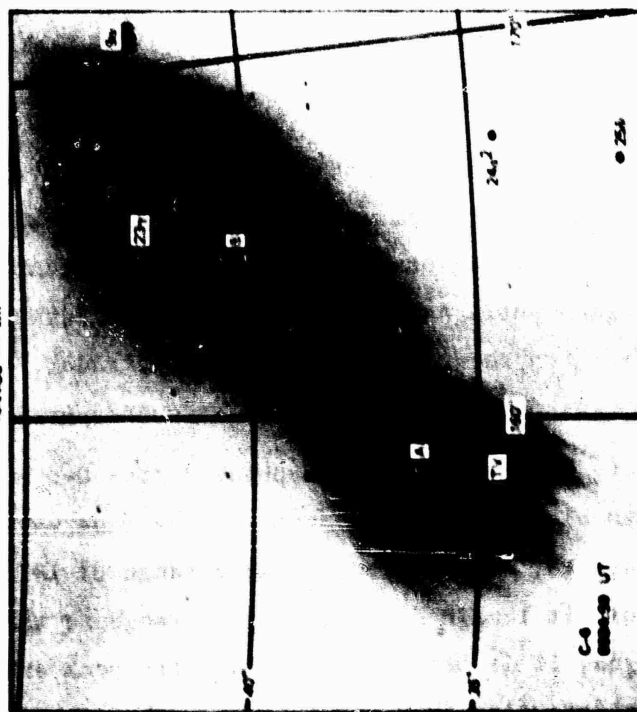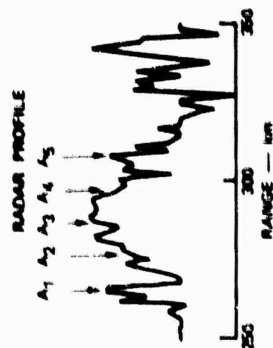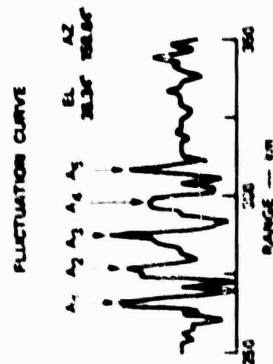
FIGURE 15   THE EVENT ESTHER CLOUD AROUND 0035 UT AND THE RADAR SIGNATURES THAT IT PRODUCED

The region probed by the FPS-85 was generally limited to the lower portion of the cloud around point A. A typical radar-derived electron density profile along the radar line of sight A and the corresponding fluctuation curve, which reveals five well defined "striations," are shown above the photographs. Projection of the radar line of sight through point A onto the Tyndall view shows that the peaks in the fluctuations do bear a close relationship to striations in the ion cloud.

We have also picked a point in the upper portion of the ion cloud not probed by radar, which appears to pierce a rather distinct striation-like feature. Projection of this line of sight on the Tyndall photograph, however, does not single out any particular striation. Points B_1 through B_4 were chosen to be at ranges of 240, 260, 280, and 300 km respectively, from C-6. In contrast to points A_1 through A_5, which are known, because of the radar-derived range information, to lie in the barium cloud, we do not know the status of any of the four B points. Thus, while it is probably correct to associate A_5 with the distinct feature that also appears to lie behind α, we cannot draw similar conclusions for any of the B points. This points out the difficulty of locating an object in space without range information.

C. Event FERN

Event FERN was the most interesting of the six releases from a phenomenology point of view. The first rocket probe first encountered the cloud at an altitude of about 130 km and apparently remained in an enhanced region until an altitude of 210 km. FERN also produced strong E- and F-region returns on the vertichirp radar. These returns persisted for many tens of minutes and had a frequency extent up to 18 KHz.

Figure 16 shows how FERN appeared from C-6 and Tyndall. The radar data, both electron density profiles and fluctuation curves, are shown in the inserts. The sharp peak at a range of 187 km is not understood, but because it remained stationary in range as the radar pointing angle was changed, it is believed to be a noise peak and not cloud-related. The radar data also show significant peaks around the 150-km range

256
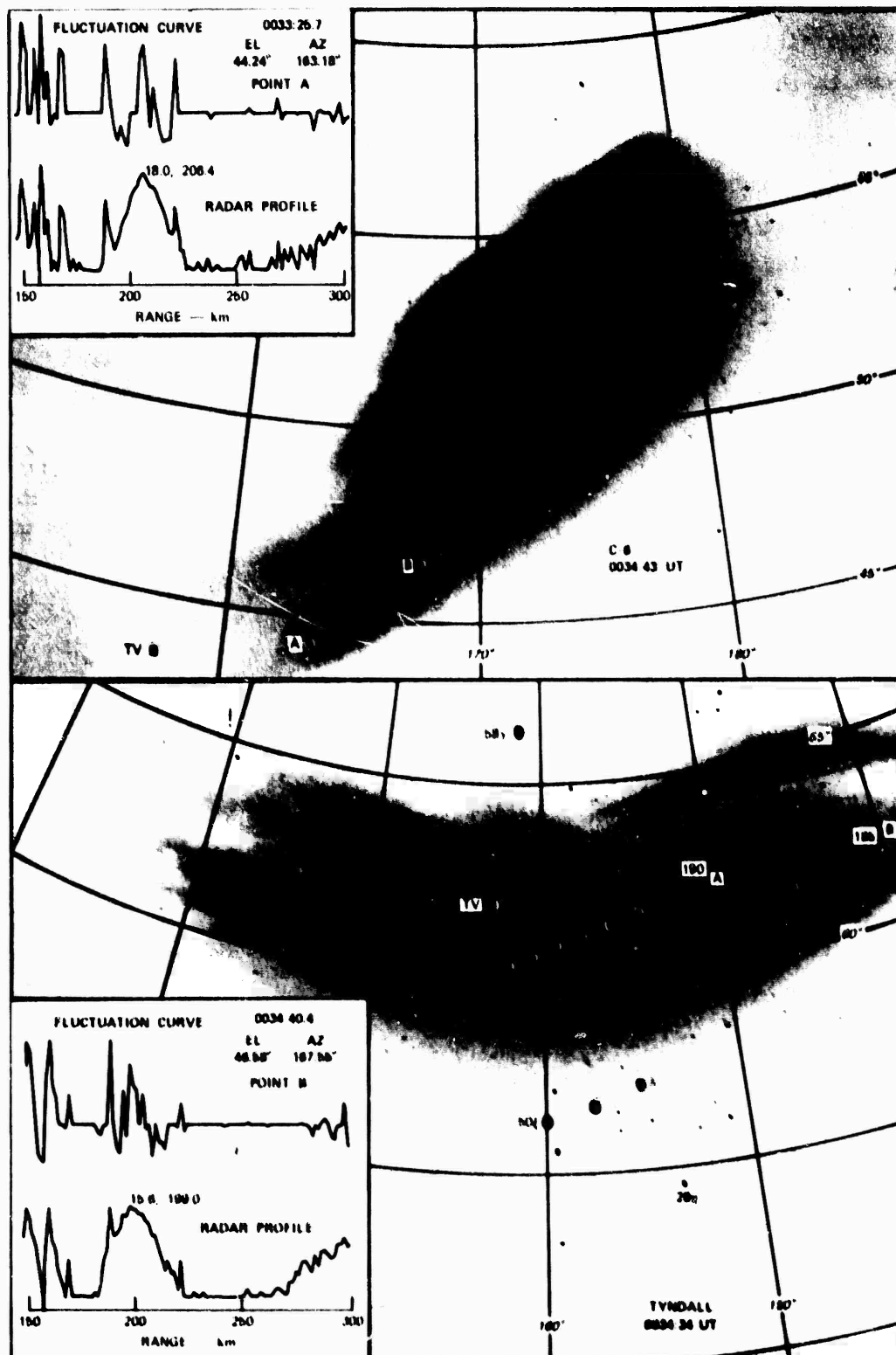
FIGURE 16   EVENT FERN AROUND 0035 UT AND ASSOCIATED RADAR SIGNATURES

(106 km altitude). Some of the features in this region are probably re-
lated to the E-layer returns seen by the Vertichirp radar.

Inspection of the C-6 view of FERN shown in Figure 16 reveals a
distinct feature that extends down and to the left and that we have identi-
fied with an A and a B. In trying to locate this feature on the Tyndall
view we have projected the lines of sight through A and B onto the Tyndall
picture. The extreme point on each projection delineates the extent of
the cloud as determined by the measured electron density profiles. From
these projections, we conclude that the bulk of the ion cloud above
point B in the C-6 view lies to the right and outside the field of view
of the Tyndall camera. The feature of interest in the C-6 view thus
appears to be such a big object that it occupies almost the entire field
of view in the Tyndall photograph.

IV DISCUSSION, CONCLUSIONS, AND RECOMMENDATIONS

The outstanding success of the FPS-85 radar in tracking the STRESS
clouds has largely relegated optical-tracking systems to a backup role
if similar test series are performed in the future. An optical-track
system does, however, provide acceptable backup to the radar. Further-
more, it provides a means for the radar to acquire or reacquire the
cloud if, as in the case of Event DIANNE, the radar gets hopelessly lost.

The TV-track system performance in the field and post-event data
analysis have led to certain conclusions that should be noted for future
reference:

(1) As the ion cloud evolves in time, or as its entire structure
becomes visible in the darkening sky, any optical tracking
system will be forced occasionally to switch track from one
part of the cloud to another in a rather discontinuous fashion.
This is a natural consequence of the physical processes op-
erating on the cloud, and the discontinuities cannot be elim-
inated by any sort of predictive algorithm. The effect of
these discontinuities can be mitigated, however, by a more
sophisticated algorithm for relaying cloud-track information
to a user. Such an algorithm should probably be structured
to account for the finite extent of the cloud in the hori-
zontal direction, and the general location of the chosen

258

track point within that horizontal dimension. A detailed study of the wide variety of clouds observed during STRESS will be very useful in developing any future optical-track systems.

(2) For an optical system used to track the striated region of a barium ion cloud, as opposed to point-tracking a single striation, it is preferable to use a single-site system with an empirical model for the cloud height. The accuracy of such a single-site solution is quite adequate for experiments like STRESS, and the track is not subject to the random fluctuations caused by two sites hunting for a common aimpoint in the cloud.

(3) There were occasions during some of the events when two or more stations did converge on a single identifiable feature and maintain track for a significant period of time. The track precision at these times was much higher than could have been obtained from the radar. On other occasions (e.g., DIANNE), the optical system was tracking trailing-edge striations that were not seen by radar because the average electron density in the radar beam was too low. Although the precision track and the low-density-region track capabilities of the optical system were not important in STRESS, they may be in some future experiments. For a reliable and consistent precision track, however, it is absolutely essential that the central-site operator be supplied with the video from the other participating sites. Only by looking at all views of the cloud can he hope to deve op a mental picture of the three-dimensional shape of the cloud, and intelligently direct aimpoint changes in the various sites. A larger field of view than used for STRESS would also be needed for accommodating late-time barium releases.

REFERENCES

1. S. P. Geller and T. N. Davis, "Tracking Barium Releases Using the TV-Track System," Technical Report No. 2, Contract F-30602-70-C-0179, University of Alaska, College, Alaska (May 1971).

2. D. R. McDaniel, "STRESS Preliminary Field Test Plan," SRI International Memorandum prepared for Director of the Defense Nuclear Agency, Washington, D.C., SRI Project 4769, SRI International, Menlo Park, Calif. (May 1976).

3. V. Gonzalez, "Project STRESS--Radar Tracking of Ion Clouds," Interim Technical Report 1, Contract DNA001-76-C-0341, SRI Project 5575, SRI International, Menlo Park, Calif. (July 1977).

BARIUM RELEASES AND PROBLEMS
OF THE NUCLEAR ENVIRONMENT

J. B. Workman

Berkeley Research Associates
Physical Dynamics, Inc.
Berkeley, California

BARIUM RELEASES AND PROBLEMS
OF THE NUCLEAR ENVIRONMENT

J. B. Workman

Berkeley Research Associates
Physical Dynamics, Inc.
Berkeley, California

ABSTRACT

Plasma enhancements in the ionosphere due to either barium re-
leases or high-altitude nuclear weapons develop fine-scale
structure by the gradient-drift process. The effects of nu-
clear weapons on radio transmission must be modeled by ap-
proximate numerical models. Barium release data are extremely
valuable in testing, modifying, and verifying such models.
This activity is discussed, and an example is treated in this
paper.

I INTRODUCTION

It is well known that striations or small-scale plasma structures
aligned with the Earth's magnetic field in the ionosphere can degrade
UHF radio transmission. In the analysis of satellite communication sys-
tems for the expected conditions in the high-altitude nuclear environ-
ment, the understanding and prediction capability of this structure is a
central issue. In recent years the Defense Nuclear Agency has sponsored
numerous research and development programs to investigate and codify
plasma striation phenomenology.

As a general proposition, it may appear both late in the day and
superfluous to be discussing and questioning the relevance of barium
cloud data and phenomenoly to problems of the nuclear environment. It
was, after all, Project SECEDE observations some years ago, that genera-
ted much of the current interest in striation phenomenology. Initially,
SECEDE was important in calling attention to a new and little understood

263

plasma mechanism, which clearly might have great significance for military systems analysis. Later, the actual data from SECEDE played a central role both in the construction and verification of the early plasma theory and in the early efforts to provide a nuclear environment predictive capability. Thus, from a historical viewpoint, there is no question that barium releases have been immensely relevant to understanding the phenomenology of striations and their potential influence on radio transmission.

The question of the relevance of barium releases to current DNA problems must turn on the ability of the technique to provide new insights or new data that are both important and not obtainable through theory or numerical simulation. The questions of relevance have therefore become much more quantitative and detailed than the broad-brush, first-cut issues of earlier programs. The purpose of the remainder of this paper will be to show the specific manner in which Project STRESS can relate to the actual needs and requirements of current military systems analysis.

Over the years, three mechanisms have been identified for producing fine-scale plasma structure in the nuclear environment. All of the mechanisms are of the fluid interchange type and, qualitatively, have many similarities in their resultant influence on the plasma. The oldest known mechanism is the Rayleigh-Taylor instability that occurs when a low-density fluid attempts to decelerate a high-density fluid. This process occurs at the debris-shocked air interface in the early phase of fireball expansion. A second mechanism is the magnetic interchange instability that operates when curved field lines (in tension) attempt to contain an ionized gas. This process is thought to occur during late-time expansion above the containment of the atmosphere (e.g., Star Fish top side above 1000 km). While both mechanisms above can be important, their limited spatial and temporal extents indicate only a minor threat to UHF communications. Prior to Project SECEDE, however, these were the only plasma structuring processes that had been deduced from actual nuclear test data.

The barium cloud work in conjunction with theoretical and numerical studies has uncovered the role of the third interchange mechanism--the gradient drift instability. This process operates whenever a neutral wind attempts to drag a plasma enhancement across magnetic field lines. Essentially, any partially ionized cloud in the Earth's field can be subject to the instability. In nuclear scenarios, it becomes of paramount importance at later times, when fireball remnants or UV halos can be blown by heave or natural winds. The spatial and temporal range of the mechanism is vast, with the result that virtually the entire battle space must be analyzed and tested for structural growth by this process. Barium cloud experiments provide an ideal field test for both studying the plasma physics and performing actual weapon effects simulations for direct systems evaluations.

In the spatial and temporal regime of greatest concern to communication system analysts, there is no known essential difference between the physics that governs the barium cloud dynamics and the physics that would govern enhanced ionization from a nuclear weapon. There is, of course, a considerable difference in the overall spatial extent of the disturbed region and, for some time periods, a significant difference in the absolute level of plasma density. However, neither of these items is fundamental to the phenomenology of fine-scale structure. As a matter of fact, because the barium cloud is smaller and less dense than a plasma enhancement from a typical weapon, it is probably easier to diagnose and relate to basic plasma theory.

With considerable indebtedness to previous barium field programs, the underlying theory of the gradient-drift instability and its application to ionospheric problems is in reasonably good shape. As an "ivory tower" scientific investigation, there would, today, be little justification for extensive new field programs. On the other hand, viewed as a "real" problem in applied physics, which must provide hard, quantitative predictions, the gradient-drift algorithms can benefit greatly from new barium programs. As a practical matter, even with the general theory in good shape, it is not possible to provide a complete numerical simulation of gradient-drift physics as it relates to

265

ionospheric problems. Scenario predictions for communication systems analysis rely on a series of approximate techniques that can only be tested, refined, and verified by a field test program. While barium releases are not the sole source of actual gradient-drift "data," they remain one of the cleanest and best sources for such information.

In the next section we will discuss the actual requirements and problems that face scenario modelers. In subsequent sections, we will outline the role of barium releases as they relate to these requirements. Finally, we will display some actual data from Project STRESS and show how it is being employed in this task.

II THE SCALE-SIZE PROBLEM

Conceptually, the physics of the gradient-drift process is reasonably simple. The actual mathematical relations, which model the plasma dynamics, are, however, highly nonlinear. The result is that the initial scale sizes in a plasma enhancement are not preserved. In a realistic nuclear scenario, the scale size range may easily exceed one million. Even in the barium cloud itself, the scale size range may exceed 10^4. Such numbers are to be compared, for example, with numerical simulations that have never exceeded a range of about 100, even in the most simplified modeling and using the largest computers available.

The fundamental problem of modeling and simulating plasma microstructure in the high-altitude nuclear environment is scale-size range. All else is detail--necessary and difficult, but not basic.

Figure 1 is a schematic that provides some description of the evolution of scale-size range in a typical high-altitude scenario. We might begin, for example, with a plasma enhancement representing a fireball that is well resolved by the range from 100 km to 1000 km. This would be the deterministic or scenario-dependent range and, of necessity, we would need to apply an "exact" numerical simulation procedure for modeling. With time, the nonlinear physics will drive the initial plasma to both larger and smaller scale-size regimes. A discussion of methods

266
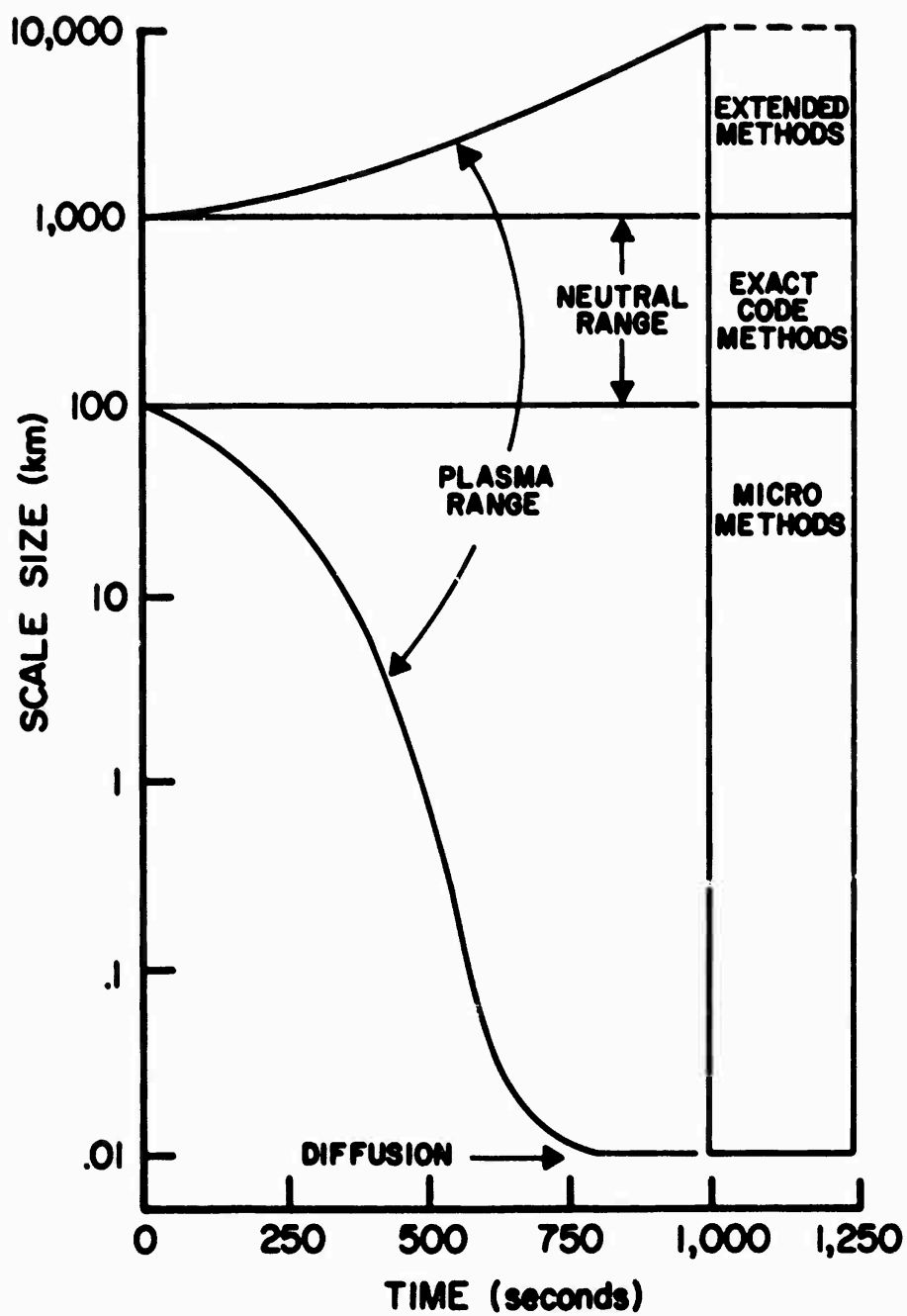
FIGURE 1   SCALE-SIZE DEVELOPMENT

267

for treating the large sizes is outside the scope of this paper and can be ignored for the specific purposes of the barium cloud relevance.

The growth of the plasma to very small sizes is the process that can be modeled only by approximate techniques, and is the regime that the barium data can address. Essentially, all of the plasma residing in this size range--too small to be computed using exact methods--has been labeled by the community as "striations." There is nothing fundamentally different about the plasma dynamics, however. Ultimately, the extension of sizes to smaller and smaller dimensions is limited by cross-field electron diffusion. Considering only classical processes, though, this limit is typically expected to be of the order of ten meters. Thus, the microstructure modeling with all of its approximations is called upon to span many orders of magnitude. Clearly, experimental data that can test or modify this modeling is invaluable.

Figure 2 is a schematic diagram that gives a rough idea of the organization of numerical routines, necessary to perform communication scenario studies. It is, of course, the microstructure modeling that is of specific interest. We will attempt to give a brief review of how such a routine interacts with a large-scale exact code in the course of generating outputs for propagation studies. Experimental data (including barium data) and research studies using numerical techniques both serve to guide the continued development of the microstructure modeling.

III POWER SPECTRAL REPRESENTATION

The general problem of modeling microstructure is that the plasma is distributed over a range of scale sizes in excess of 10^4 in at least two dimensions. Physical space data are not in general available either from experiment or numerical simulation. Actually, even if the data were available, they would be unmanageable for propagation or systems studies.

While the general deterministic description of plasma microstructure is an unresolvable problem, a series of assumptions can be made that will

268
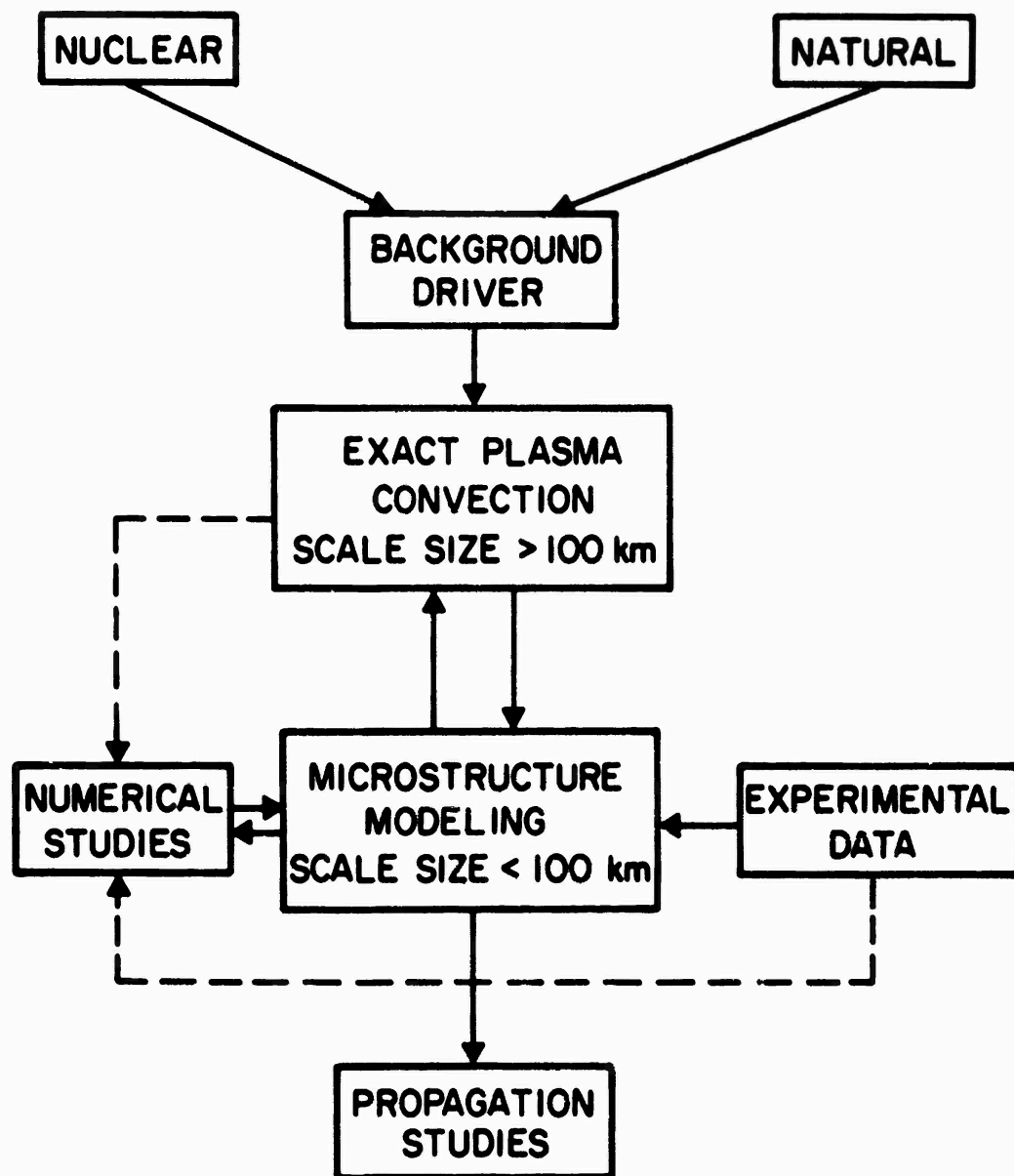
FIGURE 2   COMMUNICATION SCENARIO STUDIES — ORGANIZATION OF NUMERICAL
SIMULATION

permit an approximate solution. The plasma evolution begins in a scenario with only a limited range of large-scale sizes. Experience and intuition tell us that it is only this range that is peculiar or specific to a given example. The vast majority of smaller sizes possess general or statistical properties that are not tied to specific scenarios. Obviously, if this were not the case, there would be no point to any experimental or numerical simulation short of a real detonation. As an observational fact, we note that the overall appearance of gradient-drift microstructures is similar, regardless of the original source.

We assume that the general properties of the structure are calculable using suitable approximation physical models. Likewise, we assume that these properties are adequate for propagation studies. The nature of the general representation is a power spectrum of the plasma perturbations (from the mean).

The plasma power spectrum possesses a number of useful features that allow the simplicity necessary for actually constructing a working model.

The summation or integration of power spectral amplitudes is essentially a conserved quantity. This principle underlies model construction. Information concerning "plasma phase" is lost in the description. However, this is not necessary for either the hydrodynamics or propagation in the "many striation" limit. Transfer of power between regimes in Fourier space is governed by gradient-drift processes. The analytic format of the transfer rates is derivable from theoretical studies.

Of considerable importance is the fact that rate constants and parameters have a generality analogous to chemistry in molecular kinetics. Thus, data can be deduced from a variety of external sources including field experiments.

The distribution of power within spectral regimes is assumed to obey certain simple monotonic functions. This permits a lumped-parameter representation of each regime. From experience and for model convenience, we have chosen to divide the spectrum into four regimes. The first is

270

the macroscopic or exact code regime. It comprises the largest scales, which vary in specific patterns peculiar to the particular scenario. This regime is not modeled, but does provide the necessary inputs and boundary parameters to drive the power-spectrum model.

A connector or "reservoir" regime is defined as a convenient artifice to connect the deterministic macroscopic scales to the statistical modeling of the true microscopic regimes. Of use primarily in transient processes, this regime is assumed (somewhat arbitrarily) to have a flat noise-like spectrum (k^0).

The fully developed or "cascade" regime is assumed to dominate whenever the gradient-drift process can operate without strong transient boundary conditions. It is the classic or fully developed spectrum, which varies as $1/k^2$.

The sink or "diffusion" regime exists for the very smallest sizes, which are subject to significant cross-field diffusion. It has a steep dependence and is presently modeled with a $1/k^6$ variation based on analytic studies. Figure 3 is a schematic diagram that pictorially displays the nature of the various power spectral regimes. The function of the microstructure model is to compute the Fourier space extent and the total power for each characteristic regime.

In briefly reviewing the nature of the microscopic modeling, let us first define a one-dimensional Fourier analysis of a trace through the normalized plasma density, n/n_o:

$$\frac{n}{n_o} (x) = \sum_k f_k \, e^{i\theta_k} \, e^{ikx} \tag{1}$$

where f_k is the real positive mode amplitude, and θ_k is the plasma phase. In the wavenumber space of actual application of the model, all such traces are taken as identical regardless of direction in the two-dimensional plane perpendicular to the magnetic field. The power-spectral summation is then defined as

RESERVOIR

f_R f_C

log PSD

k_R k_C

log k

CASCADE

f_C $1/k^2$

log PSD

f_D

k_C k_D

log k

DIFFUSION

f_D

log PSD $1/k^6$

∞

k_D

log k
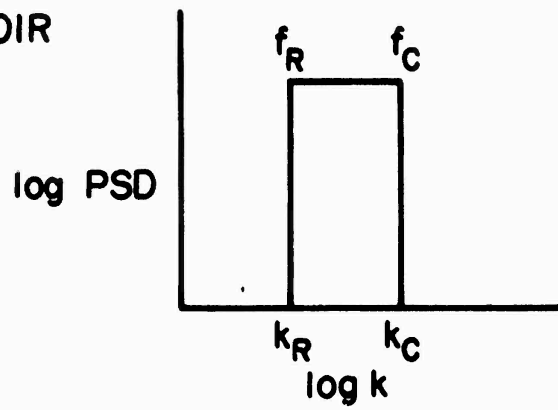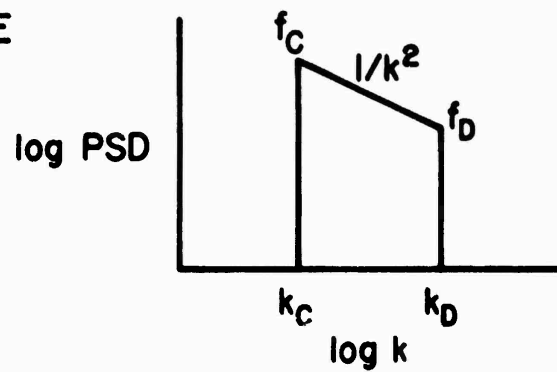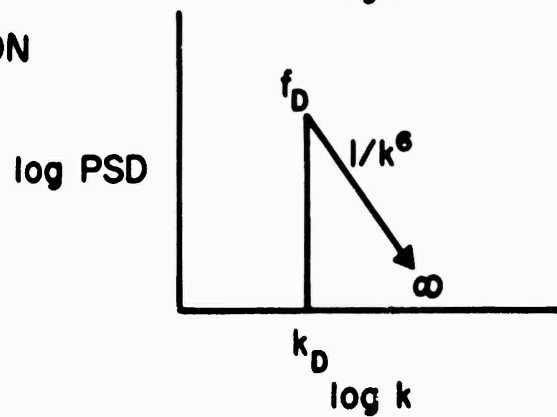
FIGURE 3   STRUCTURE REGIMES

272

$$F = \sum_k f^2(k) \quad . \tag{2}$$

For each individual regime, then, the component summation is

$$F_O = \sum \text{macroscale} \qquad 0 < k < k_R$$

$$F_R = \sum \text{reservoir} \qquad k_R < k < k_C$$

$$F_C = \sum \text{cascade} \qquad k_C < k < k_D \tag{3}$$

$$F_D = \sum \text{diffusion} \qquad k_D < k < \infty$$

and the overall summation conservation becomes

$$\frac{dF_O}{dt} + \frac{dF_R}{dt} + \frac{dF_C}{dt} + \frac{dF_D}{dt} = -\text{diffusion} \quad . \tag{4}$$

In transferring power from one wavenumber regime to another, we use a symbol, R_{mn}, for the rate, where m corresponds to the large size regime from which power is removed, and n corresponds to the smaller size regime to which power is added. For each regime, then, there exists a conservation relation of the form

$$\frac{dF_O}{dt} = -R_{OR} - R_{OC} - R_{OD}$$

$$\frac{dF_R}{dt} = R_{OR} - R_{RC} - R_{CD}$$

$$\tag{5}$$

$$\frac{dF_C}{dt} = R_{OC} + R_{RC} - R_{CD}$$

$$\frac{dF_D}{dt} = R_{OD} + R_{RD} + R_{CD} - \text{diffusion} \quad .$$

273

Simple gradient-drift theory has demonstrated that mode amplitudes in regime n grow from gradients in regime m with the following rate:

$$\frac{df_n}{dt} = - (\Delta U) \left(\frac{\nabla n}{n}\right)_m f_n$$ (6)

where ΔU is the ion-neutral slip velocity. Defining a mean regime wavenumber, $\bar{k}$, as

$$\bar{k}_m \equiv \frac{\displaystyle\sum_{k}^{m} k^2 f^2}{F_m}$$ (7)

We can rewrite Eq. (6) in Fourier form as

$$\frac{dF_n}{dt} = (\Delta U) \ \bar{k}_m \ \sqrt{F_m} \ F_n \quad .$$ (8)

Integrating over the entire regime n and expressing as a rate, we obtain

$$\frac{dF_n}{dt} = 2(\Delta U) \ \bar{k}_m \ \sqrt{F_m} \ F_n$$ (9)

$$\text{or}$$

$$R_{mn_\alpha} = 2(\Delta U) \ \bar{k}_m \ \sqrt{F_m} \ F_n \quad .$$ (10)

Expresion Eq. (10) corresponds to what has been called "seed growth." Another class of gradient-drift power transfer has been investigated that is known as bifurcation. The rate for this process has been similarly constructed to be

$$R_{mn_\beta} = 2(\Delta U)\, \bar{k}_m\, \sqrt{F_m}\, \frac{\bar{k}_m}{\bar{k}_n}\, F_m \quad . \tag{11}$$

The symbols α and β refer to seed and bifurcation respectively.

Putting all of the rate expressions back into Eq. (5), we obtain the working equations actually employed in the microstructure model:

$$\frac{1}{2}\frac{dF_R}{dt} = (\Delta U)\bar{k}_o F_R\sqrt{F_o} - \alpha_1(\Delta U)\bar{k}_R F_C\sqrt{F_R} - \alpha_2(\Delta U)\bar{k}_R F_D\sqrt{F_R}$$

$$+ \beta_1(\Delta U)\bar{k}_o F_o\sqrt{F_o}\,\frac{\bar{k}_o}{\bar{k}_R} - \beta_2(\Delta U)\bar{k}_R F_R\sqrt{F_R}\,\frac{\bar{k}_R}{\bar{k}_C}$$

$$\frac{1}{2}\frac{dF_C}{dt} = (\Delta U)\bar{k}_o F_C\sqrt{F_o} + \alpha_1(\Delta U)\bar{k}_R F_C\sqrt{F_R} - \alpha_3(\Delta U)\bar{k}_C F_D\sqrt{F_C}$$

$$+ \beta_2(\Delta U)\bar{k}_R F_R\sqrt{F_R}\,\frac{\bar{k}_R}{\bar{k}_C} - \beta_3(\Delta U)\bar{k}_C F_C\sqrt{F_C}\,\frac{\bar{k}_C}{\bar{k}_D}$$

$$\frac{1}{2}\frac{dF_D}{dt} = (\Delta U)\bar{k}_o F_D\sqrt{F_o} + \alpha_2(\Delta U)\bar{k}_R F_D\sqrt{F_R} + \alpha_3(\Delta U)\bar{k}_C F_D\sqrt{F_C}$$

$$+ \beta_3(\Delta U)\bar{k}_C F_C\sqrt{F_C}\,\frac{\bar{k}_C}{\bar{k}_D} - \epsilon D\, \bar{k}_D^2\, F_D \quad . \tag{12}$$

Founded on the best current theoretical understanding, the formulation of the microstructure model is nonetheless only a best-estimate approximation to the rigorous plasma dynamics. To allow for adjustment based on experimental data or other sources, data or other sources, one will note the coefficients α and β that have been introduced. Likewise, the classical diffusion coefficient, D, has been multiplied by an adjustable coefficient, ϵ.

To complete the set of relations in the modeling, one must introduce a number of simple constitutive relations:

$$F_R = f_R^2 (k_C - k_R)$$

$$F_C = \frac{f_C^2 k_C^2 (k_D - k_C)}{k_D k_C}$$

$$F_D = \frac{1}{5} f_D^2 k_D$$

$$f_R = f_C$$

$$f_C = \frac{k_D}{k_C} f_D$$

$$k_R = \text{Minimum plasma code dimension}$$

$$\bar{k}_o = \frac{1}{2} k_R$$

$$\bar{k}_R = \left[\frac{1}{3} (k_C^2 + k_R^2 + k_C k_R) \right]^{1/2}$$

$$\bar{k}_C = \sqrt{k_D k_C}$$

$$\bar{k}_D = \left(\frac{5}{3} \right)^{1/2} k_D \quad . \tag{13}$$

The adjustable coefficients in the modeling are set equal to unity in the absence of any external data sources. The barium release data, however, provide a vehicle for both testing the general format of the routine and indicating actual adjustments to the coefficients. The data from Project STRESS are not, at this date, sufficiently reduced to permit an absolute comparison to the model. There is, however, preliminary material to give some insight into future directions. In the next section, we will display an example of the technique for relating barium data to the microstructure model.

276

IV PRELIMINARY DATA COMPARISON

The microstructure model is intended for application where there is
a well-defined quantity of plasma that can be temporally followed in a
Lagrangian sense and where the driving conditions are reasonably uniform
in space across the plasma (but, of course, time-dependent). In a numeri-
cal simulation of a nuclear scenario, this quantity of plasma would
normally correspond to the material in a single cell of the overall,
large-scale exact code. If, for example, the large code contained
10,000 cells, there would be 10,000 parallel computations of the micro-
structure evolution. In simulating the development of structure in a
field experiment, it is desirable to try to identify the actual volume
of plasma to which the time-dependent data refers. Hopefully, this
volume is small enough to be driven by reasonably uniform spatial condi-
tions, but large enough to contain sensible average statistical micro-
structure properties.

In Project STRESS, the aircraft/satellite transmission experiment
conducted by ESL would appear to be a good candidate. By repeatedly
scanning the entire span across the structured part of the cloud, but
only this part of the cloud, they would appear to have collected an opti-
mum data set for comparison.

For an absolute comparison of field data and model computation, it
will of course be necessary to have a fully quantitative plasma density
power spectrum plotted in wavenumber coordinates. At this stage of re-
duction, there is available only an electromagnetic transmission phase
power spectrum plotted in frequency coordinates. Thus, our example com-
parison can test only qualitative behavior. In particular, we can de-
termine if power is flowing to the proper characteristic regime, but we
cannot be certain of the absolute coordinates in either spectral ampli-
tude or wavenumber coordinates. If we fit the phase data with an inverse
power law, we can subtract a unit to obtain the equivalent plasma data.

277

We will employ the ESL data for Event ESTHER, which is relatively
complete in the time span of R + 900 s to almost R + 9000 s and cor-
responds to a conveniently parameterized cloud.

Figure 4 shows the experimental spectrum at R + 900 s, while Figure 5
shows the data at R + 8300 s. We have overlaid a line corresponding to
a $1/k^3$ phase spectrum, which is labeled $1/k^2$ for its equivalent in a
plasma spectrum. All of the intervening data are of identical character.

Clearly, all of the observable data are in the cascade regime and
probably little changed in amplitude over the span of the experiment.
The horizontal coordinate spans two to three orders of magnitude, with a
midpoint magnitude that will probably correspond to an inverse kilometer.

In simulating the evolution of a single cell of isolated plasma en-
hancement. we need supply only the initial value of F_o, which the macro-
scale will feed to the microscale model, and we must specify the time-
dependent value of the slip velocity, ΔU. Preliminary data reduction
shows ΔU to be more or less constant and equal to approximately 10 m/s.
Assuming that the bulk of the initial barium ionization is contained in
the observed volume, we can estimate the spectral summation as follows.

Taking the cloud to be an initially symmetric Gaussian in the two
cross-field dimensions,

$$n(x, y) = n_o \, e^{-K_o^2(x^2 + y^2)} \quad , \tag{14}$$

the power spectrum is simply

$$\hat{n}^2(k_x , k_y) = \left(\frac{n_o \pi}{K_o^2}\right)^2 e^{-\frac{1}{2K_o^2}(k_x^2 + k_y^2)} \tag{15}$$

where K_o is the inverse characteristic dimension.

Expressed as a normalized (or detrended) spectrum in one-dimensional
form, Eq. (15) becomes

$$f^2 = e^{-k^2/2K_o^2} \quad , \tag{16}$$

278
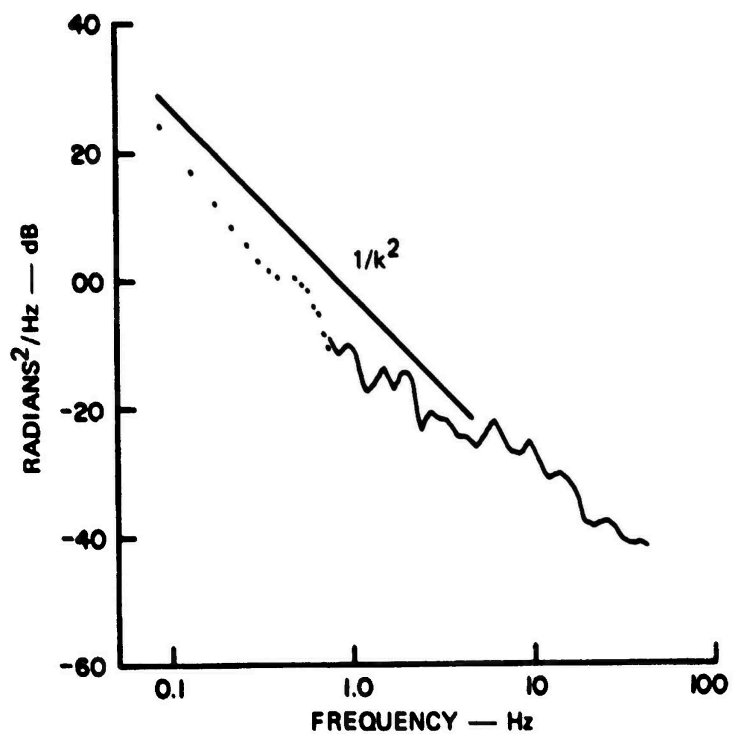
FIGURE 4   ESL DATA — ESTHER, PASS 3, 900 s
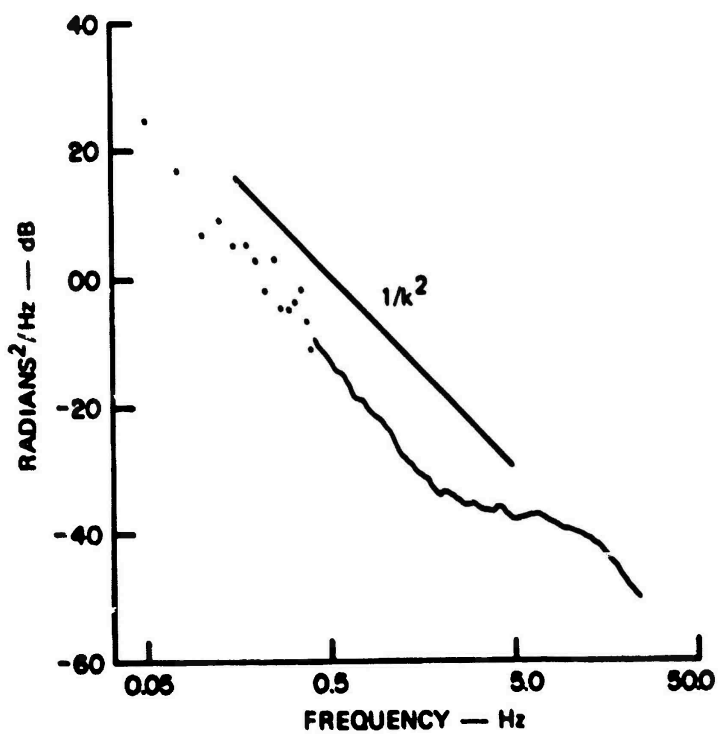
FIGURE 5   ESL DATA — ESTHER, PASS 32, 8880 s

279

$$F = \int_0^\infty f^2 \, dk = \sqrt{2\pi} \, K_0 \qquad . \qquad (17)$$

For a 48-kg release at 185 km, it is not unreasonable to take $1/K_0 = 4$ km. Thus, we will assume that F_0 (initial) is 0.63 km^{-1}.

Placing all of the power in the macroscale to start, the initial microscale power spectrum will be blank as in Figure 6. The horizontal coordinate is in inverse log kilometers. It therefore ranges from 10 km on the left to 10 cm on the right. The first series of outputs will be computed with all rate coefficients set equal to unity.

Figure 7 shows the computational output at 900 s. We immediately note that it does not correspond to the experimental data. Power has flowed into the micr. scale and created a visible reservoir region, but there is no evidence of any cascade region at this time.

Continuing the unadjusted coefficient computation, we note the first appearance of any cascade region at 1800 s, as shown in Figure 8. Finally, in Figure 9 at 8880 s, the cascade region has become significant and spans much of the wavenumber space between 1 km and 10 m. It is fairly clear in this example, however, that the model is not reproducing the character of the experimental data.

Reviewing the model output, we observe that we need to increase the flow of power out of the reservoir and into the cascade region by a sub-stantial amount to more closely approximate the nature of the data. The easiest way to achieve this effect is to increase β_2. Thus, we redo the computation but with β_2 set equal to ten.

Figures 10 and 11 display the new computational result at 900 and 8880 s. Notice that we have achieved the desired effect and the numeri-cal plot is qualitatively consistent with the experimental data.

Until the experimental data reduction is completed, it is not worth-while to pursue the comparison exercise in great detail. Nonetheless, it is hoped that this small example provides some insight into the relevance of barium data to systems analysis models. Obviously barium data, for as

280
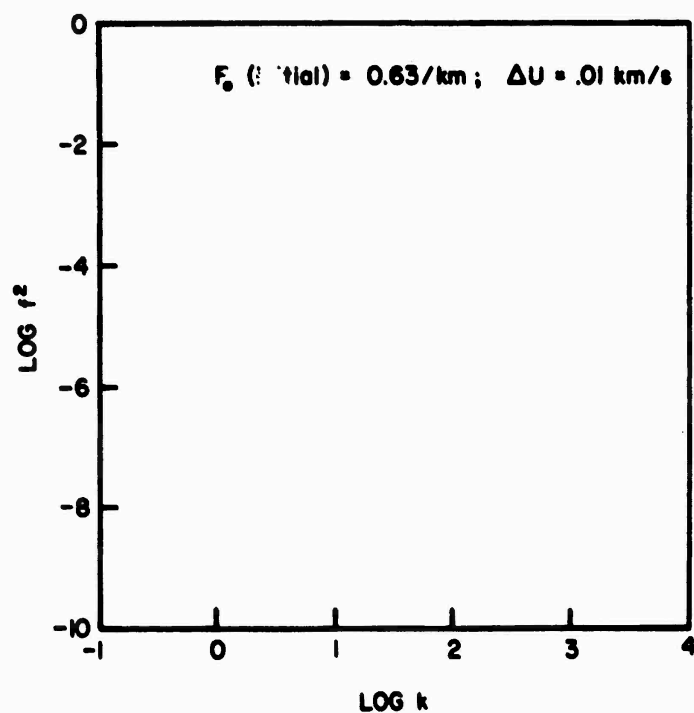
FIGURE 6   MICROSTRUCTURE MODEL — ESTHER SIMULATION
0 s, $\beta_2 = 1$
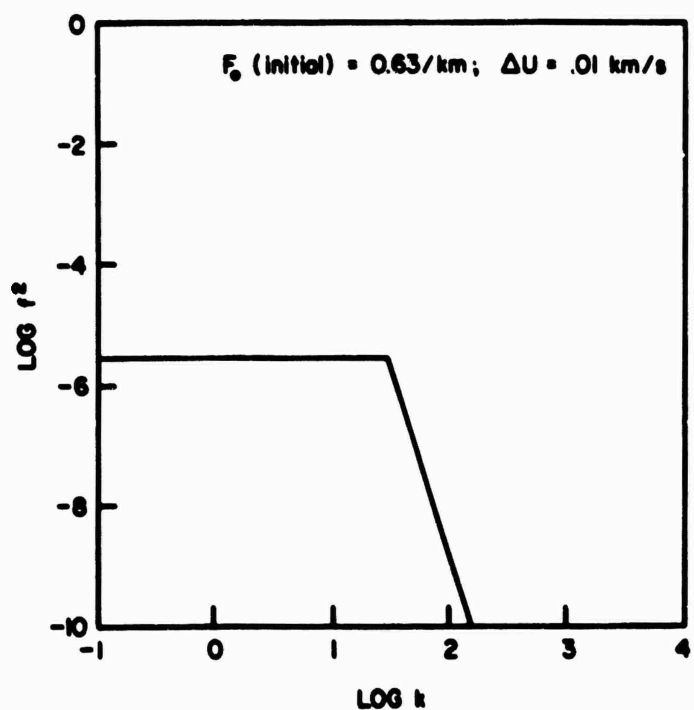
FIGURE 7   MICROSTRUCTURE MODEL — ESTHER SIMULATION
900 s, $\beta_2 = 1$

281
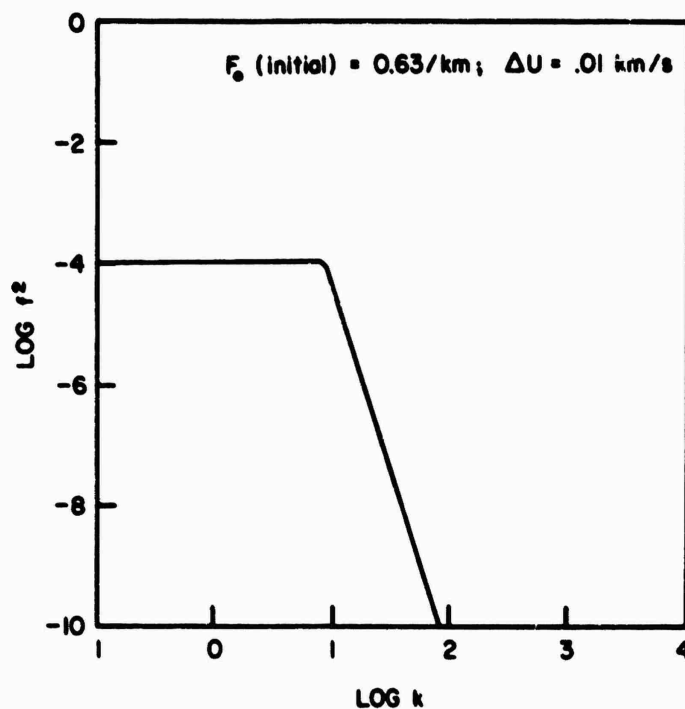
FIGURE 8   MICROSTRUCTURE MODEL — ESTHER SIMULATION
1800 s, $\beta_2 = 1$
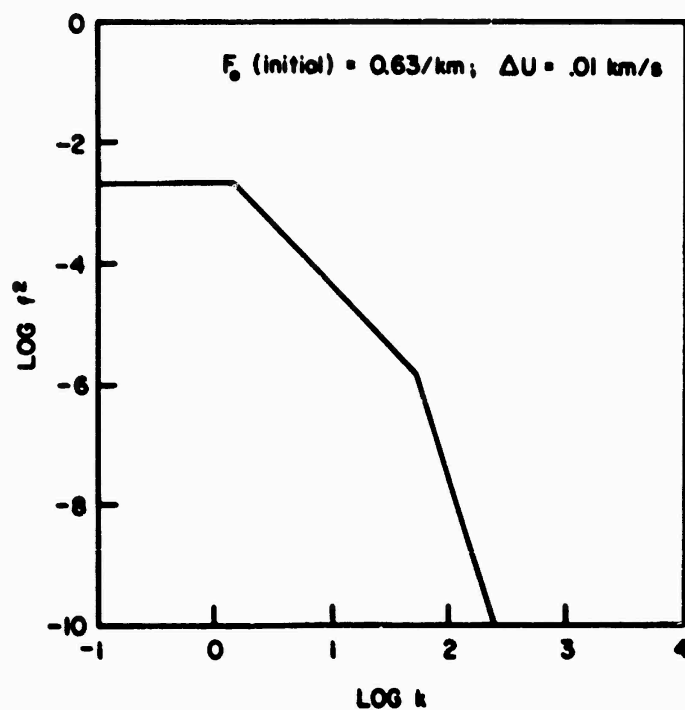
FIGURE 9   MICROSTRUCTURE MODEL — ESTHER SIMULATION
8880 s, $\beta_2 = 1$

282
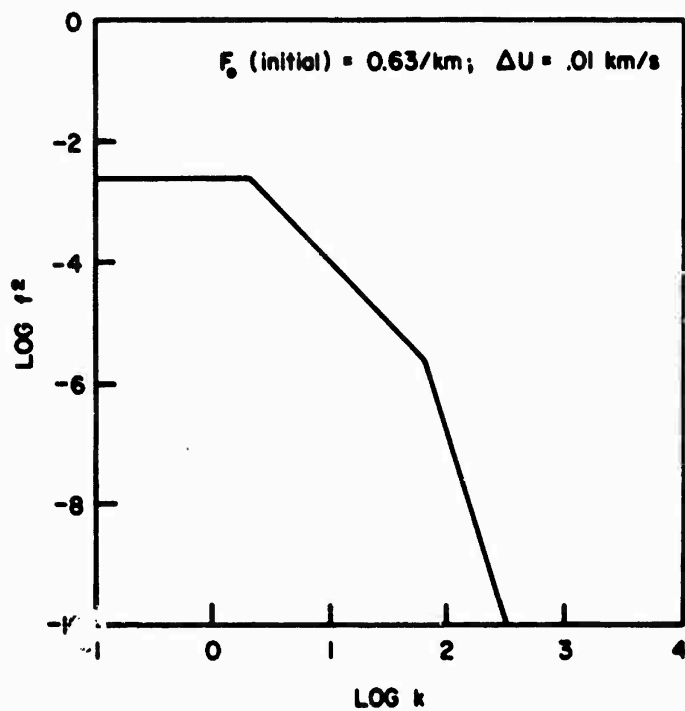
FIGURE 10   MICROSTRUCTURE MODEL — ESTHER SIMULATION
900 s, β_2 = 10
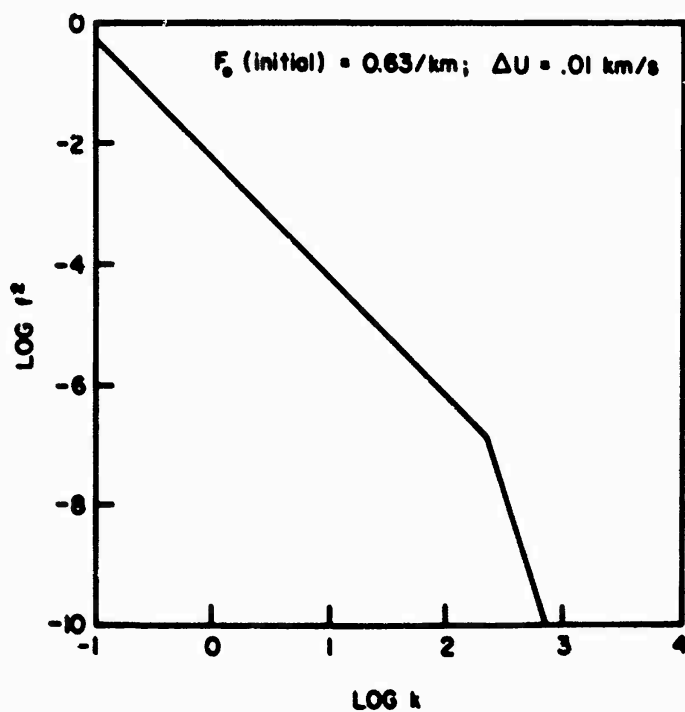
FIGURE 11   MICROSTRUCTURE MODEL — ESTHER SIMULATION
8860 s, β_2 = 10

283

wide a range of driving and temporal conditions as possible, are highly
desirable.

Because neither nuclear testing nor exact numerical simulation is
possible today, barium data provide one of the very few sources of in-
formation with which to test, modify, and verify weapon effects models.

V BIBLIOGRAPHIC NOTE

Older references that describe the relevance of Project SECEDE and
that might normally have been mentioned are all classified. It did not
seem reasonable to classify the present document merely to list these
references. A detailed document that describes the microstructure model
is in preparation by the author and will be available at a future date.
The ESL data discussed in this report were furnished by C. Prettie and
J. Lehman and their assistance in preparing this document is gratefully
acknowledged. A complete report on fully reduced ESL data will be avail-
able at a future time.

THE RELEVANCE OF BARIUM CLOUD EXPERIMENTS

S. L. Ossakow

Naval Research Laboratory
Washington, D.C.

THE RELEVANCE OF BARIUM CLOUD EXPERIMENTS

S. L. Ossakow

Naval Research Laboratory
Washington, D.C.

ABSTRACT

The effects of ionospheric irregularities on satellite C^3 systems are discussed. The methods for predicting nuclear striations (irregularities) within the context of the large zero-order or mean-flow predictive computer codes are presented. The similarities between nuclear cloud and barium cloud (striations) structure are discussed. In both environments the dominant instability mechanism is a plasma fluid type, driven by a plasma density gradient and a current perpendicular to the density gradient (with both perpendicular to the ambient magnetic field). In both the nuclear cloud and barium cloud situation, the instability is called the $\vec{E} \times \vec{B}$ gradient-drift (slip) instability. The equations governing the irregularities in each case are the same. The nonlinear evolution of this instability in the respective environments lead to a power-law power spectrum for the electron density fluctuations (irregularities) at late times. These and other features suggest that barium cloud experiments can help validate the theoretical and numerical simulation techniques used to predict striation phenomenology.

I INTRODUCTION

Many ideas explaining the structure--i.e., striations (magnetic-field-aligned electron density fluctuations)--produced in the nuclear environment have evolved since the last U.S. high-altitude nuclear detonation in 1962 and the follow-on nuclear test ban treaty. Moreover, the theoretical plasma physics capable of explaining striations did not exist in 1962. This, coupled with the sparsity of relevant nuclear data (approximately 90% of nuclear data is optical in nature) has made it

287

difficult to corroborate, in anything other than a gross fashion, many of the theoretical explanations for the structured nuclear environment. In light of the above, it has become extremely important to seek relevant non-nuclear environments that exhibit many of the fine-scale (structure) features of the nuclear situation so that our theoretical and computational results can be tested.

An understanding of the structured (irregularities, striations, electron density fluctuations) nuclear environment is extremely important for satellite C^3 and navigation systems that wish to operate successfully in such an environment. Again, our understanding of structure effects on satellite electromagnetic propagations through such a medium comes from the natural scintillating environment. For example, amplitude scintillation effects can be found in the TACSAT satellite transmissions at 250 MHz (25 to 30 dB fades) and in the COMSAT satellite transmissions at 4 to 6 GHz (a few dB of fade), both operating over the equatorial region at night (spread-F/scintillation phenomena). Much data, relating to the natural ionosphere, exists in the VHF-UHF regime to show that scintillation effects are not just a chance occurrence (e.g., scintillation effects at the equator occur on 30 to 60% of the nights). Recently, propagation studies have been carried out during Project STRESS, utilizing fully striated barium clouds. These studies have shown that LES 8/9 UHF communication signals received by an AFAL Satellite Communication System on-board a C-135 type aircraft, flown in the barium cloud shadow, are subject to 10 to 30-dB attenuations, even hours after the initial release of the barium cloud. Furthermore, there is evidence that both U.S. and Russian high-altitude nuclear detonations produced severe E- and F-region irregularities up to thousands of kilometers from the burst point. No scintillation results were reported (however, spread-F was observed), but one must keep in mind that in 1962 there were not many satellites of any kind (let alone C^3 satellites) orbiting the earth. However, it is believed that, given the severity of the nuclear-produced structure, the nuclear-striated environment cannot be more benign than the natural ionospheric or barium cloud scintillating environment.

288

II   PREDICTION TECHNIQUE

Before discussing the specific similarities for structure development in the nuclear cloud and barium cloud, let us examine the procedures used for predicting structure in the nuclear environment. These procedures, as it turns out, are the same that are utilized for predicting structure in the barium cloud environment. Basically, in order to study nuclear or barium cloud irregularities (structure) one needs (1) a background or average description of the ionosphere, (2) an instability mechanism that allows low-level fluctuations to grow in amplitude, and (3) the ability to follow the nonlinear development of these instabilities. Theoretical models or experimental data can provide Item 1. The instability (Item 2) provides a seed or generating mechanism for the particular phenomena one is investigating. By the appropriate set of derived equations, one follows the instability into the nonlinear stage. For the most part, satellite C^3 systems will be operating in the nonlinear stage of structure development.

Figure 1 shows schematically how irregularity structure is presently predicted in the nuclear situation, or barium cloud environment for that matter, except that the barium cloud environment uses more experimental data. The important point is that the nuclear environment prediction capability is based solely on theoretical and computational models. Let us review Figure 1 because it has a direct bearing on what we are trying to do. The large-scale (~50 to thousands of kilometers) zero-order (background, mean flow, or average) nuclear-produced plasma parameters (box 1) are predicted using MHD or late-time electrostatic computer codes. The outputs from these numerical calculations are average plasma density, $N(x)$ (and therefore density gradients), neutral wind velocities, $\vec{V}(x)$, electric fields, $\vec{E}(x)$, temperatures, $T(x)$, currents $\vec{J}(x)$, etc. In the barium cloud environment we are more apt to use experimental data rather than numerical codes for describing the zero-order state. These large-scale zero-order numerical calculations give no direct information on small-scale structures (a few kilometers or less) that cause scintillation problems. This is because these zero-order codes use spacing of 50 to hundreds of kilometers between mesh points (points at which calculations
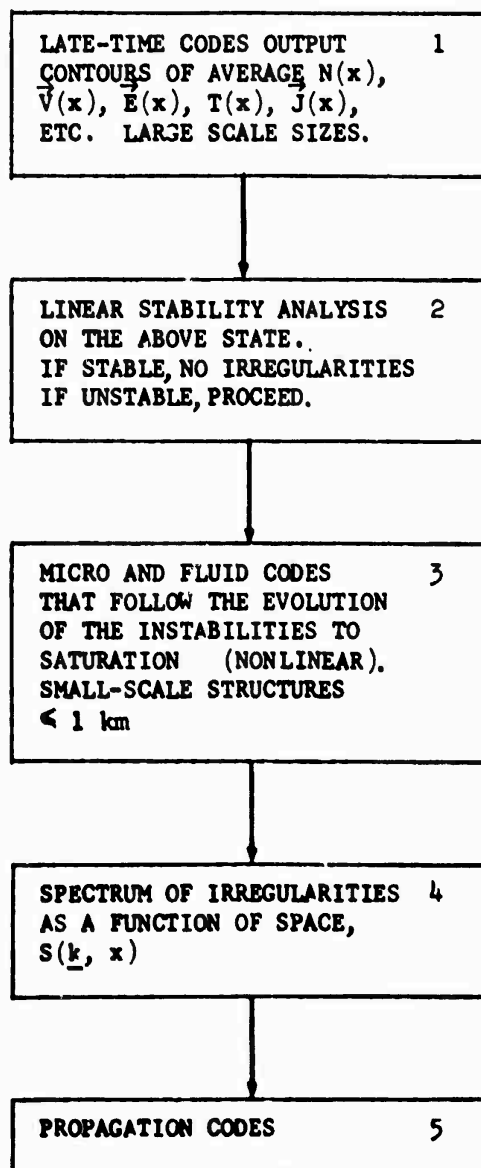
FIGURE 1   FLOWCHART SHOWING THE VARIOUS STEPS USED IN OBTAINING
THE POWER SPECTRUM OF SCINTILLATION CAUSING IRREGULARITIES
FROM THE VARIOUS NUMERICAL CODES. Note that there is a two-step
method for predicting the small-scale structures (box 3) which uses a zero-
order or average background determined in box 1. This power spectrum is
then input into the propagation codes.

are carried out). The small-scale structure is predicted by assuming that it is driven by these average or zero-order quantities--i.e., the large-scale codes provide a zero-order data base within which to study irregularity development.

Consequently, the prediction procedure is a two-step method. The stability of the zero-order plasma is studied as a function of space and time (box 2). If the plasma is determined to be stable, then no irregularities are predicted to grow. However, if the plasma is determined to be unstable (e.g., gradient-drift instability), the irregularities are predicted to grow in amplitude at a certain rate and with certain properties that are determined by theoretical and numerical studies. The growth of the irregularities is followed in both space and time into the nonlinear regime using special numerical codes designed to look at the small-scale structure (second step of two-step process). The result is a prediction of small-scale structure with certain spectral properties (box 4--e.g., percentage of density fluctuations as a function of wave-number, $k = 2\pi/\lambda$, or, equivalently, wavelength λ in the small-scale regime) that can be directly utilized by propagation codes (box 5). The propagation predictions aid in assessing satellite C^3 performance in such an environment. A knowledge of the basic mechanisms that produce scintillation-causing irregularities can be of value in mitigation techniques.

III BARIUM/NUCLEAR SIMILARITIES

Let us now turn to the specific similarities between striations produced by high-altitude nuclear weapons (nuclear clouds) and those produced by barium clouds. Both environments are artificial explosions of sorts (barium is classed as a chemical release) that produce fine-scale structures (striations) in the ionosphere. Both environments have produced much optical data, and photographs of nuclear striations and barium striations show similar-looking structures (environments). The plasma physics describing the barium cloud striations and most of the nuclear striated environment (especially at late times) is believed to be the

291

same--i.e., the gradient-drift (slip) instability is the dominant insta-
bility mechanism produced by both types of clouds. [Note: Both the
Mission Research Corporation and the Naval Research Laboratory theoreti-
cal groups have demonstrated, using calculational results from MICE and
MRHYDE (MHD computer codes), that the gradient-drift instability is the
one primarily responsible for late-time nuclear cloud striation formation.]
The basic gradient-drift instability/striation geometry for both the nu-
clear cloud (e.g., halo-heave region) and barium cloud is depicted in
Figure 2. Basically, one has a plasma density gradient, $N(y)$, and a cur-
rent perpendicular to the density gradient (in the direction of the
electric field, $\vec{E}$), with both perpendicular to the magnetic field, $\vec{B}$.
Furthermore, large barium clouds exhibit electrical properties--e.g.,
magnetic-field-line-integrated Pedersen conductivity--that are much like
the values obtained at late times in the nuclear environment (when stria-
tions occur) under many circumstances. It is these electrical properties
that determine the time evolution of the instabilities in the plasma cloud
and the background ionosphere.

In many situations the maximum linear growth rates for barium clouds
and nuclear clouds are about the same. This maximum linear growth rate
for the gradient-drift instability is given by

$$\gamma \ (s^{-1}) \approx \frac{V_{in}}{L} \tag{1}$$

where V_{in} is the relative velocity between ions and neutrals (slip velocity),
and L is the zero-order or mean flow electron density gradient scale length
perpendicular to the magentic field. For example, while the relative ve-
locity between ions and neutrals (slip velocity) is about a factor of ten
larger in the nuclear case (~1 km/s versus 100 m/s) than in the barium
case, so is the gradient scale length, (~100 km versus 10 km). Since the
growth rate is this velocity divided by the gradient scale length, the
linear growth times are about the same. Moreover, the dominant scale
size for the striations (fine structure) in both cases, far into the
nonlinear regime, is ~0.5 to 1 km (deduced mainly from optical observa-
tions). This suggests that the nonlinear quasi-final saturation mechanism,

292
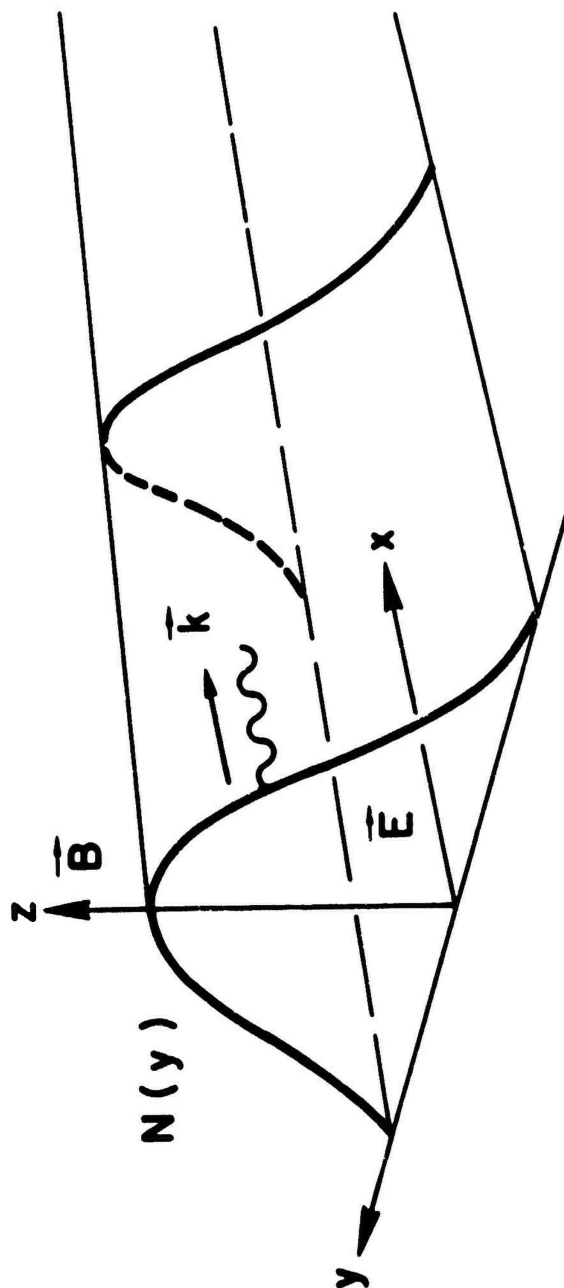
FIGURE 2   GEOMETRY FOR STRIATION PHENOMENA. The driving force is the electric field, $\vec{E}$ (or equivalent neutral wind, $\vec{V}_n$, in the y direction), in the barium or nuclear striations studies. N(y) is the plasma cloud Gaussian-like density profile, B is the ambient magnetic field, and $\vec{k}$ is the wave vector of the perturbation that develops linearly on the backside of the plasma cloud (i.e., the side in which the neutrals flow away from the cloud or, equivalently, the side opposite to the $\vec{E} \times \vec{B}$ motion).

293

in both cases, will be the same. The power spectrum for striations--i.e., the square of the amplitude of the electron density fluctuations as a function of wavenumber, k--in both the nuclear and the barium environment, is consistent with a power law $\propto k^{-m}$, where m ~ 2 to 3. (Recent rocket in-situ measurements performed during project STRESS are consistent with this power-law description for striated barium clouds.) At this point in time a total understanding of the decay of striations is not in hand. However, a very important mechanism is the diffusive or cascade decay of striations, and such a mechanism should be equally applicable to barium and nuclear phenomenology.

IV BARIUM/NUCLEAR DIFFERENCES

Although there are differences between nuclear and barium clouds, these differences are not believed to affect the plasma physics of the gradient-drift instability, which operates in both environments. To be sure, the striation phenomena in a barium cloud environment is operative over a smaller total physical region than in the nuclear case. In the barium cloud case one is talking about distances perpendicular to the magnetic field of the order of tens of kilometers to 100 km, whereas, in the nuclear case, the transverse distances are of the order of hundreds to thousands of kilometers. Also, in the nuclear case electron densities are larger. Moreover, one might expect the intensity of striations to be larger in the nuclear case than in the barium case. These differences should not affect the basic striation physics, and both environments can have severe effects on satellite C^3 systems. Scintillation effects are caused by fluctuations in electron density and depend on the signal prop-agating through a reasonable thickness of such fluctuations. Recent barium releases performed under the STRESS program have revealed striation phenomena that produced 25 to 30 dB maximum loss in amplitude of UHF 20 minutes after release (when striations were optically fully developed) as well as 25 to 30 dB maximum loss two hours after release. Also, in the nuclear case there is much field-aligned energetic-particle precipitation, including deposition in the lower ionosphere of metallic ions, disturbance of the neutral atmosphere (e.g., heave) and partical ejection that just

294

does not take place in the barium cloud environment because of the ener-
getic and processes involved. These latter differences may produce other
fine-structure phenomena in the ionosphere that cannot be produced by
barium clouds. Furthermore, the late-time recombination chemistry is
different for nuclear and barium clouds. Although this is the case, it
is not now believed that this plays a dominant role in striation decay
and therefore it should not affect diffusive or cascade decay mechanisms
operating in both environments. The important point to reiterate is that
the gradient-drift instability is operative and is responsible for the
structure in both the nuclear and barium cloud environment. Studying
striations in the barium cloud environment can directly impact how we
describe the striation phenomena in the nuclear environment and the ef-
fect on satellite C^3 systems.

V NUMERICAL SIMULATION RESULTS FOR STRIATIONS

One of the basic tools for studying the behavior of the gradient-
drift instability in the nuclear or barium cloud environment is a two-
dimensional (perpendicular to $\vec{B}$, striations are observed to be magnetic
field aligned--see Figure 2), two-level (one level for the plasma cloud
plus one level for the background ionosphere--i.e., two ion species are
followed), electrostatic plasma fluid-type numerical code that follows
the nonlinear evolution of small-scale structure due to this instability
(see Item 28 of Bibliography). Thus numerical code is a basic component
of box 3 in Figure 1. Results from this code have shown that the non-
linear phase of plasma cloud development is characterized by pinching of
original perturbations, production of secondary perturbations, a bubbling
(tunneling) through of backside striations to the front side of the cloud
(see Figure 3), and a power-law power spectrum for the striation density
fluctuations (see Figure 4: note that this is box 4 of Figure 1). All
these ideas and terminology will become clearer in the following para-
graph.

High-resolution striation simulations have been performed (Figure 3)
in which the ambient magnetic field, $\vec{B}$, is vertical (z direction; out of
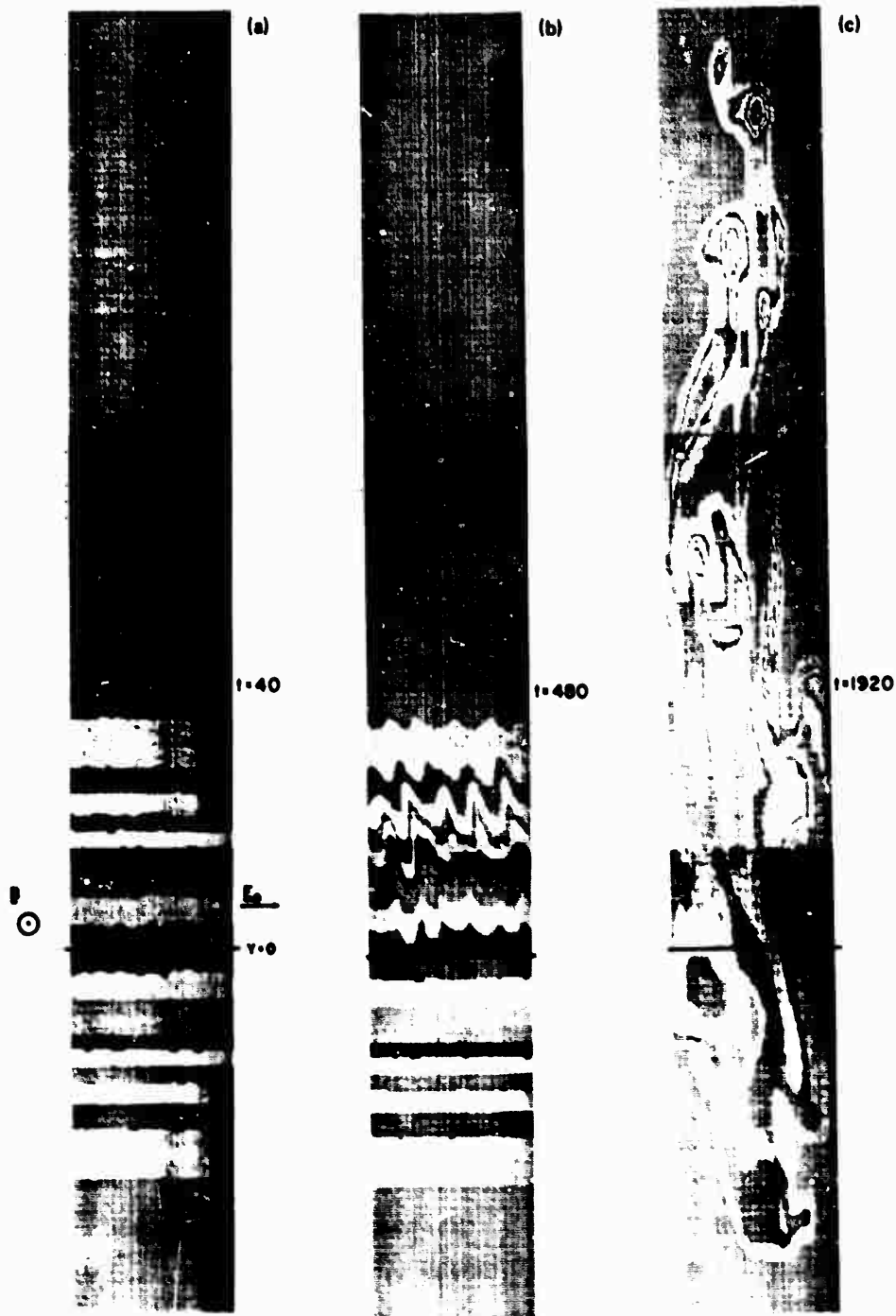
FIGURE 3   TIME DEVELOPMENT OF STRIATIONS FOR A PLASMA CLOUD THAT IS
INITIALLY GAUSSIAN IN THE y DIRECTION (centered around y · 0 and
of the form for the density $\exp-(y/L)^2$, where L · 8 km), UNIFORM IN THE
x DIRECTION, A RANDOM PERTURBATION, AND THE NUMERICAL
SIMULATION IS CARRIED OUT OVER THE TWO-DIMENSIONAL MESH
(x, y).   (a) Isodensity contours at t · 40 s.   (b) Isodensity contours at t ·
480 s.   (c) Isodensity contours at t · 1920 s.
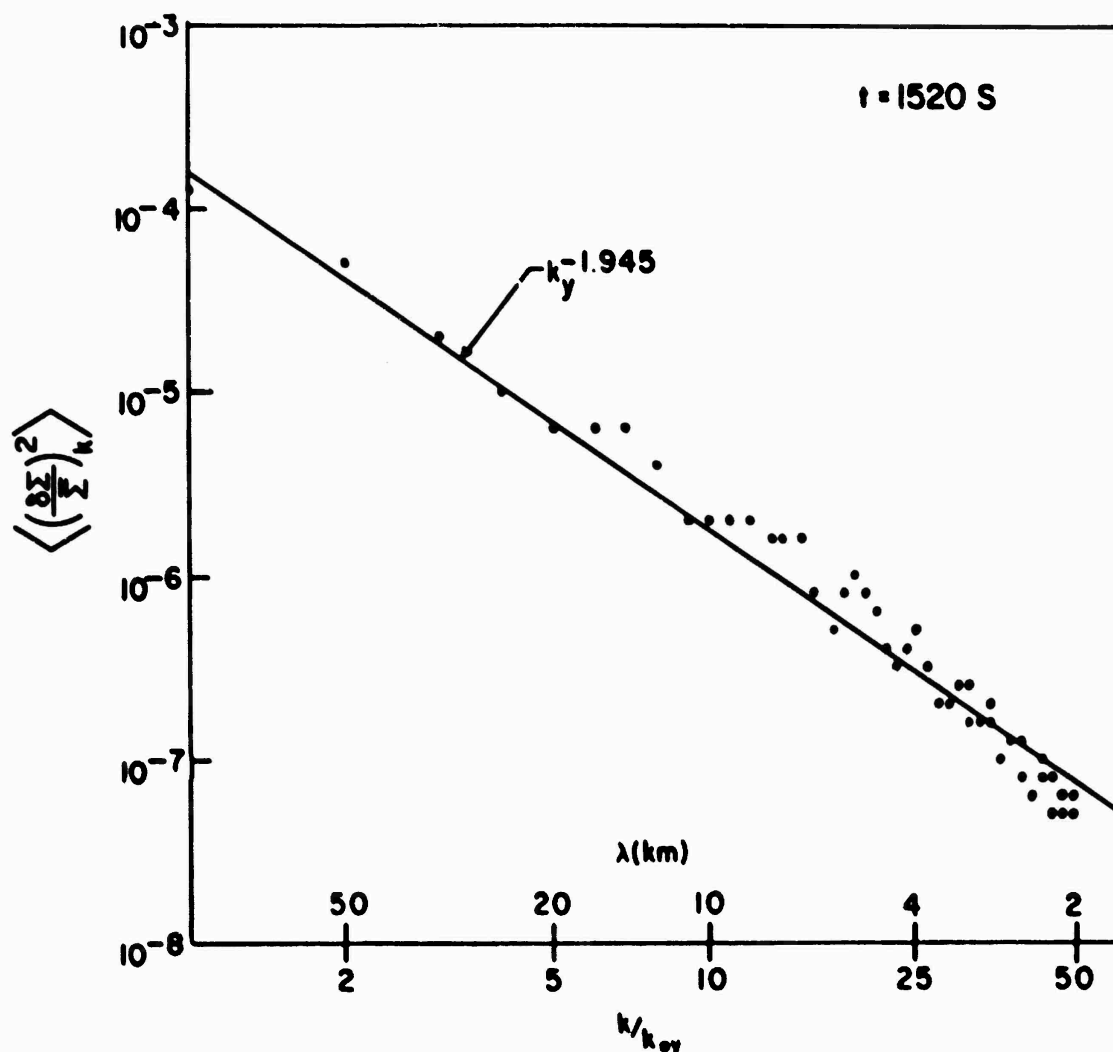
FIGURE 4   THIS REPRESENTS THE RESULTS OF FOURIER ANALYZING THE REAL
SPACE STRUCTURES OF THE NUMERICAL SIMULATION DEPICTED IN
FIGURE 3 (but for t = 1520 s) IN ORDER TO OBTAIN THE POWER
SPECTRUM FOR STRIATIONS. This is the one-dimensional power spectrum
in the y direction shown on a log-log plot, where $\langle(\delta\Sigma/\bar{\Sigma})_k^2\rangle$ is the density
fluctuation amplitude squared (normalized by the peak cloud density, $\bar{\Sigma}$), λ
is the wavelength, and k/k_{oy} is the normalized wavenumber in the y direction.
The dots represent results from the numerical simulation and the solid line is
a least-squares-power-law fit to the dots.

297

page in Figure 3), the nuclear plasma cloud (or barium cloud) is taken to be Gaussian in the y direction (direction of neutral wind or equivalent negative of $\vec{E} \times \vec{B}$ direction), and uniform in the x direction with a perturbation in the x direction (see Figure 2). The numerical simulation is performed over the two-dimensional mesh (x, y). Figure 3 is such that the x extent (short side) is 12 km and the y extent (long side) is 80 km. $\vec{E}_o$ (equivalent to a neutral wind in the y direction) was taken to be 5 mV/m, and $\vec{B}$ = 0.5 gauss (out of page). Figure 3(a) shows the isodensity contours in the plasma cloud when the striation development is in the linear regime. The alternations in color in the plasma cloud are essentially isodensity contours that have random initial perturbations superposed at t = 0. Figure 3(b) shows isodensity contours in the plasma cloud at t = 480 s. The neutral-wind motion causes striations to linearly grow on the "backside" of the cloud (i.e., the side in which the neutrals flow away from the cloud or, equivalently, the side opposite to the $\vec{E} \times \vec{B}$ motion) via the $\vec{E} \times \vec{B}$ gradient drift (slip) instability. In the nonlinear regime Figure 3(c) shows isodensity contours at t = 1920 s with finger formation, the development of fine structure with elongation and pinching off on the backside, and the penetration of structure into the front side of the cloud--i.e., nonlinear tunneling (see Item 28 of Bibliography). Fourier analysis of the real space structures (e.g., Figure 3) produces a one-dimensional power-law power spectrum for the square of the density fluctuations (striations) in the y direction $\propto$ k^{-m}, where $m \approx 2$, for the wavelength resolved in the simulation (see Figure 4).

Because of the similarities between barium cloud striation and nuclear cloud striation phenomena, the nuclear striation effects code can be validated by the results from barium cloud experiments. A comparison of neutral simulation predictions with in-situ and ground-based experimental measurements of barium cloud phenomena is expected to impact direcetly on the reliability of the program on scintillation effects due to nuclear striations.

VI SUMMARY

The picture that emerges for nuclear cloud and barium cloud phe-
nomena is that both are caused by a density-gradient type of instability
(i.e., the same types of plasma instabilities occur in both the barium
cloud ionospheric scintillating plasma and the nuclear ionospheric scin-
tillating plasma) which depends on the density gradient having a favorable
direction with respect to the driving forces (only "backside growth), at
least according to linear theory. In both cases the driving forces are
the same and the mechanism is called the $\vec{E} \times \vec{B}$ gradient drift (slip) in-
stability. Plasma fluid type equations describe the evolution of both
systems, and evolution into the nonlinear regime shows that the power
spectrum (squared amplitude of the electron density fluctuations) for
both environments is proportional to k^{-m}, where $m \sim 2$ to 3, and k is the
wavenumber (equal to $2\pi/\lambda$, where λ is the wavelength of the structures).

Basically, there exist certain characteristic modes that cause ir-
regularities to occur in plasmas whether they are barium or nuclear-
produced. If an instability is predicted to occur in the nuclear-
disturbed ionosphere, we will presently impose what we believe to be the
properties of that instability. The instabilities that will lead to
satellite signal scintillation at late times in the nuclear environment
exist in the barium cloud scintillating ionosphere. An understanding of
these instabilities in the barium cloud ionosphere will shed considerable
light on their behavior in the nuclear ionosphere. In terms of predictive
capability the basic question is, given a set of initial conditions and
driving forces, can we predict the nonlinear behavior of an instability?
If the methods are adequate to make the prediction in the barium cloud
scintillating ionosphere, then we have good reason to believe that the
methods will work in the nuclear case.

BIBLIOGRAPHY

A. <u>Nuclear Cloud and Barium Cloud Striations</u>

1. K. D. Baker, L. C Howlett, J. C. Ulwick, D. Delorey, and
N. Brossbard, "Measurements of Electron Density Structure in
Barium Clouds--Project STRESS," Utah State University Report
(May 5, 1977).

2. D. L. Book, S. L. Ossakow, and S. R. Goldman, "Altitude Depen-
dent Neutral Wind Effects on the Nonlinear Motion of a Small
Barium Cloud," <u>J. Geophys. Res.</u>, Vol. 80, p. 2879 (1975).

3. W. Chesnut, "Spatial-Frequency Analyses of Striated Nuclear
Phenomena; Part Two: A Model of the Striated Check Mate Cloud
(U)" (Report Unpublished).

4. W. G. Chesnut, "Optical-Radiance Structure and In Situ Density
Fluctuations with Relevance to Models for Electromagnetic Propa-
gation (U)" (Report Unpublished).

5. W. G. Chesnut, D. Allison, and J. C. Hodges, "Spatial-Frequency
Analyses of Striated Nuclear Phenomena; Part One: Processed
Striation Data (U)" (Report Unpublished).

6. W. G. Chesnut and G. L. Johnson, "Summary of Radar Propagation
Degradation Measurements on Event Check Mate (U)" (Report
Unpublished).

7. T. Coffey, B. E. McDonald, S. Ossakow, and D. Tidman, "Stria-
tions in a Two-Fluid MHD Code (U)" (Report Unpublished).

8. T. N. Davis, G. J. Romick, E. M. Wescott, R. A. Jeffries,
D. M. Kerr, and H. M. Peek, "Observations of the Development
of Striations in Large Barium Ion Clouds (U)," <u>Planet. Space
Sci.</u>, Vol. 22, p. 67 (1974).

9. J. H. Doles, III, N. J. Zabusky, and F. W. Perkins, "Deformation
and Striation of Plasma Clouds in the Ionosphere 3. Numerical
Simulations of a Multilevel Model with Recombination Chemistry
(U)," <u>J. Geophys. Res.</u>, Vol. 81, p. 5987 (1976).

10. S. R. Goldman, S. L. Ossakow, and D. L. Book, "On the Nonlinear Motion of a Small Barium Cloud in the Ionosphere (U)," *J. Geophys. Res.*, Vol. 79, p. 1471 (1974).

11. S. R. Goldman, A. J. Scannapieco, S. L. Ossakow, J. Pierre, and L. Baker, "Electrostatic Effects on Ionized Clouds in the Ionosphere (U)," (Report Unpublished).

12. S. R. Goldman, L. Baker, S. L. Ossakow, and A. J. Scannapieco, "Striation Formation Associated with Barium Clouds in an Inhomogeneous Ionosphere (U)," *J. Geophys. Res.*, Vol. 81, p. 5097 (1976).

13. S. R. Goldman, A. J. Scannapieco, and S. L. Ossakow, "Early Time Striation Structuring in Ionized Barium Clouds Due to the Presence of BaO Flow (U)," *J. Geophys. Res.*, Vol. 81, p. 5980 (1976).

14. R. Hubert, H. Linnerud, and W. Broste, "Checkmate Late-Time Striations (U)" (Report Unpublished).

15. R. W. Kilb, W. F. Crevier, J. B. West, and C. L. Longmire, "Striations After Nuclear Bursts (U)" (Report Unpublished).

16. R. W. Kilb, R. W. Stagat, and G. Beeler, Jr., "Striation Amplification After Low and High Yield Nuclear Bursts (U)" (Report Unpublished).

17. R. W. Kilb and R. W. Stagat, "Striation Diffusive Decay and Image Growth (U)" (Report Unpublished).

18. L. M. Linson and J. B. Workman, "Formation of Striations in Ionospheric Plasma Clouds (U)," *J. Geophys. Res.*, Vol. 75, p. 3211 (1970).

19. K. H. Lloyd and G. Haerendel, "Numerical Modeling of the Drift and Deformation of Ionospheric Plasma Clouds and of Their Interaction with Other Layers of the Ionosphere (U)," *J. Geophys. Res.*, Vol. 78, p. 7389 (1973).

20. D. R. McDaniel, Compiler, "Project SECEDE Final Program Review (U)" (Report Unpublished).

21. S. L. Ossakow, S. T. Zalesak, and N. J. Zabusky, "Recent Results on Cleavage, Bifurcation, and Cascade Mechanisms in Ionospheric Plasma Clouds (U)," NRL Memo Report 3579 (August 1977).

22. H. M. Peek, M. P. Shuler, and R. E. Hubert, "Checkmate Photographic Analysis: Late-Time Optical Phenomenology (U)" (Report Unpublished).

23. F. W. Perkins, N. J. Zabusky, and J. H. Doles III, "Deformation and Striation of Plasma Clouds in the Ionosphere, 1. (U)," J. Geophys. Res., Vol. 78, p. 697 (1973).

24. C. Prettie, A. Johnson, J. Marshall, T. Grizinski, and R. Swanson, "Project STRESS Satellite Communication Test Results (U)," AFAL Technical Report, pp. 77-158 (July 1977).

25. A. J. Scannapieco, S. L. Ossakow, D. L. Book, B. E. McDonald, and S. R. Goldman, "Conductivity Ratio Effects on the Drift and Deformation of F Region Barium Clouds Coupled to the E Region Ionosphere (U)," J. Geophys. Res., Vol. 79, p. 2913 (1974).

26. A. J. Scannapieco, S. L. Ossakow, T. P. Coffey, and J. M. Pierre, "Striation Formation in a Two-Fluid Three-Dimensional Checkmate Simulation (U)" (Report Unpublished).

27. A. J. Scannapieco, S. R. Goldman, and S. L. Ossakow, "The Checkmate Horseshoe (U)" (Report Unpublished).

28. A. J. Scannapieco, S. L. Ossakow, S. R. Goldman, and J. M. Pierre, "Late-Time Striation Spectra (U)," NRL Memo Report 3251, March 1976, and J. Geophys. Res., Vol. 81, p. 6037 (1976).

29. R. W. Stagat, A. Simon, and R. W. Kilb, "Field-Line Averaged Striation Growth (U)" (Report Unpublished).

30. H. J. Volk and G. Haerendel, "Striations in Ionospheric Ion Clouds, 1 (U)," J. Geophys. Res., Vol. 76, p. 4541 (1971).

31. J. B. Workman, "Fireball Striations," reported in Volume 1 of High Altitude Nuclear Effects Symposium (U), (Report Unpublished).

32. J. B. Workman, "Halo Striations (U)" (Report Unpublished).

33. N. J. Zabusky, J. H. Doles, III, and F. W. Perkins, "Deformation and Striation of Plasma Clouds in the Ionosphere 2. Numerical Simulation of a Nonlinear Two-Dimension Model (U)," J. Geophys. Res., Vol. 78, p. 711.

B.   Scintillations and F-Region Irregularities

34. R. K. Crane, "Spectra of Ionospheric Scintillation (U)," J. Geophys. Res., Vol. 81. p. 2041.

35. P. L. Dyson, J. P. McClure, and W. B. Hanson, "In Situ Measurements of the Spectral Characteristics of Ionospheric Irregularities (U)," J. Geophys. Res., Vol. 79, p. 1497.

36. E. J. Fremouw and C. L. Rino, "An Empirical Model for Average F-Layer Scintillation at VHF/UHF (U)," Radio Sci., Vol. 8, p. 213 (1973).

37. J. M. Goodman, Editor, Effect of Ionosphere on Space Systems and Communications (U), U.S. Government Printing Office, Washington, D.C. 20402 (January 1975).

38. S. L. Ossakow, "Research at NRL on Theoretical and Numerical Simulation Studies of Ionospheric Irregularities (U)," NRL Memo Report 2907, October 1974.

39. E. Ott and D. T. Farley, "The k Spectrum of Ionospheric Irregularities (U)," J. Geophys. Res., Vol. 79, p. 2469 (1974).

40. J. H. Pope, "High Latitude Ionospheric Irregularity Model (U)," Radio Sci., Vol. 9, p. 675 (1974).

41. C. L. Rino and E. J. Fremouw, "Statistics for Ionospherically Diffracted VHF/UHF Signals (U)," Radio Sci., Vol. 8, p. 223 (1973).

42. C. L. Rino, P. C. Livingston, and M. E. Whitney, "Some New Results on the Statistics of Radio Wave Scintillation 1. Empirical Evidence for Gaussian Statistics (U)," J. Geophys. Res., Vol. 8, p. 2051 (1976).

43. C. L. Rino, "Some New Results on the Statistics of Radiowave Scintillation 2. Scattering from a Random Ensemble of Locally Homogeneous Patches (U)," J. Geophys. Res., Vol. 81, p. 2059 (1976).

44. C. L. Rufenach, "Power-Law Wavenumber Spectrum Deduced from Iono-spheric Scintillation Observations (U)," _J. Geophys. Res._, Vol. 77, p. 4761 (1972).

45. R. C. Sagalyn, M. Smiddy, and M. Ahmed, "High-Latitude Irregularities in the Topside Ionosphere Based on Isis 1 Thermal Ion Probe Data (U)," _J. Geophys. Res._, Vol. 79, p. 4252 (1974).

46. R. R. Taur, "Simultaneous 1.5 and 4-GHz Ionospheric Scintillation Measurements (U)," _Radio Sci._, Vol. 11, p. 1029 (1976).

THEORETICAL AND NUMERICAL SIMULATION STUDIES FOR DETERMINING MINIMUM SCALE SIZES IN PLASMA CLOUD STRIATIONS

B. E. McDonald,   S. L. Ossakow,   S. T. Zalesak

Naval Research Laboratory
Washington, D.C.

N. J. Zabusky

University of Pittsburgh
Pittsburgh, Pennsylvania

THEORETICAL AND NUMERICAL SIMULATION STUDIES FOR DETERMINING MINIMUM SCALE SIZES IN PLASMA CLOUD STRIATIONS

B. E. McDonald,   S. L. Ossakow,   S T. Zalesak

Naval Research Laboratory
Washington, D. C.

N. J. Zabusky
University of Pittsburgh
Pittsburgh, Pennsylvania

ABSTRACT

We propose a fluid model for investigating the possibility
that a small-scale cutoff is present in plasma cloud striations
due to particle diffusion. The model is two dimensional and
perpendicular to the magnetic field, and assumes parameters
applicable to the F region. The nondimensionalized equations
for the model show that the plasma motion is determined by
initial plasma distribution and the value of an effective
Reynolds number. Numerical simulations carried out for random
phase initial conditions and maximum-to-minimum Pedersen con-
ductivity ratio of 11 to 1 suggest that striation formation
stops when the Reynolds number drops below about 400. We cal-
culate a diffusion constant including electron-ion collisions,
which can be dominant in high-altitude releases. We then scale
the results of the numerical simulation and conclude that the
fluid model (without kinetic corrections) predicts a minimum
scale size in the range 2.4 to 24 m for a typical choice of
ionospheric parameters. These minimum scale sizes are in
agreement with Project STRESS rocket in-situ measurements.

I INTRODUCTION

Artificial plasma clouds (i.e., nuclear or barium) detonated in the
ionosphere typically develop visible striations over periods of tens of
seconds to tens of minutes. Propagation studies carried out simultaneously

307

with barium cloud experiments during Project STRESS have shown that line-of-sight radio communication through a striated region may be subject to 10 to 30 dB of attenuation.[1] Thus, local enhancements in the ionospheric plasma density can have a great impact on propagation when small-scale structuring occurs. The resolution of the optical data from barium cloud experiments[2] and nuclear detonations[3] is insufficient to reveal structures (irregularities) smaller than hundreds of meters. However, recent in-situ rocket measurements[4] suggest that structure down to meter sizes may be present. We wish to address theoretically the question of what determines the smallest structures to be found in a striated plasma cloud.

The mechanism by which striations are produced in barium clouds[5-7] and most nuclear clouds[8,9] has been established to be the gradient-drift instability. This is an electrostatic fluid process analogous to the Rayleigh-Taylor instability. The results of the model are in need of correction for kinetic effects below scale sizes approximating the ion gyro radius. For a barium ion in the daytime F region, the gyro radius is approximately 7 m. Before carrying out the kinetic corrections (to be reported elsewhere) one should ascertain whether or not the fluid model tends to generate structures on such a small scale.

II THE ONE-LEVEL, TWO-DIMENSIONAL FLUID MODEL

For barium clouds released at altitudes of approximately 200 km or greater, electron and ion collision frequencies are small compared to their gyrofrequencies. As a result,[10] the electrical conductivity of the plasma is dominated by the scalar (Pedersen) component,

$$\Sigma \approx n \frac{ec}{B} \frac{\nu_{in}}{\Omega_i} \tag{1}$$

where n, e, c, B, ν_{in}, and Ω_i are, respectively, the ion number density, electronic charge, speed of light, magnetic field strength, ion-neutral collision frequency, and ion gyrofrequency. Assuming all parameters in (1) to be constant except n, Σ obeys a continuity equation,

308

$$\frac{\partial \Sigma}{\partial t} = - \nabla \cdot (\vec{V}\Sigma) + K\nabla^2\Sigma \tag{2}$$

where $\vec{V}$ is the plasma drift velocity, and K is a diffusion constant used to model the effects of electronic collisions. The value of K will be estimated later. Let us adopt Cartesian coordinates (x,y,z), with z in the direction of the (constant) magnetic field. We assume that all variables depend only on x and y (striations are observed to be mainly magnetic field aligned). We express the electric field as

$$\vec{E}(x,y) = E_o\hat{y} - \nabla\phi(x,y) \tag{3}$$

where E_o is the constant ambient electric field, and ϕ is the potential due to the presence of the cloud. It is convenient to use a frame moving with the ambient plasma drift velocity, $E_o c/B \hat{x}$. In this frame, we have a net plasma drift velocity

$$\vec{V} = - c/B \nabla\phi \times \hat{z} \quad . \tag{4}$$

The equation can be viewed as a solution of the electron monomemtum equation in which inertia and collision terms have been neglected. The collisional correction has been included in an approximate way in the diffusion term in Eq. (2). The set of fluid equations is closed in this simple model by quasineutrality--i.e., the constraint that the electric current be divergenceless:

$$\nabla \cdot (\Sigma\nabla\phi) = \vec{E}_o \cdot \nabla\Sigma \quad . \tag{5}$$

The more sophisticated two-layer model[7] allows polarization currents generated by the cloud to flow along the magnetic field direction and close in the lower ionosphere, where cross-field conductivities are high. However, the lower layer becomes unimportant when the cloud's conductivity is high enough to let current loops close in the cloud itself. Some of the barium releases at altitudes of approximately 200 km are known to have integrated conductivities as high as 15 times that of the ionosphere. For such large clouds, the one-level model should be adequate.

The one-level model is simple enough to allow a convenient scaling law
to emerge. The small number of variables also expedites numerical solu-
tion of the equations of motion.

III SCALING THE EQUATIONS OF MOTION

Equations (2), (4), and (5) can be put into dimensionless form as
follows. Let

$$\hat{x} = L_o \hat{x}'$$

$$t = t_o t'$$

$$\Sigma = \Sigma_o \Sigma'$$

$$V = V_o V',$$

$$\phi = L_o E_o \phi' \tag{6}$$

where L_o is an arbitrary scale, length, and

$$V_o = cE_o/B,$$

$$t_o = L_o/V_o \quad . \tag{7}$$

In Eq. (6), quantities with zero subscript are dimensional constants and
all primed variables are dimensionless. Upon expressing Eqs. (2), (4),
and (5) in terms of the dimensionless primed variables and dropping primes
from x', t', Σ', V', and ϕ', we have

$$\frac{\partial \Sigma}{\partial t} = -\nabla \cdot (\vec{V}\Sigma) + K'\nabla^2\Sigma \tag{8}$$

$$\vec{V} = -\nabla\phi \times \hat{z} \tag{9}$$

$$\nabla \cdot (\Sigma\nabla\phi) = \hat{y} \cdot \nabla\Sigma \tag{10}$$

310

where

$$K' = \frac{K}{L_o V_o} \cdot \qquad (11)$$

Note that K' is just the inverse of an effective Reynolds number, with the diffusion constant K in place of the usual kinematic viscosity. The fact that all quantities in Eqs. (8) through (10) are dimensionless means that physical systems of different sizes will evolve in the same way, providing initial conditions and boundary conditions are analogous, and K' has the same value.

Thus the model of Eqs. (8) through (10) can be used to answer the following crucial question: What criterion determines whether or not structures in a striated plasma cloud will develop into structures of smaller scale? It becomes clear from Eqs. (8) and (11) that as the length scale becomes smaller, diffusion becomes more important. For sufficiently small scales, we expect an equilibrium to be reached between the tendency toward finer structuring and the smoothing out effect of diffusion. Our approach to finding this scale will be to carry out a set of numerical simulations based on Eqs. (2) through (5) or, equivalently, Eqs. (8) through (10), and hopefully to identify an approximate value for K' at which diffusion is just able to halt further structuring of previously formed striations. Knowledge of a critical value of K' combined with estimates for the drift speed and diffusion coefficient allow calculation of a minimum length scale from Eq. (11). Drift speeds are fairly well known to be of the order of 100 m/s. However, there are no direct measurements of the diffusion constant, so it must be calculated.

IV CALCULATION OF THE DIFFUSION CONSTANT

Neglecting ion and electron inertia, the momentum equations for electrons and ions are

$$0 = \Omega_i \vec{V}_i \times \hat{z} - \nu_{in} \vec{V}_i + \nu_{ie} (\vec{V}_e - \vec{V}_i) + \frac{e}{m_i} \vec{E} - \frac{kT_i}{m_i} \nabla n/n \qquad (12)$$

$$0 = - \Omega_e \vec{V}_e \times \hat{z} - \nu_{en} \vec{V}_e + \nu_{ei} (\vec{V} - \vec{V}_e) - \frac{e}{m_e} \vec{E} - \frac{kT_e}{m_e} \nabla n/n \quad . \qquad (13)$$

311

For the purposes of this derivation we have adopted a coordinate system at rest with the neutral atmosphere. In Eqs. (12) and (13), the $\vec{V}$'s are fluid velocities, with subscripts i and e referring to ions and electrons. Similarly, ν stands for momentum transfer collision frequency, T for temperature, and m for particle mass. The gyrofrequencies are

$$\Omega_i = \frac{eB}{m_i c} \tag{14}$$

$$\Omega_e = \frac{eB}{m_e c} \quad . \tag{15}$$

Note that we have retained the electron-ion collision frequency ν_{ei} in Eq. (13). For conditions typical of a 200-km release, ν_{en} is of the order of 10^2 s^{-1}, and ν_{ei} is of the order 10^3 s^{-1}. This is because the ions, although less numerous than the neutrals, interact with electrons via a Coulomb cross section. However, the ν_{ie} term in Eq. (12) is typically much smaller than the ν_{in} term because of the low mass of the electron. Neglecting ν_{ie}, we find from Eqs. (12) and (13),

$$n\vec{V}_i = M_i^{-1} \left(\frac{e}{m_i} n\vec{E} - \frac{kT_i}{m_i} \nabla n \right) \tag{16}$$

$$n\vec{V}_e = M_e^{-1} \left(-\frac{e}{m_e} n\vec{E} - \frac{kT_e}{m_e} \nabla n \right) + \nu_{ei} M_e^{-1} n\vec{V}_i \tag{17}$$

where

$$M_i^{-1} = \begin{pmatrix} \nu_{in} & \Omega_i \\ -\Omega_i & \nu_{in} \end{pmatrix} \Big/ \left(\Omega_i^2 + \nu_{in}^2 \right) \tag{18}$$

$$M_e^{-1} = \begin{pmatrix} \nu_e & -\Omega_e \\ \Omega_e & \nu_e \end{pmatrix} \Big/ \left(\Omega_e^2 + \nu_e^2 \right) \quad , \tag{19}$$

and

$$\nu_e = \nu_{en} + \nu_{ei} \quad . \tag{20}$$

312

Let us invoke quasineutrality in the form

$$\nabla \cdot (n\vec{V}_i) = \nabla \cdot (n\vec{V}_e) \tag{21}$$

and take the divergence of Eqs. (16) and (17). We assume all parameters except n, $\vec{V}$, $\vec{V}_e$, and $\vec{E}$ to be constant. We also assume that all vectors have only x and y components. We may then eliminate $\nabla \cdot n\vec{E}$ between Eqs. (16) and (17), and find, to lowest order in ν_e/Ω_e,

$$-\nabla \cdot (n\vec{V}_i) = -\frac{c}{B} \nabla \cdot (n\vec{E} \times \hat{z}) + K\nabla^2 n \tag{22}$$

where

$$K = \frac{\nu_e}{\Omega_e} \frac{k(T_e + T_i)/m_e}{\Omega_e + \nu_e \nu_{in}/\Omega_i} \quad . \tag{23}$$

We use the convenient approximations[11]

$$\nu_{ei} \approx \left(34 + 4.18 \log_{10}(T_e^3/n_e)\right) n_e T_e^{-3/2} \tag{24}$$

$$\nu_{en} \approx 1.8 \times 10^5 \, p_n \tag{25}$$

$$\nu_{in} \approx 4 \times 10^{-10} \, n_n \tag{26}$$

where p_n and n_n are the neutral pressure and number density, T_e is in K, and all other quantities are in cgs units. For typical daytime conditions at 200 km, we have $T_e = 950K$, $T_i = 700K$, $p_n = 8.64 \times 10^{-4}$ erg cm^{-3}, $n_n = 7.0 \times 10^9$ cm^{-3}, $\Omega_e = 9 \times 10^6$ s^{-1}, and Ω_i (singly ionized Ba) = 36 s^{-1}. We know that for typical barium releases (Refs. 4 and 6), $10^6 \leqslant n_e \leqslant 10^7$ cm^{-3}. Thus, K is expected to lie between 0.6 and 6 m^2/s. When the calculation is repeated using data appropriate to 170 km and 150 km, K changes by less than a factor of 2. This is because ν_e is dominated by ionic collisions, and is insensitive to moderate changes in the neutral background.

V NUMERICAL SIMULATION

In order to estimate a critical value for K', we have solved numerically Eqs. (2) through (5) using diffusion constants K determined so as to give one of four desired K' values. The results to be presented here were obtained using a mesh of 162 by 42 grid points with constant grid spacing in both directions of 310 m and doubly periodic boundary conditions. Equation (2) was advanced in time using a flux-corrected leapfrog-trapezoid scheme, which is basically second order in time, fourth order in space. Second-order centered differences were used in Eqs. (4) and (5). The elliptic potential equation (5) was solved iteratively using the Chebychev method.[12,13] The initial condition (t = 0) was

$$\Sigma = 1 + 10 \exp\left[-(x/8 \text{ km})^2\right]\left(1 + \epsilon(x,y)\right) \quad ,$$

where ϵ was generated from a k^{-4} power spectrum and random phases. The root mean square value of ϵ was 0.03. (The dimensionality of Σ may be scaled out of Eqs. (2) and (5) with no consequence). B is taken to be 0.5 gauss and $V_o = cE_o/B = 100$ m/s.

We are not concerned here with details of relating an initial condition to a final state achieved after a long period of development. Rather we wish to determine whether or not a given configuration tends toward spontaneous generation of structure smaller than that which is present. Thus we view the time evolution to be presented here as a continuous sequence of initial conditions, hopefully at some point descriptive of structure in a striated cloud. We seek a value of the Reynolds number just low enough that a long finger-like striation will not evolve into new and smaller-scale structures.

Since we hope to identify a critical value of the Reynolds number,

$$R_e = \frac{V_o L_o}{K}$$

$$= 1/K' \tag{27}$$

314

we have carried out numerical simulations so as to keep R_e constant throughout a given computer run. Throughout each run presented here, V_o is constant, and L_o is determined self-consistently from the conductivity profile:

$$L_o(t) = \left\{ \Sigma \; [\Sigma(x,y,t)]^2 / \Sigma[\nabla\Sigma(x,y,t)]^2 \right\}^{1/2} \qquad (28)$$

where Σ without the argument (x,y,t) refers to summation over all grid points. This definition of L_o is somewhat arbitrary, but it does have the desirable feature of being sensitive to small-scale structure. Since L_o changes in time, K must change if R_e is to be held constant. Thus, during a computer run, we evaluate L_o at each time step and determine K from Eq. (27). It may be more conventional to keep K fixed and let R_e vary with L_o, but our approach allows a more direct identification of a critical R_e.

The results of four computer runs ($R_e = \infty$, 800, 400, and 300) are shown at five times ($t = 0$, 240, 360, 480, and 720 s) in Figures 1 through 5. All four cases show the breakup of the initial slab geometry into structure elongated in the x direction. However, only the top two cases ($R_e = \infty$ and 800) show a clear tendency toward further structuring. The $R_e = 400$ case appears marginal, and the $R_e = 300$ case is clearly held back by diffusion. Therefore we tentatively propose that the critical Reynolds number for the initial condition presented here ($\Sigma_{max}/\Sigma_{min} \approx 11$) is approximately 400. We intend to carry out several more simulations using finer resolution and different initial conditions to determine if $R_e = 400$ is in fact universal to the short-scale limit of the striation process. Using $R_e = 400$, and $V_o = 100$ m/s in Eq. (27), we find the following range for L_o:

For   n: $10^6 - 10^7$ cm^{-3} (29)

and   K: $0.6 - 6$ m^2/s

                            L_o: $2.4 - 24$ m
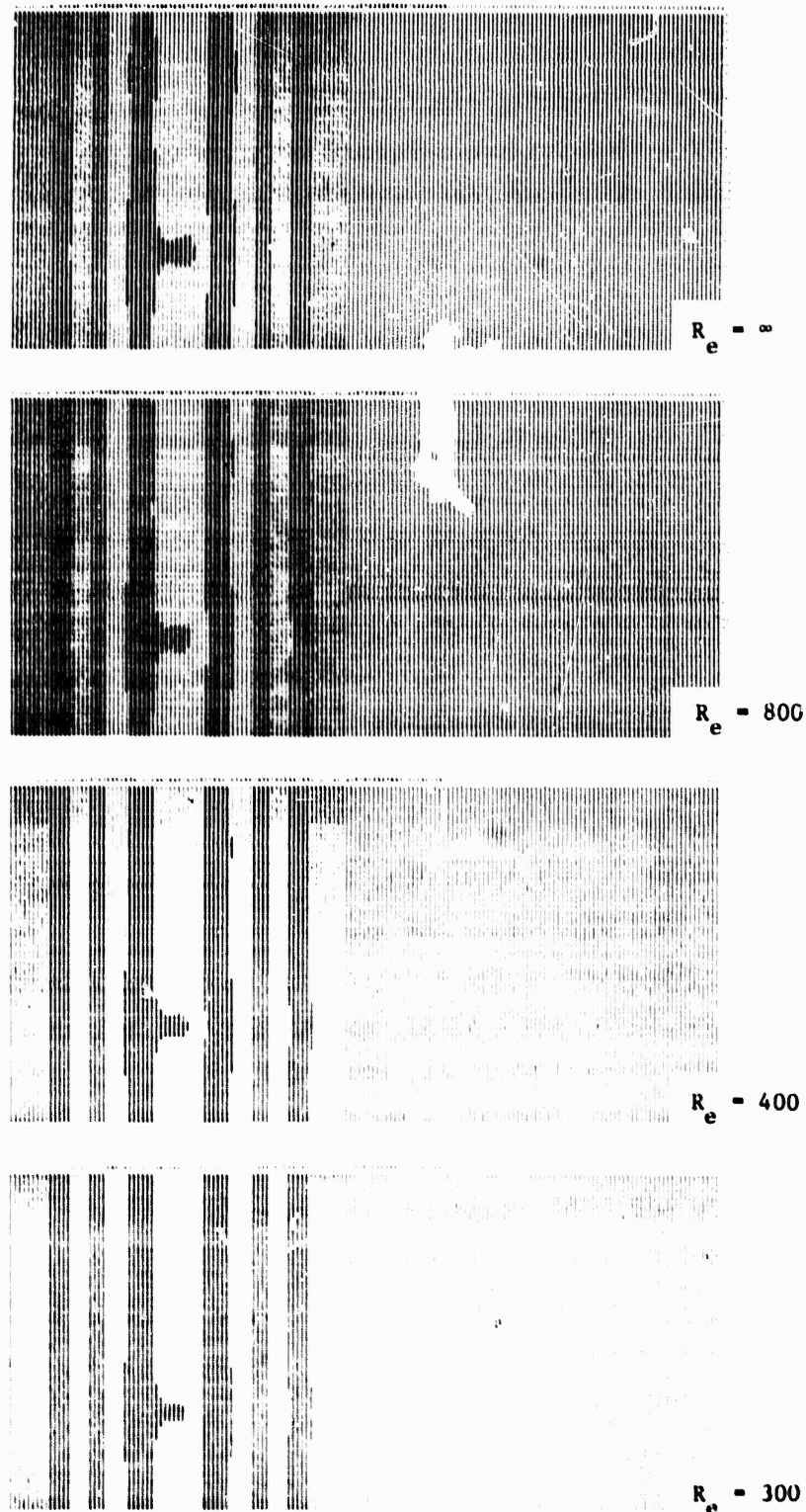
FIGURE 1 INITIAL CONDITIONS. Contours of constant Σ are boundaries between light and dark areas. A maximum Σ of 11.32 relative to the background occurs in the light vertical band containing the most noticeable bump. The vertical (y) extent of each rectangular box is 12.4 km; the horizontal (x) extent is 49.9 km. The finite difference grid is 42 by 162 points in the y and x directions, respectively. Boundaries are doubly periodic. The Reynold's numbers are (top to bottom) $R_e = \infty$, 800, 400, 300.
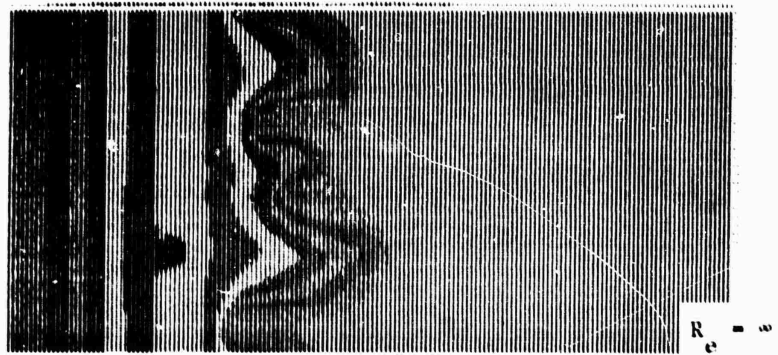
FIGURE 2   S CONTOURS AT t - 240 s
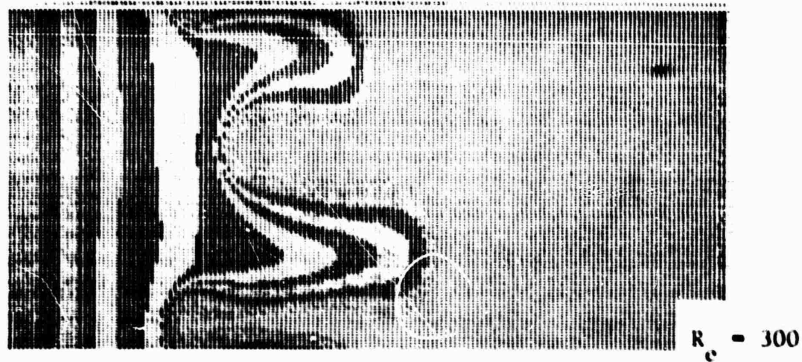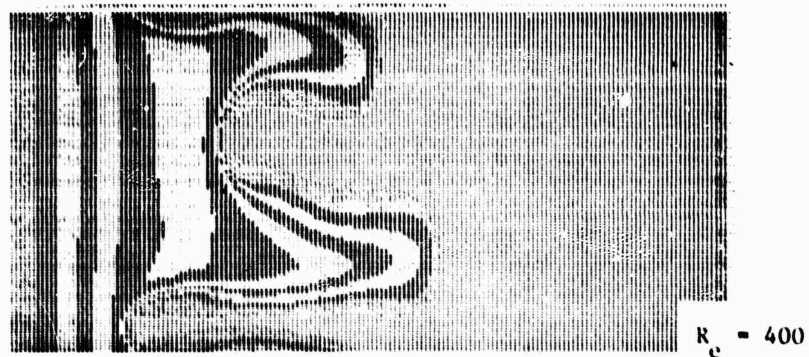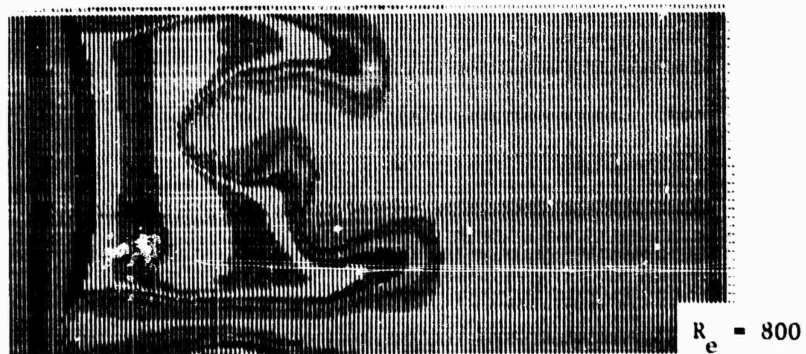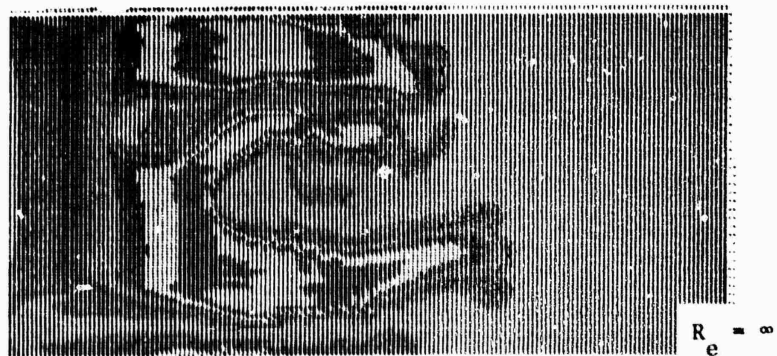
FIGURE 3 Σ CONTOURS AT t = 360 s

318

FIGURE 4   Σ CONTOURS AT t - 480 s

319
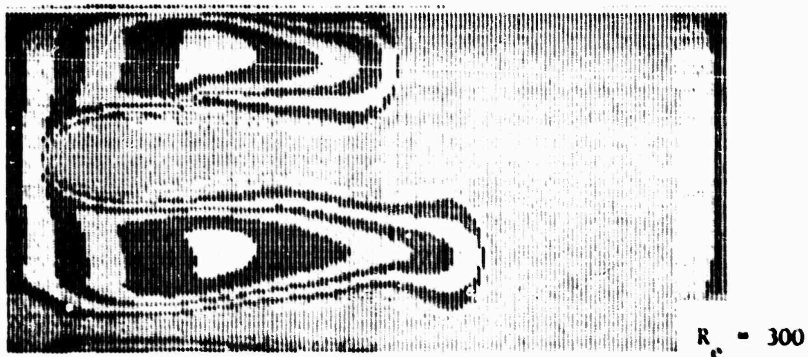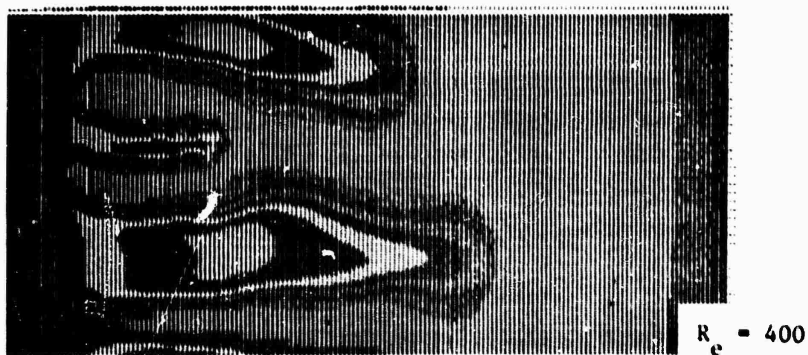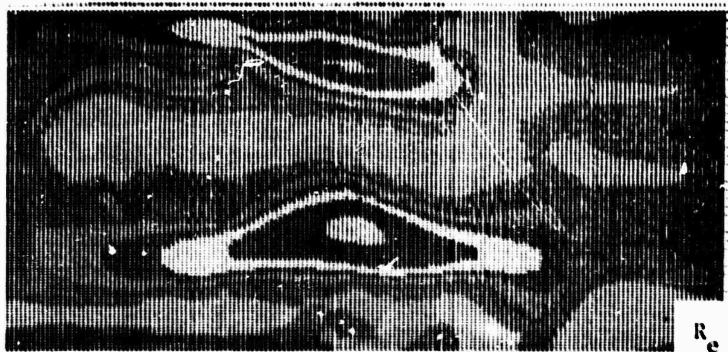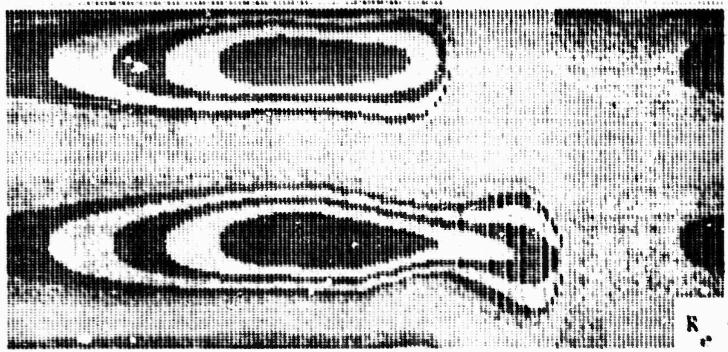
FIGURE 5 Σ CONTOURS AT t - 720 s

320

VI CONCLUDING REMARKS

The one-level, two-dimensional striation model presented here predicts, for the particular set of initial conditions considered, minimum-length scales of 2.4 to 24 m for large barium clouds near 200 km altitude. These scales are small enough that kinetic effects may be important. The kinetic corrections have not yet been calculated, and will be reported elsewhere. However, the tendency of the fluid mechanism to generate structures this small is in apparent agreement with recent Project STRESS rocket measurements[4] and with the attenuation (probably due to strong scattering or diffraction) observed in propagation experiments.[1] Further work needs to be done to determine the sensitivity of the results to initial conditions. One should also investigate the effects of ion inertia (which may be important at higher altitudes), and electrostatic coupling to the lower ionosphere in the case of small clouds.

REFERENCES

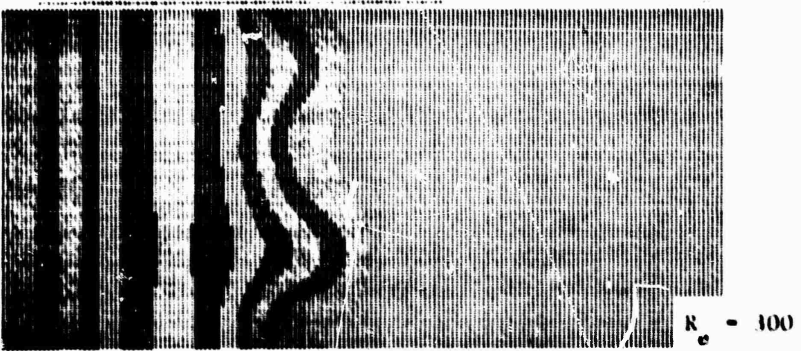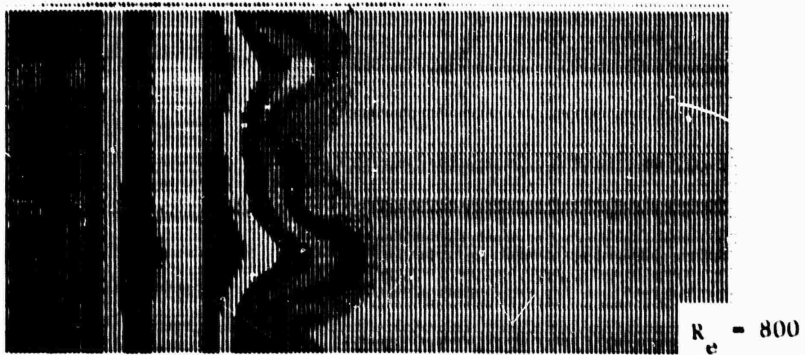1. C. Prettie, A. Johnson, J. Marshall, T. Grizinski, and R. Swanson, "Project STRESS Satellite Communication Test Results (U)," AFAL Technical Report 77-158, Air Force Avionics Laboratory, Wright-Patterson Air Force Base, Ohio (July 1977).

2. T. N. Davis, G. J. Romich, E. M. Wescott, R. A. Jeffries, D. M. Kerr, and H. M. Peek, "Observations of the Development of Striations in Large Barium Ion Clouds (U)," Planet. Space Sci., Vol. 22, p. 67 (1974).

3. W. Chesnut, "Spatial-Frequency Analyses of Striated Nuclear Phenomena; Part Two: A Model of the Striated Check Mate Cloud (U)" (Report Unpublished).

4. K. D. Baker, L. C. Howlett, J. C. Ulwich, D. Delorey, and N. Grossbard, "Measurements of Electron Density Structure in Barium Clouds-- Project STRESS (U)," Report, Utah State University, Logan, Utah (5 May 1977).

5. L. M. Linson, and J. B. Workman, "Formation of Striations in Ionospheric Plasma Clouds (U)," J. Geophys. Res., Vol. 75, p. 3211 (1970).

6. N. J. Zabusky, J. H. Doles, and F. W. Perkins, "Deformation and Stria-
    tion of Plasma Clouds in the Ionosphere, 2, Numerical Simulation of a
    Nonlinear Two-Dimensional Model (U)," J. Geophys. Res., Vol. 78,
    p. 711 (1973).

7. A. J. Scannapieco, S. L. Ossakow, S. R. Goldman, and J. M. Pierre,
    "Plasma Cloud Late Time Spectra (U)," J. Geophys. Res., Vol. 81,
    p. 6037 (1976).

8. A. J. Scannapieco, S. L. Ossakow, T. P. Coffey, and J. M. Pierre,
    "Striation Formation in a Two-Fluid Three-Dimensional Checkmate
    Simulation (U)" (Report Unpublished).

9. R. W. Kilb, W. F. Crevier, J. B. West, and C. L. Longmire, "Stria-
    tions After Nuclear Burst (U)" (Report Unpublished).

10. H. J. Volk and G. Haerendel, "Striations in Ionospheric Ion Clouds,"
    (U)," J. Geophys. Res., Vol. 76, p. 4541 (1971).

11. P. M. Banks and G. Kockarts, Aeronomy (Part A) (Academic Press, New
    York, NY, 1973).

12. R. S. Varga, Matrix Iterative Analysis (Prentice Hall, Inc., Engle-
    wood Cliffs, NJ, 1962).

13. B. E. McDonald, "Explicit Chebychev-Iterative Solution of Nonself-
    Adjoint Elliptic Equations on a Vector Computer," NRL Memo Report
    3541, U.S. Naval Research Laboratory, Washington, D.C.

SIZE, SHAPE, AND AGE OF ION CLOUDS

L. M. Linson   D. C. Baxter

Science Applications, Inc.
La Jolla, California

SIZE, SHAPE, AND AGE OF ION CLOUDS

L. M. Linson   D. C. Baxter

Science Applications, Inc.
La Jolla, California

I   INTRODUCTION

In this paper we discuss several aspects of the phenomenology of barium ion clouds. The purpose of this discussion is to establish some of the parameters that characterize the properties of the ion clouds and to report on the results of some preliminary analysis of the extensive observations that were made of the STRESS ion clouds.

The first two sections deal with the undeformed ion cloud during the first few minutes after release. The next three sections discuss some characteristics of ion clouds after they deform. Particular emphasis is placed on interpreting the electron density measurements made by the probe rockets that pass through the DIANNE and ESTHER ion clouds. In the last section we report on preliminary estimates of the equivalent age of the STRESS ion clouds in terms of their stage of development.

II   EARLY-TIME ION-CLOUD PARAMETERS

More than 90% of the ionization in a late-time barium ion cloud is deposited during the first 30 s following the release of the neutral barium atom vapor. The late-time configuration of the ionization is largely determined by the early-time characteristics of the ion cloud. As an example, the initial scale size of the ion cloud transverse to the magnetic field determines the time scale for the subsequent development of the ion cloud.

In a recently concluded study[1] of ion cloud modeling we developed
a new quantitative procedure for describing the formation of the ion
cloud from the expanding cloud of neutral barium vapor. This procedure
produces quantitative values for the parameters that characterize the
early-time ion cloud. We developed this model in order to describe the
ion clouds produced during the SECEDE II test series. We have found that
the characteristic parameters obtained from this model are consistent
with the currently available ion cloud observations made during the STRESS
test series.

Two problems have plagued previous modeling attempts. The first is
the observed fact that photographic images of early-time neutral clouds
appear to be far larger than could readily be explained by the release
of reasonable amounts of barium vapor. The amount of released vapor re-
quired by the new modeling procedure is less than half of that required
by earlier attempts. The second problem is that radar measurements indi-
cate that the early-time ion cloud is substantially narrower than the
neutral cloud. The result of the new quantitative treatment of the depo-
sition of the ion cloud from the expanding neutral vapor cloud is to pro-
duce an early-time ion cloud with a scale size transverse to the magnetic
field that is in substantial agreement with a variety of radar measure-
ments.

The modeling procedures were developed in order to describe the
properties of 48-kg barium releases at 190 km altitude with particular
emphasis on the SPRUCE ion cloud. The STRESS ion clouds were released
at altitudes 5 to 10 km lower than that of SPRUCE, which would imply a
higher local atmospheric density. This difference is compensated by the
generally lower atmospheric densities during STRESS, because STRESS was
conducted during a minimum of solar activity and SECEDE took place nearer
to a maximum in solar activity.

The different chemistry used to produce the SECEDE and STRESS ion
clouds is a significant difference. The SECEDE test series used the
older barium-cupric oxide chemical mixture while the STRESS test series
used the barium-barium nitrate chemical mixture. It is unfortunate that
we do not have as extensive a set of observations of the properties of

326

ion clouds produced by the barium-barium nitrate mixture as we have of ion clouds produced by the barium-cupric oxide mixture. However, a preliminary look at the data taken during the STRESS test series indicates that the model parameters are consistent with the limited observations that exist.

Table 1 summarizes the model parameters appropriate for 48-kg barium ion clouds produced by releases in the vicinity of 180 to 190 km altitude. Differences between these model values and values obtained by more detailed analyses of the STRESS data may serve as a motivation for a different modeling effort that is more appropriate for the barium-barium nitrate mixture. It is helpful to conceptualize the early ion cloud as having an ellipsoidally shaped Gaussian density distribution elongated in the direction of the earth's magnetic field. The density distribution transverse to the magnetic field is not precisely Gaussian-shaped. However, the deviations from a Gaussian are not large in the central portion of the ion cloud. The first entry in Table 1 is the radius transverse to the magnetic field at which the density has fallen to 1/e of the central value. This value is consistent with early-time radar measurements of ion clouds but is significantly smaller than one would estimate from photographic images of ion clouds. For modeling purposes the smaller value given in Table 1 should be used.

Table 1

EARLY-TIME ION CLOUD PARAMETERS

Parameter	Value
Ion cloud radius $\perp \bar{B}$	2.6 ± 0.2 km
Field-line ion content	$2.3 \pm 0.2 \times 10^{17}$ ions/m^2
Total ion inventory	$6 \pm 1 \times 10^{24}$ ions
Maximum peak ion concentration	$2.4 \pm 0.2 \times 10^{13}$ ions/m^3
Typical $\int n_e ds \perp \bar{B}$	$\sim 8 \times 10^{16}$ el/m^3

The second item in Table 1 is the integral of the ion concentration[*]
along the magnetic field line that passes through the maximum-density
portion of the ion cloud. The number of ions on a magnetic field line
remains essentially constant during the subsequent development of the
cloud. The total ion inventory is also a constant during the development
of the cloud. This value is in agreement with radar measurements but is
substantially less than some radiometric measurements obtained from photo-
graphs. Optical techniques for determining the ion inventory in previous
investigations have produced results that are theoretically impossible
and internally inconsistent. Until there is more consistency in the in-
terpretation of those analyses we will accept the radar measurements.

The maximum peak ion concentration occurs during the first 25 to
40 s after release. Subsequently, the ion concentration decreases as
the ion cloud expands parallel to the magnetic field. At late times the
decrease in ion concentrati   is rather slow, and a typical value of the
peak ion concentration during the time span of 1/2 to 1 hour after re-
lease is $6 \pm 2 \times 10^{12}$ ions/m^3. The last item in Table 1 does not remain
constant, and the value given is typical for an early-time cloud. How-
ever, values of the line integral of the electron concentration higher
than the quoted value can be achieved only by integrating in directions
that approach being parallel to the magnetic field or oriented in the
direction of elongation of the ion cloud transverse to the magnetic
field.

III   DISTRIBUTION OF IONIZATION PARALLEL TO $\vec{B}$

It is necessary to know the distribution of ionization parallel to
the magnetic field in order to interpret the propagation experiments that
were conducted during the STRESS test series. The rate of descent of the
peak ion concentration, the effect of neutral winds on the vertical motion

---

[*] Electron concentration and ion concentration are equal to each other and
will be used interchangeably throughout this report. Electron density
is sometimes used to mean the same quantity.

of the ion clouds, and the ionization concentration profile parallel to the magnetic field are all important. These characteristics are investigated analytically in Ref. 1. Because those results are relevant to the STRESS test series, we shall discuss two figures taken from that report and briefly summarize the principal findings.

Gonzalez[3] has measured the distribution of ionization in the ion clouds using the incoherent-scatter radar. His analysis results in electron concentration contours at 5-km altitude intervals. Figure 1 (from Ref. 2) is an example of his data format. The ESTHER ion cloud is elongated in a direction extending from west-northwest to east-southeast transverse to the magnetic field. For each of the concentration contours, one can obtain a measurement of the maximum width transverse to the direction of elongation in the region of the maximum concentration of the ion cloud.

Figure 2 shows the results of these measurements on the ESTHER ion cloud during time intervals around R + 30 and 48 min. The typical maximum widths of the iso-concentration contours obtained by Gonzalez are indicated by circles, X's, and dots. The solid lines are hand-drawn curves that pass near the data points to guide the eye, and are not analytic fits to the data. The curves differ from each other by a factor of two in concentration. The appearance of these contours is what one would obtain from a cross section of the ion cloud through the region of maximum concentration in a plane perpendicular to the direction of elongation of the ion cloud transverse to the magnetic field. The vertical and horizontal dimensions are shown to scale. The tilt of the ellipsoids is appropriate for the magnetic field dip angle of 60°. The ion cloud is much more extended parallel to the magnetic field than transverse to the magnetic field. Note that the concentration falls by more than a factor of two in less than 2.5 km. The actual electron concentration contours are narrower than shown in Figure 2 due to the finite size of the radar beam. These two times were chosen for detailed analysis by Gonzalez because they were close to the times of passage of the probe rockets. The relative positions of the probe rockets when they were in the vicinity of the maximum electron concentration contours are shown by the solid squares.

329
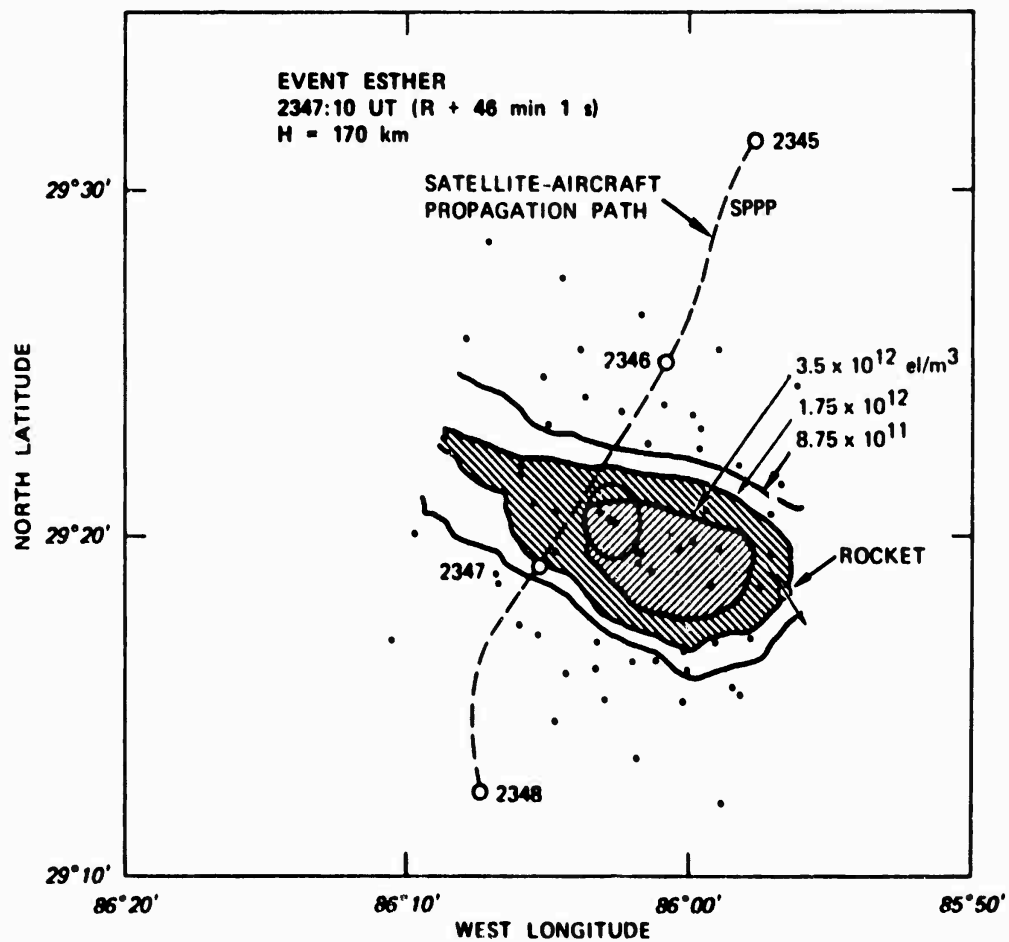
FIGURE 1   EQUIDENSITY CONTOURS ON A HORIZONTAL PLANE AT
H = 170 km — EVENT ESTHER, 2347:10 UT
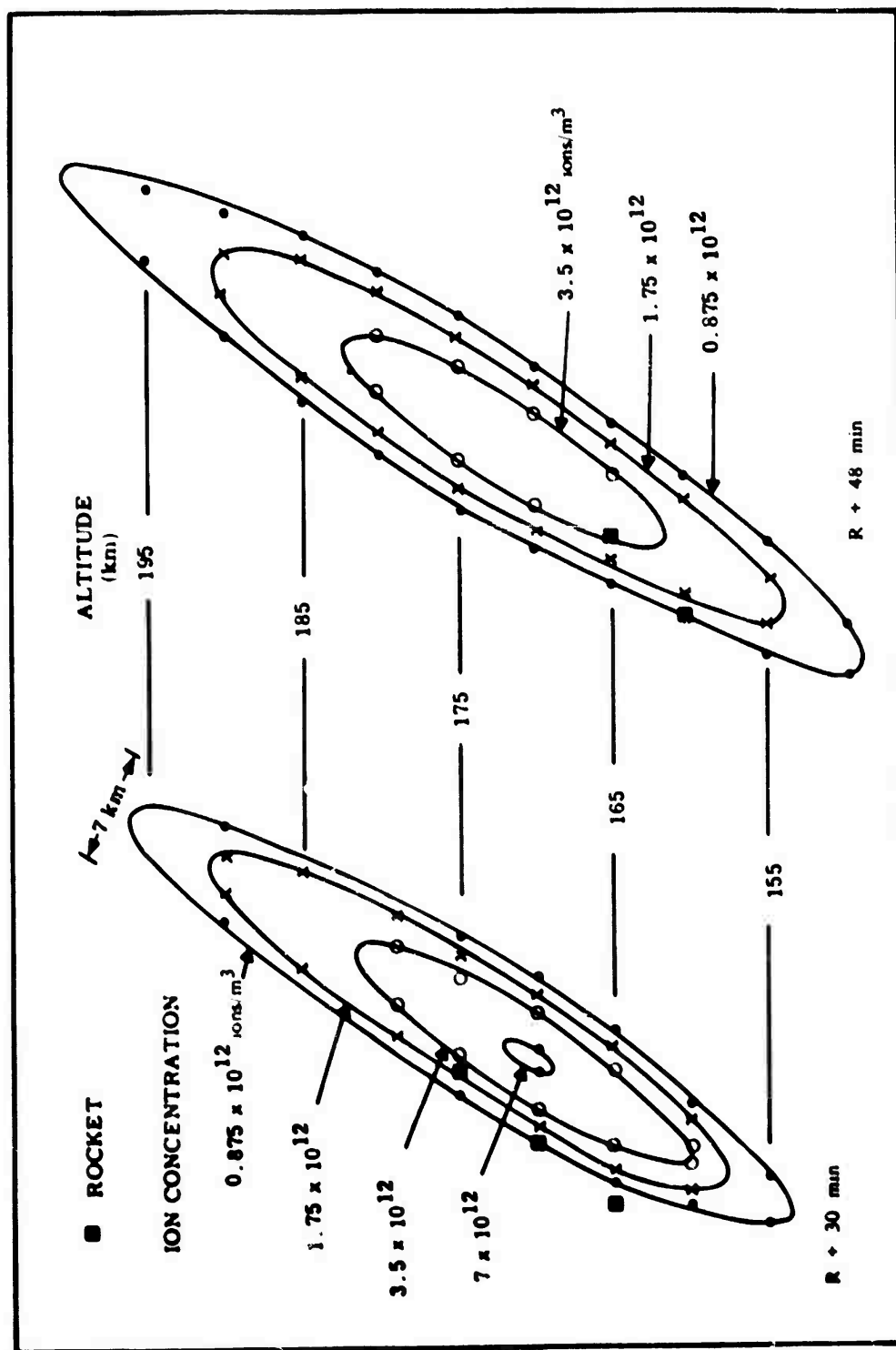
FIGURE 2   ISO-CONCENTRATION CONTOURS, EVENT ESTHER

The vertical distribution of density is not symmetric about the peak concentration. The figure on the left indicates that the peak ion concentration descended from the release altitude of 189 km to 171 km during the first 30 min after release, but the figure on the right indicates that it did not descend further during the next 18 min. This result is possible only if there is a vertical upward wind at that altitude during this time span.

The four curves in Figure 3 taken from Ref. 1 show the time development of a 48-kg barium release settling under the influence of gravity alone. These curves represent the analytic solution for an initially Gaussian-shaped cloud released at an altitude of 180 km. The final shape as shown by the lowest curve is quite broad. In order to obtain the analytic solution the atmospheric density was assumed to vary exponentially in altitude with a constant scale height. The parameters for this exponential atmospheric density model were chosen to fit the atmospheric density model employed by Chavin and Kilb[3] in their numerical simulation of Event ANNE. The density profiles obtained by Chavin and Kilb are shown by the circles and the X's in Figure 3. Because their initial cloud had a far higher ion content, we have arbitrarily rescaled their profiles to have comparable ion content. The less rapid fall-off of ion density with altitude in the numerical simulation is consistent with the use of a more realistic atmospheric density profile with increasing temperature at higher altitudes.

The excellent agreement between the analytic curves and the numerical computations indicates that both are given equivalent descriptions of the physics that was assumed to govern the descent of the ion cloud. The distributions of ionization given by the ion concentration contours of Event ESTHER in Figure 2 have a shape similar to the shape exhibited by Case 1c in Figure 3. This result is only suggestive; we have not yet obtained analytic solutions appropriate for the conditions of Event ESTHER.

The effect of constant vertical winds on the change in altitude of the peak ion concentration is shown by the curves labeled Cases 1, 3, 4, and 6 in Figure 4 taken from Ref. 1. Case 1 corresponds to no vertical winds and the agreement with the numerical simulations shown by the X's
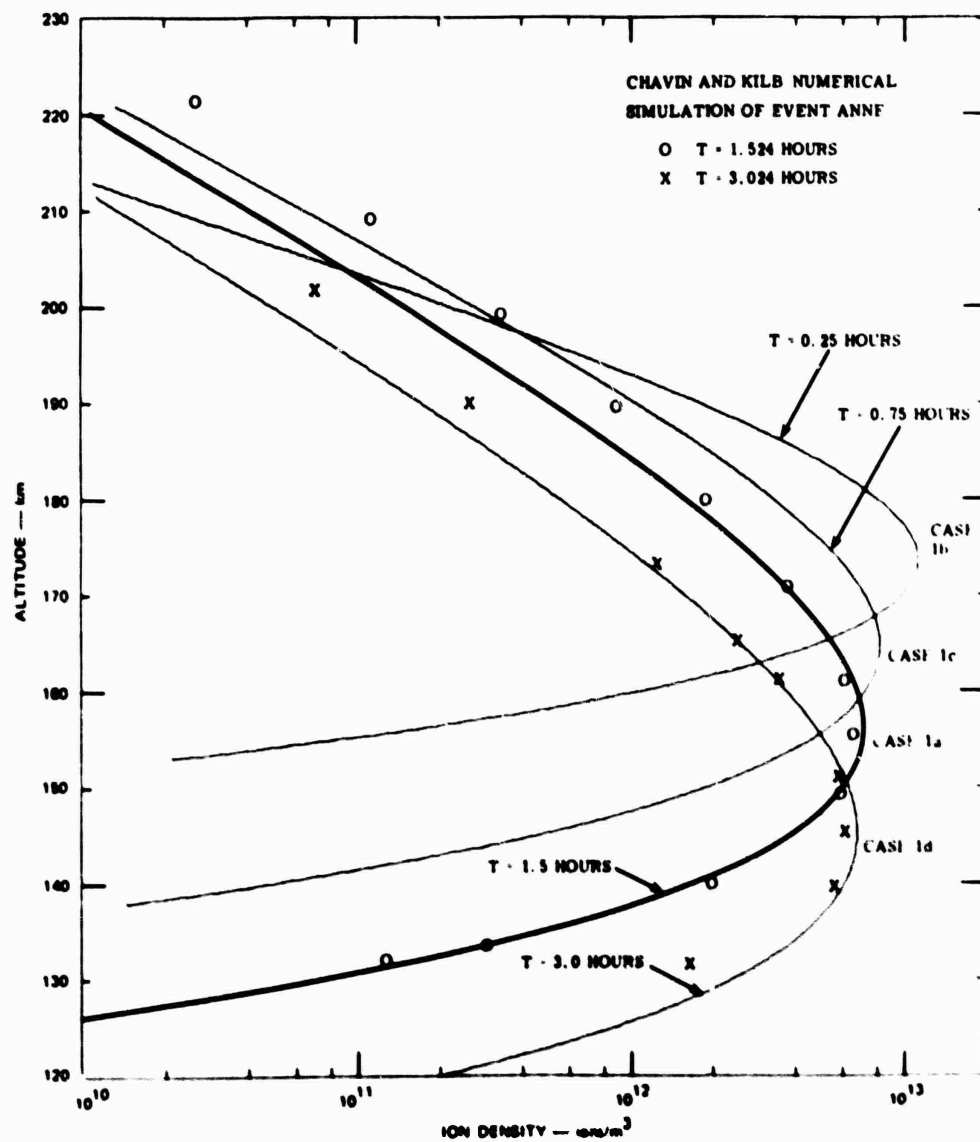
FIGURE 3   ELECTRON DENSITY PROFILES AS A FUNCTION OF TIME IN THE CASE OF NO NEUTRAL WIND, EVENT ANNE
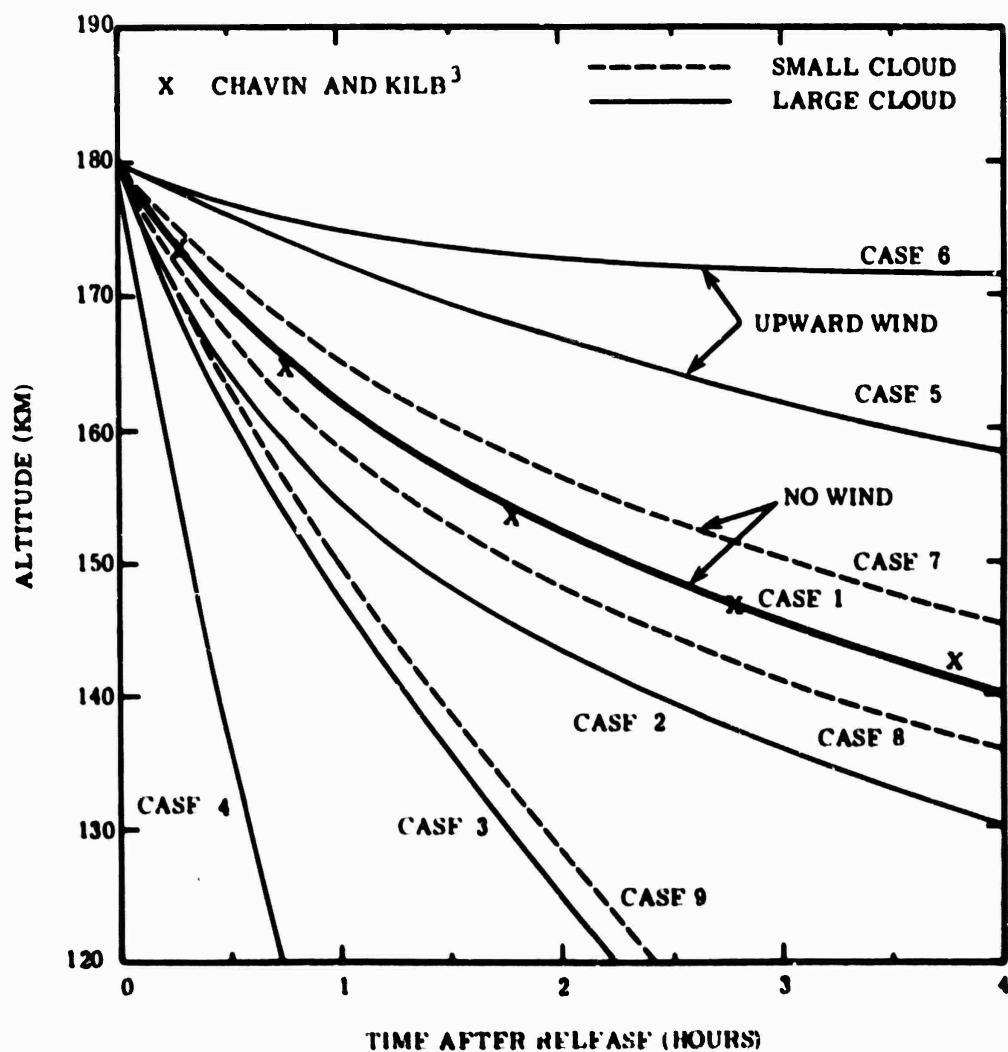
FIGURE 4   ALTITUDE OF THE PEAK ELECTRON DENSITY vs TIME WITH CONSTANT
NEUTRAL WINDS

is excellent. Cases 3 and 6 correspond to constant vertical winds of 5.2 m/s downward and upward, respectively. Case 4 is an extreme example of a large 20-m/s downward vertical wind. In this case the peak ion concentration descends by almost 44 km from a release altitude of 180 km in one-half hour. The 40-km descent in one-half hour in Event FERN suggests that there was a large (10 to 20 m/s) vertically downward wind during the time immediately following release. It is unlikely that the neutral atmosphere could sustain such a large vertical wind for such a long time over this altitude range. The presence of such large downward velocities is probably related to some kind of an atmospheric acoustic gravity-wave phenomenon.

We anticipate that the analytic model derived in Ref. 1 will aid in interpreting the observations made of the STRESS ion clouds.

IV ION-CLOUD DEFORMATIONS TRANSVERSE TO $\vec{B}$

We now turn our attention to the configuration of ionization in a plane transverse to the magnetic field. In order to better understand the rocket probe data, we briefly review some of the key characteristics regarding the time development of the ion cloud. We will also introduce the coupling parameter, η, that provides a measure of the degree to which the main ion cloud is coupled to the ambient neutral wind.

Figure 5 shows in schematic form some of the principal features that we wish to emphasize. The sketch at the top of the figure represents a view of a barium release at a large angle with respect to the magnetic field. This diagram is appropriate several minutes after release but before the ion cloud has begun to striate. The center of the spherical neutral cloud moves with velocity $\vec{V}_n$ with respect to an arbitrary fixed frame of reference labeled 0. The main ion cloud, characterized by the heavily shaded elliptically shaped region, contains the bulk of the high-density portions of the ion cloud and moves with the velocity $\vec{V}_c$. The right-hand edge of the shaded region is the low-density portion that moves with the ionospheric $\vec{V}_i$, which is equal to the ambient $\vec{E}_a \times \vec{B}/B^2$ velocity derived from the ambient ionospheric electric field, $\vec{E}_a$.

335

SCHEMATIC
$\perp \vec{B}$

NEUTRAL
CLOUD

$\vec{V}_c$

$\vec{V}_n$

$\vec{V}_i = \dfrac{\vec{E} \times \vec{B}}{B^2}$

O

SCHEMATIC
$\parallel \vec{B}$

D

d

R + ~ 15 min

R > 15 min

< 10 km   < 1 km

50-100 km
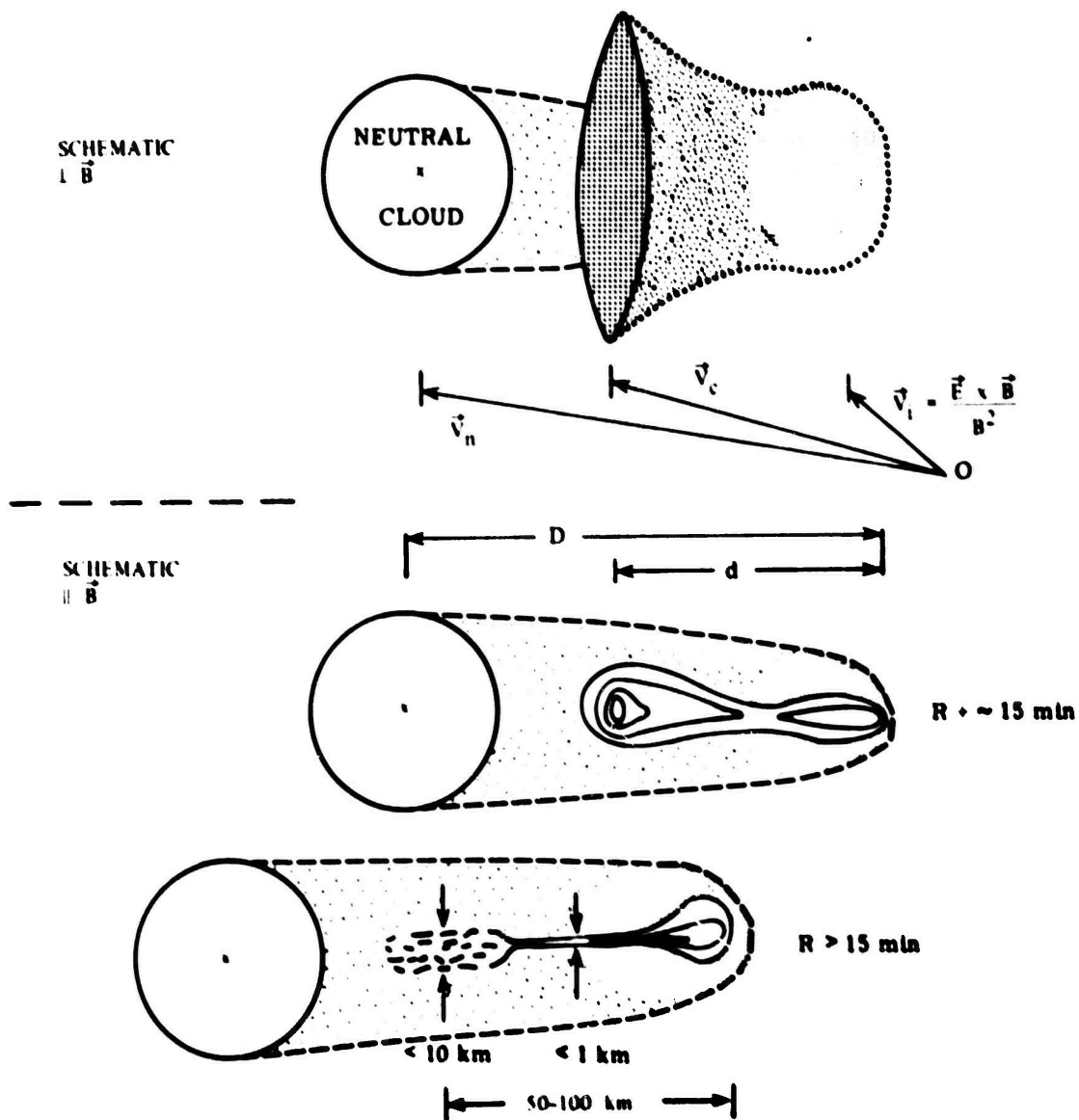
FIGURE 5   SCHEMATIC REPRESENTATION OF BARIUM CLOUD DEVELOPMENT

The ion cloud is elongated in the direction of the magnetic field and is larger in this direction than the neutral cloud. The lightly shaded region between the main ion cloud and the neutral cloud represents low-density barium ionization, often called the ion bridge, resulting from the late-time dissociation of BaO in the neutral cloud. This low-density ionization moves with the ambient ionospheric velocity $\vec{V}_i = \vec{E}_a \times \vec{B}/B^2$ is left behind as the neutral cloud blows by. The ionization concentration in the ion bridge is typically more than a factor of less than the ionization in the main ion cloud.

The middle diagram schematically presents ion concentration contours in a plane transverse to the magnetic field corresponding to the distribution of ionization at the top of the figure. The large ion concentration in the main ion cloud is represented by several distorted ion concentration contours. The contours emphasize that the backside of the ion cloud--i.e., the side closest to the neutral cloud--has a larger density gradient than the front side. The dimension of the ion cloud transverse to the direction of its elongation is narrower than the neutral cloud.

Two factors contribute to the secondary density maximum in the right-hand or leading edge of the ion cloud. One factor is the thinning of the ionization between the leading and trailing edges. The other is that the ionization deposited by the late-time ionization process is most intense in this portion because the neutral cloud had a much greater concentration of BaO at early times before it had expanded greatly by diffusion. Indeed there is a significant ionization concentration gradient in the ion bridge between the neutral cloud and the leading edge of the ion cloud. This gradient in ion concentration is represented by the shaded regions of two different gray tones. The dashed lines represent the outer edges of the ion bridge.

The two upper diagrams indicate that a single photograph can be used to estimate the coupling of the ion cloud to the ambient atmospheric neutrals. The distance from the leading edge of the ion cloud to the center of the neutral cloud is D, and the distance from the leading edge to the center of the main ion cloud is d. The ratio $\eta = d/D$, called the coupling parameter, is a measure of the coupling of the ion cloud to

the neutral cloud. Another measure of the coupling parameter η is provided by the ratio $|\vec{V}_c - \vec{V}_i|/|\vec{V}_n - \vec{V}_i|$. The determination of the distances D and d is not as easy as it would appear from these sketches because the leading edge on the right-hand side is an extended diffuse portion of the ion cloud and its appearance depends sensitively on the direction from which it is viewed.

The coupling of the ion cloud to the neutral wind depends on the depolarization of the ambient ionospheric electric field as seen in a frame of reference moving with the ambient neutral particles. Theoretical studies whose discussion is beyond the scope of this report show that the coupling parameter η is a monotonic function of the ratio of the field-line-integrated Pedersen conductivity of the ion cloud, Σ_p^c, to the field-line-integrated Pedersen conductivity of the ambient ionosphere, Σ_p^a. The velocity of the ion cloud can be written

$$\vec{V}_c = \vec{V}_i + \eta(\vec{V}_n - \vec{V}_i)$$

where

$$\eta = \eta\left(\Sigma_p^c/\Sigma_p^a\right) \sim \begin{cases} \Sigma_p^c/2\Sigma_p^a \quad , \quad \Sigma_p^c \ll \Sigma_p^a \quad ; \\ 1 \quad , \quad \Sigma_p^c \gg \Sigma_p^a \quad . \end{cases}$$

The sketch at the bottom of Figure 5 shows a schematic of the configuration of ionization at a later time after the striations have developed fully and sheets and rods have formed. The ion cloud has continued to elongate in the $\vec{V}_n - \vec{V}_i$ direction so that by a half-hour or more after release the ion cloud can extend from 50 to 100 km. All of the high-density portion of the ion cloud has evolved into sheets and rods. This sketch shows that the maximum dimension transverse to the direction of elongation is typically less than 10 km. The region between the highly structured high-density portion of the ion cloud extending all the way back toward the leading edge has thinned considerably and typically forms a narrow sheet less than 1 km in transverse width. This portion of the ion cloud is called a thin sheet because the dimension out of the paper

338

parallel to the magnetic field is typically of order 60 km. At late-time, striation structure is often seen on the back edge of the secondary maximum near what was formerly the leading edge of the ion cloud. Note that the extended sheet and the highly structured part of the ion cloud are typically embedded within the less dense ion bridge.

One never obtains photographs of ion clouds that show all of the features indicated in the bottom two sketches of Figure 5 because the ionization is extended parallel to the magnetic field and because there is only one point in the sky, called the magnetic zenith point, where the line of sight is tangent to the magnetic field line at the altitude of the ion cloud. The projection of the extended distribution of ionization parallel to the magnetic field into a field of view obscures the details of the configuration of ionization except in the vicinity of this magnetic zenith point. The sketches in Figure 5 have been inferred from the examination of a large number of photographs of different barium releases.

Some of the features identified in Figure 5 can be seen in the excellent photographs taken by Boquist et al. of Technology International Corporation.[4] Reference 4 contains some examples of these photographs. The photographs of BETTY from Site C-6 provide views of a structured ion cloud embedded within the ion bridge extending toward the neutral cloud. CAROLYN, a more slowly developing cloud, provides a clear view from Site C-6 of the rapid decrease in intensity of the ion bridge between the leading edge of the ion cloud and the neutral cloud. The fact that the middle sheet-like portion of the ion cloud is thinner than the highly-structured denser portion is evident, but the ion cloud did not pass near enough to the magnetic zenith point in order to demonstrate that this sheet is less than one kilometer thick. The late-time photographs of ESTHER from Site C-6 also show structured ionization embedded within the more extensive but diffuse remnants of the ion bridge. The best view of the highly structured high-density portion of an ion cloud was obtained from Tyndall during Event CAROLYN shortly before the sun set. Sheets and rods in this region are clearly visible.

V CONFIGURATION OF IONIZATION IN THE DIANNE ION CLOUD

In this section we discuss the distortion of the DIANNE ion cloud and show the portions of this cloud through which the probe rockets passed. The results reported in this section are preliminary and subject to refinement.

A. Distortion of the DIANNE Ion Cloud

Good photographs of the DIANNE ion cloud were not obtained until .proximately R + 15 min because the ion cloud had not separated sufficiently from the neutral cloud prior to this time and the sky background was bright. When the ion cloud was first visible, the configuration of the neutral and ion clouds appeared to be quite normal; the ion cloud appeared similar to the SPRUCE ion cloud released during the SECEDE II test series. There was, however, an unusual change in the appearance between R + 15 and R + 20 min. Photographs obtained by Linson operating the TIC remote optical equipment at a site near Grayton Beach provide a unique record of this change because the ion cloud passed through the magnetic zenith between R + 25 and R + 30 min.

Figure 6 shows sketches of the configuration of ionization as recorded on photographs taken at four different times from Grayton Beach. The denser part of the ionization appears within the closed solid lines. The dashed lines define the outer border of the less-dense ion bridge. The straight lines indicate the appearance of field-aligned striations within the ion cloud. Bear in mind that these sketches represent the outlines of the image of the ion cloud as seen in photographs and do not represent the idealized schematic structure shown in Figure 5.

There are two purposes for the sketches in Figure 6. The first is to indicate the type of deformation of the ion cloud that took place. The second is to indicate through which portion of the ion cloud the two probe rockets ST707.51-1 and ST707.51-2 passed. By R + 20 min, an unusual deformation of the ionization was seen from several different sites. In the sketches, the easternmost portion of the ion cloud is labeled A and the low-density leading edge portion of the ion cloud is labeled C. By

340
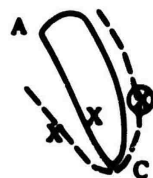
(a) R + 15 min 5 s
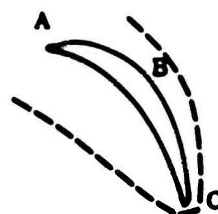
(b) R + 23 min 17 s
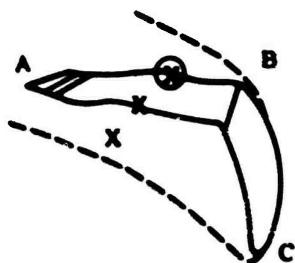
(c) R + 33 min 10 s
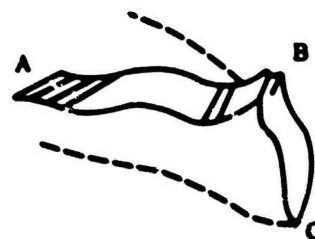
(d) R + 36 min 41 s

FIGURE 6   CONFIGURATION OF ION CLOUD, EVENT DIANNE

R + 25 min a new, pronounced feature became apparent in the ion cloud. We have labeled this feature B in the last three sketches of Figure 6.

The simplest interpretation of these photographs is that the long, thin sheet that develops behind the structured part of the ion cloud bent and developed a corner that at the latest stages appeared very cusp-like. We expect that future analysis will provide a more complete and accurate description of the deformation that took place. The neutral cloud, not shown in these sketches, was not spherical but was very ellipsoidal in shape. This observation provides prima facie evidence that there was a large neutral-wind shear present during Event DIANNE. The late-time photographs of the DIANNE ion cloud clearly show that some of the neutral cloud was further west than any portion of the ion cloud. An adequate explanation of the deformation of the ion cloud will require an unraveling of the neutral-wind shear, which undoubtedly affected the ion cloud development.

An attempt was made to obtain information on the motion of the features of the clouds labeled A, B, and C by assuming that the peak ion concentration remained at a constant altitude of 180 km. This analysis shows that feature A and feature C each moved with a nearly constant velocity. The motion of feature A was 45 m/s eastward and 23 m/s southward. The leading edge, feature C, moved at 29 m/s eastward and 43 m/s southward. Because these are not triangulated results, better numerical values of the motion of these parts of the ion cloud will be available in the future, but the conclusion that they moved with a nearly constant velocity is not likely to change. Feature B, the bend in the sheet, did not move with constant velocity, but its velocity changed throughout the time period of the optical coverage. In particular, after R + 30 min, it appeared to stop its eastward motion altogether.

Some views of the ion cloud, especially those from the aircraft, indicate that at late time there were two ion clouds present. The second concentration of ionization as seen from the aircraft probably is associated with the feature B. Because of the effects on propagation paths through the DIANNE ion cloud, it will be important to obtain a better unraveling of the configuration of ionization in these two portions of the cloud.

342

B.   Probe Rocket Passages Through the DIANNE Ion Cloud

Figure 6(a) is obtained from a photograph that was taken at the same
time that the probe rocket ST707.51-1 measured enhanced electron concen-
trations at around 162 km altitude. Baker et al.[6] provide a more complete
description of the electron concentration measurements. The three X's in
Figure 6(a) show the apparent location of the rocket projected into the
film plane when the rocket was at altitudes of 150, 162, and 173 km re-
spectively. The circled X represents the lowest altitude location. The
maximum electron concentration was measured at the location of the cen-
ter X.

The probe rocket did not go through the high-density portion of the
ion cloud. It passed closer to the low-density leading edge of the ion
cloud. This partially explains the fact that the measured electron con-
centrations are substantially less than those that existed in the main
part of the ion cloud. The first and last measurements of enhanced ioni-
zation given by the two outer X's coincide very closely with the outer
border of the ion bridge as seen in this film plane.

Figure 7, from Ref. 5, illustrates two additional factors contri-
buting to the low value of electron concentration measured by the probe
rocket. The rocket trajectory grazed the underside of the lower-altitude
portion of the ion cloud. The rocket probably did not cross the sheet
in this portion of the ion cloud and probably exited the ion cloud before
reaching the altitude of maximum electron concentration. The ion cloud
modeling indicates that the probable value of the peak ion concentration
in the main ion cloud is several factors larger than the maximum value
measured by the probe rocket ST707.51-1.

Figure 6(c) was made from a photography taken 30 s prior to the
passage of probe rocket ST707.51-2 through the ion cloud. The three X's
show the location of the probe rocket at altitudes of 174, 182, and 189
km. The maximum electron concentration is measured at the location of
the center X. The circled X represents the lowest altitude position of
the rocket. The first and third X's represent the beginning and ending
portions of the electron concentration enhancement. These locations lie

343
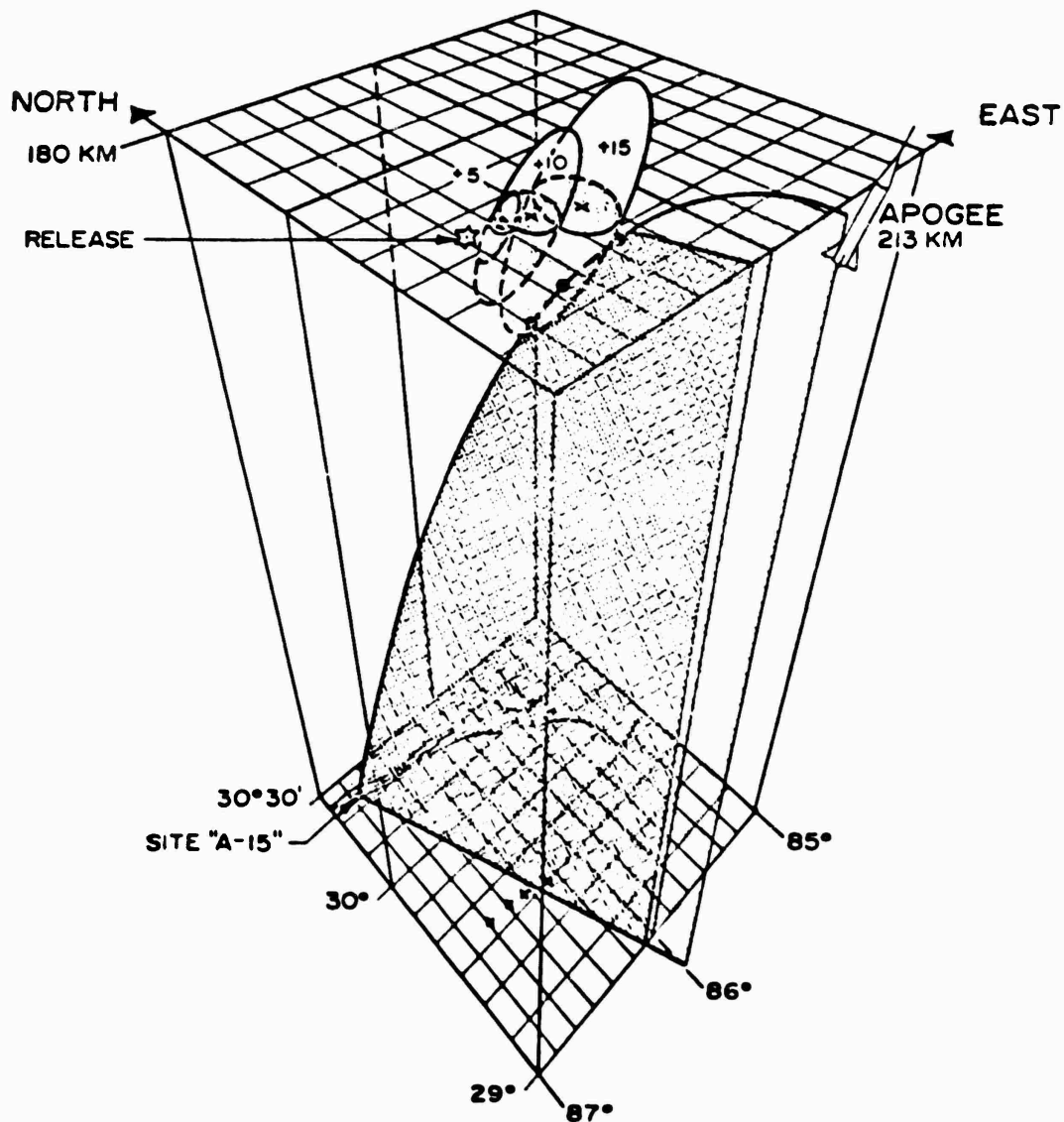
FIGURE 7   TRAJECTORY OF PROBE ROCKET ST707.51-1. Release point of Event DIANNE
is shown along with the visible ionized cloud track points at R + 5, 10, and 15 min.
Rocket entry point into the cloud, maximum point and exit point (from electron
density results) are indicated by the three dots along the trajectory. Source: Ref. 5.

within the dashed outer border of the ion bridge. The rocket probe did not pass through the high-density structured part of the DIANNE ion cloud. The simplest interpretation is that the probe passed through the thin sheet that was created by the elongation of the ion cloud as feature A moved eastward away from feature B. The very narrowness of the electron concentration profile is very strong evidence that this portion of the ion cloud does form an extremely thin sheet whose dimension transverse to the magnetic field is substantially less than 1 km.

Other evidence[6] indicates that this interpretation of the passage of this probe rocket may have to be revised. We expect that further analysis will produce a more definitive interpretation of the significance of these results in terms of models of the ion cloud.

VI THE STRUCTURED ESTHER ION CLOUD

The probe rocket ST707.51-4 passed through a high-density, highly-structured portion of the ESTHER ion cloud at R + 46 min. We present a unique interpretation of the significance of these measurements in conjunction with the measurements by Gonzalez.[3] The procedures and modeling described below show that the scale size of the striated ionization is substantially less than a more straightforward interpretation might lead one to believe. The implications of this interpretation for the theoretical description of late-time striations should be substantial.

A. Motion of the Ion Cloud

The ESTHER ion cloud was visible from R + 80 to R + 100 min and the highly-structured eastern portion of the ion cloud was then south of Cape San Blas. The appearance of the cloud was consistent with the description given in Section IV. Several of the characteristic features identified in the bottom sketch of Figure 5 are visible in the photographs of ESTHER taken by Boquist et al.[4]

Measurements made by Gonzalez[3] with the incoherent-scatter radar show that the region of maximum ion concentration was located in the midst of the highly structured eastern portion of the ion cloud. Photographs taken

345

during the time when it was visible indicate that this portion of the ion cloud was moving with a velocity of 15 m/s to the east and 20 m/s to the south. This motion is considerably slower than the earlier STRESS ion clouds. The average velocity during the hour and a half until the ion cloud became visible was slightly different from the measured velocity during the period when the cloud was visible. The average southward velocity appeared to be approximately the same as the late southward velocity, but the average eastward velocity was 24 m/s. Hence, during the time prior to the passage of the probe rocket ST707.51-4, at R + 46 min the early eastward velocity of the ion cloud was somewhat larger than its southward velocity.

The ion cloud was more than 90 km long, with the leading edge approximately midway between the eastern portion and the original release point. The direction of elongation of the ion cloud was approximately southeastward. The optical and radar measurements of the motion of the high-density part of the ion cloud are consistent with each other.

The above description of the motion of the ion cloud and the direction of elongation of the ion cloud indicates that the neutral wind first blew in an east-southeasterly direction until the time of passage of the second probe rocket, and then probably changed direction toward the southeast at R + 46 min. The slow motion of the ion cloud also indicates that the neutral-wind velocity was much lower during Event ESTHER than for the earlier STRESS ion clouds. A more slowly moving neutral cloud would tend to display a much wider ion bridge, since the neutral cloud will have had more time to diffuse before it has moved very far. The appearance of the ion bridge during Event ESTHER compared to the ion bridge of BETTY supports the conclusion that the neutral-wind velocity was slow.

B. Rocket Passage Through the Structured Ion Cloud

We present a detailed analysis of the structured ionization measured by the probe rocket ST707.51-4. Gonzalez[2] has made extensive, detailed measurements of the electron concentration in the ESTHER ion cloud at approximately R + 48 min immediately after the passage of the second probe rocket. Figure 1 shows the electron concentration contours

346

measured by the incoherent-scatter radar at an altitude of 170 km. The small circle with an arrow drawn through it shows the location of the probe rocket when it crossed this altitude. Figure 8, from Ref. 5, shows the highly structured electron concentration profiles measured by the probe rocket between 140 and 160 s after launch. Ten striations are identified in this figure. We present an interpretation of these measurements as they relate to our model of the ion cloud.

Figure 9 shows an electron-concentration contour and a small circle designating the location of the rocket when it crosses the altitude of 170 km taken from Figure 1. The solid arrow shows a projection of the rocket trajectory onto a plane at the altitude of 170 km. Short bars across the arrow identify the portion of the trajectory of this rocket that lies between 140 s and 160 s after launch. During this portion of the rocket flight the probe rocket measured the structured ionization. The two dashed arrows pointing vertically represent projections of the earth's magnetic field lines that pass through the beginning and ending segments of the rocket trajectory. At the beginning of this segment of the rocket trajectory, the probe rocket was 6.4 km below the plane shown in Figure 9, while at the end of this segment of the rocket trajectory the probe rocket was 7.8 km above this plane. The structured ionization measured by the probe rocket is aligned with the earth's magnetic field. Portions of the rocket trajectory during the time intervals in which enhanced, structured ionization was measured have been projected along the field line to the plane at an altitude of 170 km. The ten heavy black dashes in Figure 9 thus represent the intersection of the striations being measured by the probe rocket with the constant altitude of 170 km. The length of the heavy dashes is consistent with the period of time the probe rocket spent within each of the ten striations.

We assert that the sheet-like striated structure extends in the east-southeast direction. This assertion is supported by threee independent pieces of evidence. First, the ion cloud motion was east-southeastward at this time, indicating that the neutral wind was blowing in that general direction. Second, the radar measurements indicated that the electron-concentration contours were elongated in the east-scutheast direction.
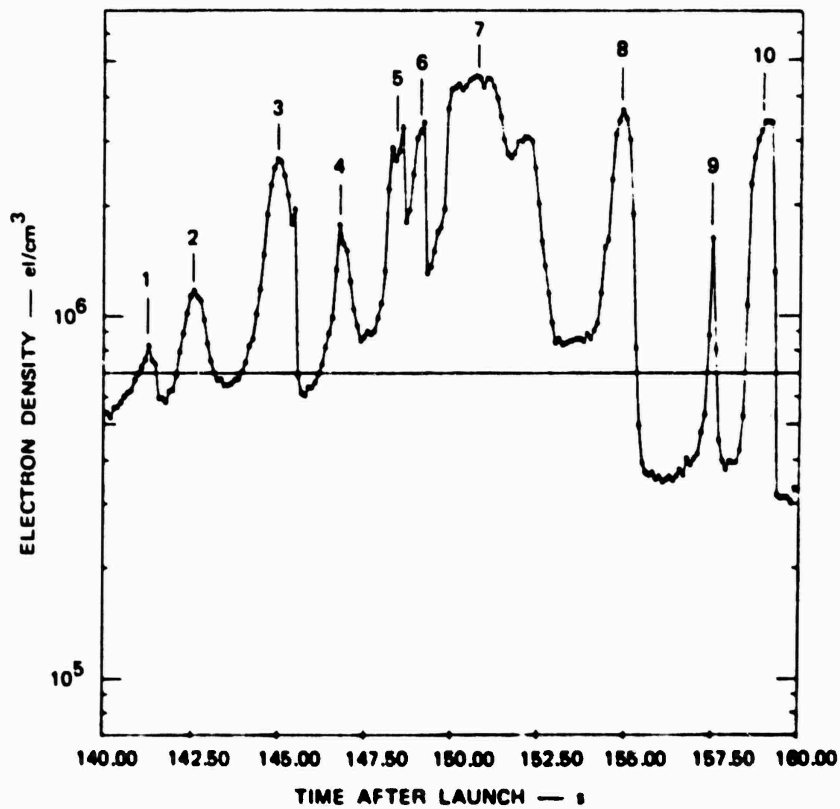
347

FIGURE 8   REGION OF ELECTRON DENSITY STRIATIONS MEASURED FROM T + 140 TO
160 s (163 to 178 km) BY PROBE ST707.51-4 (ESTHER R + 46 min). The
density striations are numbered to aid discussion. Source: Ref. 5.

348
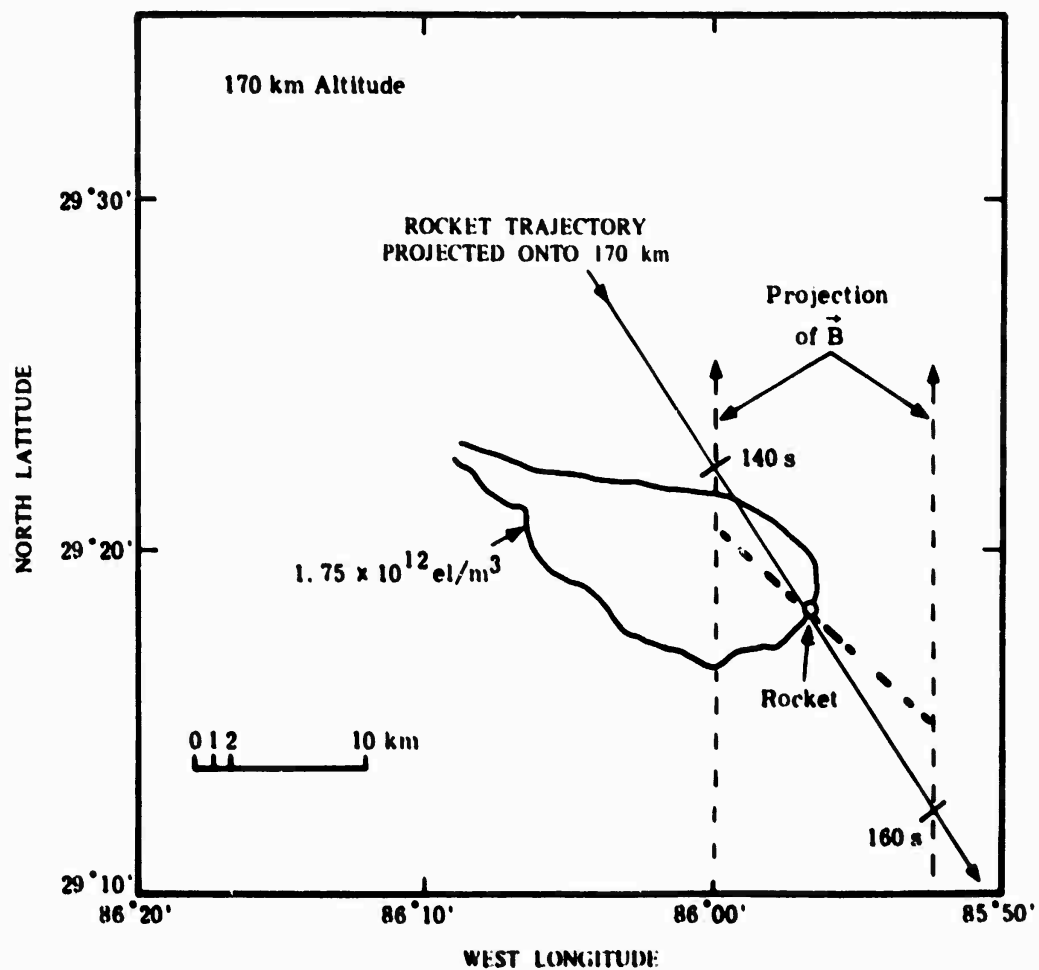
FIGURE 9   ROCKET PASSAGE THROUGH THE ESTHER ION CLOUD AT ~R + 48 min

349

Third, both of these observations are consistent with the elongation of the ion cloud at R + 1 hr 30 min when it became visible.

Figure 10 is our interpretation of the orientation of the sheet-like structures in the striated portion of the ESTHER ion cloud. The electron-concentration contours taken from Figure 1 of Gonzalez[a] are shown here for reference. The portions of these contours that would pass through the striated sheets are omitted for clarity. The ten heavy dashes shown here are the same as those discussed in Figure 9. Only two of the striations were thick enough to indicate that they had a finite width in Figure 10. The others are indicated by solid lines. These lines then represent the intersection of the striated sheet-like structure with an altitude of 170 km. These structures were not measured in this plane but were measured on the field lines that pass through the heavy dashes, and intersect the probe rocket trajectory. The extension of the sheet-like structures eastward and westward of the heavy dashes represents artistic license. The orientation of the sheets, however, is supported by strong theoretical arguments.

The width of the sheet-like region transverse to the direction of elongation of the ion cloud is identical to the width of the highest electron-concentration contour, and is less than 5.8 km as indicated in Figure 10. Because the sheet-like structures are not vertical but are aligned with the earth's magnetic field, which has a dip toward the north of 60°, the actual width occupied by the striated sheets is only 5.0 km. In other words, between 140 s and 160 s of flight time, the probe rocket traveled 19 km in the direction of the earth's magnetic field, 18 km in the direction of the elongation of the sheets, and a total of only 5 km transverse to their direction of elongation.

This interpretation of these measurements implies some rather surprising conclusions regarding the dimensions of the sheet-like striations. The rocket is traveling across the sheets at the rate of 250 m/s. If the electron concentration enhancements shown in Figure 8 represent traverses across sheets as we have just described, then the 2.5-s time ticks shown along the bottom of Figure 8 represent a distance of 625 m across the sheets. This interpretation leads to the conclusion that several of the

170 km Altitude

8.75×10^{11} el/m^3

1.75×10^{12}

3.5×10^{12}

NORTH LATITUDE

29°30'

29°20'

29°10'

0 1 2   10 km

5.8 km

86°10'   86°00'   85°50'

WEST LONGITUDE
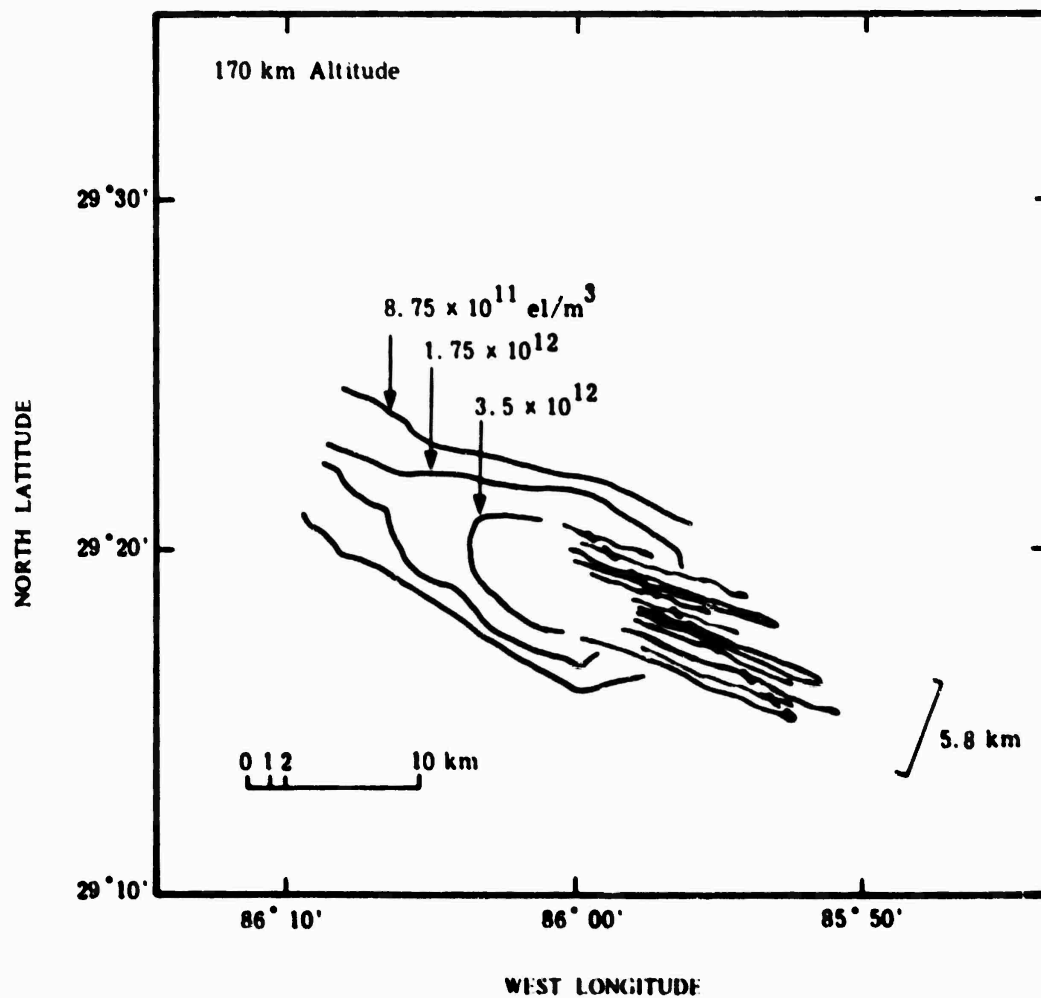
FIGURE 10   SHEET-LIKE STRUCTURE IN THE ESTHER ION CLOUD

351

sheets measured by the probe rocket have a full-width at half-max of 50 to 200 m. This observation is consistent with some unique high-resolution photographs obtained by Boquist et al.[7] of the SPRUCE ion cloud in which a sheet with full-width of approximately 60 m was seen.

The extremely narrow ninth striation could be interpreted as either a traverse through an extremely thin ion sheet, or the grazing of the steep back-side of a more rod-like striation. The location of the tenth striation far eastward of the main ion cloud and the asymmetry of the electron concentration profile in the tenth striation suggest that this measurement does not represent a traverse through an ion sheet. Traverses through ion sheets would produce fairly symmetric electron concentration distributions. The very sharp fall-off in electron concentration as the rocket exits this last striation could be interpreted as the steepened backside of a more rod-like striation. Thus the 16-m e-folding distance for the fall-off in electron concentration should be interpreted as a measure of the density gradient on the backside of the striation. The e-folding distance need not be reduced by a factor of 5 due to motion nearly perpendicular to the direction of the density gradient.

The north-south location of the sheets at this altitude is consistent with the measurements obtained by Gonzalez,[2] but it is puzzling that the incoherent-scatter radar did not measure significant ionization further east than shown by the electron concentration contours. The width of the striated region measured by the probe rocket is also consistent with the width of the high-density portion of the ion cloud measured by the incoherent-scatter radar.

VI   EQUIVALENT AGE OF THE STRESS ION CLOUDS

One of the objectives of the STRESS test series was to obtain late-time photographs of structured ion clouds in order to provide information about the process that leads to dissipation of the striated structure. For this reason the barium clouds were released earlier than the usual 6° solar depression angle that is appropriate for photography at the time of release. As a result, structured ionization was seen as late as two hours after release in the case of the FERN ion cloud.

Several different time scales are important to a discussion of the age of a structured ion cloud. One time scale is given by a simple diffusion model. The time-dependence of the Gaussian radius of a rod-like, Gaussian-shaped striation that expands by diffusion is given by $(a^2 + 4Dt)^{1/2}$ where D is the diffusion coefficient. The time it takes to double the size of the striation is $t = 3a^2/4D$. If ionization structures only double in size in two hours, the conclusion is that the effective diffusion coefficient transverse to the magnetic field is less than a^2 m^2/s, where a is measured in units of 100 m. That small scale-size structures were seen in the late-time barium ion clouds indicates that the effective diffusion coefficient transverse to the magnetic field is very small. This observation supports the conclusion[8] that diffusion of the high-density portions of an ion cloud is controlled by electron collisions.

There is a different time scale appropriate for measuring the age of a barium ion cloud in terms of its stage of development. The SPRUCE ion cloud had well-developed striation structure when the sun set on it approximately R + 27 min. The STRESS test series was to produce observations of the further development of the structured ionization in a cloud that was several times older than the SPRUCE ion cloud. The dynamical time scale for the development of ion clouds varies inversely with $|\vec{V}_n - \vec{V}_i| = |\vec{V}_n - \vec{E}_a \times \vec{B}/B^2|$, where V_i is the velocity of the ambient ionosphere due to the ambient electric field, $\vec{E}_a$. Ion clouds released when the neutral-wind velocity is lower than normal evolve more slowly and take longer to develop. Indeed, in comparing similar-sized ion clouds released at similar altitudes, it is appropriate to describe this "age" in terms of their length, d, shown in Figure 5, in the direction of the neutral wind.

We estimated the equivalent age of the STRESS ion clouds in comparison to the age of the SPRUCE ion cloud. The results of this comparison are summarized in Table 2. Because the neutral-wind velocity could not be measured during Event ESTHER we defer discussion of this event until we have discussed the others. For each of the other events, an estimate was made of the coupling parameter, η, defined in Section IV, and listed in the second column. On the basis of available information we estimate

353

Table 2

PRELIMINARY ESTIMATE OF EQUIVALENT AGE
OF STRESS ION CLOUDS AT SUNSET

Event	Coupling Parameter, η	$\|\vec{V}_n - \vec{V}_i\|$ (m/s)	Striation Onset Time (min)	Developed-Striation Time (min)	Equivalent Age at Sunset (min)
SPRUCE	0.55	55	12	24	27
ANNE	0.65	55	13 ± 2	28	30
BETTY	0.75	--	(14)	30	33
CAROLYN	0.65	50	16 ± 3	32	32
DIANNE	0.65	42	17 ± 3	34	28
ESTHER	0.65	25	~30	60	40
	0.55	32	~21	42	57

the magnitude of the neutral-wind velocity relative to the ionospheric velocity, $\|\vec{V}_n - \vec{V}_i\|$, in the third column. The fourth column contains a preliminary estimate of the time when striations have appeared in the ion cloud. These times will be refined by a more extensive examination of the complete photographic record. We also estimate the time when the structured ionization is well developed. This time is approximately twice the striation onset time, and photographs of the ion clouds at these times verify that the ion cloud indeed was highly structured. The sky brightness prevented the observation of striation development during Event ESTHER.

By taking into account the different coupling parameters and the different values of $\|\vec{V}_n - \vec{V}_i\|$, we estimated the relative time scale for development of each of the STRESS ion clouds in comparison to the time scale of development of the SPRUCE ion cloud. By adjusting the time lapse from release to sunset by the different relative time scales for ion cloud development, the equivalent age of the STRESS ion clouds in terms of the stage of development of the SPRUCE ion cloud when the sun set on it, is obtained and listed in the last column of Table 2. In terms of their stage of development, the first four STRESS ion clouds were not significantly older than the SPRUCE ion cloud.

354

For ESTHER we could not make a direct estimate of the coupling parameter. Instead, we assumed two different values for η in order to estimate the equivalent age of ESTHER when the sun set on it at approximately R + 100 min. We chose the value 0.65 to correspond with the majority of the values for the other STRESS ion clouds. We chose a second value, 0.55, because it corresponds to the value of the SPRUCE ion cloud and, because ESTHER was released during daylight, when the ratio of the cloud's conductivity to the ambient conductivity is presumable lower than for the other STRESS ion clouds.

As discussed in the previous section, the magnitude of the average velocity of the main ion cloud, $\vec{V}_c$, toward the southeast during the first hour and a half after release was 32 m/s. The average velocity of the leading edge, $\vec{V}_i$, was approximately half as large. This information combined with the two assumed values of η produces two estimates for the neutral-wind velocity relative to the leading-edge velocity, $|\vec{V}_n - \vec{V}_i|$, as shown. The resulting estimates of the striation onset time and the time for well-developed striations are also shown. These time estimates are consistent with the observation of structured ionization R + 48 min. By adjusting the time lapse between release and sunset on the ESTHER cloud by the two different estimates of the time scale for development of the ESTHER cloud, we estimate that the equivalent age of the ESTHER ion cloud was between 40 and 57 min. It is probable that in terms of its stage of development, the ESTHER ion cloud at sunset was little more than 50% older than the SPRUCE ion cloud. This conclusion is consistent with the observation that the length of the ESTHER ion cloud at sunset was little more than 50% longer than the length of the SPRUCE ion cloud when the sun set on it.

Information on the FERN ion cloud is not included in Table 2 because the FERN cloud did not behave in the normal manner. The observation of the FERN ion cloud two hours after release indicates that its development was even more complex than the development of the DIANNE ion cloud. Another sympton of its unusual behavior is the observation, made by both the incoherent-scatter radar and the probe rockets through the FERN ion cloud, that ionization associated with the release descended to low

altitudes very rapidly. Because ionization existed near the magnetic zenith of both the Tyndall and C-6 optical sites, it was possible to make some estimates of the velocity of different portions of the ion cloud. It was found that portions of the ion cloud far from the release point were moving with a smaller velocity than portions closer to the release point. This result indicates that the development of the ion cloud was complicated and nonuniform. We emphasize that its development in terms of the model description given in Section IV is not appropriate.

REFERENCES

1. L. M. Linson and D. C. Baxter, "Ion Cloud Modeling, "SAI-77-918-LJ, Final Report, Contract DNA 001-76-C-0274, Science Applications, Inc., La Jolla, California (in press).

2. V. Gonzalez, "UHF Radar Data Analysis," these Proceedings.

3. S. Chavin and R. W. Kilb, personal communication (January 1977).

4. W. Boquist et al., "High-Resolution Ground Optics Measurements," these Proceedings.

5. K. D. Baker, J. C. Ulwick, M. C. Kelley, L. C. Howlett, G. D. Allred, D. Delorey, and N. Grossbard, "Electron Density Structure in Barium Clouds--Measurements and Interpretation," these Proceedings.

6. R. D. Hake and N.J.F. Chang, "TV Tracking System," these Proceedings.

7. W. Boquist, R. Deuel, S. Hawks, P. Crawley, and D. Overbye, "High Resolution Optical Measurements of ARPA Project SECEDE II, RADC-TR-72-307, Final Technical Report, Contract F30602-71-C-0364, Technology International Corporation, Bedford, Massachusetts (November 1972).

8. L. M. Linson and J. B. Workman, "Formation of Striations in Ionospheric Plasma Clouds," J. Geophys. Res., Vol. 75, p. 3211 (June 1970).

CHEMICAL RELEASE PAYLOADS

P. Kirschner

Thiokol Corporation
Ogden, Utah

CHEMICAL RELEASE PAYLOADS

P. Kirschner

Thiokol Corporation
Ogden, Utah

I INTRODUCTION

Project STRESS, sponsored by the Defense Nuclear Agengy (DNA), is
an experiment to evaluate satellite communications in an ionosphere dis-
turbed by the plasma cloud of a large barium release. Project STRESS
was conducted in two phases: Pre-STRESS, occurring in November-December
1976, and STRESS, occurring in February-March 1977. Pre-STRESS consisted
of a single 48-kg barium release to test the overall mission requirements.
This release event, called ANNE, was conducted on 1 December 1976 at 1709
CST from Eglin Air Force Base. The STRESS events BETTY, CAROLYN, DIANNE,
ESTHER, and FERN were conducted during the period of 26 February to 14
March 1977 from the same location.

This report deals only with one portion of Project STRESS--namely,
the manufacture of the six 48-kg barium-barium nitrate payloads and the
associated field service operations at Eglin Air Force Base during the
November-December 1976 and February-March 1977 periods.

II PROGRAM HISTORY

A. General

Contract DNA001-76-C-0301 dated 30 June 1976 was received by Thiokol
Corporation on 16 July 1976. The scope of effort of this contract was to
furnish all labor, equipment, facilities, services, and materials to fabri-
cate all components and assemble four 48-kg barium payloads. Additionally,

Thiokol was to load a total of six 48-kg barium payloads with the barium-barium nitrate thermite mixture. (Two 48-kg payloads manufactured during a previous DNA contract were included in the chemical loading operation.)

Under this contract DNA supplied Thiokol with the necessary maraging steel, barium metal, and barium nitrate. Payloads were to be delivered starting on 21 December 1976 for the first unit and on 20 February 1977 for the sixth payload.

The field services modification to the contract providing for launch support at Eglin Air Force Base, Florida was received on 27 October 1976. Two trips for two payload engineers for a total of 42 days at Eglin were contracted for.

On 3 November 1976, eighteen 16-kg barium canisters were shipped from Thiokol's Wasatch Division facility located near Tremonton, Utah to the launch facility at Eglin Air Force Base without any obvious damage. The inert portion of the payloads was hand carried by the field service engineers who left for Eglin Air Force Base on 16 November 1976.

B. Pre-STRESS--Event ANNE

One 48-kg payload was assembled, checked out, and prepared for launch during the period of the 17th through the 23rd of November 1976. The first launch opportunity was scheduled for the evening of 29 November 1976. Due to a number of problems not related to the payload operation, such as unsuitable weather conditions, the first payload, Event ANNE, was not launched until 1 December 1976 at 1709 CST (2309 UT, 1 December 1976).

Payload operation was normal and the release occurred approximately 160 s after launch and could be observed visually for 45 minutes until the sun set on the cloud. Radar attempted to skin-track the rocket vehicle, but did not acquire it during its flight.

On 2 December the remaining five payloads, associated tools, and equipment were inventoried and packed for storage at Site A-15A. Field services personnel departed Eglin on 3 December.

C.   STRESS--Events BETTY, CAROLYN, DIANNE, ESTHER, and FERN

Thiokol project personnel returned to Eglin Air Force Base on 14
February 1977 to begin preparing the remaining five payloads for launch.
Due to the hazardous nature of the barium payloads, all assembly and
check-out activities were conducted at Site A-11, Building 9271. The
addition of a radar tracking beacon to the payload increased the overall
payload weight, which required changing the previously set barium release
time from 160 s to 175 s in order to maintain the desired release altitude
of 185 km. This was done only to the payload for Event BETTY in order to
leave the option open for other release times for the subsequent events.
The first opportunity to launch Event Betty was on 22 February, but vari-
ous problems delayed the launch until 26 February. Event BETTY was
launched at 2349:33.2 UT. Barium release occurred 174.2 s later at an
altitutde of 178.9 km. The payload was observed to operate normally.

Based on the lower-than-desired release altitude of BETTY, a new
release time of 190 s was programmed. The payload for CAROLYN was as-
sembled and checked out on 27 February and readied for launch on the
28th. Event CAROLYN was launched on 2 March 1977 at 2351:00 UT and re-
leased the barium cloud at an altitude of 190 km, 190.5 s after launch.
The payload operated normally.

Event DIANNE was launched on 7 March 1977 at 2358:00 UT. The barium
release occurred 188.2 s later at an altitude of 184 km. Again, the pay-
load performed normally.

Event ESTHER was launched on 13 March 1977 at 2258:00 UT. The barium
release occurred 188.8 s later at an altitude of 189 km. Normal payload
performance was observed.

Event FERN was launched on 14 March 1977 at 2243:00 UT. The barium
release occurred 188.8 s later at an altitude of 186 km. The payload
performed normally. With this launch, Project STRESS launch operations
were concluded.

Thiokol field service personnel departed Eglin Air Force Base on
15 February 1977.

III PAYLOAD DESCRIPTION

Project STRESS required that all barium releases be 48 kg and be of
the barium-barium nitrate formulation. The desired release altitude was
set at 185 km. Each 48 kg barium payload consisted of three barium can-
isters and a firing module. In addition, due to radar tracking problems
experienced during Pre-STRESS, all five STRESS payloads carried a C-band
radar beacon transponder. A nose cone completed the payload assembly
(Figure 1). The total payload weight and length including the radar
beacon and nose cone were 310 lb and 98 inches, respectively. The out-
side diameter of the payload was 9 inches.

The barium canisters were arranged in tandem with the firing module.
The C-band radar beacon module was placed between the firing module and
the nose cone. The outside diameter of the barium canisters formed the
outer surface of the payload assembly. The firing leads to the two aft-
most canisters were placed in slots located near the exterior surface of
the payload and were bonded in place. A layer of cork protected the
leads from aerodynamic heating and loading.

Each barium canister was made of maraging high-strength steel in
order to withstand the high operating pressures experienced during the
combustion process. The barium thermite grain is produced by mechanically
pressing the premixed barium metal and barium nitrate in layers into the
canister. A typical grain density of 2.8 gm/cm^3 is achieved. All ther-
mite mixing and loading operations are performed under an inert argon
atmosphere to preclude oxidation of the barium metal, or any accidental
ignition of the mixture. In order to reliably ignite this grain, a
pyrogen initiation system was designed. It consists of a TP-H1016 pro-
pellant pyrogen unit and 7 grams of boron-potassium nitrate pellets.
Two Holex 3200 squibs initiate the pyrogen system electrically (two
squibs are used for system redundancy only, one squib will initiate the
pyrogen reliably). The sustained hot gas output from the igniter plus
the gases from the barium-barium nitrate reaction from the thermite
grain will rapidly raise the gaseous products to stable burning in a
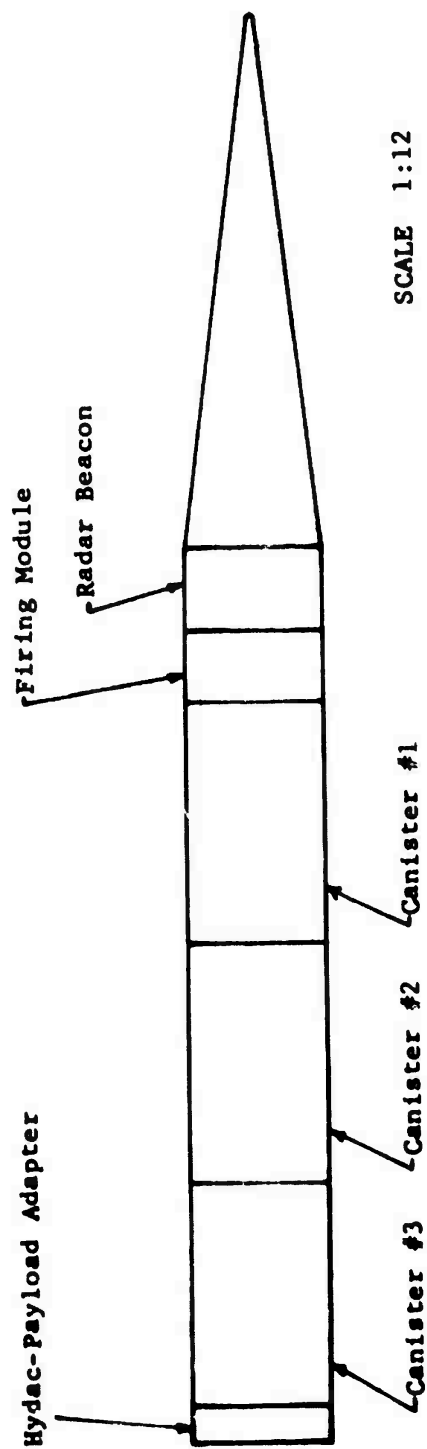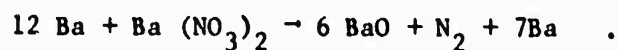vacuum environment.

Firing Module
Radar Beacon

Hydac-Payload Adapter

Canister #3

Canister #2

Canister #1

SCALE 1:12

FIGURE 1   48-kg BARIUM PAYLOAD ASSEMBLY

The barium-barium nitrate formulation reacts according to the equation:

$$12 \text{ Ba} + \text{Ba}(NO_3)_2 \rightarrow 6 \text{ BaO} + N_2 + 7\text{Ba} \quad .$$

This reaction has no extraneous metals in the combustion products and generates nitrogen to produce the high combustion pressure. Thus, no pressurizing additives need to be introduced. Typical pressures experienced and measured in ground tests are in excess of 6,000 psi as compared to 700 to 800 psi for the more standard barium-cupric oxide formulations.

A comparison between the barium-barium nitrate and barium-cupric oxide with barium azide pressurization additive formulations is shown in Table 1.

Table 1

COMPARISON OF BARIUM THERMITE FORMULATION

	2.5 Ba + CuO		12 Ba + Ba$(NO_3)_2$	
	Weight (percent)	Weight (kg)	Weight (percent)	Weight (kg)
Total chemical weight	100	16.0	100	16.0
Composition				
Barium azide, Ba$(N_3)_2$	1.8	0.29	--	--
Barium metal, Ba	79.8	12.77	86.3	13.81
Cupric oxide, CuO	18.4	2.94	--	--
Barium nitrate, Ba$(NO_2)_2$	--	--	13.7	2.19
Excess Ba available	47.8	7.65	50.4	8.05
Theoretical Ba vapor yield	17.5	2.80	28.0	4.48
Vacuum chamber Ba vapor yield	2.7	0.48	11.6	1.86

The firing module housed the two Raymond mechanical timers, battery pack assembly, barometric switches, and payload enabling Safe/Arm connectors. The circuit was designed to provide redundant initiation pulses to the barium canisters. The switch closure of the single-event timer could be preset prior to payload assembly in the field to the desired release time after launch. Timer start was initiated by the first motion of the rocket vehicle. A four-lead umbilical was incorporated into the electrical circuitry to charge, discharge, and load test the battery-pack assembly prior to flight. Barometric switches and a Safe/Arm enabling connector provided safety to personnel working on the payload.

IV CONCLUSIONS AND RECOMMENDATIONS

No problems were experienced in the procedure of mounting the payload to the rocket motor or during the flight phase. The survival of the C-band radar tracking beacon after the barium release implies that a telemetry system could survive the high shock generated by the release. This has not been the case during the recent past where telemetry systems had failed.

During the assembly process, some problems did arise. However, they were more of a minor nature. A better access to the timer setting arms would have precluded partial disassembly of the firing module. Also it is recommended that, in the future, if this payload should be utilized again, a connector be placed between the firing module and the three barium canisters. This rather minor change would permit the setting of release times as late as six hours before launch instead of 24 hours. The longer time is needed to provide adequate epoxy drying covering the electrical leads in the slots, as discussed before.

Distribution List

DEPARTMENT OF DEFENSE

Assistant to the Secretary of Defense
Atomic Energy
    ATTN: Executive Assistant

Command and Control Technical Center
Department of Defense
    ATTN: C-650

Defense Advanced Research Projects Agency
    ATTN: NMRO
    ATTN: STO

Defense Communication Engineer Center
    ATTN: Code R410 J. McLean
    ATTN: Code R820

Defense Communications Agency
    ATTN: Code 103 M. Raffensperger
    ATTN: Code 480
    ATTN: Code 810 R. Rostron
    ATTN: Code 101B

Defense Documentation Center
Cameron Station
 12 cy ATTN: DD

Defense Nuclear Agency
    ATTN: STVL
    ATTN: DDST
 4 cy ATTN: TITL
    ATTN: RAAE

Field Command
Defense Nuclear Agency
    ATTN: FCPR

Interservice Nuclear Weapons School
    ATTN: TTV

Joint Chiefs of Staff
    ATTN: J-3 WWMCCS Evaluation Office

Joint Strategic Target Planning Staff
    ATTN: JLTW-2

Livermore Division Field Command DNA
    ATTN: FCPRL

National Security Agency
    ATTN: R52 J. Skillman
    ATTN: R5

NATO School (SHAPE)
    ATTN: U.S. Documents Officer

Under Secretary of Defense for Research and
Engineering
    ATTN: Strategic & Space Systems
        (OS)

WWMCCS System Engineering Org
    ATTN: R. Crawford

DEPARTMENT OF ARMY

BMD Advanced Technology Center
    ATTN: ATC-T M. Capps

Harry Diamond Laboratories
    ATTN: DELHD-NP
    ATTN: DELHD-TI M. Weiner

U.S. Army Comm-Elec Engineering Instal Agency
    ATTN: EED-PED G. Lane

U.S. Army Foreign Science and Technical Center
    ATTN: DRXST-SD

U.S. Army Satellite Communications Agency
    ATTN: Document Control

U.S. Army Trading and Document Analysis
Activity
    ATTN: ATAA-SA

DEPARTMENT OF NAVY

Naval Electronic Systems Command
    ATTN: Code 5011

Naval Intelligence Support Center
    ATTN: STIC 12, Mr. Dubbin

Naval Ocean Systems Center
    ATTN: Code 532

Naval Research Laboratory
    ATTN: Code 7127, C. Johnson
    ATTN: Code 5430
    ATTN: Code 6700, T. Coffey
    ATTN: Code 5400, B. Wald

Naval Surface Weapons Center
    ATTN: Code F31

Navy Space Systems Activity
    ATTN: Code 52

Office of Naval Research
    ATTN: Code 461

Strategic Systems Project Office
    ATTN: NSSP-2722, F. Wimberly
    ATTN: NSP-2141

DEPARTMENT OF THE AIR FORCE

Air Force Avionics Laboratory, AFSC
    ATTN: AAD, A. Johnson

Air Force Geophysics Laboratory, AFSC
    ATTN: OPR-1, J. Ulwick
    ATTN: PHP, J. Aarons
    ATTN: PHD, J. Buchau
    ATTN: PHD, J. Mullen

Distribution List

DEPARTMENT OF THE AIR FORCE (Continued)

Air Force Technical Applications Center
       ATTN: TN

Air Force Weapons Laboratory, AFSC
       ATTN: DYC, J. Barry
       ATTN: SUL
       ATTN: DYC, J. Kamm
       ATTN: DYT, M. Fry

Foreign Technology Division
Air Force Systems Command
       ATTN: NICD Library

Rome Air Development Center
Air Force Systems Command
       ATTN: Documents Library/TSLD

Space and Missile Systems Organization/MN
Air Force Systems Command
       ATTN: MNNL, Ltc. Kennedy

Space and Missile Systems Organization/SK
Air Force Systems Command
       ATTN: SKA, M. Clavin

Space and Missile Systems Organization/YA
Air Force Systems Command
       ATTN: YAT, L. Blackwelder

Strategic Air Command/XPFS
       ATTN: NRT
       ATTN: XPFS, B. Stephan
       ATTN: ADWATE, B. Bauer

DEPARTMENT OF ENERGY

Lawrence Livermore Laboratory
       ATTN: Doc Con for Technical Information Dept.

Los Alamos Scientific Laboratory
       ATTN: Doc Con for R. Jeffries
       ATTN: Doc Con for J. Wolcott
       ATTN: Doc Con for J. Zinn

Sandia Laboratories
       ATTN: Doc Con for W. Brown
       ATTN: Doc Con for T. Wright
       ATTN: Doc Con for D. Dahlgren
       ATTN: Doc Con for J. Martin

OTHER GOVERNMENT

Central Intelligence Agency
       ATTN: OSI/PSID

Institute for Telecommunications Sciences
National Telecommunications & Info Admin
       ATTN: W. Utlaut

OTHER GOVERNMENT (Continued)

NASA
Goddard Space Flight Center
       ATTN: P. Corrigan

DEPARTMENT OF DEFENSE CONTRACTORS

Aerospace Corp.
       ATTN: N. Stockwell
       ATTN: SMFA for PWW
       ATTN: I. Garfunkel
       ATTN: J. Carter

Berkeley Research Associates, Inc.
       ATTN: J. Workman

Boeing Co.
       ATTN: D. Murray
       ATTN: G. Keister

Charles Stark Draper Lab, Inc.
       ATTN: D. Cox
       ATTN: J. Gilmore

Computer Sciences Corp.
       ATTN: J. Spoor
       ATTN: C. Nail

Cornell University
       ATTN: D. Farley, Jr.

Electrospace Systems, Inc.
       ATTN: Security, P. Phillips

FSL, Inc.
       ATTN: J. Marshall
       ATTN: C. Prettie

General Electric Co.
       ATTN: F. Reibert

General Electric Co.--TEMPO
Center for Advanced Studies
       ATTN: W. Knapp
       ATTN: DASIAC

General Research Corp.
Santa Barbara Division
       ATTN: J. Ise, Jr.
       ATTN: J. Garbarino

Geophysical Institute
University of Alaska
       ATTN: Technical Library

Illinois, University of
Department of Electrical Engineering
       ATTN: K. Yeh

Institute for Defense Analyses
       ATTN: E. Bauer

Distribution List

International Tel & Telegraph Corp.
      ATTN: Technical Library

JAYCOR
      ATTN: S. Goldman

Johns Hopkins University
Applied Physics Lab
      ATTN: T. Potemra
      ATTN: Document Librarian
      ATTN: J. Dassoulas

Kaman Sciences Corp.
      ATTN: T. Meagher

Linkabit Corp.
      ATTN: I. Jacobs

Lowell Research Foundation, University of
      ATTN: K. Bibl

M.I.T. Lincoln Lab
      ATTN: D. Towle

McDonnell Douglas Corp.
      ATTN: Technical Library Services

Mission Research Corp.
      ATTN: R. Kilb
      ATTN: R. Hendrick
      ATTN: R. Bogusch
      ATTN: F. Fajen
      ATTN: D. Sappenfield

Mitre Corp.
      ATTN: W. Foster
      ATTN: W. Hall

R & D Associates
      ATTN: W. Karzas
      ATTN: C. McDonald
      ATTN: R. LeLevier
      ATTN: B. Gabbard

Rand Corp.
      ATTN: E. Bedrozian
      ATTN: C. Crain

Science Applications, Inc.
      ATTN: D. Hamlin
      ATTN: L. Linson
      ATTN: D. Sachs

SRI International
      ATTN: R. Leadabrand
             W. Chesnut
             D. McDaniel
             C. L. Rino
             R. Hake, Jr.
             V. Gonzales

System Science Software
      ATTN: J. Cane
             E. Gaffney

Technology International Corp.
      ATTN: W. P. Boquist